

**Disruption of the medial entorhinal grid cell network in a mouse model of early  
Alzheimer's disease**

Johnson Ying

Integrated Program in Neuroscience

McGill University, Montreal

April 2023

A thesis submitted to McGill University in partial fulfillment of the requirements of the degree  
of Doctor of Philosophy in Neuroscience

© Johnson Ying 2023

## Table of Contents

Abstract .....	4
Résumé.....	5
Acknowledgements.....	7
Contribution to Original Knowledge .....	8
Contribution of Authors.....	9
List of Figures and Tables.....	11
List of Abbreviations .....	14
Other Notes .....	15
Introduction.....	16
Chapter 1: Literature Review.....	19
1.1. The spatial navigation system in rodents .....	19
1.1.1. Entorhinal-hippocampal circuitry .....	21
1.1.2. Place cells.....	27
1.1.3. Head-direction cells .....	30
1.1.4. Grid cells.....	32
1.1.5. Other spatially-tuned MEC cells.....	35
1.2. Path integration .....	36
1.2.1. Neural basis of path integration in rodents .....	38
1.2.2. Grid cells and the hippocampus.....	40
1.2.3. Grid cells and orientation coding.....	40
1.2.4. Grid cells and speed coding .....	41
1.3. Alzheimer’s disease .....	43
1.3.1. Amyloid hypothesis .....	46
1.3.2. Tau hypothesis .....	48
1.3.3. AD progression .....	50
1.3.4. Importance of early diagnosis.....	54
1.3.5. Path integration as an early cognitive marker.....	56
1.3.6. Grid cells as an early biomarker .....	57
Chapter 2: Disruption of the grid cell network in a mouse model of early Alzheimer’s disease .	59
Abstract .....	59
Introduction.....	60
Results.....	61

Discussion .....	69
Methods.....	76
References.....	90
Acknowledgements.....	94
Author Contributions .....	94
Competing Interests .....	94
Figure Legends.....	95
Supplementary Information .....	106
FORWARD TO CHAPTER 3 .....	143
Chapter 3: Grid cell disruption in a mouse model of early Alzheimer’s disease reflects reduced integration of self-motion cues and increased influence of environmental geometry .....	144
Abstract .....	145
Introduction.....	146
Results.....	147
Discussion .....	153
Acknowledgements.....	157
Author contributions .....	157
Declaration of interest.....	157
Figures and legends.....	158
Supplementary Information .....	166
Methods.....	174
References.....	180
Chapter 4: General Discussion.....	186
4.1. How can grid cell impairments explain path integration deficits .....	186
4.2. Parallels to human AD literature.....	189
4.3. Parallels to other APP mouse models .....	190
4.4. Potential circuit-level mechanisms for grid cell impairments .....	192
4.5. Grid cells and path integration tasks have clinical value .....	194
Conclusion and summary.....	196
References.....	197

## Abstract

Spatial navigation and path integration impairments are sensitive markers of pathological decline during the early stages of Alzheimer's disease (AD). To investigate the neural circuit operations that may cause these navigational deficits, we conducted *in-vivo* electrophysiological recordings of spatially-tuned neurons in the medial entorhinal cortex (MEC) and region CA1 of the hippocampus in the J20 transgenic amyloid beta (A $\beta$ ) mouse model of early AD. Entorhinal grid cells showed reduced spatial periodicity, spatial stability, and synchrony with interneurons and head-direction cells. In contrast, the spatial coding of non-grid cells within the MEC, and place cells within CA1, remained intact. Grid cell deficits emerged at the earliest incidence of A $\beta$  fibril deposition and correlated with impaired spatial memory performance in a path integration task.

To further substantiate a link between disrupted grid coding and path integration deficits in J20 mice, we investigated if disrupted early AD grid coding reflects increased noise across the network or a specific deficit in path integration, perhaps via an impairment in the integration of self-motion cues. We found that J20 grid cells were spatially unstable towards the center of the square arena but not near the borders, had qualitatively different spatial components that aligned parallel to the borders of the environment, and exhibited impaired integration of distance travelled via reduced theta phase precession. Together, our results 1) support the viability of grid cell integrity and spatial navigation deficits as early markers of AD; 2) suggest that early AD grid cell impairments reflect a preferential alignment to the external world and likely cause path integration deficits in preclinical individuals via reduced integration of self-motion cues.

## Résumé

Les troubles comportementaux de navigation spatiale et d'intégration de chemin sont des marqueurs fiables du déclin pathologique au cours des premiers stades de la maladie d'Alzheimer (MA). Pour étudier les opérations du circuit neuronal qui peuvent causer ces déficits de navigation, nous avons effectué des enregistrements électrophysiologiques de neurones accordés spatialement dans le cortex entorhinal médian (MEC) et la région CA1 de l'hippocampe dans le modèle de souris transgénique amyloïde bêta ( $A\beta$ ) J20. Les cellules de grille entorhinale ont montré une perturbation de la périodicité spatiale, de la stabilité spatiale et de la synchronie avec les interneurons et les cellules de direction de la tête. En revanche, le codage spatial des cellules non-grille dans le MEC et CA1 sont restés intacts. Les déficits des cellules de grille sont apparus à la première incidence du dépôt de fibrilles  $A\beta$  et ont coïncidé avec des performances de mémoire spatiale altérées dans une tâche d'intégration de chemin.

Pour mieux établir un lien entre le codage de grille perturbé et les déficits d'intégration de chemin chez les souris J20, nous avons étudié si les déficiences précoces de la grille AD reflétaient une plus grande influence des repères externes par rapport aux signaux d'auto-mouvement, ou simplement une augmentation du bruit neuronal. Nous avons découvert que la géométrie environnementale exerçait une plus grande influence sur le codage des cellules de la grille que l'auto-mouvement. Les cellules de la grille J20 étaient spatialement instables vers le centre de l'arène carrée mais pas près des bords, présentaient une intégration altérée de la distance parcourue via la précession de la phase thêta et étaient plus actives parallèlement aux bords. Ensemble, nos résultats 1) soutiennent la viabilité de l'intégrité des cellules de la grille et des déficits de navigation spatiale en tant que marqueurs précoces de la MA ; 2) suggèrent que les déficiences précoces des cellules de la grille AD reflètent un alignement préférentiel sur le monde extérieur et provoquent

des déficits d'intégration de chemin chez les individus précliniques via une intégration réduite des signaux d'auto-mouvement.

## Acknowledgements

I thank my supervisor, Dr. Mark P. Brandon, for giving me an opportunity to pursue something meaningful with my life when I applied for an undergraduate volunteer position 7 years ago. Mark helped me foster the right attitude and taught me the skills and patience necessary to succeed in a research environment. I thank the members of my Committee, Dr. Tak Pan Wong and Dr. Sylvain Williams, as well as my IPN mentor, Dr. Lalit Srivastava, for providing me project feedback and encouragement throughout grad school. I thank the *Fonds de la recherche en santé du Québec* and the *Canadian Institutes of Health Research* agencies for funding a large portion of my training. I thank my lab mates for numerous helpful discussions, particularly Dr. Alexandra T. Keinath, Raphael Lavoie, Dr. Hyun Choong Yong and Sooyeon Kim who significantly contributed to my scientific success and helped me work through a lot of growing pains throughout grad school. I thank my parents for supporting me throughout grad school, which allowed me to focus on research without distractions.

## Contribution to Original Knowledge

1. Grid cells are disrupted during the early stages of A $\beta$  pathology in the J20 transgenic mouse model of AD. Adult J20 grid cells showed reduced spatial periodicity, spatial stability, and synchrony with interneurons and head-direction cells. Young J20 grid cells had a less severe impairment, and only showed reduced synchrony with interneurons and head-direction cells. (Note that both “young” and “adult” refer to the early stages of pathology between 3-7 months of age in this mouse model. Data were divided between “young” and “adult” to better capture longitudinal effects).
2. In contrast, the spatial coding of other non-grid spatial cell types in the MEC and place cells in CA1 remained intact.
3. Grid cell impairment coincides with worsened PI behavior in both young and adult J20 mice, suggesting that grid cell integrity and PI performance are sensitive early markers of AD.
4. Adult J20 grid cells were spatially unstable towards the center but not near the borders.
5. Adult J20 grid cells exhibited reduced theta modulation and distance coding via theta phase precession.
6. A two-dimensional Fourier analysis revealed that reduced hexagonal symmetry in adult J20 grid cells could be directly explained by increased spatial firing aligned parallel to the borders.
7. Points 4-6 collectively suggest that early AD grid cell impairments reflect a preferential alignment to the external world and likely cause path integration deficits in preclinical individuals via reduced integration of self-motion cues.

## Contribution of Authors

### Chapter 1 and Chapter 4:

Segen, V\*., Ying, J\*. *et al.* (2022) **Path integration in normal aging and Alzheimer's disease.** *Trends Cogn. Sci.* 26, 142–158.

\*Equal first author

The literature review and discussion (Chapter 4) sections contain excerpts from a first co-authored review article about path integration in normal aging and AD. This article was written in collaboration with Vladislava Segen from Thomas Wolbers's lab in DZNE, Magdeburg.

### Chapter 2:

Ying, J. *et al.* (2022) **Disruption of the grid cell network in a mouse model of early Alzheimer's disease.** *Nat. Commun.* 13, 886.

Mark P. Brandon and I conceptualized all experiments carried out in Chapters 2 and 3. I carried out all stereotaxic surgeries and collected most of the electrophysiological dataset. All recording drives were built by Sooyeon Kim prior to implantation. Part of the electrophysiological data was collected by undergraduate volunteer students in the lab: Elena He, Kianoush Harandian, Dhanesh Patel, Aiten Ismailova, Andy Zhen, Antoine Milette-Gagnon, and Nailya Ismailova. Histological reconstruction of tetrode recording tracks were performed by Sooyeon Kim. Mark P. Brandon and Alexandra T. Keinath performed the bulk of all analyses for the neural data. I carried out all behavioral testing and wrote all behavioral analysis scripts. Immunohistochemical

experiments were performed by Raphaël Lavoie. Immunoradiographic experiments were performed by Erika Vigneault from Salah El Mestikawy's laboratory.

### **Chapter 3:**

Ying, J. *et al.* (2022) **Grid cell disruption in a mouse model of early Alzheimer's disease reflects reduced integration of self-motion cues and increased influence of environmental geometry.** *In preparation.*

Mark P. Brandon, Motoharu Yoshida, Antonio Rebores and I conceived the project and wrote the manuscript. Antonio Rebores and I conducted data analysis.

## List of Figures and Tables

### Chapter 1.

- Figure 1. Edward Tolman's sunburst maze.
- Figure 2. Main entorhinal cortex projections.
- Figure 3. Hippocampal circuit.
- Figure 4. General entorhinal-hippocampal connectivity.
- Figure 5. Major parahippocampal projections.
- Figure 6. Place cell firing properties.
- Figure 7. Head-direction cell firing properties.
- Figure 8. Grid cell firing properties.
- Figure 9. Other spatially-modulated cell types in the MEC.
- Figure 10. Homing vector computation by path integration.
- Figure 11. The amyloidogenic pathway.
- Figure 12. The amyloid cascade hypothesis.
- Figure 13. A hypothetical model of early *in-vivo* AD biomarker progression.

### Chapter 2.

- Figure 1. Reduction of grid cell spatial periodicity in adult APP transgenic mice.
- Figure 2. Medial entorhinal head direction cells, non-grid spatially-tuned cells, CA1 place cells, and medial entorhinal theta oscillations in adult APP mice.
- Figure 3. Grid cells in adult APP mice are spatially unstable.
- Figure 4. Reduced spike-time synchrony in grid cell-interneuron and grid cell-head direction cell pairs.
- Figure 5. Path integration is impaired in APP mice and worsens across age.
- Supplementary Table 1. Summary of MEC cell yield within subject.
- Supplementary Table 2. Summary of CA1 cell yield within subject.
- Supplementary Figure 1. Quantification of amyloid-beta plaques in APP mice.
- Supplementary Figure 2. Tetrode track histology for MEC recordings.

Supplementary Figure 3. Creation of raster plots indicating the strength of rotational correlation of each cell.

Supplementary Figure 4. Example of well-isolated waveforms of four grid cells recorded in nTG-a and APP-a mice.

Supplementary Figure 5. Spike isolation quality of grid cells.

Supplementary Figure 6. Spatial tuning of grid cells, but not head-direction cells or non-grid spatial cells, is disrupted across age in APP mice.

Supplementary Figure 7. Grid cell spatial tuning remains impaired in adult APP mice when duplicate cell counts are removed.

Supplementary Figure 8. Top 15 quality cells across groups.

Supplementary Figure 9. Tetrode track histology for CA1 recordings.

Supplementary Figure 10. The magnitude of theta frequency reduction in APP mice is roughly equal across all running speeds.

Supplementary Figure 11. Intact speed coding in APP mice.

Supplementary Figure 12. Mean 2D displacement is higher in grid cells, but not non-grid spatially-tuned cells or place cells, in adult APP mice.

Supplementary Figure 13. Reduced grid cell spatial stability in adult APP mice persists across different partition lengths.

Supplementary Figure 14. Positional coverage and running speeds across groups for MEC and CA1 recordings.

Supplementary Figure 15. Interneuron firing properties.

Supplementary Figure 16. Slower intrinsic theta rhythmicity and reduced theta power in APP mice.

Supplementary Figure 17. Grid cell synchrony with interneurons and head-direction cells are both impaired in APP mice.

Supplementary Figure 18. Experimental timeline for the path integration task and mouse performance across days.

Supplementary Figure 19. Overall navigation ability improves in light trials for all mice.

Supplementary Figure 20. APP mice have impaired path integration ability in light conditions.

Supplementary Figure 21. Immunohistochemical labelling of synaptic markers in MEC and CA1.

Supplementary Figure 22. We used the fitlme function in MATLAB to perform linear mixed effects analyses on the relationship between the subjects' genotype (nTG and APP),

age (young and adult) and expression of VGLUT3 and VGLUT1 levels in the MEC and CA1 respectively.

Supplementary Figure 23. Pathological expression of MEC VGLUT3 levels and CA1 VGLUT1 levels in APP mice.

Supplementary Figure 24. VGLUT3 levels in the MEC and VGLUT1 levels in the CA1 are both higher in APP mice.

### **Chapter 3.**

Figure 1. Adult APP grid cells are spatially unstable in the center of the environment.

Figure 2. Adult APP MEC neurons more frequently adopt quadrant-like spatial alignment.

Figure 3. Adult APP grid cells align parallel to the borders.

Figure 4. Adult APP grid cells have reduced theta modulation and theta phase precession.

Supplementary Figure 1. Tetrode track locations.

Supplementary Figure 2. Unbiased spatial stability analyses for grid cells.

Supplementary Figure 3. Fourier component wavelengths.

Supplementary Figure 4. Retrieval of 3-component hexagonal grid cells via correction.

Supplementary Figure 5. Grid cells, their Fourier components, and polar representations.

Supplementary Figure 6. Fourier components reflect rate map content, and not the square shape of images.

## List of Abbreviations

<b>2D</b>	Two-dimensional
<b>AD</b>	Alzheimer's disease
<b>A<math>\beta</math></b>	Amyloid beta
<b>ADRDA</b>	Alzheimer's Disease and Related Disorders Association
<b>ANOVA</b>	Analysis of variance
<b>ANCOVA</b>	Analysis of co-variance
<b>ATN</b>	Anterior thalamic nuclei
<b>APOE</b>	Apolipoprotein E
<b>APP</b>	Amyloid precursor protein
<b>CSF</b>	Cerebrospinal fluid
<b>DG</b>	Dentate gyrus
<b>EC</b>	Entorhinal cortex
<b>fMRI</b>	Functional magnetic resonance imaging
<b>FTD</b>	Frontal temporal dementia
<b>HD</b>	Head-direction
<b>LEC</b>	Lateral entorhinal cortex
<b>MEC</b>	Medial entorhinal cortex
<b>MCI</b>	Mild cognitive impairment
<b>MRL</b>	Mean resultant length
<b>NIA-AA</b>	National Institute on Aging and Alzheimer's Association
<b>NFT</b>	Neurofibrillary tangles
<b>NINCDS</b>	National Institute of Neurological and Communicative Disorders and Stroke
<b>NT</b>	Neuropil threads
<b>PET</b>	Positron emission tomography
<b>PSEN</b>	Presenilin
<b>PV</b>	Parvalbumin-expressing
<b>SR</b>	Successor representation
<b>VCO</b>	Velocity-controlled oscillator

## **Other Notes**

This is a manuscript-based thesis. Figure numbers are self-contained within each chapter (i.e., Figure 1 will be referenced numerous times in different chapters). Likewise, citation numbering and style differ depending on which journals each manuscript was published in or prepared to be submitted to. Section order (i.e., methods, acknowledgements, etc.) for each manuscript will also slightly differ depending on which journal they were submitted to. The references section at the end of the thesis applies only to chapters 1 and 4 (the literature review and discussion).

## Introduction

AD accounts for 60-80% of dementia cases and affects over 6 million people aged 65 years and over in the USA alone [1]. Worldwide, over 55 million people live with AD and other dementias [2]. The estimated global healthcare cost attributable to dementia surpassed US\$ 263 billion in 2019 and represents a major economic burden [3]. To date, there is no cure for AD and interventional trials aimed at slowing the progression of AD are largely unsuccessful [4], in part due to the lack of sensitive markers that accurately identify the early stages of pathology [5]. Recent evidence in rodents and humans suggest that behavioral impairments in spatial navigation, and more specifically, path integration, are more sensitive markers of early pathology compared to traditional diagnostic approaches [5,6]. Path integration is a cognitive function involving the integration of self-motion cues to maintain one's sense of location relative to a starting point in space [7,8]. Individuals at genetic risk of AD and those with mild cognitive impairment (MCI) display path integration impairments up to decades preceding late AD pathology [9–13]. Compared to other forms of cognitive assessments such as episodic memory tests, path integration tasks are also simpler and cheaper to implement in the clinic [5].

However, it is unclear which neural codes underlie path integration impairments during early AD. Furthermore, the neural circuit operations impacted during the initial stages of pathology remain elusive in general. Spatial navigation and path integration deficits suggest that AD pathology exerts its earliest impact on the neural systems that support spatial memory which include the MEC and the hippocampus [14–16]. The MEC and hippocampus contain many spatially-tuned neurons that include, but are not limited to: grid cells, head-direction cells, non-grid spatially selective cells and place cells, all of which may contribute to path integration deficits during early AD [17–26].

In Chapter 2, to investigate how these spatially-tuned populations are impacted during early pathogenesis, we conducted *in-vivo* electrophysiological recordings of spatially-tuned neurons in the MEC and region CA1 of the hippocampus in the J20 transgenic A $\beta$  mouse model of early AD. To ensure that we conducted our recordings during the initial stages of pathology, we restricted our experimental timeline between 3-7 months of age – a period that precedes the deposition of widespread A $\beta$  plaques that are indicative of late AD [27]. We found that entorhinal grid cells showed reduced spatial periodicity, spatial stability, and synchrony with interneurons and head-direction cells. In contrast, the spatial coding of non-grid cells within the MEC, and place cells within CA1, remained intact. Grid cell deficits emerged at the earliest incidence of A $\beta$  fibril deposition and coincided with impaired spatial memory performance in a path integration task. These results suggest that a disrupted grid cell network may cause path integration impairments during early AD.

Yet, an alternative interpretation of these results is that grid cell disruption occurs due to impaired processing of external landmarks, and early path integration deficits result from pathological processes unrelated to grid cell coding or self-motion. In Chapter 3, to further substantiate a link between disrupted grid coding and path integration deficits in J20 mice, we investigated if disrupted early AD grid coding reflects increased noise across the network or a specific deficit in path integration, perhaps via an impairment in the integration of self-motion cues. We found that J20 grid cells were spatially unstable towards the center of the square arena but not near the borders, had qualitatively different spatial components that aligned parallel to the borders of the environment, and exhibited impaired integration of distance travelled via reduced theta phase precession.

Together, our results 1) support the viability of grid cell integrity and spatial navigation deficits as early markers of AD; 2) suggest that early AD grid cell impairments reflect a preferential alignment to the external world and likely cause path integration deficits in preclinical individuals via reduced integration of self-motion cues.

## Chapter 1: Literature Review

### 1.1. The spatial navigation system in rodents

Navigation is defined as the process of moving from one point in physical space to another [28]. It is not hard to imagine how navigation is crucial to survival, whether it be foraging for resources or prey avoidance. There are at least two broad categories of navigational strategies: the stimulus-response strategy and the place strategy. In the early 20th century, stimulus-response theories of learning posited that all responses of an organism are brought about and modified by external stimuli [29]. In the context of navigation, a stimulus-response strategy is rigid and involves performing a series of motor actions determined by associations to the layout of the physical environment. It is, in a sense, habit learning, where the taken trajectory is memorized. Stimulus-response strategies primarily rely on the caudate nucleus [30].

In the same century, Edward C. Tolman argued against the idea that navigation, and more broadly, animal behavior, is nothing more than stimulus-response associations [31]. Instead, Tolman suggested that animals learn an environment by encoding it into a mental representation. This ‘cognitive map’ is formed by learning the routes and spatial relationships between locations and landmarks, which are then flexibly used to guide meaningful behavior. To test this theory, rats were trained in an apparatus to move in a fixed path via an alleyway from a start point to an end point containing a food reward (**Figure 1**). Upon successful learning of this task, rats were then placed in the sunburst maze which contained multiple isolated paths that connected to the starting point. The start and end points remained in the same position as the previous paradigm, with the alleyway now blocked. One of these arms was the shortest distance to reach the food. The authors noted that overall, rats had a higher tendency to select the shortest path despite no prior experience in the sunburst maze. A stimulus-response strategy would not allow the rats to perform as well as

they did due to the novelty of the testing conditions. Therefore, Tolman concluded that animals formed a mental representation of the environment which allowed them to adapt and plan novel routes, often referred to as a place strategy.

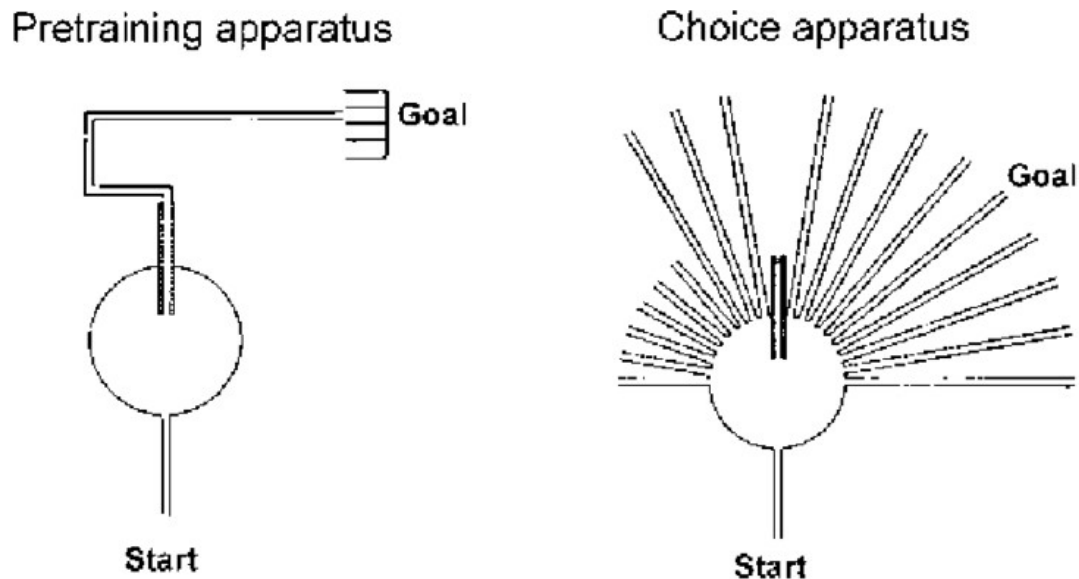


**Figure 1. Edward Tolman's sunburst maze.**

(Left) A schematic of the training apparatus where rats learned to follow a stereotyped path from the starting platform to the goal location. (Right) A schematic of the sun-burst maze which contains multiple paths radiating from the starting platform.

Figure taken from: Jeffery, K.J. *et al.* Studies of the hippocampal cognitive map in rats and humans. (2004).

The neural basis for a cognitive map was believed to involve the hippocampus following the discovery of place cells [19]. Extracellular single-cell recordings in region CA1 of the rat hippocampus revealed a group of neurons that only fired when the animal was active in specific locations of space. This finding provided the first evidence that a distinct population of neurons encoded an allocentric representation of the external world. This important discovery, along with lesion studies of the hippocampus, founded the 'cognitive map theory' of the hippocampus [23]. Later discoveries of spatially-tuned neurons in the MEC suggested that the neural basis for the

cognitive map includes surrounding parahippocampal regions [17,18,32]. The following subsections introduce the general anatomy of the rodent entorhinal-hippocampal circuit before describing place cells in the hippocampus and other various spatially-tuned neurons in the MEC.

### **1.1.1. Entorhinal-hippocampal circuitry**

The thalamus and primary sensory cortices receive unimodal sensory inputs which higher-order associational cortices then combine to form complex representations that are either unimodal or multimodal. The entorhinal cortex (EC) further processes these representations and projects to the hippocampus via the superficial layers. Hippocampal outputs project back to the deep layers of EC and then throughout the neocortex. This processing loop is not entirely hierarchical because brain regions can directly project to the hippocampus without the EC. But in general, the EC is analogous to a gateway that controls information flow into the hippocampus.

The EC is a six-layered cortical structure that can be subdivided into the lateral entorhinal cortex (LEC) and MEC, which are both reciprocally connected. The main EC inputs come from the perirhinal and postrhinal (also known as parahippocampal cortex in primates) cortices that also share reciprocal connections. In turn, the perirhinal and postrhinal cortices receive unimodal and multimodal information from various neocortical regions that are anatomically segregated. The perirhinal cortex largely receives olfactory, and lesser amounts of auditory and visual information from the piriform, insular, frontal, and temporal cortices. In contrast, the postrhinal cortex receives visual and visuospatial information from the cingulate, retrosplenial, parietal, occipital and temporal cortices [33–35]. The perirhinal and postrhinal cortices project to both EC subdivisions, but preferentially target the LEC and MEC, respectively [33]. In parallel, the EC subdivisions project back to the perirhinal and postrhinal cortices. The MEC is also reciprocally connected to the presubiculum and parasubiculum [36]. The presubiculum and parasubiculum are integration

sites of cortical and thalamic inputs. Some predominant ones include visual information from occipital cortices directly, or indirectly via the retrosplenial and postrhinal cortices, as well as idiothetic cues from thalamic nuclei [37–39]. Other minor direct cortical projections into the EC come from the amygdala, in addition to the retrosplenial, cingulate, posterior parietal, occipital, piriform, insular, and frontal cortices (**Figure 2**) [34,40].

Together, the perirhinal, postrhinal, entorhinal cortices, along with the presubiculum and parasubiculum form the parahippocampal region, which controls the bulk of cortical input flow to the hippocampus. Traditionally, the hippocampus was viewed as a unidirectional circuit whose outputs target the deep layers of EC. But the modern view is that individual hippocampal subregions also project directly to other parahippocampal areas. CA3, CA1 and the subiculum project to the presubiculum and parasubiculum. In parallel, CA1 and the subiculum project to the perirhinal and postrhinal cortices [41].

The hippocampus is a three-layered allocortical structure that comprises the dentate gyrus (DG), CA3, CA2, CA1 and the subiculum. Its C-shaped structure runs longitudinally along the septal-temporal pole, which starts from the septum (near the midline) and curves ventrally towards the temporal lobe (**Figure 3**). Alternatively, the septal-temporal pole is commonly referred to as the dorsal-ventral axis. The DG contains three sublayers: the molecular layer, the granule cell layer, and the polymorphic layer. The molecular layer contains the dendrites of granule cells. The granule layer contains the cell bodies of granule cells. Granule cells project to CA3 via axonal projections called mossy fibres from the polymorphic layer.

CA3 contains five sublayers: the stratum lacunosum-moleculare, the stratum radiatum, the stratum lucidum, the stratum pyramidale, and the stratum oriens. Mossy fibers project to CA3 pyramidal cell dendrites located in the stratum lucidum. The stratum pyramidale contains the cell

bodies of pyramidal cells. Pyramidal cell apical dendrites are in the stratum lacunosum-moleculare and the stratum radiatum, while their basal dendrites are in the stratum oriens. CA3 pyramidal cell axons recurrently target other CA3 pyramidal cells while also projecting to CA1 via the Schaffer collaterals. The distal and proximal parts of CA3 project to the proximal and distal parts of the stratum radiatum in CA1, respectively [41]. Between CA3 and CA1 is CA2. Aside from direct CA3-CA1 projections via the Schaffer collaterals, CA3 also connects to CA2 which then projects to CA1 [42]. The DG also directly projects to CA2 via the Schaffer collaterals [43]. The general anatomy of CA2 remains understudied compared to CA3 and CA1. CA1 has the same sublayers as CA3 except for the stratum lucidum. The proximal and distal parts of CA1 project to the distal and proximal parts of subiculum, respectively. CA1 and the subiculum also project to the deep layers of EC, thus completing the entorhinal-hippocampal loop. Backprojections in the hippocampus exist between CA3-DG, CA1-CA3, CA2-CA3 and subiculum-CA1 [41,44].

Layers 2 and 3 of the EC project to the hippocampus via the perforant and the temporoammonic pathways, respectively. Layer 2 targets DG, CA3, and CA2, while Layer 3 targets CA1 and subiculum [41,44]. Layer 3 might also target CA2, but this remains controversial [43,44]. The LEC and MEC project to the superficial and middle third of the dentate molecular layer, respectively [45,46]. The LEC and MEC project to the superficial and deep regions of the stratum lacunosum-moleculare of CA3, respectively [47]. Both the MEC and LEC target distal CA3, whereas proximal CA3 mainly receives inputs from the DG [47]. Via the temporoammonic pathway, the MEC projects to proximal CA1 and distal subiculum, whereas the LEC projects to distal CA1 and proximal subiculum. In parallel, there are a subset of excitatory neurons in Layer 2 of the MEC that project directly to CA1 [48]. CA1 and the subiculum project to Layers 5 and 6 of the EC, in addition to other parahippocampal regions as previously noted. The subiculum also

directly projects to the thalamus and throughout the neocortex. There is a topological organization of reciprocal connectivity between the dorsolateral–ventromedial axis of the EC (both MEC and LEC) and the septal-temporal axis of the hippocampus. The dorsolateral part of EC targets the septal hippocampus whereas the ventromedial part of EC targets the temporal hippocampus.

Although less studied, parahippocampal regions have direct projections to the hippocampus. The presubiculum and parasubiculum project to DG, CA3, CA1 and subiculum. The perirhinal cortex has connections to CA1 and subiculum, whereas the postrhinal cortex may project to all hippocampal subregions [41].

The main parahippocampal projections are shown in **Figures 4 and 5**.

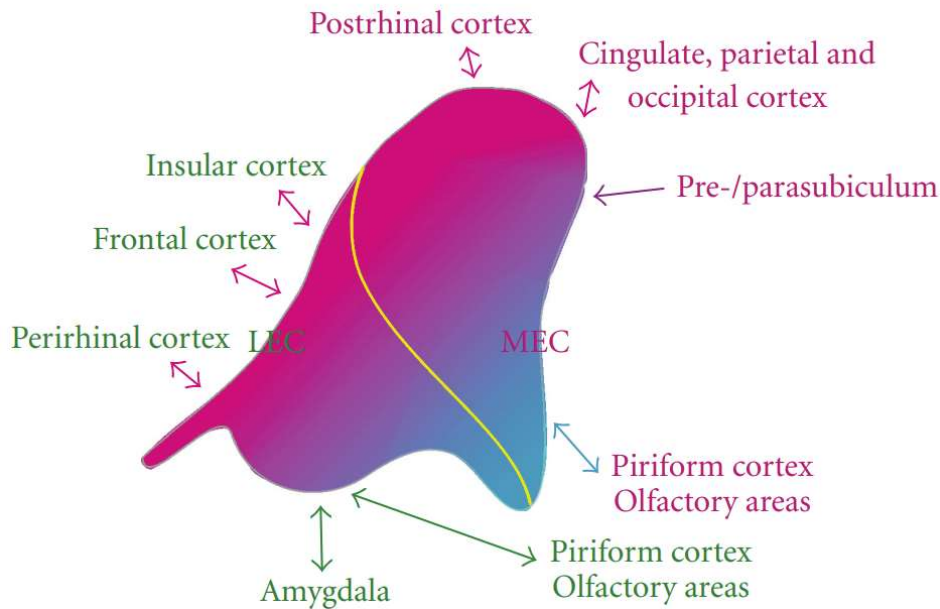


**Figure 2. Main entorhinal cortex projections.**

The entorhinal cortex has lateral and medial subdivisions. The main brain areas that project into the LEC and MEC are shown in green and magenta, respectively. Figure taken from [40].

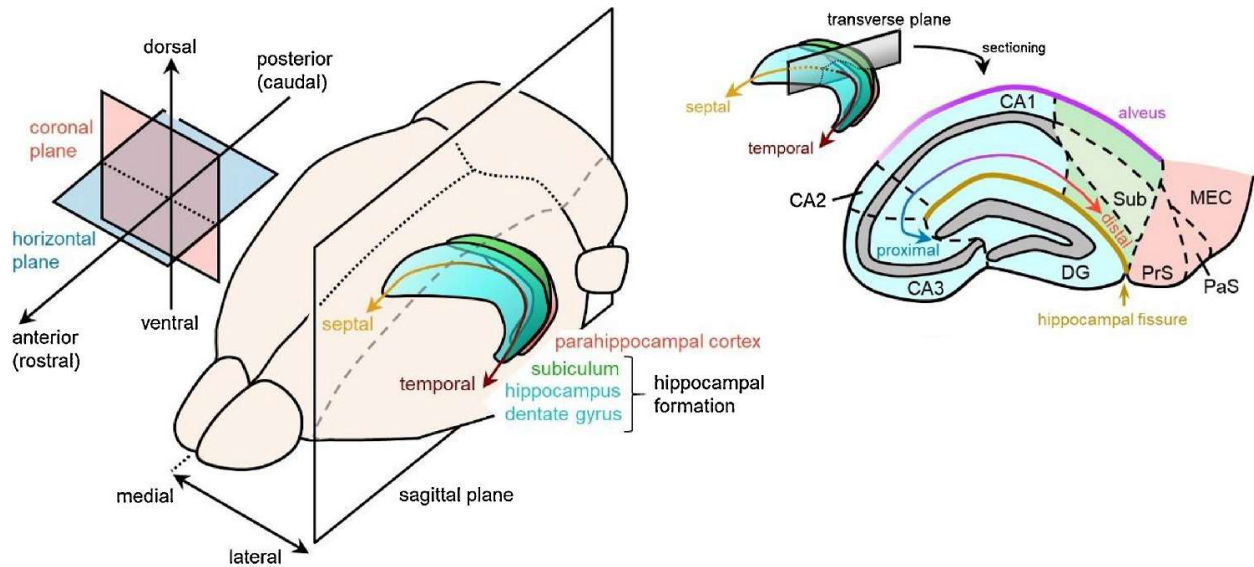


**Figure 3. Hippocampal circuit.**

(Left). The septal-temporal pole of the hippocampus starts at the septum and finishes at the temporal lobe. (Right) The hippocampus is made up of the dentate gyrus (DG), CA3, CA2, CA1 and the subiculum. Hippocampal subregions can be further divided into proximal (towards dentate gyrus) and distal regions (towards subiculum).

Figure taken from Matsumoto, N. *et al.* (2019) The subiculum: Unique hippocampal hub and more. *Neurosci. Res.* 143, 1–12.

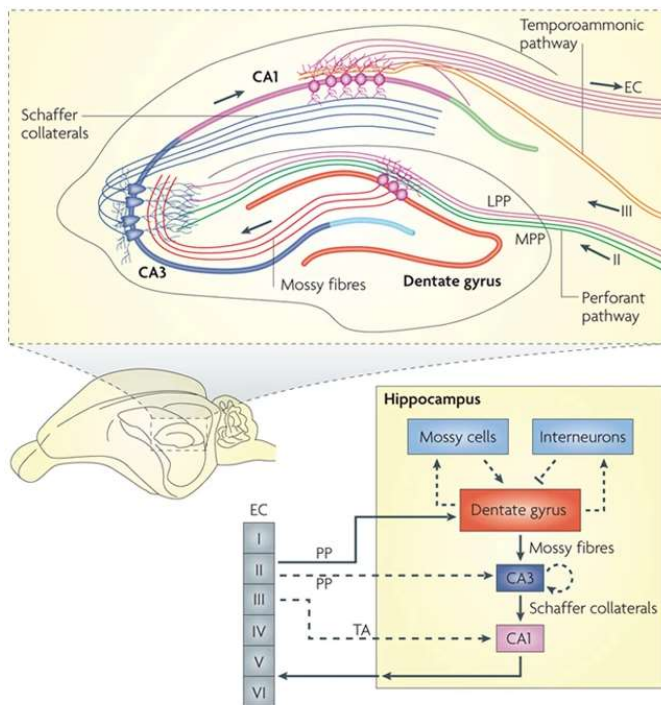


**Figure 4. General entorhinal-hippocampal connectivity.**

Layers 2 and 3 of the entorhinal cortex project to the hippocampus via the perforant (DG, CA3, CA2) and temporoammonic (CA1 and subiculum) pathways, respectively.

Granule cells in the DG receive inhibition from mossy cells and interneurons in the polymorphic layer. DG granule cells project to CA3 via axonal projections called mossy fibers. CA3 pyramidal cells have recurrent connectivity and project to CA1 via the Schaffer collaterals.

Figure taken from Deng, W. *et al.* (2010) New neurons and new memories: How does adult hippocampal neurogenesis affect learning and memory? *Nat Rev Neurosci.* 11, 339–350.



### 1.1.2. Place cells

Hippocampal place cells fire when the animal is in specific locations of space [19]. Place cells exist in CA1, CA3 and the subiculum, but only those in CA1 and CA3 will be described here. Different place cells have unique, and often non-overlapping firing fields in the same environment, providing no clear evidence for field location topography (**Figure 6a**) [49,50]. However, there is a field size topography where field sizes increase linearly from dorsal (< 1 meter in diameter) to ventral hippocampus (~10 meters in diameter) in rats [51–53]. In addition, while a place cell generally has 1 or 2 firing fields, additional fields can form in larger testing arenas [54]. These findings suggest that the cognitive map flexibly encodes space of varying scales and sizes.

When recorded in vastly distinct environments (i.e., a circular versus a rectangular arena), place cells exhibit uncorrelated firing profiles. These changes include variable field locations and firing rates, a phenomenon referred to as ‘global remapping’ [55–62]. Place representations that result from global remapping are orthogonal, such that there is no obvious pattern between place maps across different environments (**Figure 6b**). Place cells may also be silent between environments or across days, the mechanisms for which remain unknown [57,63].

Place cell representations anchor to an allocentric reference frame. Rotation of a cue card on the enclosure’s walls caused an equal rotation in the place cell representation [56]. Removal of the cue card resulted in variable responses where some place cells underwent a shift in field location, and other place cells were largely unaffected. Place cells may therefore attend to a variety of different sensory stimuli in the local environment to maintain their spatial coding [56]. In general, manipulation of non-spatial environmental features (i.e., two geometrically identical enclosures with different colors) causes place cells to undergo a less dramatic form of remapping called ‘rate remapping’ where place field locations remain the same but firing rates change (**Figure**

**6b)** [59]. Hippocampal neurons respond to many non-spatial dimensions such as behavioral goals, odors, auditory tones, and the passage of time [64–67]. How can the hippocampus be a cognitive map of physical space when its neurons encode non-spatial dimensions? On one hand, non-spatial features may be integral pieces to the overall representation of a space. Alternatively, the hippocampus might have evolved to perform higher level function such as encoding episodic memories [68].

While early studies suggested that place cell representations were generally stable across days and only underwent gradual changes across time, these findings could have been biased by small sample sizes [69–71]. Large-scale calcium imaging of hundreds of place cells simultaneously revealed that the ensemble representation of the same environment involves a unique subset of cells across days [63]. Only 15-25% of place cells fired day-to-day, meaning that the cell identity of 75-85% of the place ensemble was unique. Yet, despite this variability, the number of active place cells on any given day was sufficient to map the entire environment (**Figure 6c**). This coding scheme suggests that the hippocampal map adequately encodes space as well as changes in experience. A more recent calcium imaging study showed that place cells in CA3 are more stable day-to-day than those in CA1 [72].

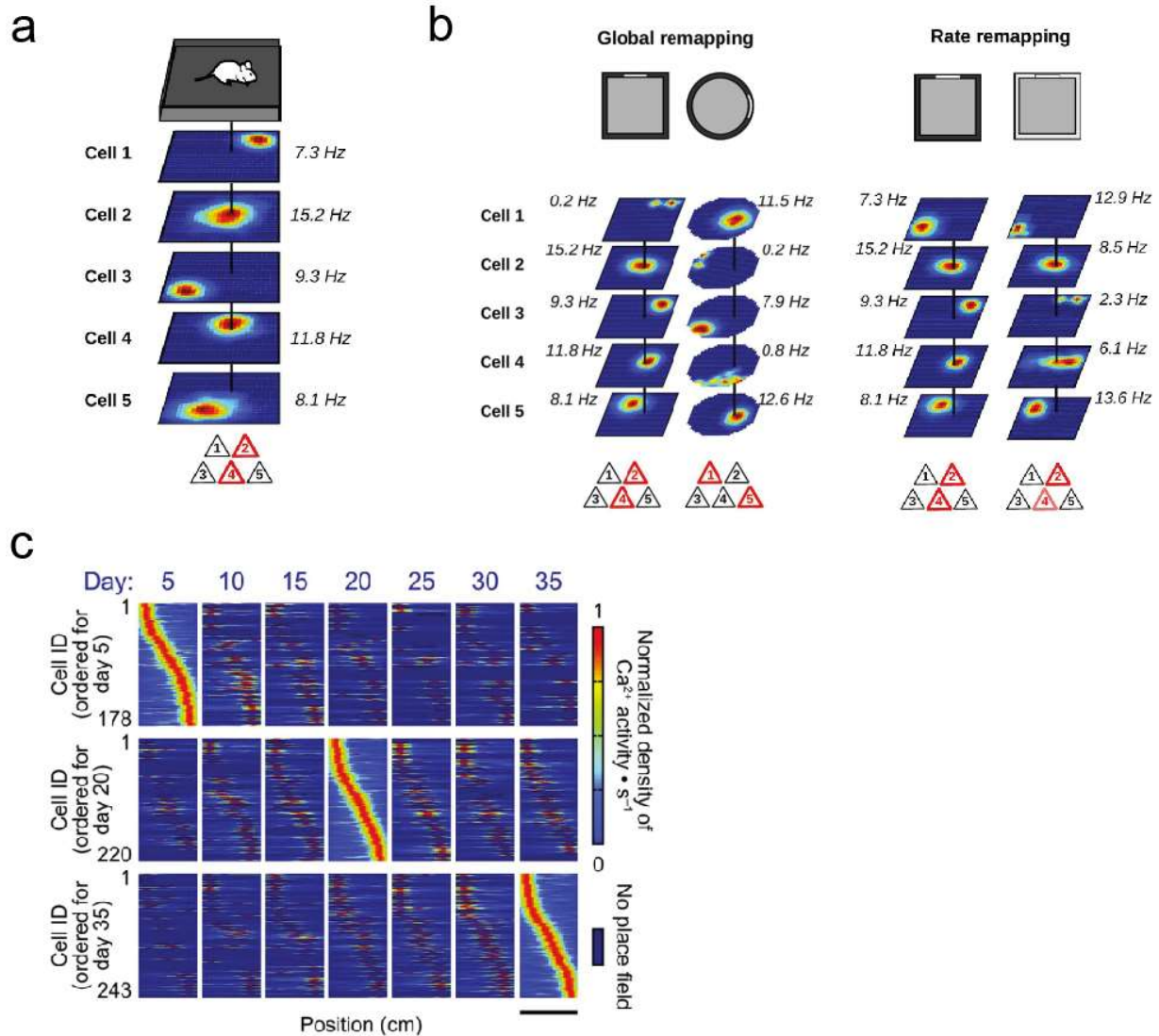


**Figure 6. Place cell firing properties.**

(a) Different place cells have unique, and often non-overlapping firing fields in the same environment, providing no clear evidence for field location topography. Firing plots shown are rate maps, where warmer colors indicate higher firing rates. (b) Global remapping: two unique populations of place cells are active in two vastly different environments. Place representations are orthogonal, meaning there is no obvious pattern between a cell's representation in one environment versus the other. Rate remapping: manipulation of non-spatial features of an environment causes changes in the existing place cell population's firing rates. (c) Large-scale calcium imaging of place cells as the animal runs on a linear track across days. The y-axis of each matrix represents cells sorted by their firing position on the track, and the x-axis represents position on the track. Note that a different place cell ensemble is active on each day of recording, yet the number of total place cells active on a given day was sufficient to map the entire linear track. Figure c taken from [63].

Figures a and b are taken from Latuske, P. *et al.* (2017) Hippocampal remapping and its entorhinal origin. *Front. Behav. Neurosci.* 11, 253.

### 1.1.3. Head-direction cells

Head-direction (HD) cells were first recorded in the dorsal presubiculum and integrate vestibular inputs to encode the animal's heading direction [73–75]. The HD circuit spans multiple brain regions including the thalamic nuclei, mammillary bodies, presubiculum, parasubiculum, retrosplenial and entorhinal cortices [76], including the MEC where grid cells are found. Each HD cell is tuned to a range of directions, referred to as the directional firing range (**Figure 7a**). The preferred firing direction is the heading direction for which a given HD cell maximally fires. For all remaining directions in range, the cell fires at lower rates. Interestingly, during development, HD cells mature faster than any other spatially-tuned neuron in rats [77,78]. The presence of a directional signal before place cells form spatial representations suggests that the HD system plays a vital role in navigation.

Similar to place cells, cue card rotations caused an equal rotation in the preferred firing direction of HD cells (**Figure 7b**) [74]. Removal of the cue card caused an unpredictable shift in directional tuning. HD cells also integrate self-motion cues aside external landmarks. Vestibular lesions impaired directional selectivity [75] and HD firing is preserved in complete darkness or when the animal is blindfolded (although with a gradual decrease in stability) [79]. Responses to both external landmarks and body-based stimuli suggest that HD cells provide an internal sense of direction relative to the outside world to support navigation.

HD cells also undergo global remapping in a novel environment by changing their preferred firing direction (without changes in tuning width). However, the relative difference in preferred firing direction between HD cells is largely preserved across environments, demonstrating an internal consistency between HD cells at the population level (**Figure 7c**) [74].

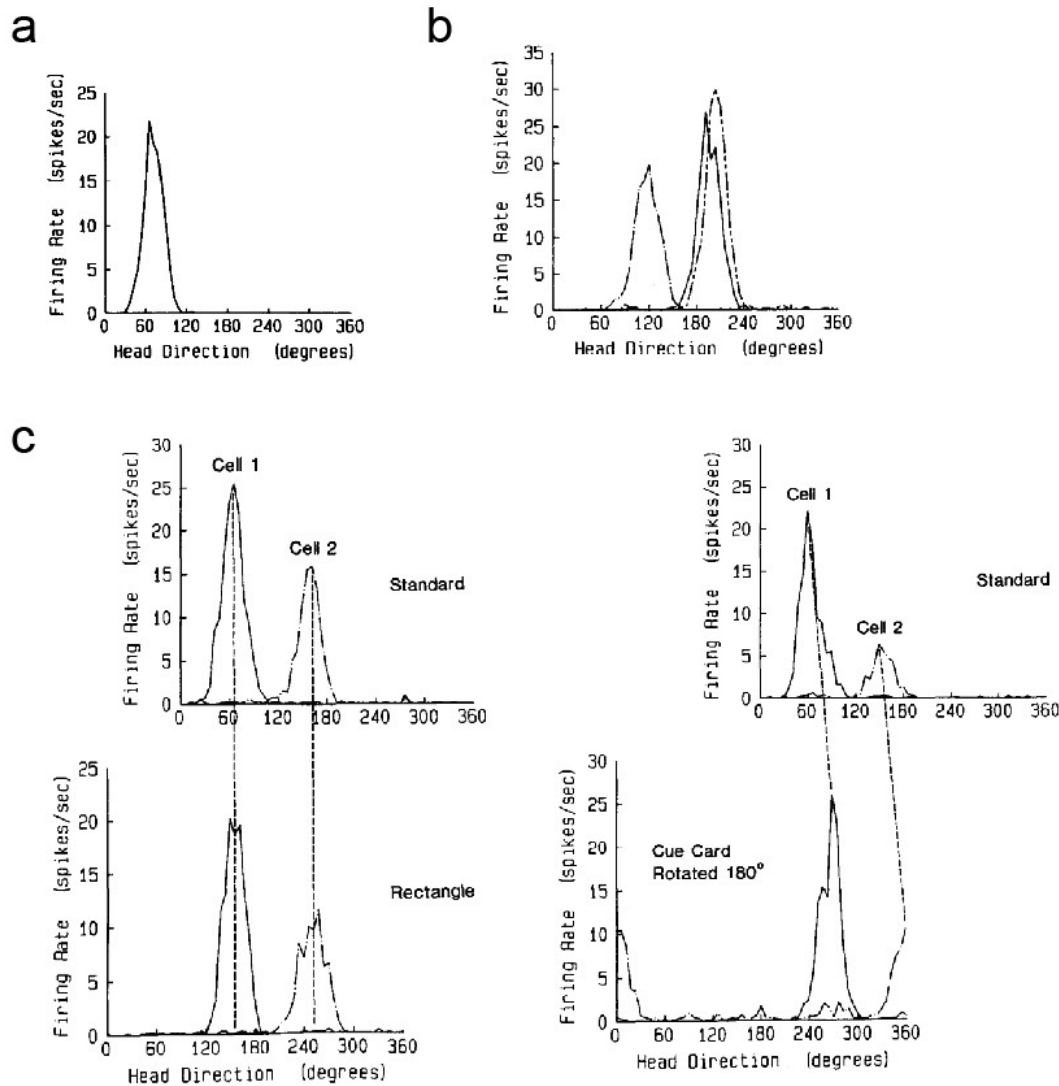


**Figure 7. Head-direction cell firing properties.**

(a) A HD cell's firing rate is modulated by the animal's heading direction. (b) Plot shows the change in preferred firing direction of a HD cell during a cue card rotation experiment. The solid line represents the baseline recording (with a preferred firing direction around 210 degrees). The dash-dot line represents a 90 degree rotation of the cue card, which caused an equal shift in the preferred firing direction (now around 120 degrees). The line with two short dashes represents the post-manipulation recording where the cue card was returned to its original position (causing the preferred firing direction to revert back to 210 degrees). (c) (Top-left and bottom-left) Plots show the change in preferred firing direction of two simultaneously recorded HD cells in two different environments (standard and rectangle). Despite a global remapping of preferring firing direction of the two HD cells, their relative difference is preserved. (Top-right and bottom-right) Plots communicate the same finding, but for a cue card rotation experiment. Figures taken from [73, 74].

#### 1.1.4. Grid cells

Grid cells have multiple firing fields that form a periodic hexagonal array that spans two-dimensional space (**Figure 8a**) [17,32]. This periodic code is theorized to provide a universal metric for space by encoding regular intervals between spatial locations. Grid cells were first recorded in the MEC, but also exist in the pre- and parasubiculum of rodents [80]. The motivation for investigating spatial coding in the MEC originated from a study that investigated CA1 place coding following CA3 lesions [81]. Removal of this intrinsic hippocampal connection did not affect CA1 place representations, suggesting that the spatial signal was external and possibly in the EC which is one synapse upstream.

Grid cells have three defining spatial coding properties: scale, orientation, and phase (**Figure 8b**). Grid scale is the spacing between firing fields. Much like place cells, there is a topographic organization of grid field size and scale along the dorsal-ventral axis of the MEC [17,82]. Grid orientation refers to the direction of the grid axes relative to the environmental boundaries. Grid phase is the offset of the grid map in the x-y plane. Depending on the size of the environment, a couple of grid cells with differing phases could sufficiently map the entire space.

Both grid scale and orientation have a modular organization. Large-scale recordings of grid cells in rats revealed that there are at least 4 modules of grid scale where grid cells within each module share the same scale but not phase (**Figure 8c**) [82]. Each module's scale increases by a multiplicative factor of  $\sim 1.42$  from the previous. Individual modules behaved differently to environmental compression (i.e., by moving a wall) and grid cells within a module acted coherently [82]. In terms of grid orientation, there are at least two subpopulations of grid cells whose initial spatial axes are offset by  $30^\circ$  or  $60^\circ$  (with a small offset of  $\sim 7.5^\circ$  from the borders) from the east wall of the square environment [82–84].

Grid cells undergo global remapping in vastly different environments [17]. In contrast to the orthogonal remapping of place cells, grid scale and orientation remain the same between contexts, with the only change being grid phase [85] (**Figure 8d**). In other words, periodicity remains intact and only shifts in absolute spatial coordinates. The relative phase relationship between grid cells remains the same across different environments, offering further evidence of internal consistency at the population level [82,85]. Much like place cells and HD cells, grid representations are modulated by rotation of an environmental cue card [17]. Grid maps are maintained in complete darkness (more so in rats than in mice) and some are modulated by the animal's heading direction and running speed [17,18,86,87]. Grid cells therefore integrate self-motion cues and are continuously updated by allocentric cues.

Rate remapping in grid cells causes changes in the firing rate of individual grid fields, implying that grid cells do not provide a pure context-invariant metric of space [88]. Grid cells also respond to non-spatial dimensions, again suggesting that the neural mechanisms supporting spatial navigation may be more generally evolved for episodic memory.

Grid patterns are slightly elliptical and not perfectly hexagonal. Grid axes have a small offset of  $\sim 7.5^\circ$  from the borders, thus causing a shearing-induced rotation of the grid's hexagonal symmetry [84]. Theoretically, it has been proposed that a  $7.5^\circ$  offset from the borders reduces coding error by maximizing orientation solutions when sensory cues are ambiguous and do not reliably signal the animal's location [89]. Therefore, environment geometry is a strong grid anchor, which is further revealed in irregular geometric enclosures. The grid pattern is distorted in trapezoidal enclosures, further suggesting that grid patterns are not purely context-invariant but also reflect features of the local environment (**Figure 8e**) [90].

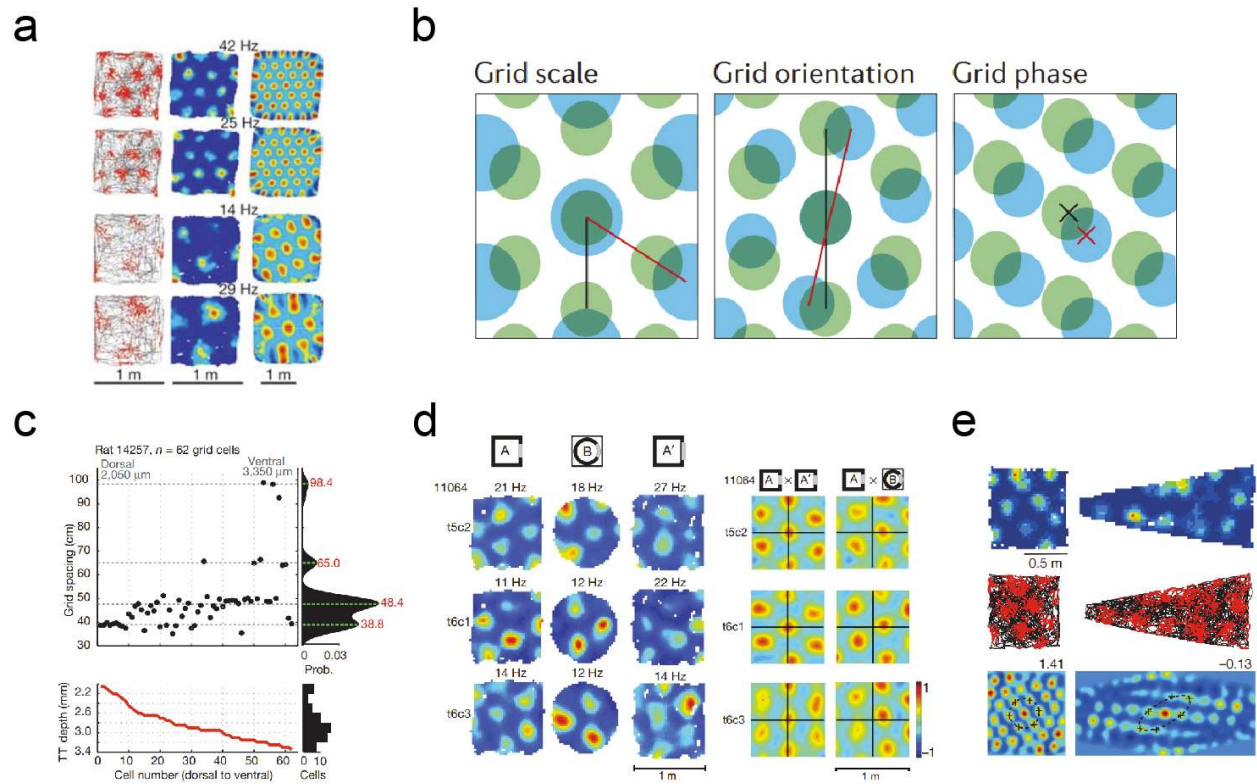


**Figure 8. Grid cell firing properties.**

(a) The first two rows are dorsal MEC grid cells (smaller spacing between fields), and the last two rows are ventral MEC grid cells. Each row shows the trajectory map, rate map and rate map autocorrelation. The trajectory map shows the animal's trajectory (black) and location of cell firing (red). The rate map is a color-coded trajectory map where warmer colors indicate higher firing rates. The autocorrelation is taken by shifting the rate map across the x and y dimensions. Highly periodic grid cells have a prominent hexagonal pattern. (b) Schematics of grid scale, grid orientation, and grid phase. (c) (Top) Grid cells recorded along the dorsal-ventral axis have grid spacing organized in discrete modules. (Bottom) Plot shows the tetrode depth at which each grid cell was recorded. (d) (Left) Rate maps of three grid cells recorded in two different environments (A and B). (Right) The cross-correlations of rate maps from the same environment (A vs. A'), and from different environments (A vs. B). Note that the cross-correlation of A vs. B is just shifted relative to A vs. A', indicating that grid scale and orientation remains the same during global remapping. (e) A grid cell recorded in a square environment (left column) and in a trapezoid (right column). Note the greater distortion of hexagonal symmetry in the autocorrelation of the trapezoid recording. Figures taken from [17, 82, 85, 90].

Figure b is taken from Moser, E.I. *et al.* (2014) Grid cells and cortical representation. *Nat. Rev. Neurosci.* 15, 466–481.

### 1.1.5. Other spatially-tuned MEC cells

**Border cells:** They are found in the MEC, subiculum, presubiculum and parasubiculum [80,91,92]. These cells fire close to boundaries (single or multiple) in the environment (**Figure 9a**). Most of these cells fire right next to borders, implying a spatial code for the geometric shape of the environment. A subset of these cells fires a certain distance away from borders and are called ‘boundary-vector cells’.

**Speed cells:** In addition to heading direction, some grid cells are modulated by movement speed [18]. Speed cells in the MEC encode running speed as a function of firing rate (**Figure 9b**) [93]. The modulation of firing rate by running speed in MEC speed cells is a mix of both linear and non-linear relationships [94].

**Object-vector cells:** These cells are found in the MEC and fire when the animal is at a specific distance and direction away from an object (**Figure 9c**) [95]. These cells provide evidence that the MEC performs vector computations between locations.

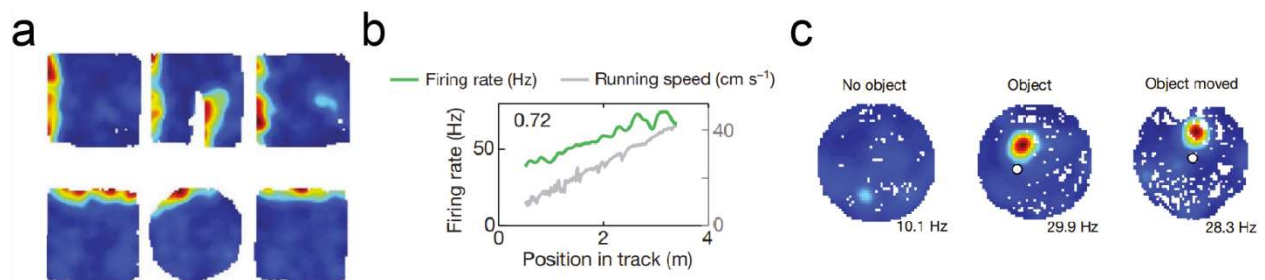


**Figure 9. Other spatially-modulated cell types in the MEC.**

(a) (First row) A border cell fires to existing boundaries of an environment, in addition to added boundaries (middle panel). (Second row) Another border cell fires to boundaries irrespective of environmental shape. (b) A speed cell’s firing rate is modulated by the running speed of the animal on a linear track. (c) An object-vector cell’s firing is modulated by the presence of an object (white dot). Moving this object in space changes the cell’s firing representation. Warmer colors in rate maps indicate high firing rates. Figures taken from [91, 93, 95].

## 1.2. Path integration

Path integration is a cognitive function whereby self-motion cues including optic flow, vestibular feedback, proprioception, and motor efference copy combine with external landmarks to support navigation [6,7]. The process is automatic and continuous, persisting whether landmark information is available or not [96,97]. If landmark information is available, then path integration involves a mix of largely visual and self-motion cues. If landmark information is absent, then path integration primarily involves vestibular and proprioceptive cues. At the behavioral level, path integration is often defined as the computation of the shortest path from point A to B in the absence of external landmarks. Classic path integration experimental paradigms in rodents and humans are homing tasks where the subject must compute the shortest vector from a current position towards a goal location when external landmark information is unavailable (**Figure 10a**). This homing vector can be computed in complete darkness but contains some degree of angular error, demonstrating that path integration is susceptible to noise in the absence of external cues [7].

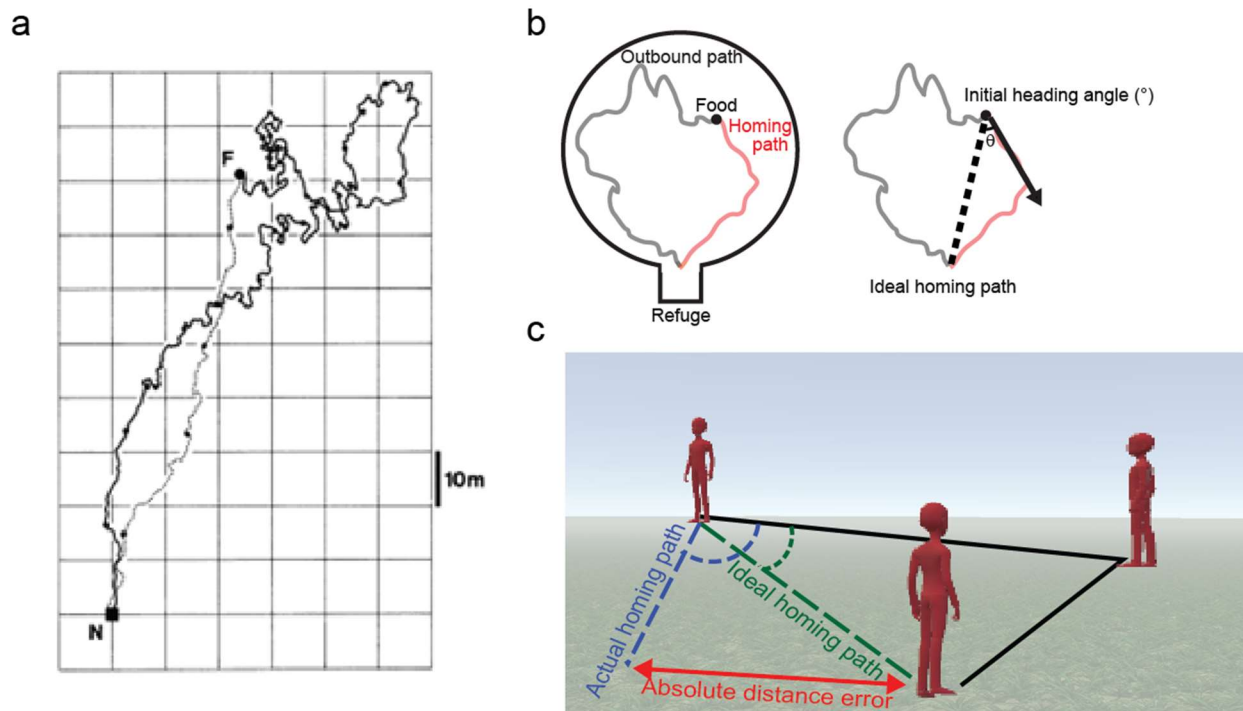


**Figure 10. Homing vector computation by path integration.**

(a) A schematic of an ant's foraging trip. The outbound path from the nest (N) to a food item (F) is depicted by solid line, and the return path is shown by the stippled line. The outbound path here is 354.5m and the homing path is 113.2m. Note that the homing path is relatively straight like a vector but has some degree of angular error. (b) A rodent food-foraging task in complete darkness. The initial heading angle between the ideal homing path and the actual homing path is a measurement of path integration error. (c) A triangle completion task for human subjects. The absolute distance between the end points of the ideal homing path and the actual homing path is a measurement of path integration error. Figures taken from [5, 98].

It was shown in desert ants that the amount of error accumulation approximated homing vector computation (**Figure 10a**) [98,99]. Ants were trained to navigate from a refuge nest to an artificial feeder. The complexity of this outbound path was experimentally controlled. Upon reaching the feeder, the ants were transferred to a different test environment in which they immediately moved in what they believed was the direction of the refuge. Importantly, the direction of this homing vector can be approximated by the angular turns taken throughout the outbound path [98]. Similarly, longer distances covered on the outbound path also led to greater uncertainty on the return [99,100]. Popular rodent and human path integration task designs follow the same experimental principles. Rodent tasks commonly involve a food-foraging scenario in complete darkness where the animal first leaves a refuge to forage for food in an open arena [5]. Upon finding the food, the animal must then return to the starting refuge for consumption. The angular offset between the ideal homing vector and the real homing path is a behavioral readout of the degree of error accumulation (**Figure 10b**). In parallel, human path integration is commonly assessed using the triangle completion task where blindfolded subjects are initially guided along two straight segments of a triangular shape from a starting location [5]. The subjects must then navigate back to the start point by themselves and the degree to which they miss the target location is quantified as the degree of path integration error (**Figure 10c**).

### **1.2.1. Neural basis of path integration in rodents**

The hippocampus and MEC are two key regions that support path integration. Hippocampal and medial entorhinal lesions in rodents disrupted path integration performance, while the MEC also contains neurons that encode distance travelled on a linear track in near-darkness [101–105]. Beyond the hippocampus and MEC, structural and functional MRI studies in humans reveal the importance of the retrosplenial cortex, the parahippocampal (postrhinal in rodents) cortex, the medial prefrontal cortex, the cerebellum, as well as the connectivity between the medial temporal lobe, parietal, and prefrontal cortices for path integration performance [5]. Therefore, while the following subsections focus on hippocampal and entorhinal spatially-tuned neurons, path integration is more nuanced and involves the integration of multiple sources of information across a distributed brain network.

Place cells encode space in response to self-motion cues, in addition to landmark information [106–111]. Place fields not only persist in darkness, but do not reliably form without proprioceptive inputs via active movement [107,110]. In path integration tasks conducted on linear tracks, some place cells encoded the fixed distance to a moving start location [108,111]. In particular, when external cues are unreliable, place cells rely on self-motion cues to maintain accurate spatial coding. For instance, if rats are disoriented prior to being placed in an open arena, then simultaneously recorded place cells and thalamic HD cells were not reliably anchored to an external cue card [106]. Between multiple recording sessions in the same environment following disorientation, rotations of the cue card did not result in an equal rotation of place fields and HD directional selectivity in disorientated animals. In some cases, place cells and HD cells often corotated their firing fields away from the cue card and were strongly coupled, suggesting that animals relied more on internal direction instead of external landmarks [106]. Experimental control

of the animal's internal direction is achievable by masking external cues in the open arena [109]. When landmark information is unavailable, rotation of the environment with the animal caused an equal rotation in place fields. In contrast, rotation of the environment alone did not cause corotation in place fields, whereas rotation of the animal alone almost always did. These results suggest that place cells utilize both landmark and self-motion cues depending on availability [109].

Grid cells persist in darkness (more so in rats than in mice), stabilize quickly in novel environments, and lose their spatial periodicity when self-motion information is eliminated during passive transport of the animal [17,86,87,112]. Yet, in contrast to the unstable and orthogonal nature of place cell representations across contexts, grid cells consistently encode all contexts across days while also maintaining the same spatial scale and spatial phase relationships with other grid cells between environments [56,63,85]. Furthermore, some grid cells are modulated by heading direction and movement speed, making them ideal candidates to encode self-motion [18,26]. The first causal study linking grid cells to PI performance demonstrated that genetic knockdown of NMDA glutamate receptors caused a disruption of grid cell spatial periodicity which resulted in impaired path integration performance [113]. In contrast, place cells in the hippocampus and spatially-selective cells in the MEC remained unaltered. Prior to this report, it was also shown that mice lacking GluA1-containing AMPA receptors had disrupted grid cell spatial coding which correlated to impaired path integration performance [114]. These lines of evidence suggest that grid cells play an important role in path integration, and the following subsections describe how they could do so by integrating hippocampal inputs, as well as information about heading direction and movement speed.

### **1.2.2. Grid cells and the hippocampus**

Grid cells require excitatory feedback inputs from the hippocampus [115]. Temporal inactivation of the hippocampus resulted in a gradual loss of grid cell spatial periodicity, suggesting that place cells may contribute to path integration by providing an important spatial signal to maintain grid coding. In support of this view, developmental studies in rats showed that grid cells mature the slowest relative to place and HD cells [77,78]. Prior to the emergence of an adult-like grid cell network, place cells developed key spatial coding properties and path integration capabilities that could support grid coding [111,116,117]. That being said, place cell spatial coding was initially concentrated along the environmental borders and only reliably encoded the center after maturation of the grid cell network [117]. Reduced spatial coding in the center where landmarks are relatively scarce compared to the borders implies limited path integration function by place cells without inputs from grid cells. Therefore, while place cells respond to self-motion, their predominant role in path integration may be to provide feedback signals to the MEC regarding associations between external landmarks that update the grid cell path integrator [56,85,118]. In parallel, the context-invariant properties of grid cells may complement place coding by providing inputs to the hippocampus that are self-motion dominant [17,85,118]. In line with this theory, within virtual reality environments where velocity gain manipulations decouple external landmarks from the animal's movements, place cell and grid cell activities were predominantly influenced by visual and self-motion, respectively [119].

### **1.2.3. Grid cells and orientation coding**

A link between HD cells and path integration was reported in a food-foraging task in complete darkness [120]. On each trial, the rat was let out from a refuge into an open arena to randomly forage for a food pellet. Upon finding the food, the mouse then returned to the refuge

for consumption. The authors found that the initial heading direction on inbound paths correlated to an equal angular shift in the preferred firing direction of simultaneously recorded HD cells. This association between perceived orientation error by the HD network and behavioral performance confirms a link between HD cells and path integration.

Another study confirmed a causal role of the HD network for path integration performance [121]. The authors optogenetically inactivated the nucleus prepositus which relays vestibular cues to the HD network. Inactivation caused HD cells in the anterior thalamic nucleus to become unstable only in the dark when no visual cues were available. Importantly, path integration performance in a food-foraging task in complete darkness was also impaired.

At the physiological level, inactivation of HD cells in the anterior thalamic nucleus impaired grid spatial periodicity, demonstrating that integration of vestibular feedback by HD cells is necessary for grid cell coding [122]. Of interesting note, during inactivation of the hippocampus, the gradual loss of grid cell spatial periodicity was accompanied by increased HD tuning in 74% of non-directional grid cells and unaffected HD tuning in conjunctive grid-by-head-direction cells [115]. These results suggest that under circumstances when associations between external landmarks no longer reliably update the grid path integrator (or at the very least, when grid spatial coding is perturbed), grid cells rely on vestibular feedback to sustain some baseline level of activity [115,118].

#### **1.2.4. Grid cells and speed coding**

In addition to heading direction, some grid cells are also modulated by translational movement speed. The discovery of MEC speed cells that encode movement speed as a function of firing rate suggests a dedicated entorhinal circuit that tracks how fast the animal moves [93]. Movement speed positively modulates theta oscillation (4-12 Hz) firing frequency in the

hippocampus and MEC [123–127]. Disruption of theta oscillations via inactivation of the medial septum impaired grid spatial periodicity [128,129], but increased the strength of firing rate modulation by movement speed in grid cells [94]. Similar to how grid cells exhibited stronger directional tuning during inactivation of the hippocampus [115], speed inputs appear to exert a greater influence over grid cells when spatial periodicity is impaired. In contrast, HD cells did not show any changes in speed modulation during septal inactivation and conjunctive grid-by-head-direction cells maintained their directional tuning [94,128]. Preservation of the HD network suggests that vestibular and proprioceptive information streams in the MEC independently contribute to grid coding. Similarly, grid cell spatial periodicity was impaired when speed modulation of theta rhythmicity was abolished via passive transport of the animals across an arena during a food-foraging task, but HD cells remained unaffected [112].

During inactivation of the septum, interneurons also had increased firing rate modulation by movement speed. Part of the speed input to grid cells might originate from fast-spiking parvalbumin-expressing (PV) interneurons in the MEC, a portion of which are modulated by movement speed [93,130,131]. PV interneurons may convey speed information via their recurrent connectivity with a subset of grid cells [130,132]. Direct silencing of MEC PV interneurons impaired grid spatial periodicity and diminished speed coding in speed cells [133]. The loss of grid spatial coding might therefore result from faulty integration of proprioceptive-based self motion by interneurons, which would be detrimental to path integration behavioral performance. In support of this view, septal lesions disrupted path integration performance in a food-foraging task, where distance estimates derived from self-motion were impaired but directional estimates were moderately spared [134,135].

Beyond rodents, single-unit recordings of place and grid cells have been conducted in humans [20,21]. Functional magnetic resonance imaging (fMRI) has identified place, grid and HD-like patterns, highlighting similar path integration mechanisms across species [20,136,137]. That being said, self-motion information alone cannot maintain an accurate path integration system which must rely on external cues as corrective mechanisms [7,8]. External cues may be landmarks and boundaries, but also multisensory cues (e.g., visual, auditory, olfactory, etc.) which spatially-tuned cells integrate alongside self-motion information [17,56,65,66,85,138].

### **1.3. Alzheimer's disease**

AD is a neurodegenerative disorder that accounts for 60-80% of dementia cases, with symptoms involving progressive memory loss, cognitive impairment, and functional decline. The first case of AD was reported in 1901 by the German physician, Alois Alzheimer [139]. At the time, Alzheimer noted that his patient, Auguste Deter, showed many clinical symptoms associated with the disease today. After Auguste passed away in 1906, her brain was examined by Alzheimer and colleagues who identified the first presence of amyloid plaques and neurofibrillary tangles (NFTs). Today, A $\beta$  plaques and NFTs are the most common pathological markers of AD [140]. Yet, the exact cause of AD in the general population remains unknown, spurring a number of alternative hypotheses beyond amyloidopathy/tauopathy and numerous risk factors that may not be mutually exclusive [141–144].

Much of the molecular understanding of AD comes from the study of A $\beta$  within the last four decades. In 1984, A $\beta$  was first isolated from amyloid fibrils of AD patients and characterized as a 4.2 kiloDalton peptide [145]. Glenner and Wong theorized that these peptides may be the proteolytic cleavage products of a larger precursor protein. In 1985, this A $\beta$  peptide was determined to be 40-42 amino acids long and found in amyloid plaques from AD patients [146].

In 1987, the precursor protein from which the A $\beta$  peptides were derived was cloned and characterized [147–150]. This amyloid precursor protein (APP) is a cell-surface receptor that is cleaved via two pathways (**Figure 11**) [151]. The non-amyloidogenic pathway involves a chain of proteolytic cleavages by  $\alpha$ -secretase and  $\gamma$ -secretase, resulting in harmless peptides that do not form plaques. On the other hand, the amyloidogenic pathway involving  $\beta$ -secretase and  $\gamma$ -secretase releases A $\beta$  peptides (also called monomers) into the extracellular space. There, the monomers form toxic oligomers which eventually aggregate into A $\beta$  plaques. The amyloid hypothesis posits that the release of A $\beta$  peptides triggers a series of events that eventually causes late-stage AD [140,152,153].

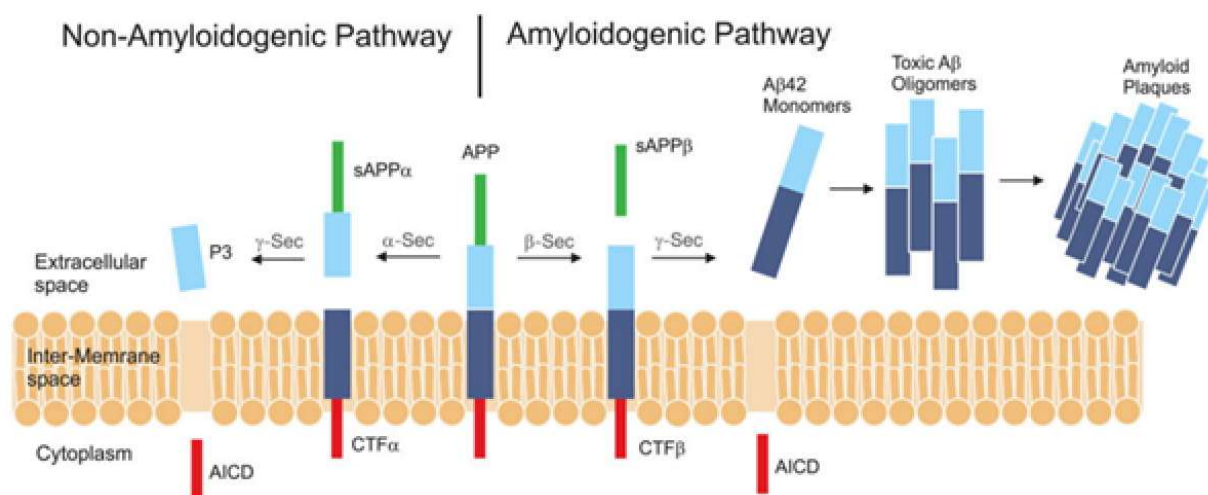


**Figure 11. The amyloidogenic pathway.**

A schematic of APP cleavage. The non-amyloidogenic pathway involves a chain of proteolytic cleavages by  $\alpha$ -secretase and  $\gamma$ -secretase. The end products are P3 and AICD which do not form plaques. The amyloidogenic pathway involves  $\beta$ -secretase and  $\gamma$ -secretase and releases A $\beta$  peptides/monomers. These monomers aggregate to form oligomers, and eventually plaques. Figure taken from [148].

The first *APP* mutation discovered in 1990, APP E693Q (Dutch), caused increased amyloid deposition in a Dutch family with inherited cerebral hemorrhage [154]. Shortly after, the first mutation to cause early-onset familial AD was characterized as APP V717I (London) [155].

Variants of this mutation occur on the C-Terminal of the A $\beta$  domain and result in longer A $\beta$  peptides being released into the extracellular space. Specifically, this results in increased A $\beta$ 42 (A $\beta$  peptides that are 42 amino acids long) levels while A $\beta$ 40 levels do not change [156,157]. A number of other autosomal-dominant *APP* mutations exist, and while each cause specific changes, the general end result is an overaccumulation of A $\beta$  peptides [158]. Besides *APP*, two other genes that cause early-onset familial AD are presenilin 1 and 2 (*PSEN1*, *PSEN2*) [159–161].

Mutations *APP*, *PSEN1*, and *PSEN2* determine those at risk of early-onset familial AD. Their predictability offers a powerful advantage for researchers to study independent contributions of each mutation. One method is the introduction of *APP* mutations into the genome of transgenic animals to mirror amyloidopathy seen in AD patients. One of the first successful models was the PDAPP mouse that had the *APP* V717F (Indiana) mutation and exhibited many pathological hallmarks of AD [162]. To date, there are numerous *APP* mouse models and the extent to which these mice recapitulate actual pathology in human patients is continuously debated [163]. No animal model of a disease is perfect, and multiple AD mouse lines should be studied in parallel.

On the other hand, early-onset familial AD accounts for less than 5% of all AD cases. Most AD patients have a form of late-onset AD that is referred to as ‘sporadic AD’. Unlike familial AD that generally occurs prior to 60 years of age, sporadic AD affects patients after 60 years of age and arises due to a mix of genetic and environmental factors. Furthermore, mutations in *APP*, *PSEN1*, and *PSEN2* do not occur in sporadic AD patients, although there is some evidence in larger cohorts suggesting that this is not entirely true [164].

The most important genetic risk factor of sporadic AD is *APOE* which encodes the lipid transporter apolipoprotein E (ApoE). In the brain, ApoE plays a pivotal role in transporting lipids such as cholesterol to neurons. Humans have one of three versions of *APOE* polymorphic alleles:

*APOE-ε2*, *APOE-ε3*, and *APOE-ε4*. Those with the E4 polymorphic allele are at increased risk of developing sporadic AD and an earlier onset [165,166]. On average, 25% of the healthy population (Aβ-negative) carried one or two copies of *APOE-ε4*. In contrast, 64% and 66% of Aβ-positive MCI and AD subjects were positive for *APOE-ε4*, respectively [167]. No other gene has been as extensively studied as *APOE-ε4*, and large-scale genome-wide association studies may prove useful in identifying other important genes that contribute to sporadic AD [168]. While there are distinctions between familial and sporadic AD such as age onset and environmental contributions, both forms of disease exhibit similar major neuropathological features including Aβ and NFTs [169]. In this sense, characterizing amyloidopathy in the context of familial AD (such as in transgenic *APP* mouse models) will improve the understanding of sporadic AD.

### 1.3.1. Amyloid hypothesis

The discoveries involving Aβ peptides, the gene encoding APP located on chromosome 21, the neurotoxicity of Aβ, and the first *APP* mutation linked to increased amyloid deposition were four key discoveries that laid the foundation for the amyloid hypothesis [145–150,154,170]. This theory postulates that the aggregation of these peptides (either soluble Aβ oligomers or Aβ plaques) gives rise to a series of events (neuronal death, synaptic dysfunction, neuroinflammation and interactions with tau proteins to form tangles) that ultimately result in AD (**Figure 12**) [171]. While there have been several changes to the hypothesis over the decades, the central assumption remains that the accumulation of Aβ is the key initiator of events that later trigger clinical AD.

Mutations in *APP*, *PSEN1*, and *PSEN2* lead to Aβ overaccumulation in early-onset AD patients by directly influencing how APP is cleaved via the amyloidogenic pathway. The exact mechanisms for Aβ accumulation in sporadic patients are less clear, but they involve *APOE-ε4* [165,172]. One study suggests that *APOE-ε4* does not affect Aβ production, but rather hinder Aβ

clearance [173]. The authors created multiple mouse lines that expressed human *APP* crossed with different human *APOE* isoforms (*APOE-ε2*, *APOE-ε3*, and *APOE-ε4*). Mice with the *APOE-ε4* gene showed the most amount of Aβ clearance, well before the deposition of Aβ plaques. Furthermore, the degree of Aβ synthesis via APP cleavage did not change between the different mouse strains, implying that *APOE* isoforms do not contribute to Aβ production. These results support existing evidence that suggest familial AD is caused by increased Aβ production, and sporadic AD is, in part, due to reduced Aβ clearance [157,174]. In both cases, the overaccumulation of Aβ brings forth a cascade of events that include synaptic dysfunction, neuroinflammation and the formation of NFTs (**Figure 12**). The eventual consequences are widespread synaptic loss and neuronal death which lead to dementia.

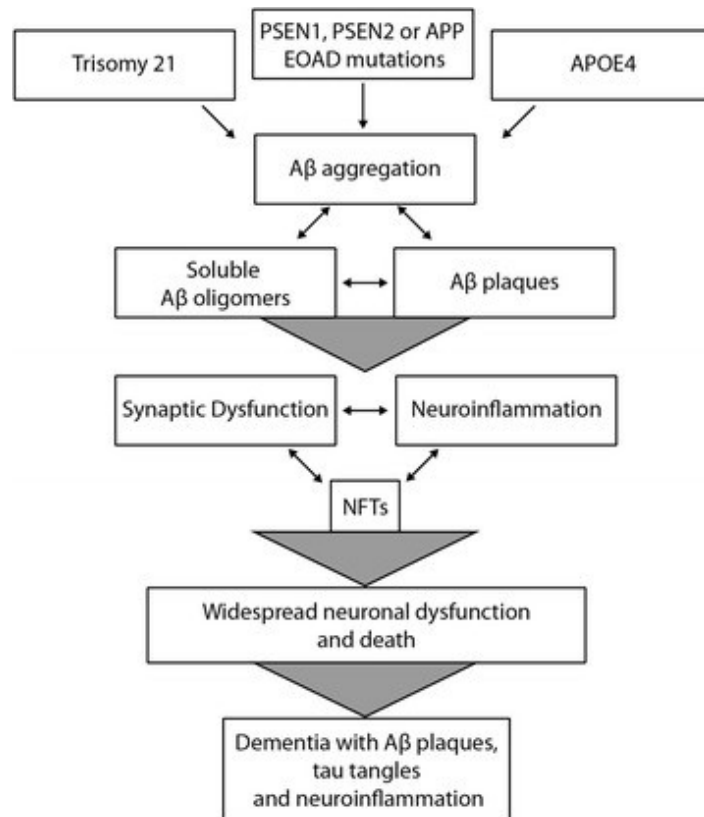


### **Figure 12. The amyloid cascade hypothesis.**

The buildup of A $\beta$  in patients with trisomy 21 and/or early-onset familial AD is caused by genetic mutations that influence APP cleavage. In sporadic patients, the mechanisms are less clear but involves *APOE*- $\epsilon$ 4. The aggregation of A $\beta$  monomers into oligomers and plaques causes a series of downstream events that result in the classic symptoms of dementia. Figure taken from [168].

One significant addition to the hypothesis has been the focus on soluble A $\beta$  oligomers. It has been shown that plaque load weakly correlates to cognition, whereas synapse loss and levels of soluble A $\beta$  are better predictors [175,176]. Furthermore, plaques are also present in cognitively normal adults, although to a lesser extent [177]. Plaques may therefore be the inevitable result of earlier pathogenesis or normal aging. In contrast, soluble A $\beta$  deposition precedes clinical AD by as early as decades and induces a host of AD symptoms in the absence of plaques [178–180].

### **1.3.2. Tau hypothesis**

In 1986, phosphorylated and aggregated tau proteins were identified as the main protein compositions of NFTs in AD brains [181]. The tau hypothesis states that abnormal phosphorylation and aggregation of tau are the main initiators of AD. Tau is a microtubule-associated protein that is commonly found in the axons and participates in microtubule dynamics. Hyperphosphorylated tau dissociates from microtubule assemblies and aggregates into oligomeric structures, followed by paired helical filaments, and finally NFTs intracellularly, or neuropil threads (NTs) extracellularly. Similar to the amyloid cascade, the propagation of tauopathy eventually leads to synaptic dysfunction, neuroinflammation and neuronal loss [182].

While amyloidopathy and tauopathy are often competing hypotheses, it remains unclear if they are independent of the other. The Braak staging system (next section) shows that A $\beta$  and tau accumulate in different brain regions [183]. A $\beta$  initially deposits in associational cortices, whereas tau first accumulates in the transentorhinal region [183]. It seems unlikely that A $\beta$  causes tauopathy

if both pathologies do not start in the same brain regions. Furthermore, tauopathy can progress via A $\beta$ -independent regulators in the absence of amyloidopathy, one of which is *APOE- $\epsilon$ 4*. In tau transgenic mouse models with *APOE- $\epsilon$ 2*, *APOE- $\epsilon$ 3* and *APOE- $\epsilon$ 4* isoforms, E4 mice had the greatest amount of brain atrophy and neuroinflammation [184]. In contrast, mice with the *APOE* gene knocked out did not exhibit these changes. Furthermore, an E4 allele led to greater neurodegeneration in individuals with a sporadic primary tauopathy. For a detailed review of A $\beta$ -independent regulators of tauopathy that include cholesterol metabolism, the endocytic system, *APOE- $\epsilon$ 4* and microglia, see [185].

There is also evidence in support of the alternative, classic view that A $\beta$  drives tauopathy and/or exacerbates tauopathy via interaction. Temporally, A $\beta$  is found in the brain during preclinical AD before tau or major cognitive impairments are apparent [177]. Throughout the clinical stages of AD, A $\beta$  levels generally plateau whereas tau levels start to increase [186]. Various imaging studies also indicate that the progression of tauopathy better correlates with cognitive decline as opposed to A $\beta$  (see [185] for a summary). These findings support the belief that while amyloidopathy is not the strongest correlate of disease progression, A $\beta$  accumulation might be the initial event that causes later tauopathy-mediated neurodegeneration. There are also reports that tau accumulation is generally higher in A $\beta$ -positive individual instead of those that are A $\beta$ -negative [185]. For instance, NFT spread in those with sporadic primary tauopathies is limited when subjects are not A $\beta$ -positive [185,187–189]. Lastly, transgenic mouse models also offer evidence in support of interactions between amyloid and tau (see [185] for a summary). Tauopathy progresses faster in in triple transgenic mouse mice expressing both human tau with *APP* or *PSEN1*, as opposed to single transgenic mice expressing only human tau [190]. Not to mention, in the 3xTg-AD triple transgenic model that express tau and APP transgenes at comparable levels in

the same brain regions, extracellular A $\beta$  develops before tau which further validates the amyloid cascade hypothesis [191]. Interestingly, 3xTg mice showed impaired long-term potentiation synaptic responses, but 2xTg without the APP transgene did not [191]. These triple transgenic mice support the amyloid hypothesis, but it is unclear to what extent they mirror pathology in human subjects. Furthermore, it should be noted that familial AD transgene expression is not representative of the sporadic population.

### **1.3.3. AD progression**

The anatomical progression of AD was first described by Braak and Braak in accordance with the spread of NFTs and NTs, but not amyloid deposits [183]. This work gave rise to the Braak staging system which differentiates between six stages of AD and is still widely adopted.

**Stages I-II:** NFTs and NTs first appear in the transentorhinal region, a strip of cortex connecting the EC to the temporal lobe. Milder levels of NFTs form in the EC, CA1 of the hippocampus, the antero-dorsal nucleus of the thalamus (where HD cells can be found), and the basal forebrain. The number of NFTs and NTs progressively accumulates within the transentorhinal region. Given that the hippocampus is generally spared, and other cortical regions appear unaffected, these stages are referred to as ‘the transentorhinal stages’.

**Stages III-IV:** NFTs and NTs severely increase in the transentorhinal region and EC while only a moderate amount accumulates in CA1. Milder changes take place in the basal forebrain, thalamic regions, and the amygdala. These stages are referred to as ‘the limbic stages’, given that hippocampal regions (and limbic regions) are moderately affected whereas cortical regions are still relatively unaffected.

**Stages V-VI:** Previously affected regions worsen, with the entire hippocampus showing NFTs and NTs. Furthermore, many cortical regions are severely affected, leading these final stages to be referred to as ‘the isocortical stages’.

Extracellular amyloid deposits (not to be confused with plaques) varied between individuals and did not allow for accurate differentiation of multiple stages. In general, amyloid deposits first appeared in the basal parts of the cortex with mild presence in the entorhinal layers. Amyloid progressively spread to other cortical areas, while generally sparing the hippocampus. The final stages of pathology involved widespread amyloid throughout all cortical regions, with fewer deposits seen in the hippocampus and subcortical regions. Similarly, the distribution of amyloid plaques varied between individuals and were not useful for stage differentiation.

The modern understanding of AD progression is informed by the development of brain imaging techniques such as positron emission tomography (PET) scans that track non-soluble A $\beta$  and tau deposits [192,193], as well as the ability to detect soluble A $\beta$  and tau in cerebrospinal fluid (CSF) [194]. PET imaging not only confirms that A $\beta$  and tau accumulate in different brain regions, but increased tau PET signals better correlate with cognitive decline in MCI and AD patients as opposed to A $\beta$  signals [195–198]. Importantly, tau PET imaging also accurately reproduces the progression of tauopathy initially described by the Braak staging system [199,200]. A recent longitudinal tau PET imaging study investigated how tau Braak staging correlates with amyloid progression and cognitive impairments in MCI and AD subjects [201]. Up until Braak stage III, subjects had modest tau-PET signals and mild cognitive impairments regardless of their A $\beta$  status. However, tau progression beyond stage III only took place in patients that were A $\beta$ -positive, reaffirming the belief that amyloidopathy is a pre-requisite for more severe forms of tau-mediated neurodegeneration [201].

Both PET imaging and CSF biomarkers may be used to monitor living patients and confirm any signs of early AD. In 1984, the National Institute of Neurological and Communicative Disorders and Stroke (NINCDS) and the Alzheimer's Disease and Related Disorders Association (ADRDA) published a list of criteria for AD diagnosis [202]. These criteria aimed to determine if a patient likely had dementia via cognitive assessments, an outcome which could only be confirmed post-mortem. In 2011, these guidelines were expanded by the National Institute on Aging and Alzheimer's Association (NIA-AA) to include the use of imaging or CSF biomarkers to support or confirm an existing AD diagnosis [203]. However, these biomarkers could only be used in research settings and not in the clinic due to lack of standardization. In 2018, the NIA-AA published a 'research framework' which relabeled AD as a biological construct defined by the presence of biomarkers. This framework acknowledges that AD starts before clinical symptoms are apparent. In particular, both PET imaging and CSF concentrations of A $\beta$  and tau were suggested to be reliable diagnostic tools [204]. Importantly, the goal of this framework is still intended for research, and not meant to replace cognitive AD diagnostics which remain the focus in clinical settings.

In 2013, a hypothetical model of early biomarker progression was proposed by Jack and colleagues (**Figure 13**) [186]. The model describes the temporal evolution of different AD biomarkers which include amyloid deposition (measured by CSF A $\beta$ 42 and amyloid PET imaging) and neurodegeneration (measured by CSF tau, MRI, and FDG-PET imaging). Importantly, the model considers amyloidopathy and tauopathy as independent processes that may interact with one another. The Braak stages show that NFTs better separate disease phases, suggesting that tauopathy might be the initiator of AD [183]. Indeed, autopsies of individuals below the age of thirty show that formation of abnormally phosphorylated tau precedes amyloid deposition [205].

Yet, A $\beta$  also plays an initiating role given that familial AD arises via A $\beta$  overproduction [155]. To corroborate these findings, the model posits that there is an abnormality detection threshold for all *in-vivo* biomarkers. Tauopathy could exist early on before A $\beta$  but is undetectable *in-vivo* and/or is inconsequential. An independent rise of A $\beta$  levels past the threshold (through unrelated processes) could accelerate the tauopathy trajectory and form NFTs. These changes then lead to abnormal signals in MRI and FDG-PET imaging before cognitive impairments appear. The clinical AD spectrum involves pre-clinical, mild cognitive impairment (MCI) and dementia. The category a patient falls under varies according to risk factors in combination with *in-vivo* biomarkers.

*In-vivo* biomarkers provide a longitudinal understanding of early pathology, which is a desirable advantage over post-mortem analysis. These biomarkers occur decades before clinical symptoms and may help the detection of asymptomatic patients. Yet, biomarkers do not guarantee the appearance of cognitive impairments which may be influenced by risk factors and individual variability [206]. The study of novel biomarkers will likely establish a more accurate timeline of early pathology. Furthermore, treating amyloidopathy and tauopathy as independent processes might be productive. Given the many alternative theories of AD (at least for sporadic patients) [141–143], an integrated understanding of pathology is likely more informative than conforming to a central, dominant hypothesis.

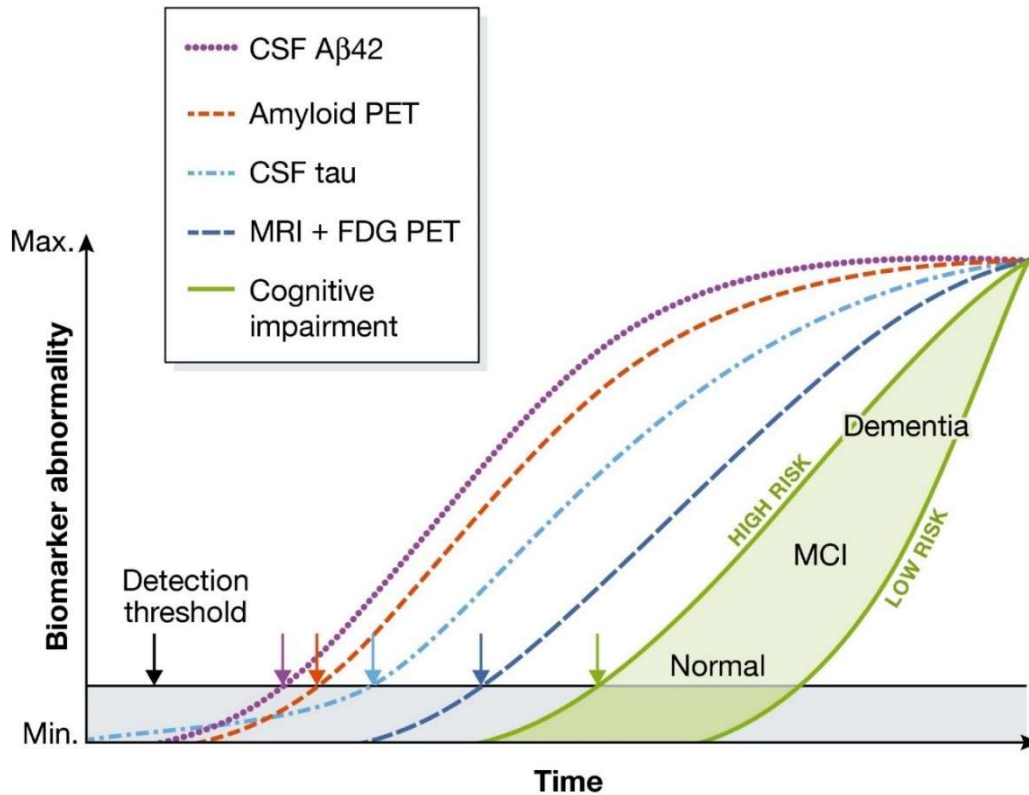


**Figure 13. A hypothetical model of early *in-vivo* AD biomarker progression.**

CSF A $\beta$ 42, amyloid PET imaging, CSF tau, and MRI + FDG-PET imaging are represented by the purple, red, light blue, and dark blue curves, respectively. The gray area indicates biomarker changes that cannot yet be detected by CSF or PET imaging. As CSF A $\beta$ 42 levels associated with pathophysiology rise above the detection threshold, there is an acceleration of tauopathy. The green area represents the onset of cognitive symptoms associated with clinical diagnosis of AD. The magnitude of cognitive impairment depends on individual risk. Importantly, the model treats A $\beta$ opathy and tauopathy as independent processes that interact.

Figure taken from Selkoe, D.J. and Hardy, J. (2016) The amyloid hypothesis of Alzheimer's disease at 25 years. *EMBO Mol. Med.* 8, 595–608.

A $\beta$ , amyloid  $\beta$ -protein; FDG, fluorodeoxyglucose; MCI, mild cognitive impairment.

### 1.3.4. Importance of early diagnosis

There is no cure for AD, in part because interventions do not effectively treat symptoms of late stage AD [5,207,208]. The lack of treatments highlights the importance of establishing reliable biomarkers to identify healthy individuals at risk and to prioritize their recruitment into clinical

trials early on. The 2018 research framework proposed by NIA-AA aims to do this, but also acknowledges that novel biomarkers aside from amyloidopathy, tauopathy and neurodegeneration should be considered when relevant [204].

In contrast, cognitive markers of early pathology are lacking. A study compared the detection sensitivity of the NIA-AA research framework biomarkers versus clinical diagnostic approaches (such as cognitive markers) in individuals between 60 to 89 years of age [209]. The results indicated that biologically-defined AD was more prevalent than clinically-diagnosed AD at any age group, highlighting the discrepancy in sensitivity between biomarkers and cognitive markers. As cognitive assessments remain a staple in the clinic, it is desirable to identify novel cognitive markers that signal earlier stages of pathology.

Current clinical AD diagnoses heavily rely on episodic memory tests [210]. Yet, episodic memory loss is also common in other pathologies such as frontal temporal dementia (FTD), or general aging [210,211]. In delayed recall tasks, AD is distinguished by impaired memory consolidation, whereas FTD and general aging cause impaired memory retrieval [210]. These tasks involve a patient being given a list of content (e.g., words) to remember (in association with semantic cues), and later asked to recall the encoded material. The presentation of semantic cues during the encoding phase helps ensure that the material was effectively encoded. These same cues can be re-presented during the recall phase to test for retrieval ability. If cue presentation improves recall performance, as is the case in FTD patients, then the impairment is related to memory retrieval. In contrast, presentation of a cue does not improve recall performance in AD patients, suggesting an impairment in memory encoding. Aside from this specific distinction, episodic memory assessments are largely insensitive to AD pathophysiology and offer limited clinical

utility [6,212]. Therefore, the efficacy of future interventional trials depends on the identification of novel markers that reliably detect early pathology.

### **1.3.5. Path integration as an early cognitive marker**

Given the relationship between entorhinal grid cells and path integration, in addition to the EC being one of the first regions affected by AD pathology [183,213], path integration impairments may be sensitive early cognitive markers of AD. In general, spatial navigation tasks offer fewer verbal, cultural and educational biases amongst subjects, offering a more globalized diagnosis approach than current cognitive tests [6]. Multiple studies have demonstrated that path integration performance reliably differentiates AD patients or those at risk from healthy older adults. When performing a real-world variant of the triangle completion task without access to visual cues, amnesic MCI and AD patients had greater difficulty estimating the start location compared to healthy older adults [10]. In another study where subjects performed a virtual triangle completion task, young *APOE-ε4* carriers (as young as 18 years of age) at genetic risk of AD also demonstrated path integration impairments [12]. In particular, the impairment observed in young carriers (18-42 years) worsened in older carriers (42-75 years). The experimenters controlled for the presence of visual cues in the virtual environment to ensure that participants relied on self-motion. In a different virtual task where visual information was available, path integration performance reliably differentiated *APOE-ε4* carriers from non-carriers [13]. These results suggest that path integration performance is a sensitive cognitive marker to detect those at risk of sporadic AD up to decades before clinical onset.

To establish a better link between behavioral performance and pathology, a separate study reported that path integration performance by MCI subjects in a virtual triangle completion task correlated with AD biomarkers [11]. Not only did MCI patients perform worse than healthy adults,

but MCI patients with positive AD biomarkers performed worse than those with negative biomarkers. In particular, levels of CSF A $\beta$  and tau independently correlated to performance. Compared to standard neuropsychological assessments and a hippocampus-dependent spatial memory task, path integration performance offered the greatest sensitivity in classifying these two MCI subgroups [11].

### **1.3.6. Grid cells as an early biomarker**

The link between grid cell computations and path integration suggests that a disrupted grid cell network underlies path integration impairments during early AD. In young *APOE*- $\epsilon$ 4 carriers, grid-like representations detected using fMRI were reduced and correlated to impaired path integration performance [9,12]. While it is unclear if grid-like fMRI activity reflects the activity of single grid cells, impaired path integration in older *APOE*- $\epsilon$ 4 carriers is accompanied by altered functional connectivity between the entorhinal (where grid cells are found) and retrosplenial cortices [13]. Furthermore, multiple mouse models of tauopathy and amyloidopathy individually show a shared disruption of grid cell and place cell coding during the later stages of pathology [214–221]. However, prior to the data presented in this thesis, no rodent study examined whether grid cell coding was disrupted during the earliest stages of pathology, and if such an impairment also correlated to path integration deficits. In addition, these rodent studies mostly involved tau models; the only reported study of grid cell coding in an amyloid model during late-stage pathology suffered from low sample sizes of recorded cells which rendered the conclusions difficult to interpret.

To better establish a link between grid cells (and potentially other spatially-tuned cells) and path integration deficits during early AD, we conducted *in-vivo* electrophysiological recordings of spatially-tuned neurons in the MEC and region CA1 of the hippocampus in the J20 transgenic A $\beta$

mouse model. To ensure that we conducted our recordings during the initial stages of pathology, we restricted our experimental timeline between 3-7 months of age – a period that precedes the deposition of widespread A $\beta$  plaques that are indicative of late AD [27]. We also separately tested J20 mice on a path integration task to observe whether a degraded grid cell network correlated to impaired path integration performance.

## **Chapter 2: Disruption of the grid cell network in a mouse model of early Alzheimer's disease**

**Authors:** Johnson Ying<sup>1,2</sup>, Alexandra T. Keinath<sup>1</sup>, Raphael Lavoie<sup>1</sup>, Erika Vigneault<sup>1</sup>, Salah El Mestikawy<sup>1,2</sup>, Mark P. Brandon<sup>1,2,\*</sup>

### **Affiliations:**

<sup>1</sup>Department of Psychiatry, Douglas Hospital Research Centre, McGill University, Montreal, QC, Canada.

<sup>2</sup>Integrated Program in Neuroscience, McGill University, Montreal, QC, Canada.

\*Correspondence to: mark.brandon@mcgill.ca

### **Abstract**

Early-onset familial Alzheimer's disease (AD) is marked by an aggressive buildup of amyloid beta (A $\beta$ ) proteins, yet the neural circuit operations impacted during the initial stages of A $\beta$  pathogenesis remain elusive. Here, we report a coding impairment of the medial entorhinal cortex (MEC) grid cell network in the J20 transgenic mouse model of familial AD that over-expresses A $\beta$  throughout the hippocampus and entorhinal cortex. Grid cells showed reduced spatial periodicity, spatial stability, and synchrony with interneurons and head-direction cells. In contrast, the spatial coding of non-grid cells within the MEC, and place cells within the hippocampus, remained intact. Grid cell deficits emerged at the earliest incidence of A $\beta$  fibril deposition and coincided with impaired spatial memory performance in a path integration task. These results demonstrate that widespread A $\beta$ -mediated damage to the entorhinal-hippocampal circuit results in an early impairment of the entorhinal grid cell network.

## Introduction

The molecular and synaptic underpinnings of A $\beta$  pathology during the earliest stages of familial AD are well-documented, but the impact that these changes have on neural coding has not been resolved<sup>1,2</sup>. The emergence of spatial memory deficits in patients with preclinical AD and those with Mild Cognitive Impairment with high levels of cerebrospinal fluid A $\beta$  suggest that A $\beta$  pathology exerts its earliest impact on the neural systems that support spatial memory<sup>3,4</sup>. Extensive work in both animals and humans have pinpointed the MEC-hippocampal circuit as essential brain regions for spatial memory performance<sup>5-7</sup>. At the level of neural coding, the MEC-hippocampal circuit contains a myriad of spatially-tuned cell types including place cells in the hippocampus, as well as grid cells, head direction cells, and non-grid spatially-selective cells in the MEC<sup>8-12</sup>. Decades of theoretical work have proposed how these functional cell types work in concert to support spatial memory<sup>13-17</sup>. Yet, it remains unknown how these spatially-tuned populations are impacted at the earliest stages of A $\beta$ -mediated pathogenesis when spatial memory is impaired.

To address this question, we recorded spatially-tuned neurons from the hippocampus and MEC of the J20 transgenic mouse model of familial AD that expresses a mutant form of human amyloid precursor protein (APP), referred to here as ‘APP mice’<sup>18</sup>. In this model, elevated and comparable levels of soluble A $\beta$  throughout the entorhinal cortex and hippocampus are present at 3 months of age<sup>19</sup>. By 5-7 months of age, small A $\beta$  fibrils are detectable in the hippocampus but neither of these regions demonstrate widespread amounts of A $\beta$  plaques that are indicative of late AD pathology<sup>19</sup>. We confirmed that APP mice expressed little-to-no plaques by 6 months of age in the MEC and hippocampus (Supplementary Fig. 1). Between 3-7 months of age, APP mice exhibit several amyloid-related processes that we refer to

collectively as ‘early A $\beta$  pathology’. These include neuroinflammation, 10-20% neuronal loss, and reduced presynaptic terminal density throughout the entorhinal cortex and hippocampus (detailed pathology description in Methods, Subjects)<sup>20-23</sup>.

In this work, we show that early A $\beta$  pathology reduces grid cell spatial coding in an age-dependent manner preceding the widespread expression of A $\beta$  plaques. In contrast, the spatial coding of non-grid cells within the MEC, and place cells within the hippocampus, is unaffected. The grid cell impairments correlate with worsened spatial navigation performance in a path integration task, thus pointing to both grid cell integrity and path integration performance as possible early markers of AD in familial and sporadic populations.

## Results

### Grid cell spatial tuning in APP mice is impaired across age

We obtained *in vivo* recordings of MEC neurons (n cells = 4524) from 38 APP transgenic and 30 non-transgenic (nTG) littermates as they foraged for water droplets in an open field arena (Summary of MEC recordings, Table S1; MEC Tetrode locations, Supplementary Fig. 2). We observed an age-related disruption in the spatial periodicity of grid cells in APP mice (Fig. 1a-d, Supplementary Figs. 3, 4, 5). Young APP mice (3-4.5 months) had grid cells with tuning comparable to those of age-matched nTG mice (Fig. 1). In contrast, grid cells recorded in adult (4.5-7 months) APP mice exhibited reduced spatial periodicity and spatial information (bits/spike) in comparison to those from young APP mice and age-matched nTG mice (Fig. 1). Peak spatial firing and mean firing rates of grid cells did not reliably differ between groups and across age (Fig. 1e). A two-way ANOVA was conducted to determine the effects of age and genotype on grid score between groups. A significant interaction effect was discovered, supporting the view that grid cell spatial periodicity is reduced across age in APP mice (ANOVA, age main effect:  $P = 1.89 \times 10^{-7}$ ;

genotype main effect:  $P = 0.011$ ; interaction effect:  $P = 3.86 \times 10^{-4}$ , Supplementary Fig. 6). To ensure that these results are not biased by oversampling the same cells across days, we removed duplicate grid cells and re-ran our analyses. Grid cell spatial periodicity remained impaired in adult APP mice, and the significant interaction effect persisted (ANOVA, age main effect:  $P = 4.5 \times 10^{-4}$ ; genotype main effect:  $P = 0.013$ ; interaction effect:  $P = 0.046$ , Supplementary Fig. 7).

### **Spatial tuning of non-grid MEC cells remains intact in APP mice**

In contrast to the age-dependent impairment observed in grid cells, entorhinal head direction cells, which encode the orientation of the animal's head in polar coordinates<sup>10</sup>, did not differ in their directional tuning or firing rates between groups or across age (Fig. 2a, Supplementary Fig. 8). Similarly, there was no difference between groups in the average firing field size of non-grid spatially-tuned neurons, which fire in a non-periodic but spatially reliable manner (Fig. 2b, Supplementary Fig. 8). Mean firing rates did not differ between groups, but spatial peak firing rates were, however, oddly elevated in adult nTG mice (Fig. 2b).

To examine if spatial coding by downstream hippocampal place cells was disrupted when adult APP mice exhibit a degraded grid cell code, we obtained *in vivo* recordings from region CA1 of the hippocampus (n cells = 992) from 6 adult APP and 6 adult nTG mice (Summary of CA1 recordings, Table S2; CA1 Tetrode locations, Supplementary Fig. 9). Place cells in adult APP and nTG mice were similarly tuned for spatial location and had similar peak spatial and mean firing rates (Fig. 2c, Supplementary Fig. 8). Spatial tuning remained largely preserved across groups when varying our cell selection threshold (spatial peak firing rates between 0 and 8 Hz), with the exception of thresholds less than 1 Hz (Fig. 2d). Mean firing rates were higher in APP place cells at peak firing selection thresholds of 6 Hz and greater, suggesting that the overall mean firing rate is higher in adult APP mice than those in adult nTG mice (Fig. 2d). These results demonstrate that

the hippocampal place code remains grossly intact when the entorhinal grid code is degraded in adult APP mice, mirroring findings observed in early development and during inactivation of the medial septum<sup>24-26</sup>. Our findings are consistent with previous work showing that the spatial tuning of place cells in Tg2576 APP mice remained intact at the earliest incidence of A $\beta$  plaques, but was subsequently impaired when A $\beta$  plaques become widespread<sup>27</sup>. Moreover, our results suggest that impaired grid coding in adult APP mice is not the result of disrupted feedback from the hippocampus<sup>28</sup>.

Prior work has reported a selective disruption of grid cell spatial periodicity without impairment of other spatial codes when the power of entorhinal theta oscillations (6-10 Hz) is reduced via inactivation of the medial septum<sup>25,26</sup>. We therefore examined entorhinal theta oscillations across nTG and APP mice and found that theta power remained intact in adult APP mice across running speeds (ANCOVA, APP-a vs nTG-a, main effect:  $P = 0.99$ ; interaction between running speed and theta power:  $P = 0.096$ ; APP-a vs APP-y, main effect:  $P = 0.051$ ; interaction between running speed and theta power:  $P = 0.56$ ; Fig. 2e). In both young and adult APP mice, the overall baseline frequency of theta oscillations was lower while the gain in theta frequency across running speeds was preserved (ANCOVA, APP-a vs nTG-a, main effect:  $P = 0.01$ ; interaction between running speed and frequency:  $P = 0.51$ ; APP-y vs nTG-y, main effect:  $P = 0.0001$ ; interaction between running speed and frequency:  $P = 0.82$ ; Fig. 2e), revealing that the baseline frequency of theta oscillations was reduced in APP mice prior to the onset of grid cell disruption. Theta frequency reduction in both young and adult APP mice was roughly 0.2 Hz across all running speeds (Supplementary Fig. 10). Assuming that this reduction in theta frequency has no effect on grid cell periodicity in young APP mice, these results indicate that impaired grid cell coding in adult APP mice cannot be explained by a disruption of the theta-generating circuit.

Speed cells in the MEC encode the animal's running speed by firing rate and are assumed to provide a speed signal for grid cell formation<sup>29</sup>. To determine if impaired speed cells could explain the disrupted grid cell periodicity in adult APP mice, we examined the running speed vs firing rate correlation of MEC cells that were not characterized as either grid cells, head direction cells and non-grid spatially-tuned cells (Supplementary Fig. 11). No significant differences were found between groups when varying our cell selection threshold (running speed vs firing rate correlation values between 0.1 and 0.9), suggesting that MEC speed cells remained unaffected by APP pathology (Supplementary Fig. 11a). Running speed vs firing rate correlations of grid cells was also non-significant between groups, providing further evidence for an intact speed code (Supplementary Fig. 11b, c).

### **Grid cells in adult APP mice are spatially unstable**

To characterize the nature of reduced grid cell periodicity in adult APP mice, we examined the spatial firing properties of grid cells in further detail. In contrast to grid cells recorded in adult nTG mice, grid cells in adult APP mice exhibited larger firing fields when accounting for differences in spatial scale (Fig. 3a). We reasoned that an increase in field size in adult APP mice could reflect a drifting or unstable grid pattern over time. Consistent with this, a partitioned rate map stability analysis revealed that the overall grid pattern in adult APP mice exhibited reduced spatial stability (Fig. 3b-d). The reduced stability of grid cells in adult APP mice was not due to changes in the orientation of grid fields, indicating that instability reflected an inconsistent spatial phase of the grid pattern over time (Fig. 3e). In contrast, non-grid spatially-tuned cells and hippocampal place cells of adult APP mice remained spatially stable across time (Fig. 3b-d). A two-way ANOVA was conducted to further confirm that the spatial instability was specific to grid cells, but not non-grid spatially-tuned cells and place cells in adult APP mice. The ANOVA

design's factors consisted of genotype and cell type, and both significant main and interaction effects were discovered (ANOVA, genotype main effect:  $P = 0.0038$ ; genotype main effect:  $P = 0.0084$ ; interaction effect:  $P = 0.013$ , Supplementary Fig. 12). Pairwise comparisons using Tukey's Test revealed greater spatial instability in APP-a grid cells, but not in APP-a non-grid spatially-tuned cells or place cells (APP-a grid cells vs. nTG-a grid cells:  $P = 0.0064$ ; APP-a non-grid cells vs. nTG-a non-grid cells:  $P = 1$ ; APP-a place cells vs. nTG-a place cells:  $P = 0.99$ ). Instability persisted in adult APP grid cells when partition lengths were extended from 3 minutes to 5, 6 and 10 minutes (Supplementary Fig. 13). Consistent with previous literature<sup>30,31</sup>, positional coverage and running speeds were higher in adult APP mice, suggesting that greater displacements were not biased by insufficient exploration of the open field environment (Supplementary Fig. 14).

### **Grid cells in APP mice have reduced spike-time synchrony with interneurons and head direction cells**

Given that inhibition constitutes a major input for grid cell generation<sup>32,33</sup>, we analyzed the firing properties of interneurons in APP mice. Across age, mean firing rates became elevated in adult APP mice (ANOVA, genotype main effect:  $P = 0.0038$ ; genotype main effect:  $P = 0.0084$ ; interaction effect:  $P = 0.013$ , Supplementary Figs. 15, 16), alluding to possible changes in inhibitory networks within the MEC. In particular, we noted that a significant proportion of interneurons in young and adult APP mice had slower theta rhythmicity and theta power, suggesting a potential early impairment in spike-timing dynamics between grid cells and interneurons preceding the loss of grid cell spatial periodicity (Supplementary Figs. 15, 16). By computing spike-time cross-correlations between simultaneously recorded MEC cells, we observed that synchrony between grid cells and interneurons were qualitatively reduced in young APP mice in comparison to nTG mice (Fig. 4a-b). In fact, young APP grid cells and interneurons

appeared anti-synchronous at a temporal lag of ~25ms, suggesting the start of an early impairment of the grid cells' ability to temporally integrate inhibitory signals. Surprisingly, the same reduction in synchrony was also qualitatively observed between grid cells and head direction cells, which appeared to worsen across age (Fig. 4a-b).

A two-way ANOVA was conducted to determine the effects of age and genotype on the mean co-activity within a 25 ms time window for grid cell-interneuron and grid cell-head direction cell pairs (Supplementary Fig. 17, Fig. 4c). There was no significant interaction effect in either group (ANOVA: grid-interneuron interaction effect:  $P = 0.091$ ; grid-head direction interaction effect:  $P = 0.083$  Supplementary Fig. 17, Fig. 4c), confirming the absence of any age-dependent reduction in synchrony. However, there was a significant main effect of genotype in both groups, indicating that grid cell-interneuron and grid cell-head direction cell synchrony were impaired overall in both young and adult APP mice (ANOVA: grid-interneuron genotype main effect:  $P = 1.3 \times 10^{-5}$ ; grid-head direction genotype main effect:  $P = 0.012$ , Supplementary Fig. 17). In support of this view, synchrony was significantly lower in adult APP mice compared to adult nTG mice, and was unaffected compared to young APP mice (Fig. 4c). However, the lack of statistical significance between young APP and young nTG mice implies that this reduction may be milder in the earliest stages of pathology (Fig. 4c). These findings are noteworthy for two reasons. First, given the importance of inhibitory and head direction information for grid cell spatial firing<sup>32-34</sup>, these results suggest that disrupted grid cell spatial periodicity across age in APP mice (Fig. 1) arises in part due to the temporal decoupling of grid cells from inhibitory and head direction inputs within the local MEC network. Second, this decoupling starts (albeit mildly) at an age when the grid pattern is still intact, implying that grid cell coding is affected by early pathology preceding the complete loss of spatial periodicity.

## **Grid cell impairments in APP mice correlate with worsened path integration performance**

Prior work has shown that APP mice exhibit spatial memory deficits on the Morris water maze and the radial arm maze by as early as 3-4 months of age<sup>21,30</sup>. Given the proposed role of grid cells in supporting path integration<sup>17,35</sup>, we hypothesized that APP mice would also experience spatial memory deficits related to path integration. To test this hypothesis, we conducted a path integration task to assess the animals' ability to return directly to their refuge after finding a food pellet in an open field in complete darkness with an independent, non-implanted cohort of APP and nTG mice (n mice = 12 APP-y, 9 APP-a, 10 nTG-y, 8 nTG-a; Fig. 5a, Supplementary Fig. 18a). APP and nTG mice demonstrated a similar inclination to return to the refuge prior to consumption of the pellet (Supplementary Fig. 18b-d). However, we observed that APP mice were impaired in all measures of path integration ability relative to age-matched controls, with the greatest behavioral deficits in adult APP mice. In particular, the probability of arriving at the refuge during the initial wall contact decreased in APP mice across age (APP-a: 29%, APP-y: 38%, nTG-y: 58%, nTG-a: 57%; Fig. 5b, c), suggesting that they had a greater difficulty in estimating their position relative to the refuge. In further support of this possibility, adult APP mice exhibited increased error in both their initial heading direction and the angular difference between the refuge and the first wall encountered during the return trajectory (Fig. 5d, e). With regards to overall navigational efficiency, adult APP mice travelled longer distances to return to the refuge and exhibited greater thigmotaxis by spending a larger proportion of the return path along the periphery of the environment (Fig. 5d, e). All groups showed improved performance when visual cues were made available (Supplementary Fig. 19), though APP mice remained impaired across all measures of task performance which worsened with age (Supplementary Fig.

20). Together, these results show that path integration abilities decline with age in APP mice, closely mirroring the time course of the spatial coding deficits observed in the grid cell network.

Lastly, we characterized which molecular changes could explain these early network alterations in the entorhinal-hippocampal circuit. A recent meta-analysis confirmed that synapse loss and changes in synaptic marker expression are major events in AD pathogenesis<sup>36</sup>. Likewise, altered synaptic function could also affect circuit function such as grid cell coding that is known to require both excitatory and inhibitory drive<sup>28,32,33</sup>. For these reasons, we carried out immunohistochemistry in the MEC and CA1 to visualize and quantify the expression of synaptic markers that include VGLUT1, VGLUT3, VACHT, VGAT and NR1 (Supplementary Fig. 21). VGLUT1, VGLUT3 VACHT and VGAT are neurotransmitter transporters whereas NR1 is a subunit of NMDA receptors that was previously shown to be necessary for both grid cell integrity and path integration ability<sup>35</sup> (detailed marker descriptions in Methods, Immunohistochemical labelling of synaptic markers).

To interpret the most robust pathological changes, we ran linear mixed models to pinpoint which marker expression levels were most affected by early A $\beta$  pathology. Out of the ten experimental groups, two cases were significantly modulated by the effect of the subject's genotype: VGLUT3 in the MEC and VGLUT1 in CA1 (VGLUT3 in MEC, genotype effect:  $P < 0.01$ ; VGLUT1 in CA1, genotype effect:  $P < 0.01$ ; Supplementary Fig. 22). We observed an increase of VGLUT3 in both young and aged APP mice, indicating that CCK-positive interneurons are exerting greater influence in inhibitory circuits within the MEC (Supplementary Figs. 23, 24). However, VGAT levels were not significantly different (Supplementary Figs. 21, 22), suggesting that early A $\beta$  pathology targets a specific inhibitory circuit while sparing overall inhibitory drive. Taken together with our spike-time cross-correlation analysis (Fig. 4), these findings

pinpoint inhibitory mechanisms as one of the earliest network changes in the MEC. An increase of VGLUT1 was also detected in CA1 of young APP mice that stayed elevated across age (Supplementary Figs. 22, 23). This finding explains the higher mean firing rate of adult APP place cells (Fig. 2d), and supports existing evidence showing that hyperexcitability is a major pathological symptom of AD<sup>37</sup>. Taken together, these results provide an in-depth overview of the early network changes in the MEC-hippocampal circuit susceptible to A $\beta$  pathology at the molecular, physiological, and behavioral levels.

## **Discussion**

To identify the impact of A $\beta$  pathology on neural coding in the MEC-hippocampal circuit, we obtained single-unit recordings during the initial stages of disease in an APP mouse model of familial AD. These data revealed a disruption in entorhinal grid cell coding when initial A $\beta$  fibrils are detected. In contrast, the spatial tuning of other functional cell types in the MEC and region CA1 of the hippocampus was preserved. Theta power and modulation of theta by running speed remained intact in adult APP mice, yet grid cells exhibited reduced theta rhythmicity and spatial stability. Grid cells in young APP mice appeared to be decoupled from interneurons and head direction cells, which worsened across age. These changes in grid cell coding corresponded with impaired performance of adult APP mice in a path integration task. Together, these results reveal that early A $\beta$  pathology targets the entorhinal grid cell network within the MEC-hippocampal circuit.

Our results address several possible circuit-level explanations that could underlie reduced grid cell coding in APP mice. Prior studies have shown that inputs from the anterior thalamic nuclei (ATN), the dorsal hippocampus, and the medial septum are each independently necessary for normal grid cell function. Entorhinal head direction cells, which

are dependent on direct and indirect inputs from the ATN<sup>34</sup>, were preserved in adult APP mice, suggesting that projections from the ATN were intact. Place cells in the dorsal hippocampus remained spatially selective, stable, and had high firing rates, indicating that reduced feedback from the hippocampus cannot explain grid cell deficits in adult APP mice<sup>28</sup>. Finally, theta power and speed modulation of theta were preserved in adult APP mice, suggesting that medial septal theta-generating inputs to the MEC are conserved<sup>25,26</sup>. Nevertheless, our findings could still indicate a subtle impairment of basal forebrain inputs that innervate the grid cell network; one candidate could be decreased septal cholinergic inputs<sup>38</sup>, as a selective loss of basal forebrain cholinergic neurons in the nucleus basalis of Meynert is observed in familial AD patients<sup>39,40</sup>.

We also observed that grid cells recorded in APP mice had reduced spike-timing synchrony with interneurons and head direction cells. This is interesting because interneuron mean firing rates and head direction cell directional selectivity were not lower in APP mice. These results are particularly noteworthy because grid cells require excitatory, inhibitory and head direction inputs<sup>28,32-34</sup>. While we did not observe any obvious impairments in those systems specifically in terms of basic firing properties, their temporal integration within the grid cell network could potentially disrupt spatial coding. The temporal decoupling of grid cells from local inputs therefore provides a network-level explanation for the reduced grid cell spatial periodicity and stability observed in adult APP mice. On that note, we could not analyze grid cell-place cell synchrony, given that we did not record from the MEC and CA1 simultaneously. This decoupling is also weakly present in young APP mice (as suggested by a two-way ANOVA, but insignificant via direct non-parametric testing), alluding to the possibility that grid cell coding is impaired prior to the complete loss of spatial periodicity. It could be that the temporal

decoupling is progressive and worsens with age, but we cannot directly confirm this idea with the current data and the lack of a significant effect size in young APP mice. Lastly, the cross-correlation analyses should not be used to draw conclusions regarding the amount of inhibition or excitation integrated by grid cells, which require other experiments to validate.

We also characterized whether local network-level changes can be accounted for at the molecular level. Based on our quantification of synaptic markers, VGLUT3 levels were pathologically elevated in the MEC of APP mice. These findings pinpoint specific inhibitory mechanisms as one of the earliest network changes in the MEC, as VGAT levels indicative of global inhibition were unaltered. However, these findings are hard to relate to the observed grid cell impairment. On the other hand, an increase of VGLUT1 was also detected in CA1 of young APP mice that stayed elevated across age. This finding explains the higher mean firing rates of adult APP place cells and is consistent with the hypothesis that hyperexcitability is a major pathological symptom of AD<sup>37</sup>. We applied a linear mixed model and only considered marker expression levels that were significantly modulated by the subject's genotype. By doing so, a more subtle effect amongst other markers might have been deliberately missed. For instance, there was a slightly lower NR1 expression in adult APP mice relative to adult nTG mice, and it is known that this NMDA receptor subunit is necessary for grid cell firing<sup>35</sup>.

Our results suggest that grid cells contribute to path integration, and possibly other forms of spatial memory. Young APP mice were modestly impaired in our path integration task despite an intact grid cell spatial periodicity. In parallel, prior work has shown spatial memory impairments in this APP mouse line at the same age in the radial arm and Morris water mazes<sup>21,30</sup>. An early disruption of the spike-timing relationship between grid cells and other MEC cell types in young APP mice could potentially underlie these behavioral impairments. Likewise, reduced

grid cell spatial periodicity and stability could explain the more pronounced path integration impairments in adult APP mice. Our behavioral data showed that in addition to increased travel distance and angular errors in the return path, adult APP mice spent more time along the environment periphery. This suggests that adult APP mice could not plan effective routes back to the refuge and instead adopted a thigmotaxic strategy. The severity of grid cell deficits paralleling the worsened behavioral performance provides compelling evidence to suggest that this microcircuit is linked to path integration and perhaps other forms of spatial memory. There are likely other undetermined factors that explain the spatial memory impairment observed in these mice at a young age, but our findings are consistent with the current understanding of how grid cells are necessary for proper path integration function<sup>17,35</sup>.

Of particular importance, our results reveal that A $\beta$ -mediated perturbations at the synaptic level do not uniformly impact neural computations. APP mice express soluble A $\beta$  oligomers throughout the entorhinal cortex and exhibit a reduced density of presynaptic terminals and neuronal loss across all entorhinal layers by 6 months of age<sup>20</sup>, yet only the grid cell subnetwork within the MEC was disrupted. Similar and widespread changes are observed throughout the hippocampus, but the spatial coding of place cells was not disrupted.

Place cells have also been recorded in other APP-related mouse models. The spatial tuning of place cells in the Tg2576 APP mouse model remained intact at the earliest incidence of A $\beta$  plaques<sup>27</sup>, similar to our results. However, differences in place cell physiology have also been reported. In the 3xTg triple transgenic mouse model displaying both APP and tau pathology, place cells exhibited spatial instability on a linear track preceding the detection of plaques which seems to be in conflict with our findings<sup>41</sup>. One explanation for this difference is environmental influence. As the mouse's freedom of movement is constrained on a one-

dimensional track, the direction of instability is spatially restricted. In contrast, instability in an open field can occur in 360 degrees and averaging these directional shifts over time may ultimately cancel out to give the impression that APP place cells are stable. It could be that a linear track is more sensitive at detecting precise changes in place cell stability that may not meaningfully impact overall spatial coding in a two-dimensional environment. Alternatively, this difference could be due to the presence of tau pathology in 3xTg mice. In a different study involving a chimeric APP mouse model where the onset of APP expression could be controlled, place cell stability was also impaired on a linear track<sup>42</sup>. However, this disruption took place 9.5 months following APP expression, a pathogenic timepoint that is much later than ours which could explain their results. Lastly, a study reported that grid cells and place cells were disrupted in an APP knock-in mouse model<sup>43</sup>. Despite already have moderate levels of plaque formation throughout the brain, these young APP knock-in mice still did not show any impaired place cell coding, which are consistent with our findings.

It is certain that inherent differences within mouse models may contribute to variability between results<sup>41,42</sup>, but so can the experimental design. Our place cell results are best comparable to those recorded from Tg2576 mice<sup>27</sup> because recordings were done in an open field during the earliest detection of amyloid plaques. From this perspective, our results are consistent with what is currently known about A $\beta$  pathology and place cell coding. To this growing body of knowledge, we show that impairments in grid cell firing emerge prior to place cell disruption. Importantly, both extracellular and intracellular A $\beta$ -related processes may be pathogenic drivers of the reported network changes and should be further investigated. Despite the popular belief that extracellular A $\beta$  initiates many aspects of pathology, there is a wide body of evidence showing that intracellular A $\beta$  does the same<sup>44-47</sup>.

Alternatively, functional magnetic resonance imaging (fMRI) has revealed that the lateral entorhinal cortex (LEC) could be the first region affected in early AD<sup>48</sup>. The LEC is an important node in the entorhinal-hippocampal circuit and has also been studied in APP mouse models. In PDAPP mice, the location of amyloid deposits in the dentate gyrus greatly coincided with the termination of afferent projections from the LEC<sup>49</sup>. In terms of single-unit physiology, a report showed cells in Tg2576 mice displayed hyperactivity in the LEC by as early as 3 months of age<sup>50</sup>. Physiological changes in the LEC as a result of A $\beta$  may precede the reported grid cell impairments and merit further investigation.

There is concern regarding the use of transgenic APP mice such as the J20 model that overexpresses non-physiological A $\beta$  given that recent APP knock-in mice express pathological profiles that are more faithful of AD pathogenesis. Caution should be exerted when relating conclusions of this study to human AD populations. Nevertheless, we took advantage of the robust phenotypic nature of J20 mice to identify the specific parts of the MEC-hippocampal spatial coding circuit most impacted by early APP pathology. Importantly, AD is also a multifaceted neurodegenerative disease marked by pathological markers other than A $\beta$ , such as widespread neurofibrillary tangles consisting of the hyperphosphorylated-tau protein. Therefore, the results of our study do not provide a complete overview of grid cell dysfunction in AD. Yet, it is interesting to note that prior work using a tau transgenic mouse line has shown that grid cell spatial coding is preserved when tau is initially restricted to axonal and somatodendritic compartments, but is subsequently impaired once tau has accumulated extensively in entorhinal cell bodies<sup>51</sup>.

Reports on multi-study validation of data-driven disease progression in human AD patients<sup>52,53</sup> predict that cohorts of familial AD and *APOE*- $\epsilon$ 4-positive subjects exhibit

cerebrospinal fluid biomarkers in a distinct sequence: amyloid- $\beta$ 1–42, phosphorylated tau, and then total tau. However, in the broader AD population, total tau and phosphorylated tau are found to be earlier biomarkers than A $\beta$ . The combined findings that early A $\beta$  and advanced tau pathologies each independently target the grid cell network highlight the vulnerability of this entorhinal subnetwork and raise the possibility that spatial memory deficits in AD are linked directly to grid cell integrity. Indeed, functional imaging in young adults at genetic risk of AD (*APOE*- $\epsilon$ 4 carriers) revealed a reduced grid-like hexa-symmetric signal in the MEC that correlated with spatial memory and path integration impairments<sup>54–56</sup>. These convergent lines of evidence support the viability of grid cell integrity and spatial navigation deficits as early markers of AD<sup>4</sup>, and as dependent variables to assess the efficacy of AD therapeutics.

## Methods

### Subjects

J20 APP male mice (B6.Cg-Zbtb20 Tg(PDGFB-APP<sup>SwInd</sup>) 20Lms/2Mmjax) were obtained from Jackson Laboratories (MMRRC stock #34836) and bred with female C57/BL6/j mice. Mice were individually housed on a 12-h light/dark cycle and underwent experiments during the light cycle. Housing room conditions of the mice were maintained at 20-22 degrees Celsius and 21-30% humidity. All experimental procedures were performed in accordance with McGill University and Douglas Hospital Research Centre Animal Use and Care Committee (protocol #2015-7725) and in accordance with Canadian Institutes of Health Research guidelines.

In J20 mice, layers 2, 3 and 5 of the MEC undergo progressive neuronal loss and by 7.5 months of age, all layers experienced a combined loss of 16.3% in comparison to age-matched controls<sup>18</sup>. The entorhinal cortex as a whole exhibits a reduced density of presynaptic terminals (quantified by synaptophysin-immunoreactivity) by 7 months of age<sup>20</sup>. Similarly, by 6 months of age, region CA1 of the hippocampus in APP mice exhibits a 10%+ loss of neurons compared to age-matched controls<sup>21</sup>. Synapse loss is observed as early as 3 months of age in CA1, confirmed both by synaptic marker-immunoreactivity and electron microscopy<sup>22</sup>. In addition to these processes, the complement-dependent pathway and microglia undergo aberrant upregulation that is dependent on soluble A $\beta$  oligomeric levels in the hippocampus<sup>22</sup>. Furthermore, gliosis (activated astrocytes) and neuroinflammation (activated microglia) become elevated across age in the hippocampus of 6-month-old APP mice<sup>21</sup>. Lastly, *in vitro* slice electrophysiology experiments revealed that both basal synaptic transmission recorded in CA1 and long-term potentiation in the Schaffer collateral-CA1 synapse are impaired in 3 month-old APP mice<sup>23</sup>. To examine the impact of these A $\beta$ -

mediated changes on neural coding circuit during these early stages of A $\beta$  pathology, we focused on APP mice between 3-7 months of age.

Single-unit recording data in the (MEC) were collected from 68 APP mice and littermates with negative transgene expression across four experimental groups: young APP mice (3-4.5 months of age), adult APP mice (4.5-7 months of age), young non-transgenic (nTG) mice (3-4.5 months of age), adult nTG mice (4.5-7 months of age). Thirty-one males and 37 females were used. Ten animals fell into multiple age groups. The male/female ratios were 6:5, 16:16, 9:5, and 11:10 for young APP, adult APP, young nTG, and adult nTG mice respectively. Single-unit recording data in region CA1 of the hippocampus were collected from six adult APP mice (3:3 male/female ratio) and six adult nTG mice (2:4 male/female ratio).

A separate, non-implanted cohort of APP and nTG mice were tested in the path integration behavior task. Mice were separated into the same four experimental groups defined above. The male/female ratios were 6:6, 6:3, 5:5, and 4:4 for young APP, adult APP, young nTG, and adult nTG mice respectively.

## **Surgery**

On the day of surgery, mice were anesthetized with isoflurane (0.5% - 3% in O<sub>2</sub>) and administered carprofen (0.01 ml/g) subcutaneously. For each mouse, three anchor screws were secured to the skull and a ground wire was positioned either above the cerebellum at midline position or the left visual cortex. A 'versadrive' containing four independently movable tetrodes (Axona, Inc) was implanted on top of the right MEC at the following stereotaxic coordinates: 3.4 mm lateral to the midline, 0.25-0.40 mm anterior to the transverse sinus. For hippocampal implants, the versadrive was implanted on top of the right CA1 at the following stereotaxic coordinates: 1.5 mm lateral to the midline, 1.9 mm posterior from bregma. Tetrodes were gold-plated to lower impedances to

150-250 k $\Omega$  at 1 kHz prior to surgery. The versadrive was angled at eight degrees in the posterior direction for MEC implants and was not angled for CA1 implants. Following placement, the versadrive was secured in place using Kwik-Sil (to prevent exposure of the brain) and dental acrylic (to secure the versadrive to the skull and anchor screws). The ground wire was soldered to the implant, and tetrodes were lowered 1.0 mm and 0.5 mm from the dorsal surface for the MEC and CA1 respectively. All surgical procedures were performed in accordance with McGill University and Douglas Hospital Research Centre Animal Use and Care Committee (protocol #2015-7725) and in accordance with Canadian Institutes of Health Research guidelines.

### **Neural Recordings**

Three days post-surgery, mice were placed on water restriction and maintained at 85% of their *ad libidum* weight for the duration of experiments. Mice were tested in six different open field environments. The majority of MEC recordings were done in a 75 x 75 cm box (1109 recordings), but a number of them also took place in a ten-sided maze with a 63.8 diameter (9 recordings), a 50 x 50cm box (121 recordings), a 84 x 84 cm box (23 recordings), a 90 x 90 cm box (1 recording), and a 100 x 100 cm box (58 recordings). All CA1 recordings were done in the same 75 x 75 cm box. As mice explored their environments, water droplets were randomly scatter throughout to motivate the subjects to adequately sample the entire open field. Once mice reliably provided good trajectory coverage, tetrodes were turned quickly until theta rhythmic units were observed which indicated that the tetrodes had entered the MEC. Tetrodes were then advanced in increments of 25 microns to sample new putative MEC neurons, which was later confirmed by histology. For the CA1 cohort, sleep recordings were carried out prior to open field exploration to detect sharp wave and ripple activity. Once ripple amplitude was stable across days, tetrodes were no longer turned. Occasionally, tetrodes were either advanced or retracted depending on fluctuations in ripple

amplitude and unit activity. In most cases for both MEC and CA1 recordings, neurons were not stable enough between recordings to reliably determine whether cells were re-sampled across days and thus we have included all cells recorded into our analysis.

To record spikes and local field potentials, versadrives were connected to a multichannel amplifier tethered to a digital Neuralynx (Bozeman, MT) recording system, and data were acquired using Cheetah 5.0 software (Neuralynx, Inc). Signals were amplified and band-pass filtered between 0.6 kHz and 6 kHz. Spike waveform thresholds were adjusted before commencing each recording and ranged between 35-140  $\mu$ V depending on unit activity. Waveforms that crossed threshold were digitized at 32 kHz and recorded across all four channels of the given tetrode. Local field potentials were recorded across all tetrodes.

### **Histology**

Animals were anesthetized with Isoflurane and perfused intracardially using saline, followed by 4% paraformaldehyde. Animal heads were left in 4% paraformaldehyde for between 24-72 hours following perfusion, before brains were extracted. Brains were left to sink in a 30% sucrose solution, and then frozen and stored in a -80°C freezer. Sagittal brain sections (40 $\mu$ m) were sliced using a cryostat and Nissl-stained with a Cresyl violet solution. In cases where brain slices repeatedly came off the glass slides during Nissl-staining, slices were instead mounted using a fluorescent DAPI labeling mounting medium.

Tetrode tracks were characterized to be in either the superficial or deep layers based on the location of the track tip. Only data collected from tetrodes within the MEC were included in the analysis.

For hippocampal recordings, all tetrode tips that picked up single-units were determined to be in region CA1 of the dorsal hippocampus. Tips from tetrodes located outside of CA1 did not pick up any single-units.

### **Spike sorting**

Single-units were isolated ‘offline’ manually using Offline Sorter 2.8.8 (Plexon, Inc) individually for each recording session. Neurons were separated based on the peak amplitude and principal component measures of spike waveforms. Evaluation of the presence of biologically realistic interspike intervals, temporal autocorrelations, and cross correlations was used to confirm single-unit isolation. The experimenter was blind to the age and genotype of the subjects and only well-separated clusters were included in analysis.

### **Position, direction and velocity estimation**

For all electrophysiological recordings, positional data was acquired at 30 frames per second at 720 x 480 pixel resolution (4.9 pixels per cm) using a camera purchased from Neuralynx (Bozeman, MT). The camera was elevated at a height such that it fully captured all recording environment sizes used. The estimated position of the animal was calculated as the centroid of a group of red and green diodes positioned on the recording head stage. Head direction was calculated as the angle between the red and green diodes. Up to five lost samples due to occlusion of tracking LEDs, or reflections in the environment were replaced by a linear interpolation for both position and directional data. Running velocity was calculated using a Kalman filter. Rate maps were constructed by calculating the occupancy-normalized firing rate for 3cm x 3cm bins of position data. Data were smoothed by a two-dimensional convolution with a pseudo-Gaussian kernel involving a three pixel (9 cm) standard deviation. To visualize periodicity of grid fields, we

computed the spatial autocorrelation of the smoothed rate maps using Pearson's product moment correlation coefficient as described in Supplementary Fig. 3.

### **Gridness score**

To quantify the spatial periodicity of MEC neurons, we calculated a 'gridness score' as described in Brandon et al., 2011<sup>25</sup>. Briefly, this metric quantifies the hexagonal spatial periodicity in firing rate maps, while also accounting for elliptical eccentricity along one of two mirror lines that exist in a hexagonal lattice structure. Distortion along one of the mirror lines was corrected after determining the major and minor axes of the grid based on the six fields closest to the central peak of the rate map autocorrelogram. The entire autocorrelogram was compressed along the major axis so that the major axis became equal to the minor axis. Large eccentricities (where the minor axis was less than half of the major axis) were not corrected. From the compressed autocorrelogram, we extracted a ring that encased the six peaks closest to the center peak but excluded the central peak to report periodicity between fields. We then calculated a rotational autocorrelation of this ring and observed the periodicity in paired pixel correlations across 180 degrees of rotation. The gridness score was computed as the difference between the lowest correlation observed at 60 or 120 degrees of rotation and the highest correlation observed at 30, 90, or 150 degrees of rotation. To ensure that our finding that grid cell reduction was not observed because of double-sampling grid cells across recording sessions, we made efforts to reduce putative double-sampling. Recordings of grid cells with cluster centroids within 0.2mV on subsequent days were considered to be putative duplicate recordings, and the grid cell recording with the best separation index was chosen for statistics on gridness across groups in Supplementary Fig. 7. We used the full set of recordings for all other analyses.

### **Directionality**

Polar histograms of firing rate by head direction were generated to visualize the pattern of spiking dependent upon the animal's direction. To construct the polar plots, head direction was collected into bins of 6 degrees and the number of spikes in each bin was divided by the time spent facing that direction. The mean resultant length (MRL) of the polar plot was taken as a metric of head direction selectivity.

### **Cell selection**

We categorized each entorhinal neuron as a grid cell, head direction cell, or non-grid spatially-tuned cell. We performed a shuffling procedure to set significance criteria to determine grid cells and head direction cells. Spike trains from each neuron recorded were randomly shifted in time by at least 30 seconds. We then calculated gridness and directionality measures. This process was repeated 50 times for each neuron, and the 99<sup>th</sup> percentile of the resulting distribution of scores was determined as the significance criteria for both measures. This results in a gridness threshold of 0.54 and directionality threshold of 0.21 which we used to define grid cells and head direction cells in our full dataset. Any cell recorded in the MEC which did not qualify as a grid cell but had a split-half correlation  $\geq 0.6$  was categorized as a non-grid spatially-tuned cell. Putative interneurons in the MEC were selected by having a narrow wave form ( $<0.3$ ms) and a mean firing rate of at least 0.5 Hz. Hippocampal neurons were classified as putative place cells if they had 1) a minimum mean firing rate of 0.1 Hz, 2) a maximum mean firing rate of 5.0 Hz, and 3) a spatial peak rate of greater than 5.0 Hz. Duplicate place cells sampled across recording sessions were removed for Fig. 2d and Fig. 3d.

### **Spatial 2D displacement analysis**

To quantify noise in the two-dimensional (2D) phase of grid cells (and other cell types) on short timescales, we began by dividing the first 30 minutes of each recording into 10 epochs of three

minutes each. For each epoch, we computed the resulting rate map. Next, for all pairwise comparisons of epoch rate maps, we computed the spatial cross-correlation between rate maps over a window of  $\pm 5$  pixel ( $\pm 15$  cm) lags in both dimensions. The peak of this cross-correlogram captures the 2D translation necessary to best align the current pair of rate maps. Because the periodic nature of the grid pattern might lead to multiple local maxima in the cross-correlogram, we first computed the patch of correlation values nearest the center for which all contiguous correlation values were at least 50% of the maximum correlation value. We then chose the maximum correlation in this patch as our peak. The distance from the center (no difference in alignment) to this peak was computed as our measure of 2D phase-shift between these epochs. The average across all pairwise comparisons of epochs was then the final measure of 2D phase noise for that cell.

### **Speed modulation of theta power and frequency**

Local field potential traces obtained from the MEC were referenced to a cortical reference electrode and downsampled to 500 Hz. Power between 1-15Hz was calculated using a Morlett Wavelet with a 0.25 Hz bandwidth to obtain a power spectrum for each sample. Theta-by-Speed spectrograms were calculated as the power between 5-15 Hz divided by power in the delta band (2-4 Hz) across running speeds. The average Theta-by-Speed spectrogram is show in Fig. 2e. To quantify speed modulation of theta power, the mean power between 7-12 Hz across speeds was extracted from each Theta-by-Speed spectrogram across speeds (Fig. 2e). To quantify speed modulation of theta frequency, the frequency of the peak power for each running speed was extracted from the Theta-by-Speed spectrogram (Fig. 2e). Analysis of co-variance (ANCOVA) was performed on these extracted data.

### **Single-cell temporal autocorrelations and intrinsic frequency**

The spike times of each cell were binned at 5ms intervals and the temporal autocorrelation for the given spike train was computed. The obtained signal was smoothed by a Gaussian kernel with 2 bin standard deviation, zero padded to  $2^{13}$  samples and the power spectrum was calculated using the Chronux toolbox function MTSPECTRUMC from Matlab. The intrinsic frequency of a given cell was then taken as the frequency with the max power in the 6-12 Hz range.

### **Cross-correlations and synchrony analysis**

To examine spiking synchrony unbiased cross-correlations were computed between simultaneously recorded grid cells, head direction cells, and putative interneurons with 5ms temporal bins from a lag of -400 to 400ms. The resulting cross-correlations were convolved with a 25ms gaussian and normalized to their median absolute deviation for comparison.

### **Path integration task**

Data were collected in a ten-sided maze (diameter = 63.8 cm) surrounded by black curtains. Steel bars were screwed into the walls of the testing room and hovered over the maze. A plastic base was positioned on these bars and acting as the ceiling for the maze. On this ceiling, an infrared camera purchased from Neuralynx was positioned and acquired positional data at 30 frames per second at 720 x 480 pixel resolution (6.13 pixels per cm). Black curtains were positioned on top and around this plastic base which draped over the maze and ensured a complete darkness environment. Within the maze, 10 refuge enclosures connected to the open environment were closed off by top-down sliding doors that acted as walls. For all trials, the same refuge was used for each subject. When the door was slid open, the mouse could voluntarily enter or exit the refuge by their own volition. The height of these walls (and the entire maze throughout) was 27.6 cm.

Mice were placed on food restriction and maintained at 85% of their *ad libidum* weight throughout training and testing phases. In each trial, the mouse was kept in the same refuge enclosure separated

from the open environment by the sliding door. The maze was operated in darkness via a pulley system which consisted of a rope fastened to the top of the sliding door. This rope extended outside of the curtains by passing through 2 clamps that were installed along the steel bars above the maze. This setup mimicked a pulley system where the experimenter could pull on the rope and open the sliding door while the curtains were draped over the maze. The handle of the rope end was twisted into a knot; at the start of each trial, the rope was pulled, and the knot was looped onto a third clamp fastened to a table post. Doing so kept the sliding door held up throughout the duration of each trial. At the end of a trial, the knot was lifted from the clamp which closed the door. This setup allowed the experimenter to quickly operate the door without needing to physically interact with the maze.

Once the mouse was let into the open environment, it had to forage for a randomly placed small food pellet and return to the refuge prior to consumption. These food pellets were the same kind as administered in the subjects' cages, but smaller in size weighing less than 0.2 g. Successful trials were defined as events where the mouse picked up the food pellet and navigated to the refuge before consumption. Failed trials were defined as events where the mouse failed to return to its refuge before consuming the pellet. Incomplete trials were defined as events where the mouse failed to retrieve the pellet before returning to its refuge.

Visual cues were set up along the walls of the environment to allow for increased allocentric-guided behavior in the light trials. The three visual cues used consisted of a triangle, square, and three stripes constructed using tape and were positioned on three almost-equally spaced walls (given that the environment is ten-sided, a cue couldn't be completely equally-spaced from the other two). White noise played throughout all trials to account for potential auditory cues that may affect the mouse's return trajectory. Furthermore, the maze environment was wiped using

Peroxyguard following every five consecutive trials to reduce the extent to which olfactory cues influenced behavior. In light trials, room lighting was turned on and the curtains were pushed to the side. In dark trials, room lighting was turned off and the curtains completely covered the arena. The mouse's movements were tracked using an overhead infrared camera, and the maze was lit using an infrared light.

*Path Integration Behaviour Timecourse.* Mice reached 85% of their *ad libidum* weight before experiments commenced. Mice first underwent a training phase where they achieved a minimum of eight successful trials out of ten total complete trials within a session in light conditions. Incomplete trials did not count as a completed trial. Mice went through consecutive light training days until they reached the success criteria. During failed trials, the experimenter punished the mouse by holding it by the tail suspended in air for ten seconds before placing it back into the refuge.

Following light training, mice then underwent five consecutive days of dark training. The same protocol as the light training applied to dark training. Mice were required to achieve a minimum of eight successful trials out of ten total complete trials within a session in any of the five days. All mice reported in the dataset achieved success criteria. Four mice that did not pass the training criteria were excluded from analysis. These mice included two young nTG mice, one young APP mouse, and one aged APP mouse.

Following dark training, mice then underwent five consecutive days of light and dark testing. In days 1, 3 and 5, five light trials were conducted, followed by five dark trials. Incomplete trials counted as trials. This was repeated until the mouse achieved ten complete trials in each of the light and dark conditions. On days 2 and 4, the same protocol applied, but the mouse started with five dark trials, followed by five light trials.

### **Analysis of path integration behavior**

All path integration behavioral data were recorded at 30 frames per second. The positional coordinates of the mice for each trial were obtained using an open-source deep learning tracker algorithm called DeepLabCut<sup>57</sup>. DeepLabCut was only used to quantify positional data in the path integration task and not for electrophysiological recordings. Custom Matlab scripts were used to analyze various behavioral parameters from the mice's positional data.

### **Genotyping**

Tail samples were collected at weaning for genotyping, and just prior to brain perfusion for additional confirmation. DNA samples were extracted and amplified using the REDExtract-N-Amp™ Tissue PCR Kit (MilliporeSigma, XNAT-100RXN) and the primer sequence and PCR protocol provided by The Jackson Laboratory (MMRRC, 34836-JAX). Genotyping results were visualized using a QIAxcel instrument (Qiagen).

### **Immunofluorescence**

Mice were anesthetized with Isoflurane (Baxter, FDG9623) and intracardially perfused with 0.05% heparin (Sandoz, 10750) in ice-cold saline followed up cold and filtered 4% paraformaldehyde that was freshly made from powder (MilliporeSigma, 158127-500g). Extracted brains were cryopreserved in 30% sucrose (MilliporeSigma, S0389-1Kg), flash frozen in 2-methylbutane (Fisher Scientific, 03551-4), and kept at -80°C until sliced on a cryostat (Leica, CM3050-S). Sagittal sections (40µm) were collected on microscope slides for on-slide staining. Each slide had two positive controls (APP animals 18 months old) and at least one brain section from the remaining experimental groups (young APP, adult APP, young nTG, adult nTG). The same combinations of brain sections were used for both MEC and hippocampal staining. Sections that were too damaged were discarded. All slides were processed at the same time using the purified

mouse monoclonal anti-beta-amyloid 1-16 antibody (6E10) (Biolegend, catalog number 803001) at a dilution of 1:500 for 30 minutes, along with the M.O.M.<sup>®</sup> Fluorescein Kit (Vector Laboratories, catalog number FMK-2201). Slides were mounted with DAPI containing Fluoromount-G (SouthernBiotech, catalog number 0100-20).

### **Analysis of Immunofluorescence**

Images for each section were acquired within the same session at 10x magnification with the same exposure settings (FITC: 250 ms, DAPI: 50 ms) on a slide scanner (Olympus, VS120) within one week of the immunofluorescence assay. The images were digitally processed using ImageJ<sup>47</sup>. ROIs were manually drawn for both MEC and the hippocampus and clear visually identifiable artifacts were removed from ROIs. Rolling ball background subtraction (70 $\mu$ m radius) was applied to every image. ROI areas were measured, and fluorescence intensity was extracted. A threshold was set for analysis to capture the plaque fluorescence signal (6000 a.u.), based on beta amyloid plaques observed in positive control animals. Using RStudio (RStudio Team 2016), the sections were grouped by structure: MEC or hippocampus. For each animal, the normalized fluorescence was calculated as the total fluorescence divided by the total area.

### **Immunoautoradiographic labelling of synaptic markers**

Immunoautoradiography experiments were performed on fresh frozen mouse brain sections (10 $\mu$ m) as described previously<sup>58,59</sup>. Brain slices were taken at the level of the MEC (bregma 2.76 to 3.90) and the hippocampus (bregma -1.0 to -2.0). Slices were incubated overnight at 4° with rabbit polyclonal antiserum specific of VGLUT1 (dilution 1:10,000), VGLUT3 (dilution 1:20,000, Synaptic Systems, catalog number 135203, Göttingen Germany), VGAT (dilution 1:10,000, Synaptic Systems, catalog number 131002, Göttingen Germany), VACHT (dilution 1:10,000, Synaptic Systems, catalog number 139103, Göttingen Germany), NR1 (dilution 1:10,000,

Synaptic Systems, catalog number 114103, Göttingen Germany) and then with anti-rabbit [125I]-IgG (PerkinElmer, 0.25  $\mu$ Ci/ml final dilution) for 2hr at 4°. Sections were then washed in PBS, rapidly rinsed in water, dried, and exposed to x-ray films (Biomax MR, Kodak) for 5 days. Standard radioactive microscales were exposed to each film to ensure that labeling densities were in the linear range. Densitometry measurements were performed with MCID analysis software 7.1 (InterFocus, Ltd) on sections for each region per mouse (4 mice per experimental group for a total of 16 mice).

VGLUT1, VGLUT3, VACH and VGAT are vesicular transporters that mediate neurotransmission from the presynaptic side. VGLUT1 is necessary for the vesicular accumulation of glutamate and is a general marker for glutamatergic drive in synapses. In the context of grid cells, excitatory drive is a prerequisite for grid cell generation<sup>28</sup>. VGLUT3 is a specific marker for synapses made by CCK-positive basket cells in the MEC. VACHT expression in the MEC marks presynaptic cholinergic terminals from the medial septum. The severe loss of cholinergic neurons is a hallmark of Alzheimer's disease and a possible role of acetylcholine for grid cell activity has previously been reported. VGAT mediates vesicular accumulation of GABA and is a general marker for inhibitory drive which is important for grid cell generation<sup>32,33</sup>. In the case of NR1, it is a subunit of NMDA receptors that has previously been shown to be necessary for both the generation of grid cells and path integration ability<sup>35</sup>.

### **Data availability**

All data supporting the key findings of this study are available within the article, Supplementary Information and Source Data, or via request to the corresponding author. Source data are provided with this paper.

## Code availability

All custom codes supporting the key findings of this study are available at the following GitHub page: <https://github.com/johnson-ying/ying-et-al-2021>, or via request to the corresponding author.

## References

1. Ferreira, S. T., Lourenco, M. V., Oliveira, M. M. & De Felice, F. G. Soluble amyloid-beta oligomers as synaptotoxins leading to cognitive impairment in Alzheimer's disease. *Front. Cell. Neurosci.* **9**, 191 (2015).
2. Alifragis, P. & Marsh, J. Synaptic dysfunction in Alzheimer's disease: the effects of amyloid beta on synaptic vesicle dynamics as a novel target for therapeutic intervention. *Neural Regen. Res.* **13**, 616 (2018).
3. Howett, D. *et al.* Differentiation of mild cognitive impairment using an entorhinal cortex-based test of virtual reality navigation. *Brain* **142**, 1751–1766 (2019).
4. Coughlan, G., Laczó, J., Hort, J., Minihane, A.-M. & Hornberger, M. Spatial navigation deficits - overlooked cognitive marker for preclinical Alzheimer disease? *Nat. Rev. Neurol.* **14**, 496–506 (2018).
5. Morris, R. G., Garrud, P., Rawlins, J. N. & O'Keefe, J. Place navigation impaired in rats with hippocampal lesions. *Nature* **297**, 681–683 (1982).
6. Smith, M. L. & Milner, B. The role of the right hippocampus in the recall of spatial location. *Neuropsychologia* **19**, 781–793 (1981).
7. Steffenach, H.-A., Witter, M., Moser, M.-B. & Moser, E. I. Spatial memory in the rat requires the dorsolateral band of the entorhinal cortex. *Neuron* **45**, 301–313 (2005).
8. O'Keefe, J. & Dostrovsky, J. The hippocampus as a spatial map. Preliminary evidence from unit activity in the freely-moving rat. *Brain Res.* **34**, 171–175 (1971).
9. Hafting, T., Fyhn, M., Molden, S., Moser, M.-B. & Moser, E. I. Microstructure of a spatial map in the entorhinal cortex. *Nature* **436**, 801–806 (2005).
10. Sargolini, F. *et al.* Conjunctive representation of position, direction, and velocity in entorhinal cortex. *Science* **312**, 758–762 (2006).
11. Ekstrom, A. D. *et al.* Cellular networks underlying human spatial navigation. *Nature* **425**, 184–188 (2003).
12. Jacobs, J. *et al.* Direct recordings of grid-like neuronal activity in human spatial navigation. *Nat. Neurosci.* **16**, 1188–1190 (2013).
13. Hasselmo, M. E., Hinman, J. R., Dannenberg, H. & Stern, C. E. Models of spatial and temporal dimensions of memory. *Curr. Opin. Behav. Sci.* **17**, 27–33 (2017).
14. O'Keefe, J. & Nadel, L. *The Hippocampus as a Cognitive Map*. (Oxford University Press, 1978).

15. Samsonovich, A. & McNaughton, B. L. Path integration and cognitive mapping in a continuous attractor neural network model. *J. Neurosci.* **17**, 5900–5920 (1997).
16. Burgess, N. & O’Keefe, J. Neuronal computations underlying the firing of place cells and their role in navigation. *Hippocampus* **6**, 749–762 (1996).
17. McNaughton, B. L., Battaglia, F. P., Jensen, O., Moser, E. I. & Moser, M.-B. Path integration and the neural basis of the “cognitive map.” *Nat. Rev. Neurosci.* **7**, 663–678 (2006).
18. Mucke, L. *et al.* High-level neuronal expression of abeta 1-42 in wild-type human amyloid protein precursor transgenic mice: synaptotoxicity without plaque formation. *J. Neurosci.* **20**, 4050–4058 (2000).
19. Harris, J. A. *et al.* Transsynaptic progression of amyloid- $\beta$ -induced neuronal dysfunction within the entorhinal-hippocampal network. *Neuron* **68**, 428–441 (2010).
20. Nagahara, A. H. *et al.* Early BDNF treatment ameliorates cell loss in the entorhinal cortex of APP transgenic mice. *J. Neurosci.* **33**, 15596–15602 (2013).
21. Wright, A. L. *et al.* Neuroinflammation and neuronal loss precede A $\beta$  plaque deposition in the hAPP-J20 mouse model of Alzheimer’s disease. *PLoS One* **8**, e59586 (2013).
22. Hong, S. *et al.* Complement and microglia mediate early synapse loss in Alzheimer mouse models. *Science* **352**, 712–716 (2016).
23. Saganich, M. J. *et al.* Deficits in synaptic transmission and learning in amyloid precursor protein (APP) transgenic mice require C-terminal cleavage of APP. *J. Neurosci.* **26**, 13428–13436 (2006).
24. Bjerknes, T. L., Dagslott, N. C., Moser, E. I. & Moser, M.-B. Path integration in place cells of developing rats. *Proc. Natl. Acad. Sci. U. S. A.* **115**, E1637–E1646 (2018).
25. Brandon, M. P. *et al.* Reduction of theta rhythm dissociates grid cell spatial periodicity from directional tuning. *Science* **332**, 595–599 (2011).
26. Koenig, J., Linder, A. N., Leutgeb, J. K. & Leutgeb, S. The spatial periodicity of grid cells is not sustained during reduced theta oscillations. *Science* **332**, 592–595 (2011).
27. Cacucci, F., Yi, M., Wills, T. J., Chapman, P. & O’Keefe, J. Place cell firing correlates with memory deficits and amyloid plaque burden in Tg2576 Alzheimer mouse model. *Proc. Natl. Acad. Sci. U. S. A.* **105**, 7863–7868 (2008).
28. Bonnevie, T. *et al.* Grid cells require excitatory drive from the hippocampus. *Nat. Neurosci.* **16**, 309–317 (2013).
29. Kropff, E., Carmichael, J. E., Moser, M.-B. & Moser, E. I. Speed cells in the medial entorhinal cortex. *Nature* **523**, 419–424 (2015).
30. Cheng, I. H. *et al.* Accelerating amyloid-beta fibrillization reduces oligomer levels and functional deficits in Alzheimer disease mouse models. *J. Biol. Chem.* **282**, 23818–23828 (2007).

31. Meilandt, W. J. *et al.* Neprilysin overexpression inhibits plaque formation but fails to reduce pathogenic Aβ oligomers and associated cognitive deficits in human amyloid precursor protein transgenic mice. *J. Neurosci.* **29**, 1977–1986 (2009).
32. Buetfering, C., Allen, K. & Monyer, H. Parvalbumin interneurons provide grid cell-driven recurrent inhibition in the medial entorhinal cortex. *Nat. Neurosci.* **17**, 710–718 (2014).
33. Miao, C., Cao, Q., Moser, M.-B. & Moser, E. I. Parvalbumin and somatostatin interneurons control different space-coding networks in the medial entorhinal cortex. *Cell* **171**, 507–521.e17 (2017).
34. Winter, S. S., Clark, B. J. & Taube, J. S. Spatial navigation. Disruption of the head direction cell network impairs the parahippocampal grid cell signal. *Science* **347**, 870–874 (2015).
35. Gil, M. *et al.* Impaired path integration in mice with disrupted grid cell firing. *Nat. Neurosci.* **21**, 81–91 (2018).
36. de Wilde, M. C., Overk, C. R., Sijben, J. W. & Masliah, E. Meta-analysis of synaptic pathology in Alzheimer’s disease reveals selective molecular vesicular machinery vulnerability. *Alzheimers. Dement.* **12**, 633–644 (2016).
37. Palop, J. J. *et al.* Aberrant excitatory neuronal activity and compensatory remodeling of inhibitory hippocampal circuits in mouse models of Alzheimer’s disease. *Neuron* **55**, 697–711 (2007).
38. Coyle, J. T., Price, D. L. & DeLong, M. R. Alzheimer’s disease: a disorder of cortical cholinergic innervation. *Science* **219**, 1184–1190 (1983).
39. Whitehouse, P. J., Price, D. L., Clark, A. W., Coyle, J. T. & DeLong, M. R. Alzheimer disease: evidence for selective loss of cholinergic neurons in the nucleus basalis. *Ann. Neurol.* **10**, 122–126 (1981).
40. Liu, A. K. L., Chang, R. C.-C., Pearce, R. K. B. & Gentleman, S. M. Nucleus basalis of Meynert revisited: anatomy, history and differential involvement in Alzheimer’s and Parkinson’s disease. *Acta Neuropathol.* **129**, 527–540 (2015).
41. Mably, A. J., Gereke, B. J., Jones, D. T. & Colgin, L. L. Impairments in spatial representations and rhythmic coordination of place cells in the 3xTg mouse model of Alzheimer’s disease. *Hippocampus* **27**, 378–392 (2017).
42. Zhao, R., Fowler, S. W., Chiang, A. C. A., Ji, D. & Jankowsky, J. L. Impairments in experience-dependent scaling and stability of hippocampal place fields limit spatial learning in a mouse model of Alzheimer’s disease. *Hippocampus* **24**, 963–978 (2014).
43. Jun, H. *et al.* Disrupted place cell remapping and impaired grid cells in a knockin model of Alzheimer’s disease. *Neuron* **107**, 1095–1112.e6 (2020).
44. LaFerla, F. M., Green, K. N. & Oddo, S. Intracellular amyloid-β in Alzheimer’s disease. *Nat. Rev. Neurosci.* **8**, 499–509 (2007).

45. Bayer, T. A. & Wirths, O. Intracellular accumulation of amyloid-Beta - a predictor for synaptic dysfunction and neuron loss in Alzheimer's disease. *Front. Aging Neurosci.* **2**, 8 (2010).
46. Saido, T. & Leissring, M. A. Proteolytic degradation of amyloid  $\beta$ -protein. *Cold Spring Harb. Perspect. Med.* **2**, a006379 (2012).
47. Leissring, M. A. & Turner, A. J. Regulation of distinct pools of amyloid  $\beta$ -protein by multiple cellular proteases. *Alzheimers. Res. Ther.* **5**, 37 (2013).
48. Khan, U. A. *et al.* Molecular drivers and cortical spread of lateral entorhinal cortex dysfunction in preclinical Alzheimer's disease. *Nat. Neurosci.* **17**, 304–311 (2014).
49. Reilly, J. F. *et al.* Amyloid deposition in the hippocampus and entorhinal cortex: quantitative analysis of a transgenic mouse model. *Proc. Natl. Acad. Sci. U. S. A.* **100**, 4837–4842 (2003).
50. Xu, W., Fitzgerald, S., Nixon, R. A., Levy, E. & Wilson, D. A. Early hyperactivity in lateral entorhinal cortex is associated with elevated levels of A $\beta$ PP metabolites in the Tg2576 mouse model of Alzheimer's disease. *Exp. Neurol.* **264**, 82–91 (2015).
51. Fu, H. *et al.* Tau pathology induces excitatory neuron loss, grid cell dysfunction, and spatial memory deficits reminiscent of early Alzheimer's disease. *Neuron* **93**, 533-541.e5 (2017).
52. Archetti, D. *et al.* Multi-study validation of data-driven disease progression models to characterize evolution of biomarkers in Alzheimer's disease. *NeuroImage Clin.* **24**, 101954 (2019).
53. Young, A. L. *et al.* A data-driven model of biomarker changes in sporadic Alzheimer's disease. *Brain* **137**, 2564–2577 (2014).
54. Doeller, C. F., Barry, C. & Burgess, N. Evidence for grid cells in a human memory network. *Nature* **463**, 657–661 (2010).
55. Kunz, L. *et al.* Reduced grid-cell-like representations in adults at genetic risk for Alzheimer's disease. *Science* **350**, 430–433 (2015).
56. Bierbrauer, A. *et al.* Unmasking selective path integration deficits in Alzheimer's disease risk carriers. *Sci. Adv.* **6**, eaba1394 (2020).
57. Mathis, A. *et al.* DeepLabCut: markerless pose estimation of user-defined body parts with deep learning. *Nat. Neurosci.* **21**, 1281–1289 (2018).
58. Amilhon, B. *et al.* VGLUT3 (vesicular glutamate transporter type 3) contribution to the regulation of serotonergic transmission and anxiety. *J. Neurosci.* **30**, 2198–2210 (2010).
59. Vigneault, É. *et al.* Distribution of vesicular glutamate transporters in the human brain. *Front. Neuroanat.* **9**, 23 (2015).

## **Acknowledgements**

We graciously thank S. Kim, Z. Ante, K. Harandian, Q. He, A. Ismailova, D. Patel, A. Zhen, and A. Milette-Gagnon for their assistance in experiments. We also thank J. Poirer, M. Hasselmo, J. Hinman, S. Villeneuve, S. Williams, R. Rozeske, J. Lee, J. Robinson and E. Vachon-Pressseau for comments on earlier versions of this manuscript and to all members of the Brandon laboratory for helpful discussions.

This work was funded by CIHR Project Grants #367017 and #377074, an NSERC Discovery Grant #74105, a Scottish Rite Charitable Foundation Grant, a Canada Fund for Innovation Grant, and a Canada Research Chairs award to M.P.B. J.Y is supported by a Doctoral Training Grant from the Fonds de recherche du Québec, and previously by a Master's Training Grant from the Fonds de recherche du Québec and a CIHR Master's Training Fellowship.

## **Author Contributions**

J.Y. contributed to experimental design, recordings, analysis of data, and wrote the manuscript. R.L. contributed to immunohistochemistry quantifications. A.T.K contributed to analysis of data. E.V. and S.E.M contributed to immunoautoradiographic quantifications. M.P.B contributed to experimental design, analysis of data, and wrote the manuscript.

## **Competing Interests**

Authors declare no competing interests.

## Figure Legends

**Fig. 1: Reduction of grid cell spatial periodicity in adult APP transgenic mice.** **a** Firing rate maps for grid cells from each experimental group. Each row includes 15 grid cells with the highest grid scores sorted in descending order. The spatial peak firing rate and grid score are indicated in the rate map's top-left and top-right, respectively. **b** Grid scores (nTG-y vs. nTG-a:  $P = 0.12$ ; nTG-y vs. APP-y:  $P = 0.73$ ; APP-y vs. APP-a:  $P = 1 \times 10^{-7}$ ; nTG-a vs. APP-a:  $P = 2.5 \times 10^{-6}$ ) between groups (cells,  $n = 64$  for nTG-y;  $n = 99$  for nTG-a;  $n = 74$  for APP-y;  $n = 50$  for APP-a). **c** Scatter plot displays grid score by age recorded (in days). A two-way ANOVA was conducted to examine the effects of age and genotype on grid score. There was a significant interaction between the effects of age and genotype:  $F(1, 280) = 11.99$ ,  $P = 6.2 \times 10^{-4}$ . **d** Color-coded rotational correlations are shown, sorted in descending order of the grid score value. All neurons within the top 20% of grid scores are shown. The max grid score in each experimental group is displayed at the top of the respective plot. **e** Spatial information (nTG-y vs. nTG-a:  $P = 0.77$ ; nTG-y vs. APP-y:  $P = 0.34$ ; APP-y vs. APP-a:  $P = 6.5 \times 10^{-6}$ ; nTG-a vs. APP-a:  $P = 1.2 \times 10^{-3}$ ), spatial peak firing rate (nTG-y vs. nTG-a:  $P = 0.59$ ; nTG-y vs. APP-y:  $P = 0.79$ ; APP-y vs. APP-a:  $P = 0.77$ ; nTG-a vs. APP-a:  $P = 0.27$ ), and mean firing rate (nTG-y vs. nTG-a:  $P = 0.99$ ; nTG-y vs. APP-y:  $P = 0.086$ ; APP-y vs. APP-a:  $P = 0.13$ ; nTG-a vs. APP-a:  $P = 0.79$ ) between groups (cells,  $n = 64$  for nTG-y;  $n = 99$  for nTG-a;  $n = 74$  for APP-y;  $n = 50$  for APP-a). nTG-y, non-transgenic young; nTG-a, non-transgenic adult; APP-y, APP young; APP-a, APP adult. Wilcoxon rank sum tests (two-sided) corrected for multiple comparisons using a Bonferroni-Holm correction were applied to analyze the data in Fig. 1 **b** and **e**. Data in bar graphs are presented as median values  $\pm 25^{\text{th}}$  and  $75^{\text{th}}$  percentiles;  $**P < 0.01$ ,  $***P < 0.001$ ; n.s., not significant. Source data are provided as a Source Data file.

**Fig. 2: Medial entorhinal head direction cells, non-grid spatially-tuned cells, CA1 place cells, and medial entorhinal theta oscillations in adult APP mice.** **a** (Top) Polar plots of eight head-direction cells for each group. Directional peak firing rate and mean resultant length (MRL) are indicated in the top-left and top-right, respectively. (Bottom) MRL (nTG-y vs. nTG-a:  $P = 0.051$ ; nTG-y vs. APP-y:  $P = 0.45$ ; APP-y vs. APP-a:  $P = 0.41$ ; nTG-a vs. APP-a:  $P = 0.11$ ), spatial peak firing rate (nTG-y vs. nTG-a:  $P = 0.44$ ; nTG-y vs. APP-y:  $P = 0.21$ ; APP-y vs. APP-a:  $P = 0.96$ ; nTG-a vs. APP-a:  $P = 0.073$ ), and mean firing rate (nTG-y vs. nTG-a:  $P = 0.18$ ; nTG-y vs. APP-y:  $P = 0.28$ ; APP-y vs. APP-a:  $P = 0.87$ ; nTG-a vs. APP-a:  $P = 0.08$ ) between groups (cells,  $n = 295$  for nTG-y;  $n = 244$  for nTG-a;  $n = 305$  for APP-y;  $n = 471$  for APP-a). **b** (Top) Rate maps of eight non-grid spatially-tuned cells for each group. Spatial peak firing rate and split-half reliability scores are indicated in the top-left and top-right, respectively. (Bottom) Average firing field size (nTG-y vs. nTG-a:  $P = 0.40$ ; nTG-y vs. APP-y:  $P = 0.66$ ; APP-y vs. APP-a:  $P = 0.64$ ; nTG-a vs. APP-a:  $P = 0.37$ ), spatial peak firing rate (nTG-y vs. nTG-a:  $P = 0.028$ ; nTG-y vs. APP-y:  $P = 0.49$ ; APP-y vs. APP-a:  $P = 0.73$ ; nTG-a vs. APP-a:  $P = 0.032$ ), and mean firing rate (nTG-y vs. nTG-a:  $P = 0.76$ ; nTG-y vs. APP-y:  $P = 0.37$ ; APP-y vs. APP-a:  $P = 0.50$ ; nTG-a vs. APP-a:  $P = 0.93$ ) between groups (cells,  $n = 82$  for nTG-y;  $n = 83$  for nTG-a;  $n = 106$  for APP-y;  $n = 119$  for APP-a). **c** (Top) Rate maps of eight CA1 place cells in nTG and APP adult mice. (Bottom) Same as **(a)**, but panels compare spatial information (nTG-a vs. APP-a:  $P = 0.08$ ), spatial peak firing rate (nTG-a vs. APP-a:  $P = 0.32$ ), and mean firing rate (nTG-a vs. APP-a:  $P = 0.31$ ) between groups (cells,  $n = 118$  for nTG-a;  $n = 109$  for APP-a). **d** Comparison of spatial information (0 Hz:  $P = 0.03$ ; 0.5 Hz:  $P = 0.03$ ; 1.0 Hz:  $P = 0.028$ ; 1.5 Hz:  $P = 0.057$ ; 2.0 Hz:  $P = 0.10$ ; 2.5 Hz:  $P = 0.15$ ; 3.0 Hz:  $P = 0.16$ ; 3.5 Hz:  $P = 0.28$ ; 4.0 Hz:  $P = 0.18$ ; 4.5 Hz:  $P = 0.12$ ; 5.0 Hz:  $P = 0.08$ ; 5.5 Hz:  $P = 0.16$ ; 6.0 Hz:  $P = 0.11$ ; 6.5 Hz:  $P = 0.12$ ; 7.0 Hz:  $P = 0.30$ ; 7.5 Hz:  $P = 0.31$ ; 8.0 Hz:  $P = 0.41$ ) and mean firing rates (0 Hz:  $P = 0.64$ ; 0.5 Hz:  $P = 0.64$ ; 1.0 Hz:  $P = 0.70$ ; 1.5 Hz:  $P = 0.81$ ; 2.0 Hz:  $P = 0.95$ ; 2.5 Hz:  $P = 0.99$ ; 3.0 Hz:  $P = 0.90$ ; 3.5 Hz:  $P = 0.82$ ; 4.0 Hz:  $P = 0.85$ ; 4.5 Hz:  $P = 0.73$ ; 5.0 Hz:  $P = 0.31$ ; 5.5 Hz:  $P = 0.24$ ; 6.0 Hz:  $P = 0.048$ ; 6.5 Hz:  $P = 0.016$ ; 7.0 Hz:  $P = 0.025$ ; 7.5 Hz:  $P = 0.027$ ; 8.0 Hz:  $P = 0.039$ ) of CA1 place cells in adult nTG and APP mice when varying the cell selection criteria of peak spatial firing rate. The colored dots indicate the number of place cells (cells, 0 Hz:  $n = 210$  for nTG-a;  $n = 233$  for APP-a; 0.5 Hz:  $n = 210$  for nTG-a;  $n = 233$  for APP-a; 1.0 Hz:  $n = 209$  for nTG-a;  $n = 231$  for APP-a; 1.5 Hz:  $n = 205$  for nTG-a;  $n = 224$  for APP-a; 2.0 Hz:  $n = 197$  for nTG-a;  $n = 212$  for APP-a; 2.5 Hz:  $n = 187$  for nTG-a;  $n = 202$  for APP-a;

3.0 Hz:  $n = 172$  for nTG-a;  $n = 185$  for APP-a; 3.5 Hz:  $n = 159$  for nTG-a;  $n = 166$  for APP-a; 4.0 Hz:  $n = 147$  for nTG-a;  $n = 148$  for APP-a; 4.5 Hz:  $n = 136$  for nTG-a;  $n = 127$  for APP-a; 5.0 Hz:  $n = 118$  for nTG-a;  $n = 109$  for APP-a; 5.5 Hz:  $n = 103$  for nTG-a;  $n = 94$  for APP-a; 6.0 Hz:  $n = 91$  for nTG-a;  $n = 77$  for APP-a; 6.5 Hz:  $n = 83$  for nTG-a;  $n = 62$  for APP-a; 7.0 Hz:  $n = 75$  for nTG-a;  $n = 54$  for APP-a; 7.5 Hz:  $n = 61$  for nTG-a;  $n = 49$  for APP-a; 8.0 Hz:  $n = 56$  for nTG-a;  $n = 45$  for APP-a) that passed the selection threshold. **e** (Left) Spectrograms compare the MEC theta frequency and power as a function of the animal's running speed. (Right) MEC theta power and frequency are independently displayed as a function of the animal's running speed. Data are presented as mean values  $\pm$  99% confidence intervals. nTG-y, non-transgenic young; nTG-a, non-transgenic adult; APP-y, APP young; APP-a, APP adult. Wilcoxon rank sum tests (two-sided) corrected for multiple comparisons (where applicable) using a Bonferroni-Holm correction were applied to analyze the data in Fig. 2 **a-d**. Data in bar graphs are presented as median values  $\pm$  25<sup>th</sup> and 75<sup>th</sup> percentiles; Boxplot elements present data as a median dot, interquartile range boxes extend from 25<sup>th</sup> to 75<sup>th</sup> percentile, whiskers extend from smallest values to the largest values; \* $P < 0.05$ ; n.s, not significant. Source data are provided as a Source Data file.

**Fig. 3: Grid cells in adult APP mice are spatially unstable.** **a** Normalized firing field size of grid cells (nTG-y vs. nTG-a:  $P = 0.076$ ; nTG-y vs. APP-y:  $P = 0.76$ ; APP-y vs. APP-a:  $P = 0.52$ ; nTG-a vs. APP-a:  $P = 0.0025$ ) between groups (cells,  $n = 64$  for nTG-y;  $n = 99$  for nTG-a;  $n = 74$  for APP-y;  $n = 50$  for APP-a). **b** Each grid cell recording was split into 10 three-minute partitions. Two-dimensional spatial cross-correlations were computed across all partition pairs. Example cross-correlations of the first partition to subsequent partitions in two grid cells recorded from a nTG and an APP mouse are shown to the right. **c** (Left) Schematic shows that two-dimensional spatial displacement was calculated as the distance between the peak correlation pixel and the center pixel of the cross-correlation. Note that this analysis makes no conclusions about the magnitude of the peak correlation pixel, and strictly assesses the shift of said peak value. (Right) Two-dimensional displacement of grid cells, non-grid spatially-tuned cells and place cells as a function of lags between partitions. Dots indicate mean values and error bars indicate SEM. **d** Two-dimensional displacement of grid cells (nTG-y vs. nTG-a:  $P = 0.76$ ; nTG-y vs. APP-y:  $P = 0.76$ ; APP-y vs. APP-a:  $P = 9.1 \times 10^{-4}$ ; nTG-a vs. APP-a:  $P = 3.4 \times 10^{-4}$ ), non-grid spatially-tuned cells (nTG-y vs. nTG-a:  $P = 0.74$ ; nTG-y vs. APP-y:  $P = 0.24$ ; APP-y vs. APP-a:  $P = 0.19$ ; nTG-a vs. APP-a:  $P = 0.87$ ), and place cells (nTG-a vs. APP-a:  $P = 0.37$ ) between groups (grid cells,  $n = 61$  for nTG-y;  $n = 95$  for nTG-a;  $n = 73$  for APP-y;  $n = 49$  for APP-a; non-grid spatially-tuned cells,  $n = 77$  for nTG-y;  $n = 80$  for nTG-a;  $n = 98$  for APP-y;  $n = 115$  for APP-a; place cells,  $n = 114$  for nTG-a;  $n = 96$  for APP-a). **e** Two-dimensional rotational displacement of one grid cell partition relative to another in the cross-correlation (nTG-y vs. nTG-a:  $P = 0.15$ ; nTG-y vs. APP-y:  $P = 0.87$ ; APP-y vs. APP-a:  $P = 0.73$ ; nTG-a vs. APP-a:  $P = 0.15$ ) between groups (grid cells,  $n = 61$  for nTG-y;  $n = 95$  for nTG-a;  $n = 73$  for APP-y;  $n = 49$  for APP-a). nTG-y, non-transgenic young; nTG-a, non-transgenic adult; APP-y, APP young; APP-a, APP adult. Wilcoxon rank sum tests (two-sided) corrected for multiple comparisons using a Bonferroni-Holm correction were applied to analyze the data in Fig. 3 **a** and **d-e**. Data in bar graphs are presented as median values  $\pm 25^{\text{th}}$  and  $75^{\text{th}}$  percentiles; \*\*\* $P < 0.001$ ; n.s., not significant. Source data are provided as a Source Data file.

**Fig. 4: Reduced spike-time synchrony in grid cell-interneuron and grid cell-head direction cell pairs.** **a** Spike-time cross-correlations between grid cell-interneuron pairs (left) and grid cell-head direction cell pairs (right) for all experimental groups (rows). Each panel displays the normalized correlation (by median) by time lag (in ms). Black curves indicate median values and gray contours indicate median absolute deviation. Lighter gray columns indicate the 25 ms time window in each lag direction from 0 ms. **b** Color-coded raster plots show the magnitude of co-activity within a 400 ms time window. Y-axes are sorted in descending order by cell-pairs with the maximum co-activity within a 25 ms time window, and numbers indicate the number of cell-pairs in each experimental group. **c** The mean co-activity within a 25 ms time window for grid-interneurons pairs (nTG-y vs. nTG-a:  $P = 0.30$ ; nTG-y vs. APP-y:  $P = 0.13$ ; APP-y vs. APP-a:  $P = 0.51$ ; nTG-a vs. APP-a:  $P = 0.0018$ ), and grid-head direction pairs (nTG-y vs. nTG-a:  $P = 0.33$ ; nTG-y vs. APP-y:  $P = 0.56$ ; APP-y vs. APP-a:  $P = 0.078$ ; nTG-a vs. APP-a:  $P = 0.038$ ) between groups (grid-interneuron pairs,  $n = 60$  for nTG-y;  $n = 115$  for nTG-a;  $n = 34$  for APP-y;  $n = 54$  for APP-a; grid-head direction pairs,  $n = 73$  for nTG-y;  $n = 110$  for nTG-a;  $n = 34$  for APP-y;  $n = 30$  for APP-a). nTG-y, non-transgenic young; nTG-a, non-transgenic adult; APP-y, APP young; APP-a, APP adult. Wilcoxon rank sum tests (two-sided) corrected for multiple comparisons using a Bonferroni-Holm correction were applied to analyze the data in Fig. 4 c. Data in bar graphs are presented as median values  $\pm$  25<sup>th</sup> and 75<sup>th</sup> percentiles; \* $P < 0.05$ , \*\* $P < 0.01$ ; n.s, not significant. Source data are provided as a Source Data file.

**Fig. 5: Path integration is impaired in APP mice and worsens across age.** **a** Schematic of food-foraging task in total darkness. Mice left their refuge to forage for a randomly placed food pellet. Upon discovery, they navigated back to the refuge prior to consumption. **b** (Left) The probability of reaching the refuge at the initial wall encounter is depicted in a polar plot. (Right) Probability density plot compares the likelihood of arriving at each of the ten walls between groups. W1 and W10 refer to the ten walls in consecutive order. **c** Polar plots compare the probability of reaching the refuge at the initial wall encounter between groups. Probability values are indicated below polar plots for each group. **d** The initial wall angle (nTG-y vs. nTG-a:  $P = 0.50$ ; nTG-y vs. APP-y:  $P = 6.3 \times 10^{-15}$ ; APP-y vs. APP-a:  $P = 0.11$ ; nTG-a vs. APP-a:  $P = 5.6 \times 10^{-15}$ ), the initial heading angle (nTG-y vs. nTG-a:  $P = 0.22$ ; nTG-y vs. APP-y:  $P = 3.1 \times 10^{-10}$ ; APP-y vs. APP-a:  $P = 1.9 \times 10^{-5}$ ; nTG-a vs. APP-a:  $P = 9.5 \times 10^{-17}$ ), the normalized distance travelled (nTG-y vs. nTG-a:  $P = 0.0083$ ; nTG-y vs. APP-y:  $P = 1.2 \times 10^{-6}$ ; APP-y vs. APP-a:  $P = 1.2 \times 10^{-6}$ ; nTG-a vs. APP-a:  $P = 3.9 \times 10^{-11}$ ), and the proportion of the return path spent along the periphery (nTG-y vs. nTG-a:  $P = 0.74$ ; nTG-y vs. APP-y:  $P = 0.011$ ; APP-y vs. APP-a:  $P = 7.1 \times 10^{-5}$ ; nTG-a vs. APP-a:  $P = 1.6 \times 10^{-7}$ ) between groups (behavior trials,  $n = 377$  for nTG-y;  $n = 307$  for nTG-a;  $n = 500$  for APP-y;  $n = 311$  for APP-a). **e** The increase (measured in degree change) of the initial wall angle (nTG-a vs. APP-a: r.s  $P = 0.42$ ; k.s  $P = 2.3 \times 10^{-11}$ ) and the initial heading angle (nTG-a vs. APP-a: r.s  $P = 0.019$ ; k.s  $P = 8.1 \times 10^{-6}$ ) across age, as well as the increase (measured as a % increase) of the normalized distance travelled (nTG-a vs. APP-a: r.s  $P = 0.0029$ ; k.s  $P = 8.5 \times 10^{-4}$ ) and the proportion of the return path spent along the periphery (nTG-a vs. APP-a: r.s  $P = 0.014$ ; k.s  $P = 0.0013$ ) across age between groups (behavior trials,  $n = 307$  for nTG-a;  $n = 311$  for APP-a). The median change for each group is indicated above the respective bars. The  $P$  values obtained from a two-sided Wilcoxon rank sum test (r.s) and a two-sample, two-sided Kolmogorov-Smirnov test (k.s) are both indicated. nTG-y, non-transgenic young; nTG-a, non-transgenic adult; APP-y, APP young; APP-a, APP adult. Wilcoxon rank sum tests (two-sided) corrected for multiple comparisons using a Bonferroni-Holm correction were applied to analyze the data in Fig. 5 **d**. Wilcoxon rank sum tests (two-sided) and two-sample Kolmogorov-Smirnov tests (two-sided) were applied to analyze the data in Fig. 5 **e**. Data in bar graphs are presented as median values  $\pm 25^{\text{th}}$  and  $75^{\text{th}}$  percentiles; \* $P < 0.05$ , \*\* $P < 0.01$ , \*\*\* $P < 0.001$ ; n.s, not significant. Source data are provided as a Source Data file.

Figure 1

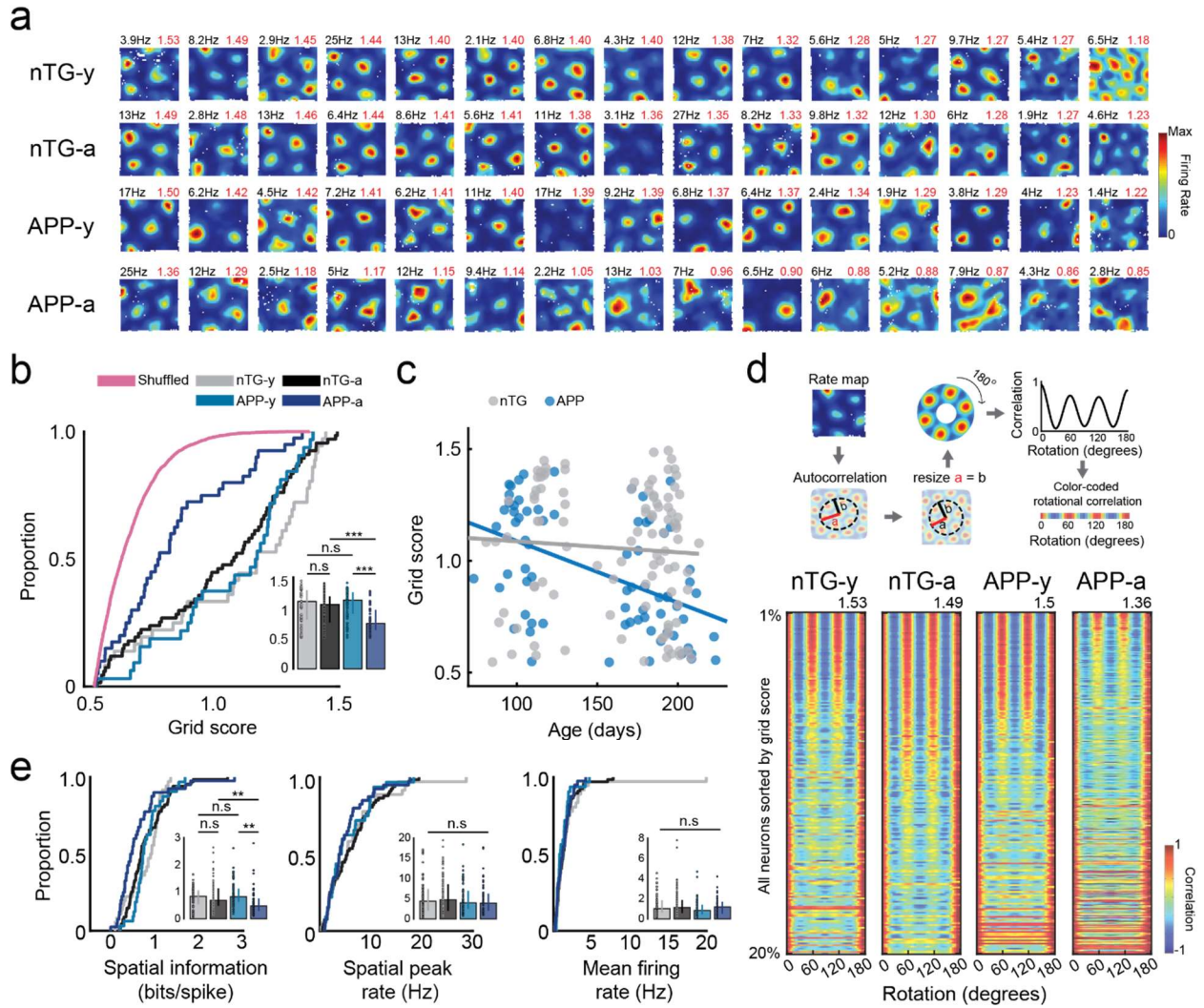


Figure 2

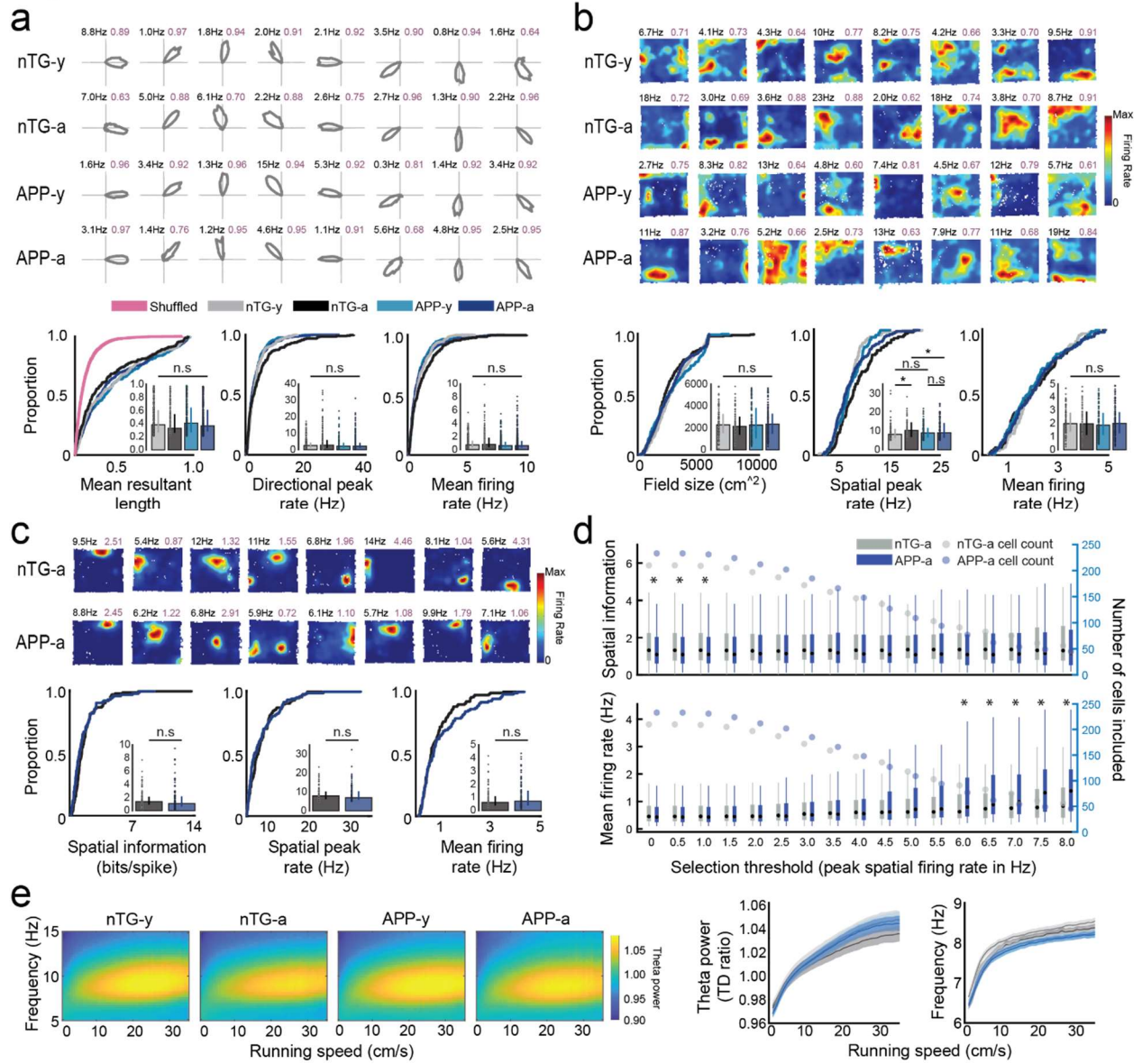


Figure 3

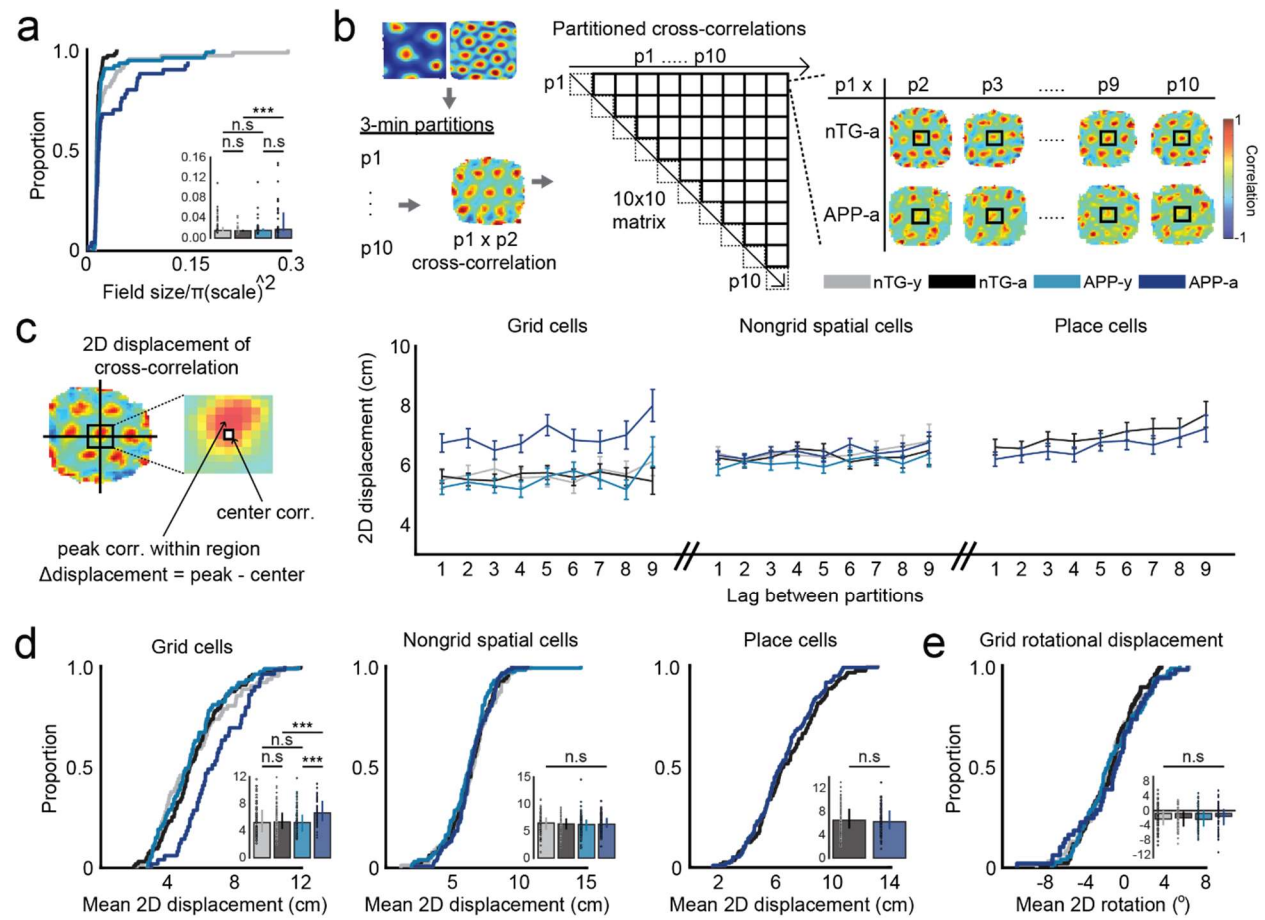


Figure 4

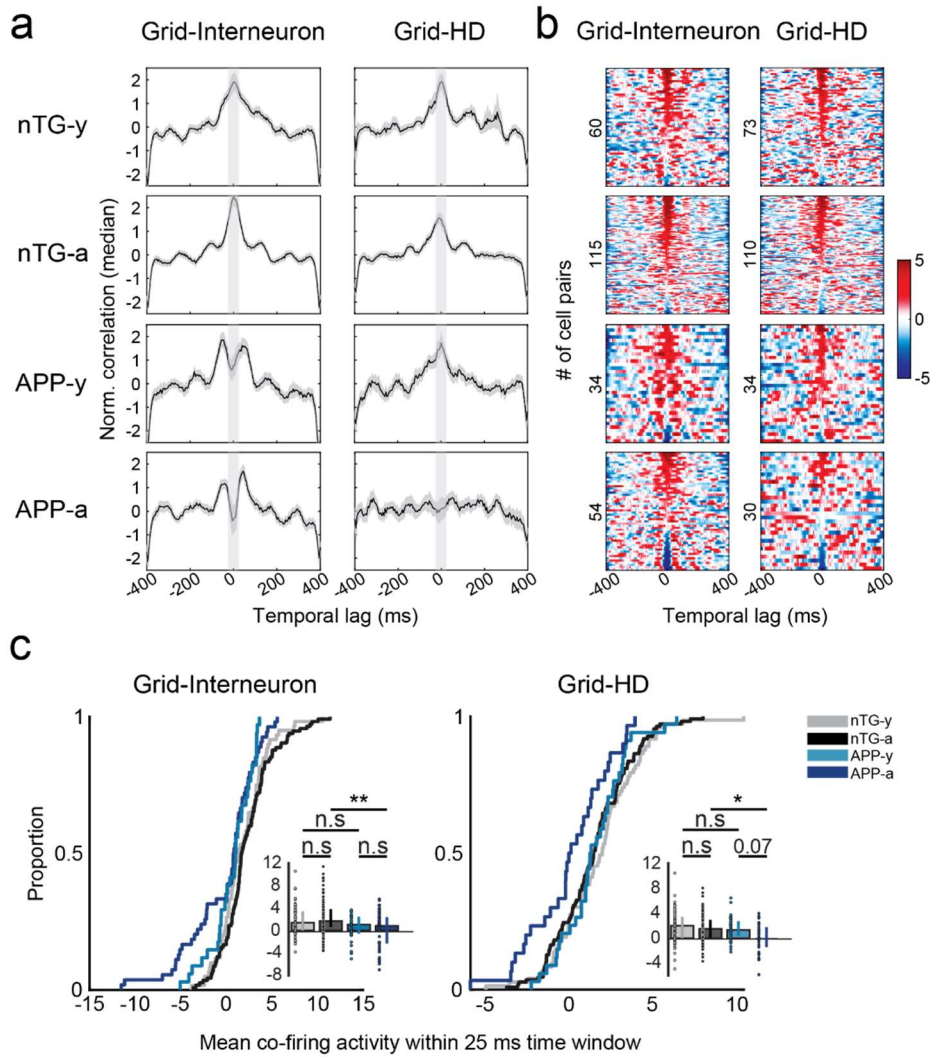
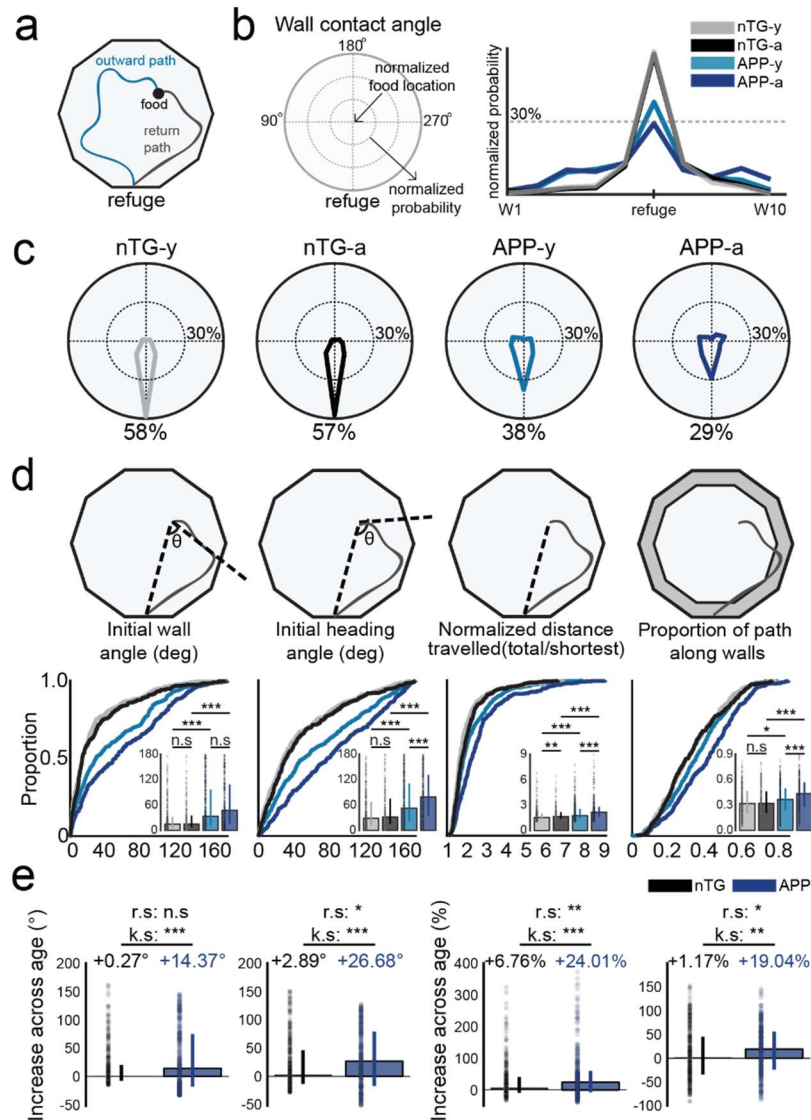


Figure 5



## Supplementary Information

Contains:

- **Supplementary Tables 1-2**
- **Supplementary Figures 1-24**

**Supplementary Table 1. Summary of MEC cell yield within subject.**

<b>Animal ID#</b>	<b>Genotype</b>	<b>Sex</b>	<b>Age Group</b>	<b># recording sessions</b>	<b># total cells</b>	<b># total cells MEC</b>	<b># grid cells</b>	<b># HD cells</b>	<b># Non-grid spatial cells</b>
12015	nTG	F	A	5	21	18	0	7	0
12040	APP	M	A	11	35	35	1	5	1
12375	nTG	F	Y	21	114	114	1	35	14
12378	nTG	F	Y	9	28	28	1	12	0
12644	nTG	F	A	7	32	0	0	0	0
12646	APP	F	A	2	3	3	1	3	0
12655	nTG	F	A	5	15	4	0	2	0
12656	nTG	F	A	8	36	0	0	0	0
12746	nTG	F	A	10	36	36	2	20	3
12748	nTG	F	A	33	97	97	16	25	7
12756	nTG	F	A	10	36	8	0	3	4
12757	nTG	F	A	18	64	55	0	20	4
12758	APP	F	A	24	112	40	1	17	0
12759	APP	F	A	23	70	70	0	30	3

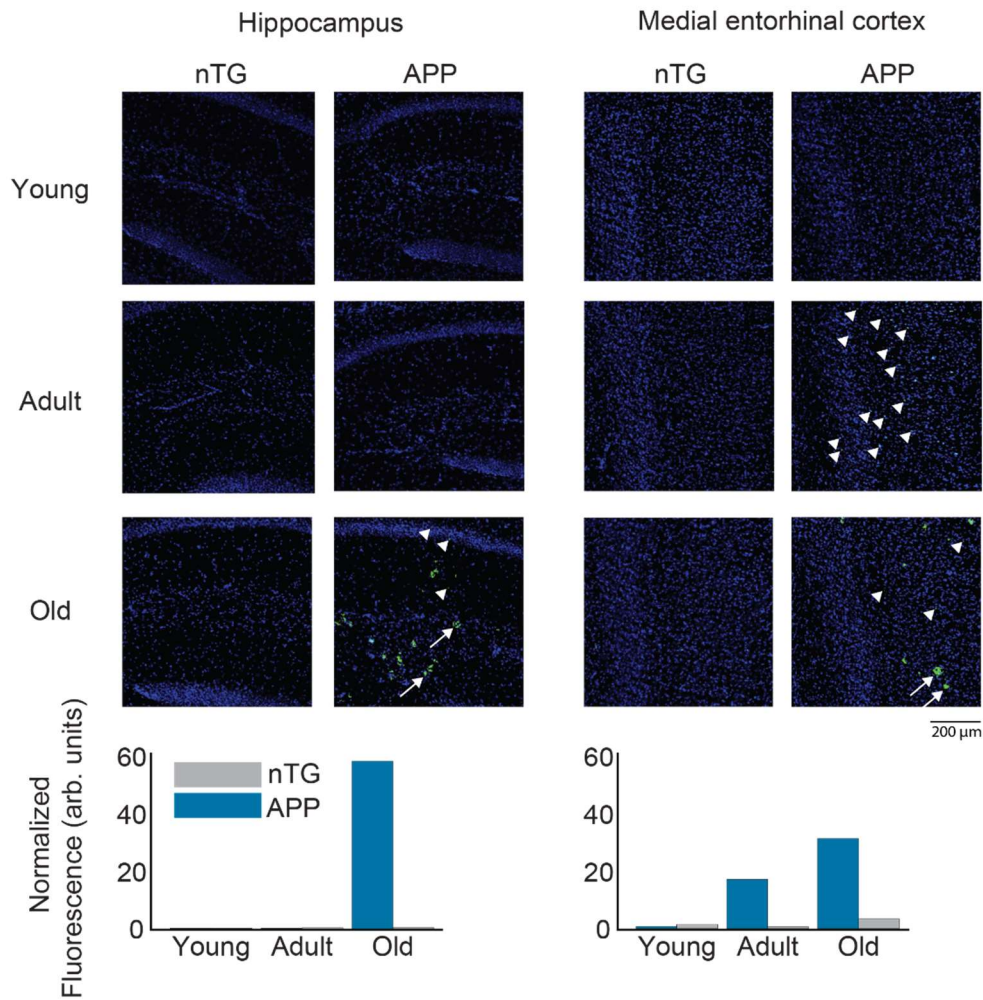
12784	APP	M	A	18	81	81	1	26	7
12785	APP	M	A	22	32	32	2	11	2
12786	nTG	M	A	18	60	60	1	9	7
12787	nTG	M	A	24	153	91	1	13	9
12788	APP	M	A	7	9	7	0	4	0
12790	APP	M	A	18	79	79	2	27	2
12791	nTG	M	A	38	192	192	1	49	17
12792	APP	M	A	14	31	31	1	11	1
12794	nTG	M	A	14	29	29	0	7	1
13530	APP	F	Y	10	29	5	0	3	0
13532	APP	F	Y	28	117	117	4	38	10
13534	APP	F	Y	30	142	142	27	21	31
13601	nTG	F	Y	18	67	7	0	0	0
13630	nTG	M	Y, A	33	260	260	79	45	29
13631	nTG	M	Y	16	95	95	0	38	6
13683	APP	F	A	12	64	64	1	17	3
13781	nTG	M	A	16	46	16	5	4	2
13782	nTG	M	A	26	168	168	31	54	20
13783	nTG	M	A	23	104	104	7	20	6
13784	nTG	M	A	14	65	11	1	2	1
13791	APP	F	A	14	43	43	0	5	0
13792	APP	F	A	13	40	40	0	5	2
13794	APP	F	Y	17	63	63	0	24	7
13795	APP	M	Y	21	91	64	0	15	3
13798	nTG	M	Y	19	106	106	7	16	10
13799	APP	M	Y	25	86	86	31	13	3
13827	nTG	M	Y	17	84	84	0	36	4

13828	APP	M	A	19	52	52	8	17	0
13884	nTG	F	Y, A	22	57	29	1	12	2
13885	nTG	F	Y, A	25	87	87	6	23	7
13894	APP	F	A	17	86	86	2	12	14
13895	nTG	F	Y	18	63	63	1	17	0
13927	APP	F	A	23	97	97	0	44	2
13928	nTG	F	Y	10	20	20	0	10	0
13931	APP	F	A	16	53	53	1	12	10
14012	APP	F	A	13	40	40	0	18	0
14014	APP	M	A	15	62	62	1	12	1
14015	APP	M	A	15	80	80	0	30	4
14020	APP	F	A	12	47	47	0	20	3
14117	APP	F	A	12	29	29	0	9	2
14118	APP	F	A	12	34	34	6	3	4
14125	APP	M	A	15	59	59	12	10	1
14574	APP	F	Y, A	22	71	71	0	10	11
14593	APP	F	A	20	63	63	6	21	7
14598	APP	M	A	14	57	36	0	20	0
14599	APP	M	A	25	68	68	2	9	8
14623	APP	M	A	25	94	63	1	9	28
14754	APP	M	Y, A	30	175	139	1	31	0
14756	APP	M	Y, A	30	267	267	3	127	26
14757	APP	M	Y, A	34	168	164	8	43	7
14847	nTG	F	Y, A	21	63	63	0	25	1
14849	nTG	M	Y, A	20	95	52	1	16	1
15035	APP	F	Y, A	30	188	188	2	45	22
15036	nTG	F	Y	25	108	64	1	19	10

**Supplementary Table 2. Summary of CA1 cell yield within subject.**

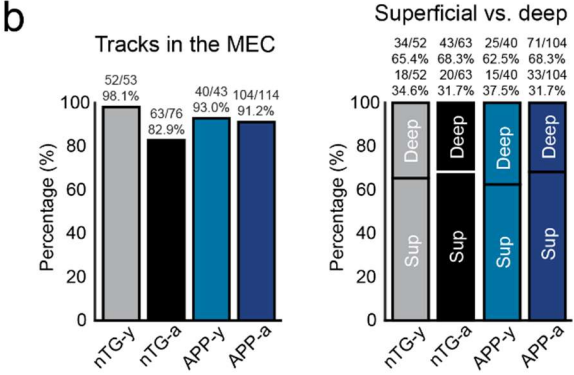
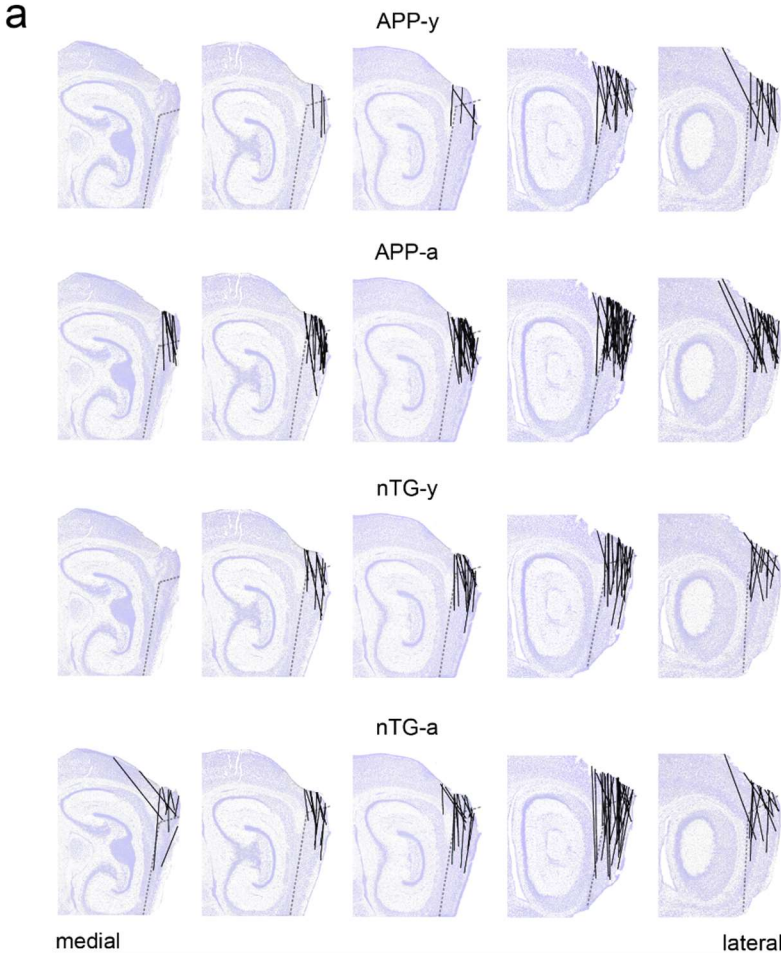
<b>Animal ID#</b>	<b>Genotype</b>	<b>Sex</b>	<b># recording sessions</b>	<b># total cells</b>	<b># place cells</b>
16129	APP	F	17	58	28
16130	nTG	F	15	74	58
16132	nTG	M	14	60	27
16133	APP	M	14	102	76
16135	nTG	M	24	137	79
16153	nTG	F	2	9	4
16154	APP	F	17	138	45
17624	APP	F	22	53	18
17625	nTG	F	18	87	37
17627	APP	F	19	115	51
17628	nTG	F	18	74	49
17903	APP	M	8	85	33

## Supplementary Figure 1



**Supplementary Figure 1. Quantification of amyloid-beta plaques in APP mice.** Representative examples of magnified brain sections of the hippocampus and medial entorhinal cortex of nTG and APP mice across 3 different age groups: young (3-4.5 mo.), adult (4.5-7 mo.) and old (18 mo.). Arrows and arrowheads indicate the presence of two different kinds of fluorescent morphologies. Adult APP mice have low levels of fluorescence in the medial entorhinal cortex, but the fluorescent signal is intracellular and does not resemble the bigger and widespread morphology observed in the hippocampus and medial entorhinal cortex of old APP mice. The fluorescence signal in adult APP mice might therefore represent early deposition of fibrillar amyloid-beta prior to the formation of mature plaques.

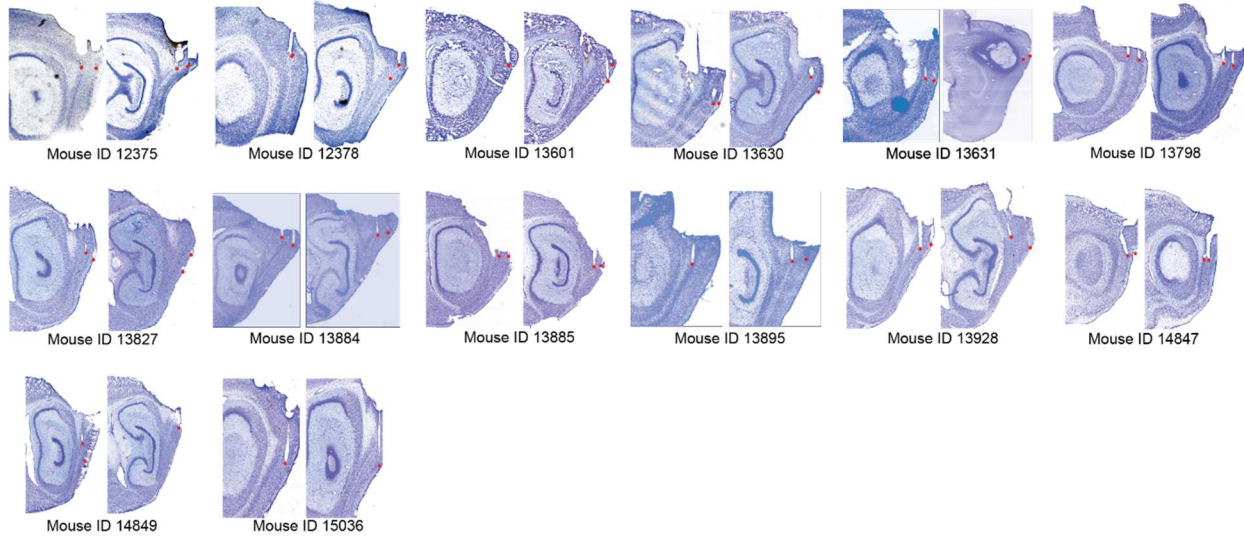
# Supplementary Figure 2. Page 1



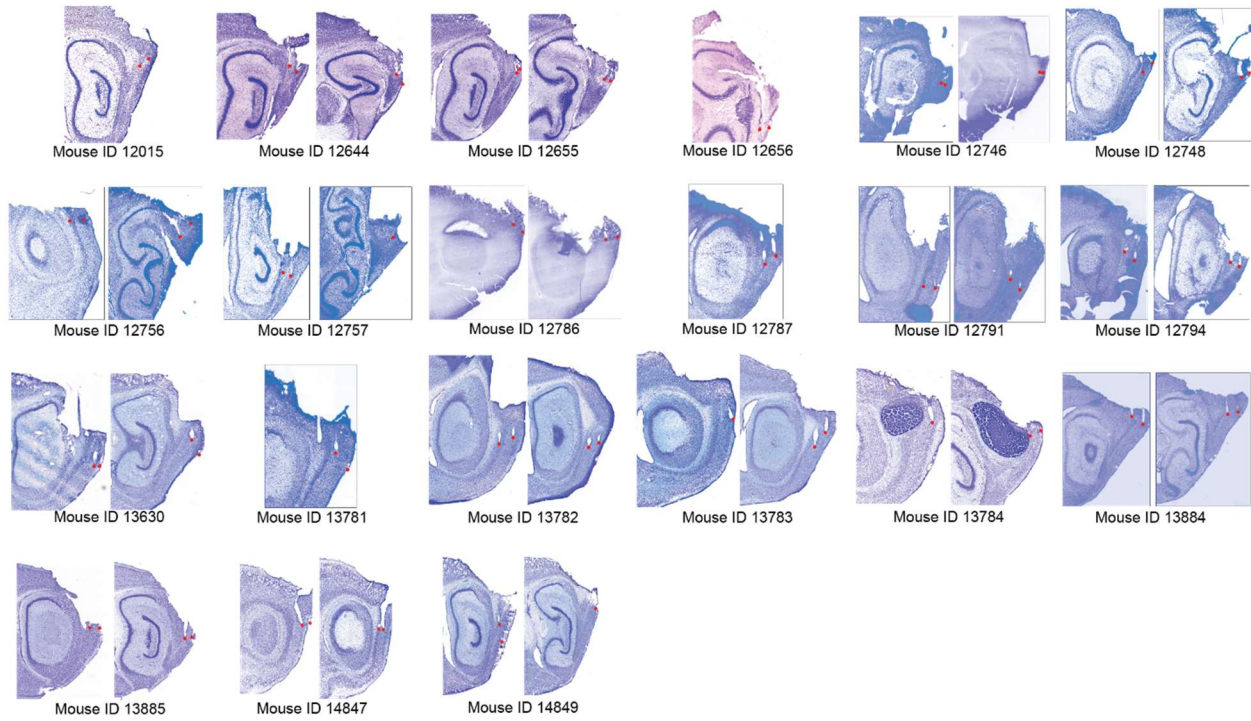
# Supplementary Figure 2. Page 2

C

nTG-y

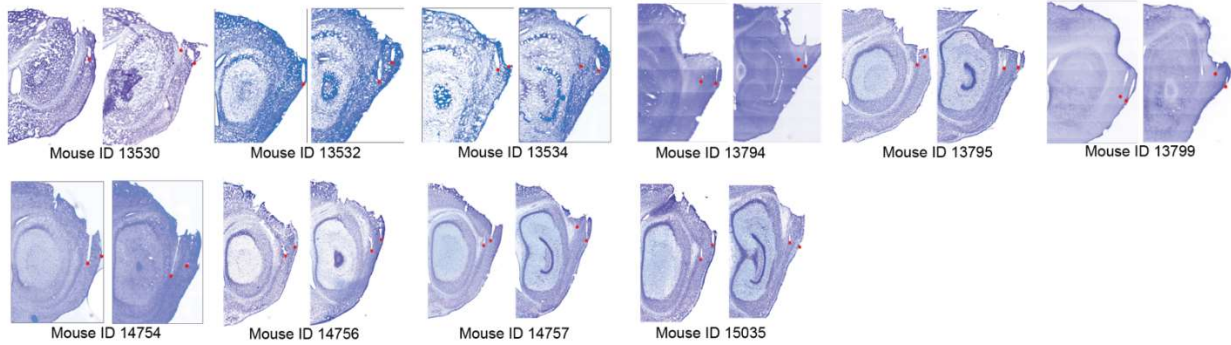


nTG-a

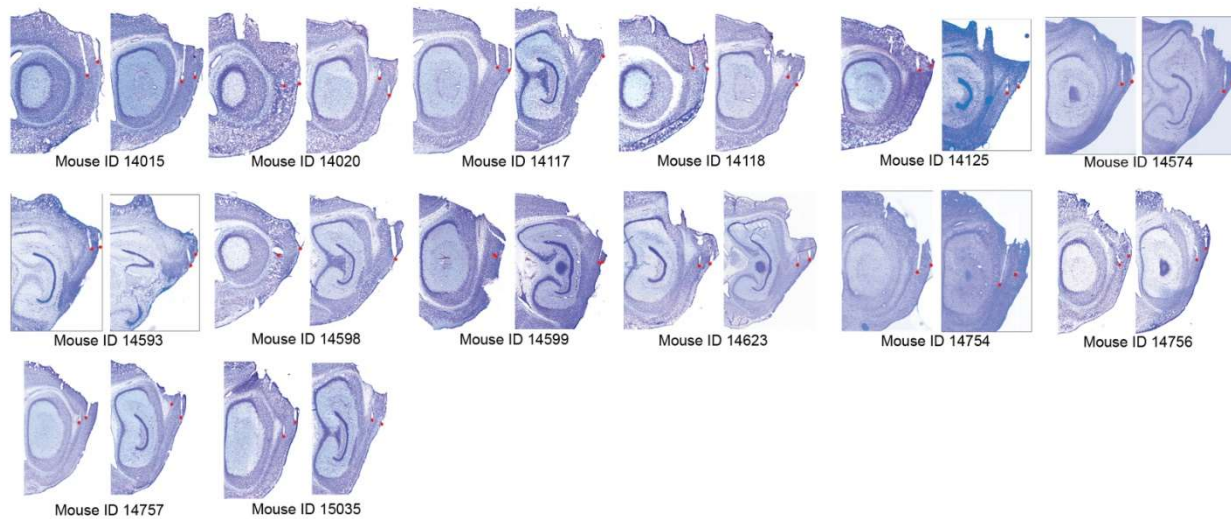
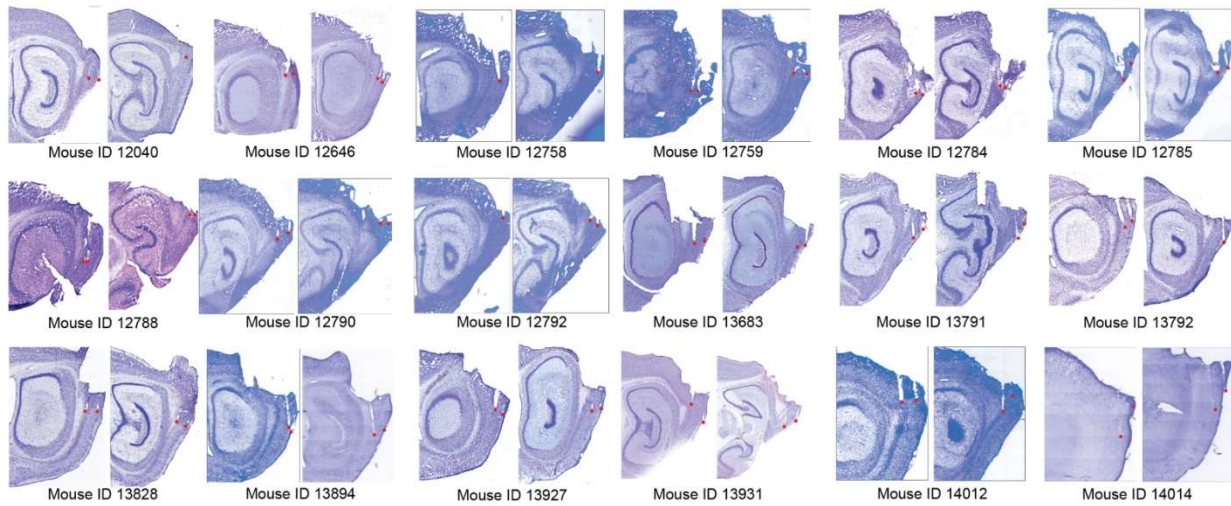


# Supplementary Figure 2. Page 3

## APP-y

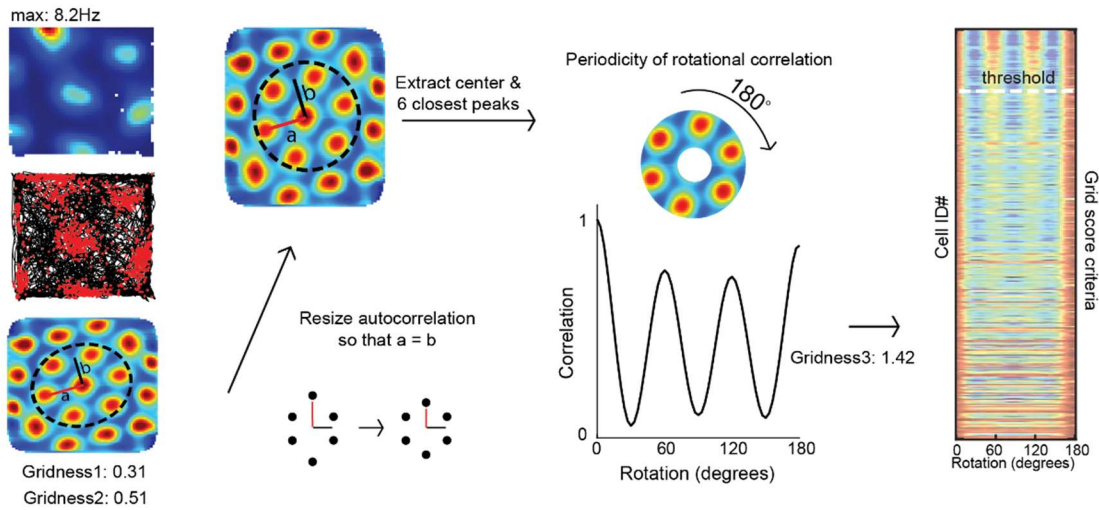


## APP-a



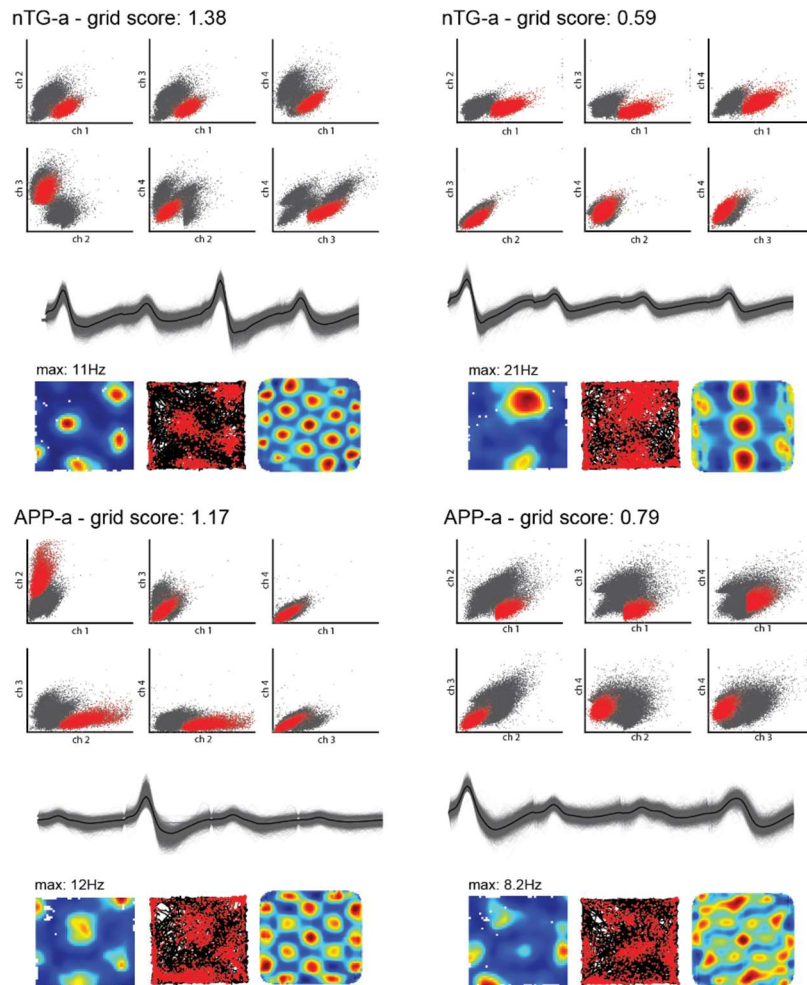
**Supplementary Figure 2. Tetrode track histology for MEC recordings.** **a** Averaged sagittal brain sections from the most lateral part of MEC (far right) to the start of parasubiculum (far left). The individual track locations obtained from each animal were plotted along these sections by experimental group. **b** Quantification of track locations shown in (a). (Left) Comparison of the percentage of tetrode tips located in the MEC between groups. (Right) Comparison of the percentage of tetrode tip in either the superficial or deep layers of MEC between groups. **c** Track locations of each animal ordered by genotype and age. The tips of tracks are highlighted with a red dot.

### Supplementary Figure 3



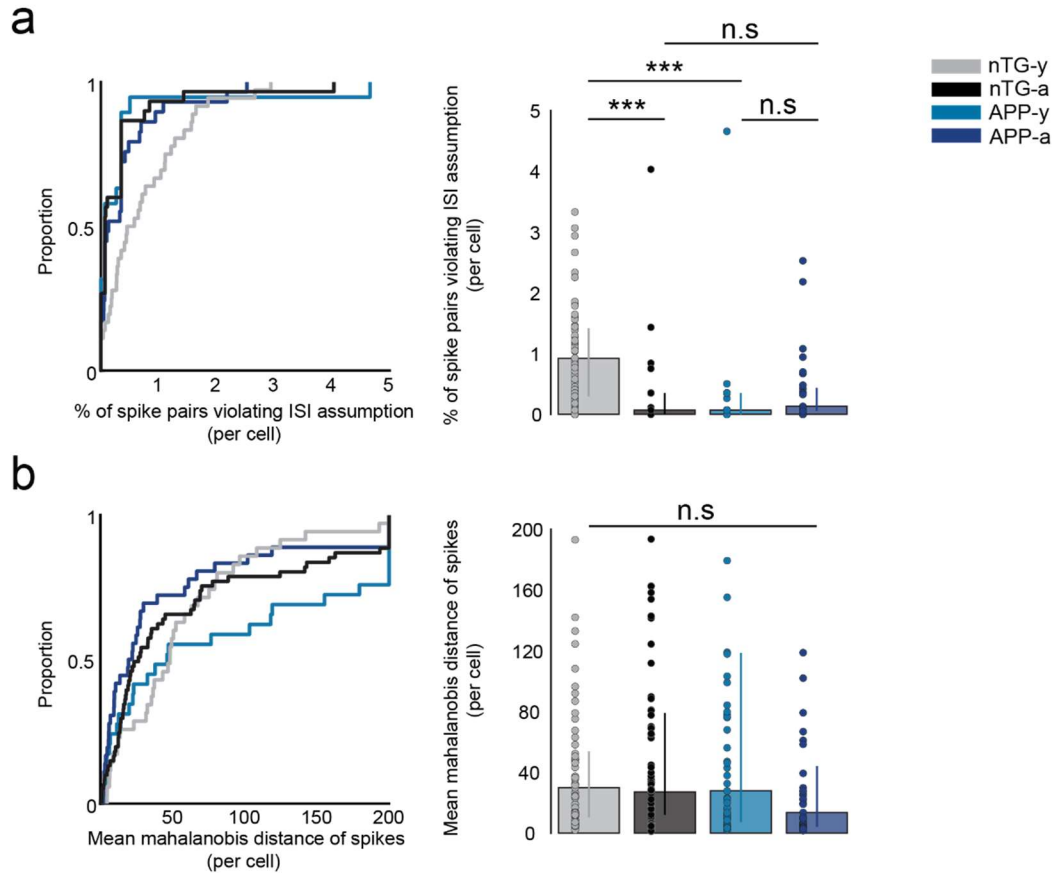
**Supplementary Figure 3. Creation of raster plots indicating the strength of rotational correlation of each cell.** Autocorrelations of grid cell rate maps were resized to ensure that the major and minor axes,  $a$  and  $b$ , were equal in length. The resulting image was then rotated 180 degrees to compute a color-coded row indicating the correlation strength at each degree of rotation. These rows were then sorted by decreasing order of grid score in a raster plot.

## Supplementary Figure 4



**Supplementary Figure 4. Example of well-isolated waveforms of four grid cells recorded in nTG-a and APP-a mice.** Cells with a high and low grid score were selected in each group for comparison. Each panel consists of the cell's grid score, the unit location in the six possible conformations of cluster space sorted by waveform amplitude, individual waveforms recorded across the four recording channels (grey) and the average waveform (black), the cell's rate map, trajectory map and rate map autocorrelation.

## Supplementary Figure 5



**Supplementary Figure 5. Spike isolation quality of grid cells. a** Percentage of spike pairs with an interspike interval (ISI) less than 1 millisecond (nTG-y vs. nTG-a:  $P = 1.3 \times 10^{-5}$ ; nTG-y vs. APP-y:  $P = 1.2 \times 10^{-4}$ ; APP-y vs. APP-a:  $P = 0.30$ ; nTG-a vs. APP-a:  $P = 0.45$ ), between groups (cells,  $n = 61$  for nTG-y;  $n = 30$  for nTG-a;  $n = 19$  for APP-y;  $n = 30$  for APP-a). These instances are considered non-physiological and may be due to faulty isolation or the presence of noisy spikes.

**b** Mean mahalanobis distance of spikes per grid cell (nTG-y vs. nTG-a:  $P = 0.65$ ; nTG-y vs. APP-y:  $P = 0.58$ ; APP-y vs. APP-a:  $P = 0.066$ ; nTG-a vs. APP-a:  $P = 0.18$ ), between groups (cells,  $n = 61$  for nTG-y;  $n = 97$  for nTG-a;  $n = 74$  for APP-y;  $n = 45$  for APP-a). nTG-y, non-transgenic young; nTG-a, non-transgenic adult; APP-y, APP young; APP-a, APP adult. Wilcoxon rank sum tests (two-sided) corrected for multiple comparisons using a Bonferroni-Holm correction were applied to analyze the data in Supplementary Fig. 5 **a-b**. Data in bar graphs are presented as median values  $\pm$  25<sup>th</sup> and 75<sup>th</sup> percentiles; \*\*\* $P < 0.001$ ; n.s, not significant. Source data are provided as a Source Data file.

## Supplementary Figure 6

**Two-way ANOVA: Grid cells**

Source	Sum Square	df	MS	F	p
Age	1.97	1	1.97	28.54	= 1.89e-7
Genotype	0.45	1	0.45	6.54	= 0.011
Interaction	0.89	1	0.89	12.90	= 3.86e-4
Error	19.55	283	0.0069		
Total	22.27	286			

**Two-way ANOVA: Head-direction cells**

Source	Sum Square	df	MS	F	p
Age	0.19	1	0.19	3.71	= 0.054
Genotype	0.17	1	0.17	3.25	= 0.072
Interaction	0.01	1	0.01	0.2	= 0.65
Error	67.45	1311	0.05		
Total	67.77	1314			

**Two-way ANOVA: Non-grid spatial cells**

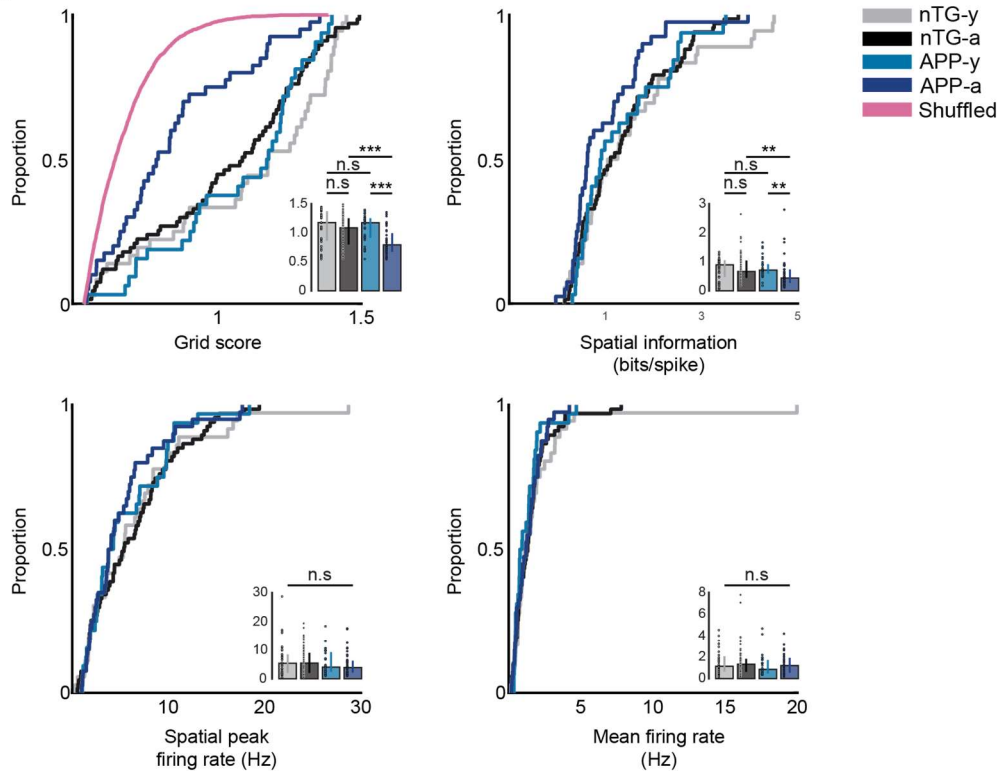
Source	Sum Square	df	MS	F	p
Age	941105	1	941105	0.48	= 0.49
Genotype	933809	1	933809	0.47	= 0.49
Interaction	735051	1	735051	0.37	= 0.54
Error	7.6e8	386	1969180		
Total	7.6e8	389			

**Supplementary Figure 6. Spatial tuning of grid cells, but not head-direction cells or non-grid spatial cells, is disrupted across age in APP mice.** Two-way unbalanced ANOVAs compare the effects of age, genotype, and interaction on spatial tuning scores for grid cells (grid score), head-direction cells (mean resultant length) and non-grid spatial cells (field size cm<sup>2</sup>).

df = degrees of freedom, MS = mean square.

## Supplementary Figure 7

a



b

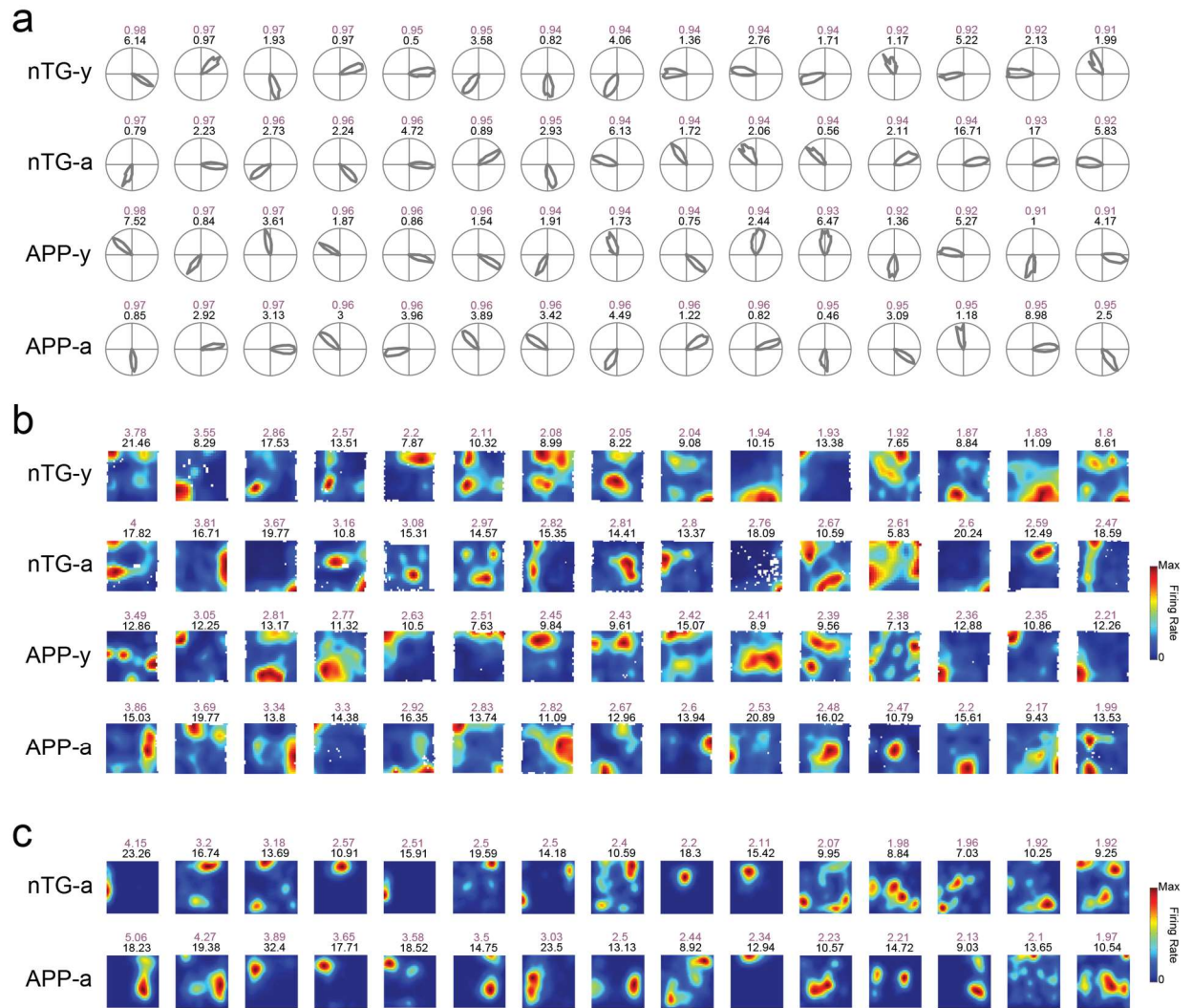
**Two-way ANOVA: Grid cells**

Source	Sum Square	df	MS	F	p
Age	0.90	1	0.90	12.81	= 0.00045
Genotype	0.44	1	0.44	6.31	= 0.013
Interaction	0.28	1	0.28	4.04	= 0.046
Error	12.06	171	0.07		
Total	13.62	174			

**Supplementary Figure 7. Grid cell spatial tuning remains impaired in adult APP mice when duplicate cell counts are removed.** **a** Grid score (nTG-y vs. nTG-a:  $P = 0.19$ ; nTG-y vs. APP-y:  $P = 0.44$ ; APP-y vs. APP-a:  $P = 4.1 \times 10^{-4}$ ; nTG-a vs. APP-a:  $P = 0.0031$ ), spatial information (nTG-y vs. nTG-a:  $P = 0.73$ ; nTG-y vs. APP-y:  $P = 0.70$ ; APP-y vs. APP-a:  $P = 0.0044$ ; nTG-a vs. APP-a:  $P = 0.0072$ ), spatial peak firing rate (nTG-y vs. nTG-a:  $P = 0.89$ ; nTG-y vs. APP-y:  $P = 0.64$ ; APP-y vs. APP-a:  $P = 0.73$ ; nTG-a vs. APP-a:  $P = 0.22$ ), and mean firing rate (nTG-y vs. nTG-a:  $P = 0.67$ ; nTG-y vs. APP-y:  $P = 0.23$ ; APP-y vs. APP-a:  $P = 0.45$ ; nTG-a vs. APP-a:  $P = 0.80$ ) between groups (cells,  $n = 36$  for nTG-y;  $n = 67$  for nTG-a;  $n = 32$  for APP-y;  $n = 40$  for APP-a). **b** Two-way unbalanced ANOVAs comparing the effects of age, genotype, and interaction on grid scores for grid cells. df= degrees of freedom, MS = mean square. nTG-y, non-transgenic

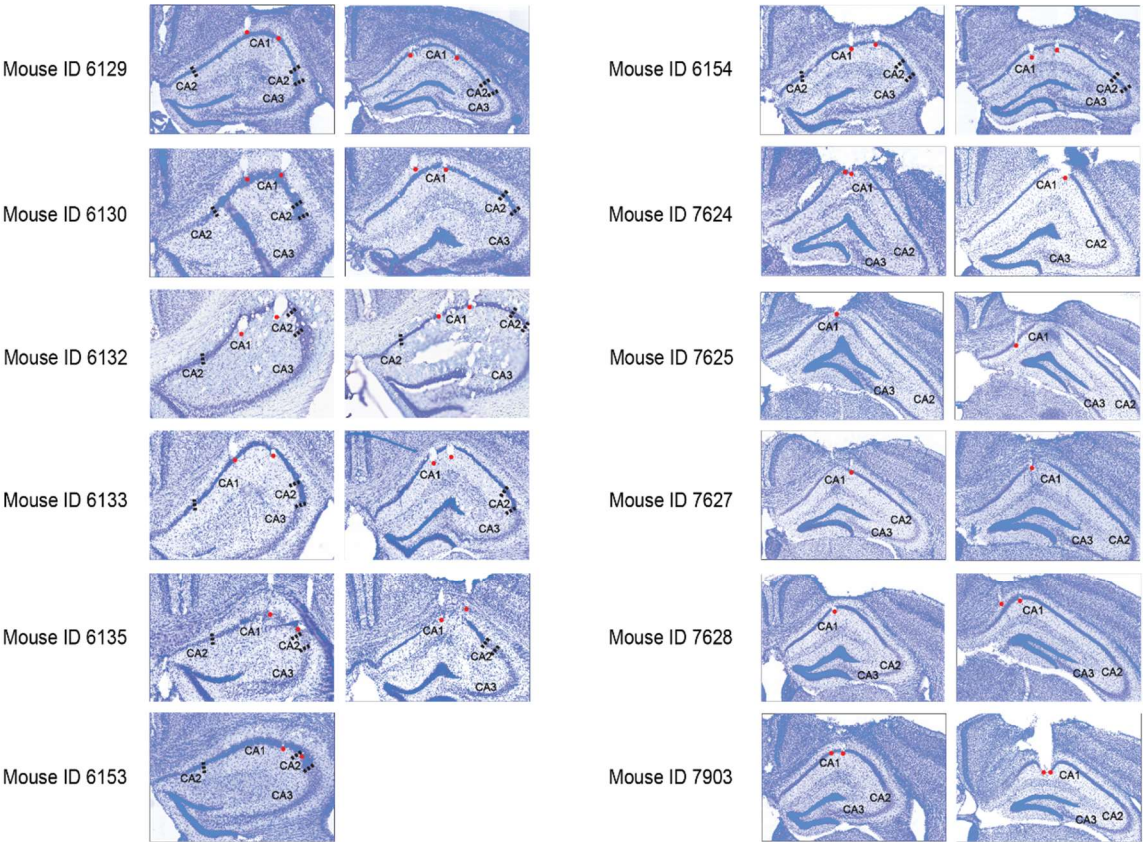
young; nTG-a, non-transgenic adult; APP-y, APP young; APP-a, APP adult. Wilcoxon rank sum tests (two-sided) corrected for multiple comparisons using a Bonferroni-Holm correction were applied to analyze the data in Supplementary Fig. 7 a. Data in bar graphs are presented as median values  $\pm$  25<sup>th</sup> and 75<sup>th</sup> percentiles; \*\* $P < 0.01$ , \*\*\* $P < 0.001$ ; n.s, not significant. Source data are provided as a Source Data file.

# Supplementary Figure 8



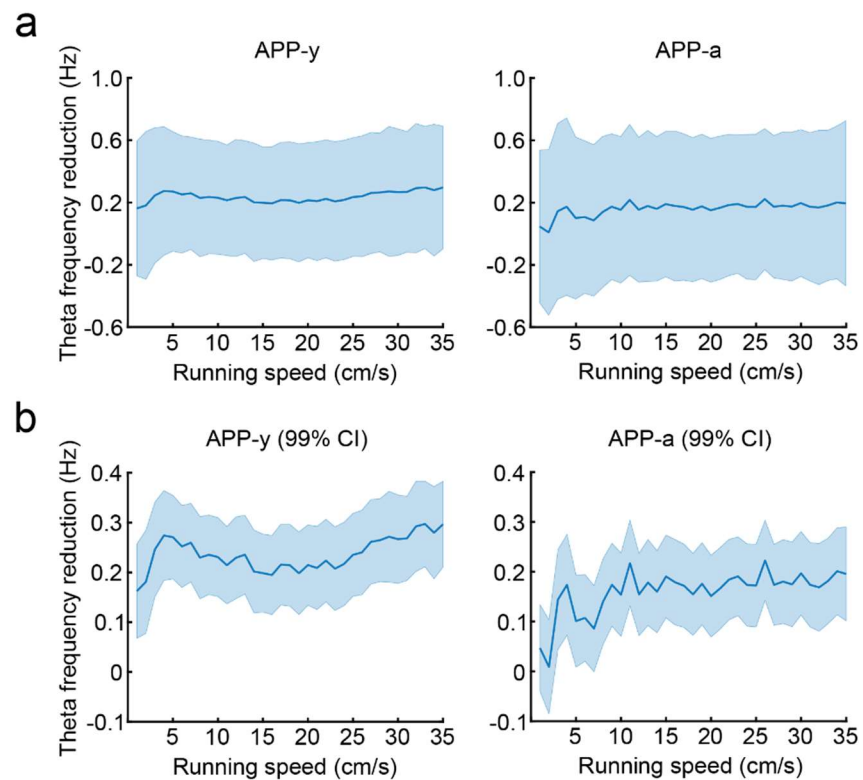
**Supplementary Figure 8. Top 15 quality cells across groups. a** Polar rate maps for head direction cells from each experimental group. Each row includes 15 head direction cells with the highest mean resultant scores sorted in descending order. The mean resultant length (light purple) and peak firing rate (Hz) (black) of each cell are indicated on top of their respective rate maps. **b** Same as (a) but for non-grid spatially-tuned cells. Cells are sorted by the highest spatial information scores in descending order. The spatial information (light purple) and peak firing rate (Hz) (black) of each cell are indicated on top of their respective rate maps. **c** Same as (a) but for place cells. Cells are sorted by the highest spatial information scores in descending order. The spatial information (light purple) and peak firing rate (Hz) (black) of each cell are indicated on top of their respective rate maps.

# Supplementary Figure 9



**Supplementary Figure 9. Tetrode track histology for CA1 recordings.** Track tips in each animal are shown in red dots.

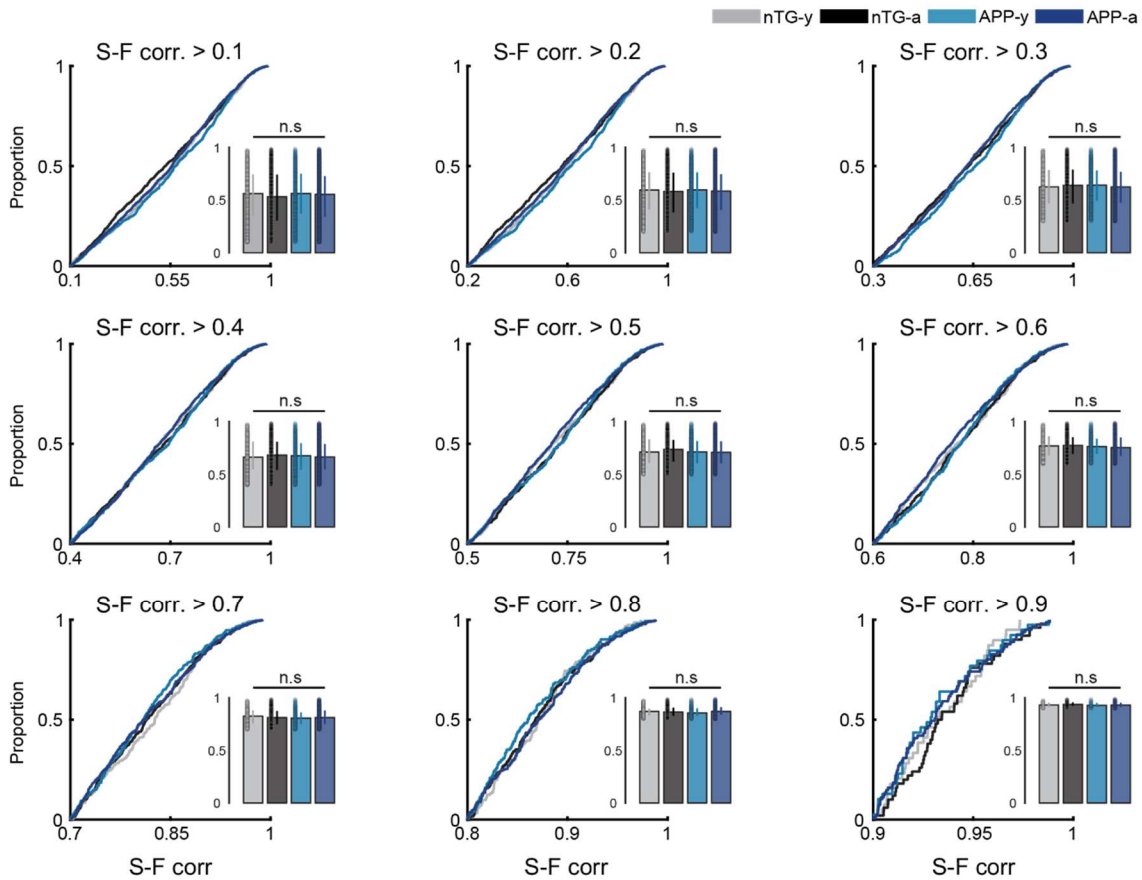
## Supplementary Figure 10



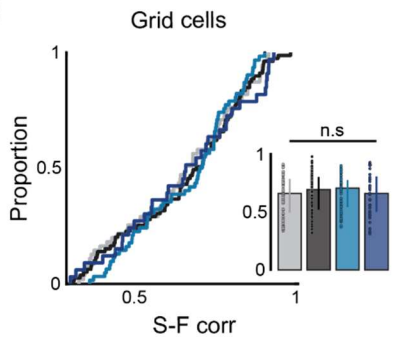
**Supplementary Figure 10. The magnitude of theta frequency reduction in APP mice is roughly equal across all running speeds. a** Reduction of theta frequency in APP-y (left) and APP-a (right) mice across running speeds (APP mice theta frequencies were subtracted from age-matched non-transgenic counterparts). Data are presented as mean values  $\pm$  standard deviation. **b** Same as (a) but data are presented as mean values  $\pm$  99% confidence intervals.

# Supplementary Figure 11

a



b



c

Two-way ANOVA: S-F corr. for grid cells

Source	Sum Square	df	MS	F	p
Age	0.00065	1	0.00065	0.02	= 0.88
Genotype	0.0034	1	0.0034	0.11	= 0.74
Interaction	0.00512	1	0.00512	0.17	= 0.68
Error	6.71	225	0.0298		
Total	6.72	228			

**Supplementary Figure 11. Intact speed coding in APP mice.** a Running speed vs. firing rate correlation (S-F corr.) of putative speed cells. Cells were selected via a S-F corr. threshold ranging from 0.1-0.9.

0.1: nTG-y-nTG-a:  $P = 0.17$ ; nTG-y-APP-y:  $P = 0.69$ ; APP-y-APP-a:  $P = 0.23$ ; nTG-a-APP-a:  $P = 0.42$ ;  $n = 772$  nTG-y; 949 nTG-a; 686 APP-y; 1515 APP-a

0.2: nTG-y-nTG-a:  $P = 0.21$ ; nTG-y-APP-y:  $P = 0.72$ ; APP-y-APP-a:  $P = 0.16$ ; nTG-a-APP-a:  $P = 0.70$ ;  $n = 696$  nTG-y; 846 nTG-a; 619 APP-y; 1368 APP-a

0.3: nTG-y-nTG-a:  $P = 0.71$ ; nTG-y-APP-y:  $P = 0.41$ ; APP-y-APP-a:  $P = 0.23$ ; nTG-a-APP-a:  $P = 0.47$ ;  $n = 629$  nTG-y; 725 nTG-a; 552 APP-y; 1206 APP-a

0.4: nTG-y-nTG-a:  $P = 0.61$ ; nTG-y-APP-y:  $P = 0.65$ ; APP-y-APP-a:  $P = 0.93$ ; nTG-a-APP-a:  $P = 0.29$ ;  $n = 537$  nTG-y; 620 nTG-a; 493 APP-y; 1033 APP-a

0.5: nTG-y-nTG-a:  $P = 0.42$ ; nTG-y-APP-y:  $P = 0.49$ ; APP-y-APP-a:  $P = 0.78$ ; nTG-a-APP-a:  $P = 0.15$ ;  $n = 442$  nTG-y; 507 nTG-a; 407 APP-y; 859 APP-a

0.6: nTG-y-nTG-a:  $P = 0.64$ ; nTG-y-APP-y:  $P = 0.74$ ; APP-y-APP-a:  $P = 0.39$ ; nTG-a-APP-a:  $P = 0.06$ ;  $n = 340$  nTG-y; 400 nTG-a; 308 APP-y; 658 APP-a

0.7: nTG-y-nTG-a:  $P = 0.32$ ; nTG-y-APP-y:  $P = 0.06$ ; APP-y-APP-a:  $P = 0.40$ ; nTG-a-APP-a:  $P = 0.86$ ;  $n = 238$  nTG-y; 297 nTG-a; 224 APP-y; 447 APP-a

0.8: nTG-y-nTG-a:  $P = 0.53$ ; nTG-y-APP-y:  $P = 0.13$ ; APP-y-APP-a:  $P = 0.06$ ; nTG-a-APP-a:  $P = 0.35$ ;  $n = 142$  nTG-y; 167 nTG-a; 119 APP-y; 244 APP-a

0.9: nTG-y-nTG-a:  $P = 0.54$ ; nTG-y-APP-y:  $P = 0.72$ ; APP-y-APP-a:  $P = 0.99$ ; nTG-a-APP-a:  $P = 0.22$ ;  $n = 35$  nTG-y; 44 nTG-a; 30 APP-y; 80 APP-a

**b** Grid cell S-F corr. (nTG-y-nTG-a:  $P = 0.65$ ; nTG-y-APP-y:  $P = 0.66$ ; APP-y-APP-a:  $P = 0.99$ ; nTG-a-APP-a:  $P = 0.98$ ) between groups ( $n = 55$  nTG-y; 79 nTG-a; 62 APP-y; 33 APP-a). **c** Two-way unbalanced ANOVA comparing the effects of age and genotype on S-F corr. of grid cells. df = degrees of freedom, MS = mean square. Wilcoxon rank sum tests (two-sided) with Bonferroni-Holm's correction were applied to Supplementary Fig. 11 **a-b**. Data in bar graphs are presented as medians  $\pm$  25<sup>th</sup> and 75<sup>th</sup> percentiles; n.s., not significant. Source data are provided as a Source Data file.

## Supplementary Figure 12

Two-way ANOVA: Mean 2D displacement

Source	Sum Square	df	MS	F	p
Genotype	33.79	1	33.79	8.43	= 0.0038
Cell type	38.57	2	19.29	4.81	= 0.0084
Interaction	34.83	2	17.41	4.34	= 0.013
Error	3296.64	822	4.01		
Total	3410.74	827			

Pairwise comparisons: Tukey's test

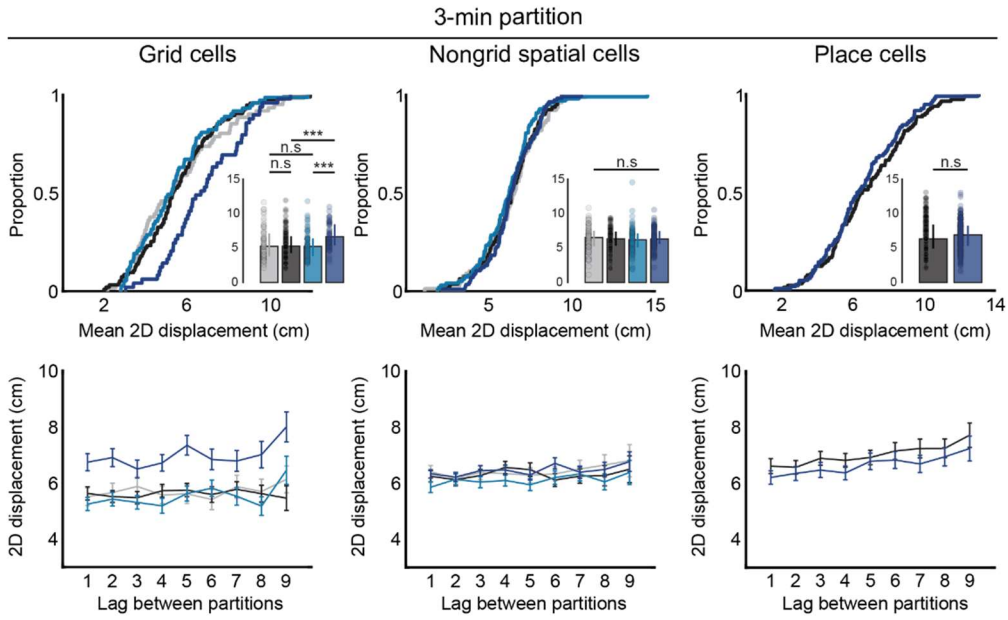
Comparisons	Mean diff.	95% C.I. for true mean diff.		p
		LL	UL	
<b>nTG-a grid - APP-a grid</b>	<b>-1.23</b>	<b>-2.23</b>	<b>-0.23</b>	<b>0.0064</b>
nTG-a grid - nTG-a nongrid	-0.69	-1.56	0.17	0.2
nTG-a grid - APP-a nongrid	-0.79	-1.58	0.00	0.049
nTG-a grid - nTG-a place	-1.08	-1.77	-0.39	0.00012
nTG-a grid - APP-a place	-1.18	-1.87	-0.49	1.60E-05
APP-a grid - nTG-a nongrid	0.54	-0.50	1.57	0.68
APP-a grid - APP-a nongrid	0.44	-0.54	1.41	0.8
APP-a grid - nTG-a place	0.15	-0.75	1.04	1
APP-a grid - APP-a place	0.05	-0.84	0.94	1
<b>nTG-a nongrid - APP-a nongrid</b>	<b>-0.10</b>	<b>-0.93</b>	<b>0.73</b>	<b>1</b>
nTG-a nongrid - nTG-a place	-0.39	-1.13	0.35	0.66
nTG-a nongrid - APP-a place	-0.49	-1.22	0.25	0.41
APP-a nongrid - nTG-a place	-0.29	-0.94	0.36	0.8
APP-a nongrid - APP-a place	-0.39	-1.03	0.26	0.53
<b>nTG-a place - APP-a place</b>	<b>-0.10</b>	<b>-0.61</b>	<b>0.42</b>	<b>0.99</b>

**Supplementary Figure 12. Mean 2D displacement is higher in grid cells, but not non-grid spatially-tuned cells or place cells, in adult APP mice.** Two-way unbalanced ANOVAs compare the effects of genotype, cell type, and interaction on the mean 2D displacement scores for grid cells, non-grid spatially-tuned cells and place cells. Grid cells, non-grid spatially-tuned cells and place cells were included in the “Cell type” factor. Pairwise comparisons with Tukey’s test at a corrected alpha value of 0.05 are shown at the bottom. The 3 comparisons of interest (nTG-a grid - APP-a grid; nTG-a nongrid - APP-a nongrid; nTG-a place - APP-a place) are bolded.

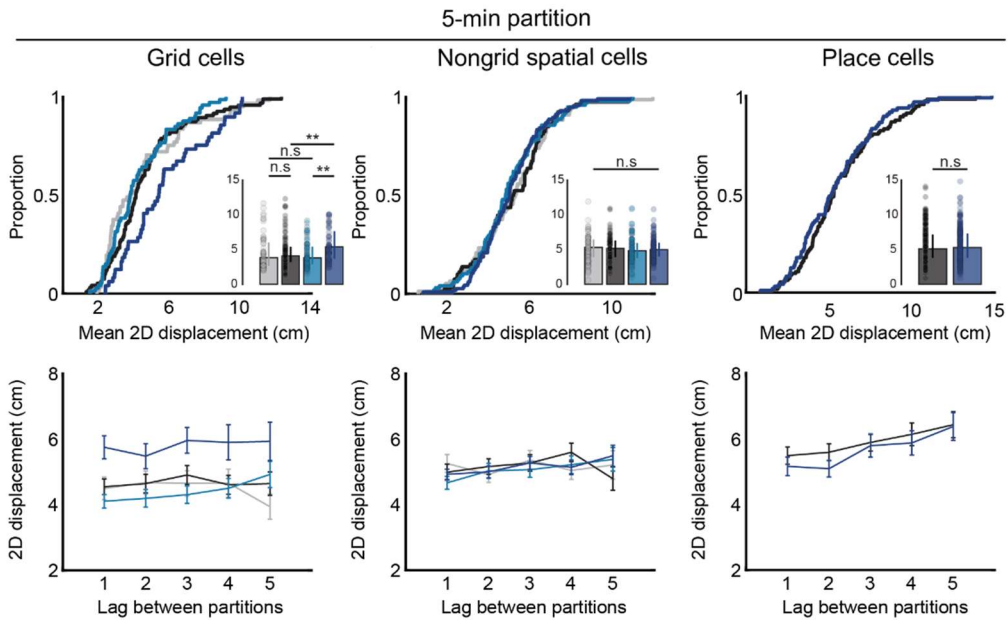
df = degrees of freedom, MS = mean square.

# Supplementary Figure 13. Page 1

a

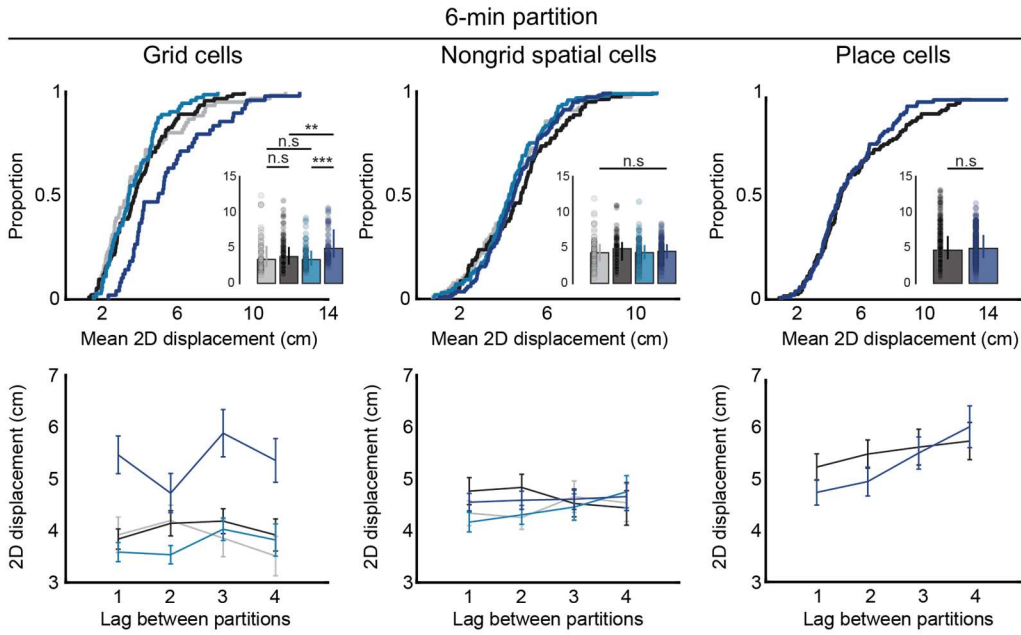


b

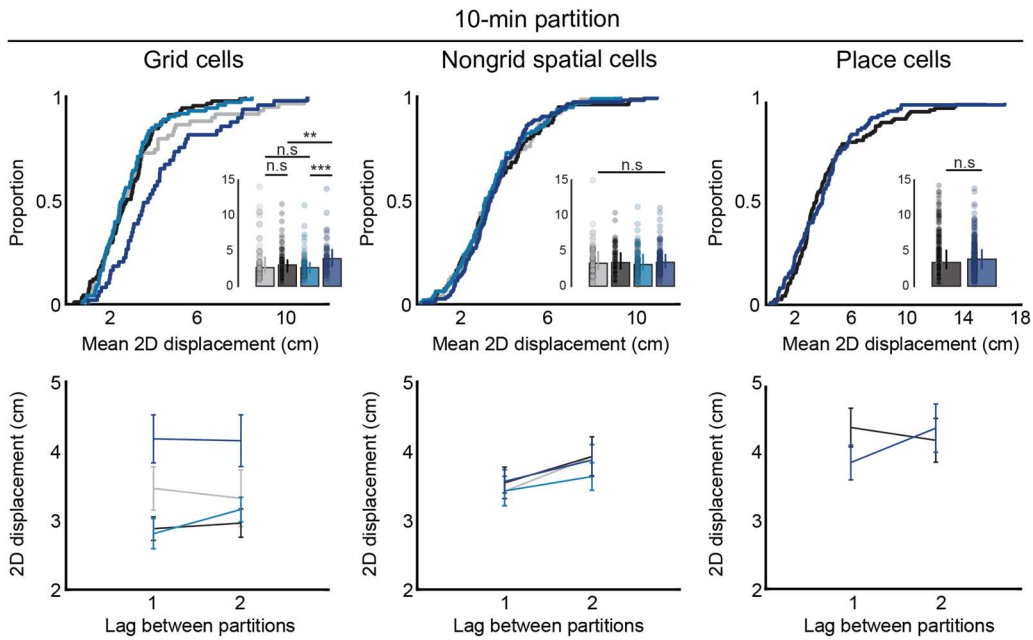


# Supplementary Figure 13. Page 2

**c**

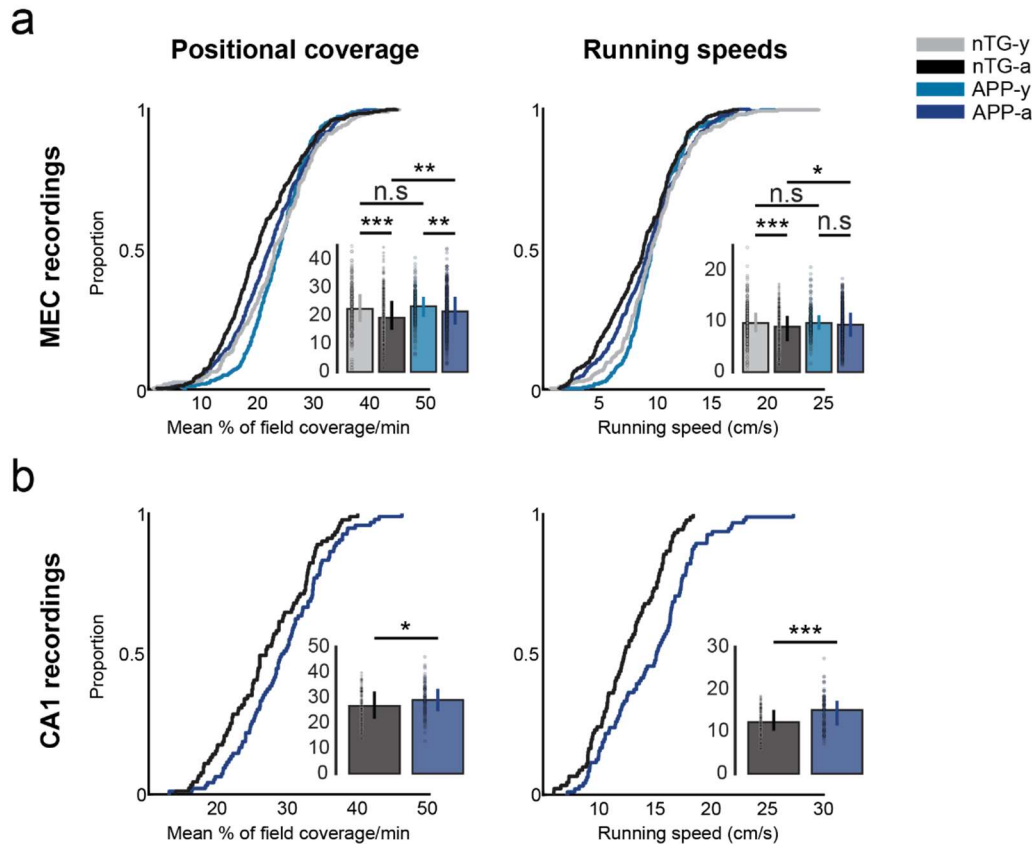


**d**



**Supplementary Figure 13. Reduced grid cell spatial stability in adult APP mice persists across different partition lengths. a** 3-minute partition analyses. Two-dimensional displacement of grid cells (nTG-y-nTG-a:  $P = 0.76$ ; nTG-y-APP-y:  $P = 0.76$ ; APP-y-APP-a:  $P = 9.1 \times 10^{-4}$ ; nTG-a-APP-a:  $P = 3.4 \times 10^{-4}$ ), non-grid spatially-tuned cells (nTG-y-nTG-a:  $P = 0.74$ ; nTG-y-APP-y:  $P = 0.24$ ; APP-y-APP-a:  $P = 0.19$ ; nTG-a-APP-a:  $P = 0.87$ ), and place cells (nTG-a-APP-a:  $P = 0.35$ ) between groups (grid cells,  $n = 61$  nTG-y; 95 nTG-a; 73 APP-y; 49 APP-a; non-grid spatially-tuned cells, 77 nTG-y; 80 nTG-a; 98 APP-y; 115 APP-a; place cells, 243 nTG-a; 247 APP-a). (bottom-row) Two-dimensional displacement of grid cells, non-grid spatially-tuned cells and place cells as a function of lags between partitions. Dots indicate mean values and error bars indicate SEM. **b-d** Five-minute (grid cell: nTG-y-nTG-a:  $P = 0.35$ ; nTG-y-APP-y:  $P = 0.98$ ; APP-y-APP-a:  $P = 0.0019$ ; nTG-a-APP-a:  $P = 0.01$ ; non-grid cell: nTG-y-nTG-a:  $P = 0.92$ ; nTG-y-APP-y:  $P = 0.35$ ; APP-y-APP-a:  $P = 0.65$ ; nTG-a-APP-a:  $P = 0.58$ ; place cell: nTG-a-APP-a:  $P = 0.67$ ), 6-minute (grid cell: nTG-y vs. nTG-a:  $P = 0.39$ ; nTG-y vs. APP-y:  $P = 1$ ; APP-y vs. APP-a:  $P = 6.0 \times 10^{-5}$ ; nTG-a vs. APP-a:  $P = 0.0025$ ; non-grid cell: nTG-y vs. nTG-a:  $P = 0.31$ ; nTG-y vs. APP-y:  $P = 0.96$ ; APP-y vs. APP-a:  $P = 0.41$ ; nTG-a vs. APP-a:  $P = 0.67$ ; place cell: nTG-a vs. APP-a:  $P = 0.47$ ) and 10-minute (grid cell: nTG-y vs. nTG-a:  $P = 0.93$ ; nTG-y vs. APP-y:  $P = 0.53$ ; APP-y vs. APP-a:  $P = 8.4 \times 10^{-4}$ ; nTG-a vs. APP-a:  $P = 0.0026$ ; non-grid cell: nTG-y vs. nTG-a:  $P = 0.92$ ; nTG-y vs. APP-y:  $P = 0.65$ ; APP-y vs. APP-a:  $P = 0.35$ ; nTG-a vs. APP-a:  $P = 0.79$ ; place cell: nTG-a vs. APP-a:  $P = 0.61$ ) partitions between groups. Wilcoxon rank sum tests (two-sided) corrected for multiple comparisons using Bonferroni-Holm's correction were applied to Supplementary Fig. 13 **a-d**. Data in bar graphs are presented as median values  $\pm$  25<sup>th</sup> and 75<sup>th</sup> percentiles; \*\* $P < 0.01$ , \*\*\* $P < 0.001$ ; n.s, not significant. Source data are provided as a Source Data file.

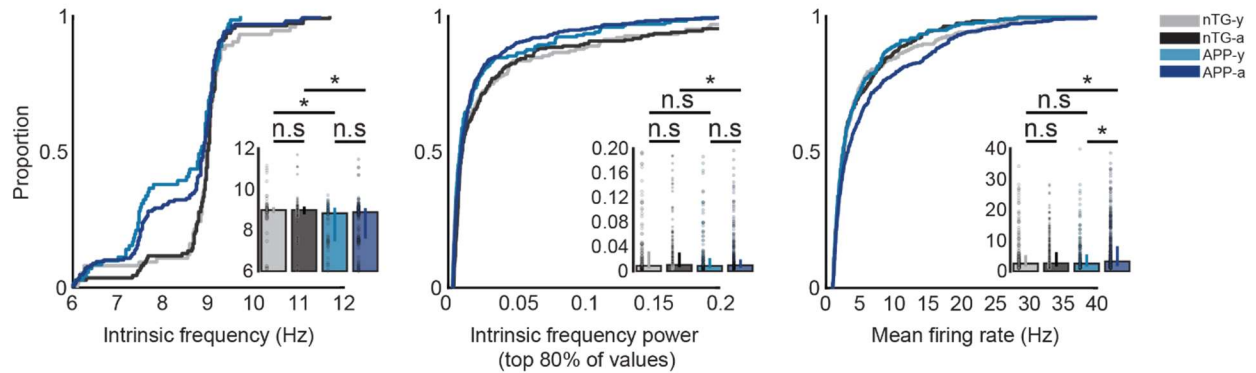
## Supplementary Figure 14



**Supplementary Figure 14. Positional coverage and running speeds across groups for MEC and CA1 recordings.** **a** Mean % of the environment covered per minute (nTG-y vs. nTG-a:  $P = 3.3 \times 10^{-5}$ ; nTG-y vs. APP-y:  $P = 0.51$ ; APP-y vs. APP-a:  $P = 0.0053$ ; nTG-a vs. APP-a:  $P = 0.0041$ ), and average running speed (nTG-y vs. nTG-a:  $P = 9.1 \times 10^{-4}$ ; nTG-y vs. APP-y:  $P = 0.91$ ; APP-y vs. APP-a:  $P = 0.099$ ; nTG-a vs. APP-a:  $P = 0.047$ ) between groups (recording session,  $n = 270$  for nTG-y;  $n = 302$  for nTG-a;  $n = 253$  for APP-y;  $n = 492$  for APP-a) for MEC recordings. **b** Mean % of the environment covered per minute (nTG-a vs. APP-a:  $P = 0.017$ ), and average running speed (nTG-a vs. APP-a:  $P = 1.4 \times 10^{-4}$ ) between groups (recording session,  $n = 91$  for nTG-a;  $n = 96$  for APP-a) for CA1 recordings. nTG-y, non-transgenic young; nTG-a, non-transgenic adult; APP-y, APP young; APP-a, APP adult. Wilcoxon rank sum tests (two-sided) corrected for multiple comparisons using a Bonferroni-Holm correction were applied to analyze the data in Supplementary Fig. 14 **a-b**. Data in bar graphs are presented as median values  $\pm 25^{\text{th}}$

and 75<sup>th</sup> percentiles; \* $P < 0.05$ , \*\* $P < 0.01$ , \*\*\* $P < 0.001$ ; n.s, not significant. Source data are provided as a Source Data file.

## Supplementary Figure 15



**Supplementary Figure 15. Interneuron firing properties.** Intrinsic frequency (nTG-y vs. nTG-a:  $P = 0.99$ ; nTG-y vs. APP-y:  $P = 0.038$ ; APP-y vs. APP-a:  $P = 0.49$ ; nTG-a vs. APP-a:  $P = 0.023$ ), intrinsic frequency power (for the top 80% of values) (nTG-y vs. nTG-a:  $P = 0.056$ ; nTG-y vs. APP-y:  $P = 0.58$ ; APP-y vs. APP-a:  $P = 0.38$ ; nTG-a vs. APP-a:  $P = 0.034$ ), and mean firing rate (nTG-y vs. nTG-a:  $P = 0.95$ ; nTG-y vs. APP-y:  $P = 0.82$ ; APP-y vs. APP-a:  $P = 0.034$ ; nTG-a vs. APP-a:  $P = 0.028$ ) of interneurons between groups (cells, intrinsic frequency:  $n = 74$  for nTG-y;  $n = 111$  for nTG-a;  $n = 71$  for APP-y;  $n = 167$  for APP-a; intrinsic frequency power:  $n = 164$  for nTG-y;  $n = 218$  for nTG-a;  $n = 170$  for APP-y;  $n = 350$  for APP-a; mean firing rate:  $n = 205$  for nTG-y;  $n = 272$  for nTG-a;  $n = 213$  for APP-y;  $n = 437$  for APP-a). nTG-y, non-transgenic young; nTG-a, non-transgenic adult; APP-y, APP young; APP-a, APP adult. Wilcoxon rank sum tests (two-sided) corrected for multiple comparisons using a Bonferroni-Holm correction were applied to analyze the data in Supplementary Fig. 15. Data in bar graphs are presented as median values  $\pm$  25<sup>th</sup> and 75<sup>th</sup> percentiles; \* $P < 0.05$ ; n.s, not significant. Source data are provided as a Source Data file.

## Supplementary Figure 16

**Two-way ANOVA: Intrinsic frequency (Hz)**

Source	Sum Square	df	MS	F	p
Age	0.58	1	0.58	0.60	= 0.44
Genotype	20.42	1	20.42	21.23	= 0.0000054
Interaction	0.61	1	0.61	0.63	= 0.43
Error	403.04	419	0.96		
Total	423.90	422			

**Two-way ANOVA: Intrinsic frequency power (top 80% of values)**

Source	Sum Square	df	MS	F	p
Age	$9 \times 10^{-5}$	1	$9 \times 10^{-5}$	0.03	= 0.85
Genotype	$3.74 \times 10^{-2}$	1	$3.74 \times 10^{-2}$	14.72	= 0.0001
Interaction	$5.80 \times 10^{-4}$	1	$5.80 \times 10^{-4}$	0.23	= 0.63
Error	2.28	897	$2.54 \times 10^{-3}$		
Total	2.33	900			

**Two-way ANOVA: Mean firing rate (Hz)**

Source	Sum Square	df	MS	F	p
Age	147.70	1	147.70	3.06	= 0.081
Genotype	63.60	1	63.60	1.32	= 0.25
Interaction	326.10	1	326.10	6.75	= 0.0095
Error	$5.42 \times 10^4$	1123	48.34		
Total	$5.50 \times 10^4$	1126			

**Supplementary Figure 16. Slower intrinsic theta rhythmicity and reduced theta power in APP mice.** Two-way unbalanced ANOVAs compare the effects of age, genotype, and interaction on the intrinsic frequency, intrinsic frequency power (for the top 80% of values), and mean firing rates of interneurons between groups.

df = degrees of freedom, MS = mean square.

## Supplementary Figure 17

**Two-way ANOVA: Grid cell-interneuron synchrony**

Source	Sum Square	df	MS	F	p
Age	2.38	1	2.38	0.27	= 0.60
Genotype	173.58	1	173.58	19.8	= 0.000013
Interaction	25.16	1	25.17	2.87	= 0.09
Error	2270.69	259	8.77		
Total	2520.39	262			

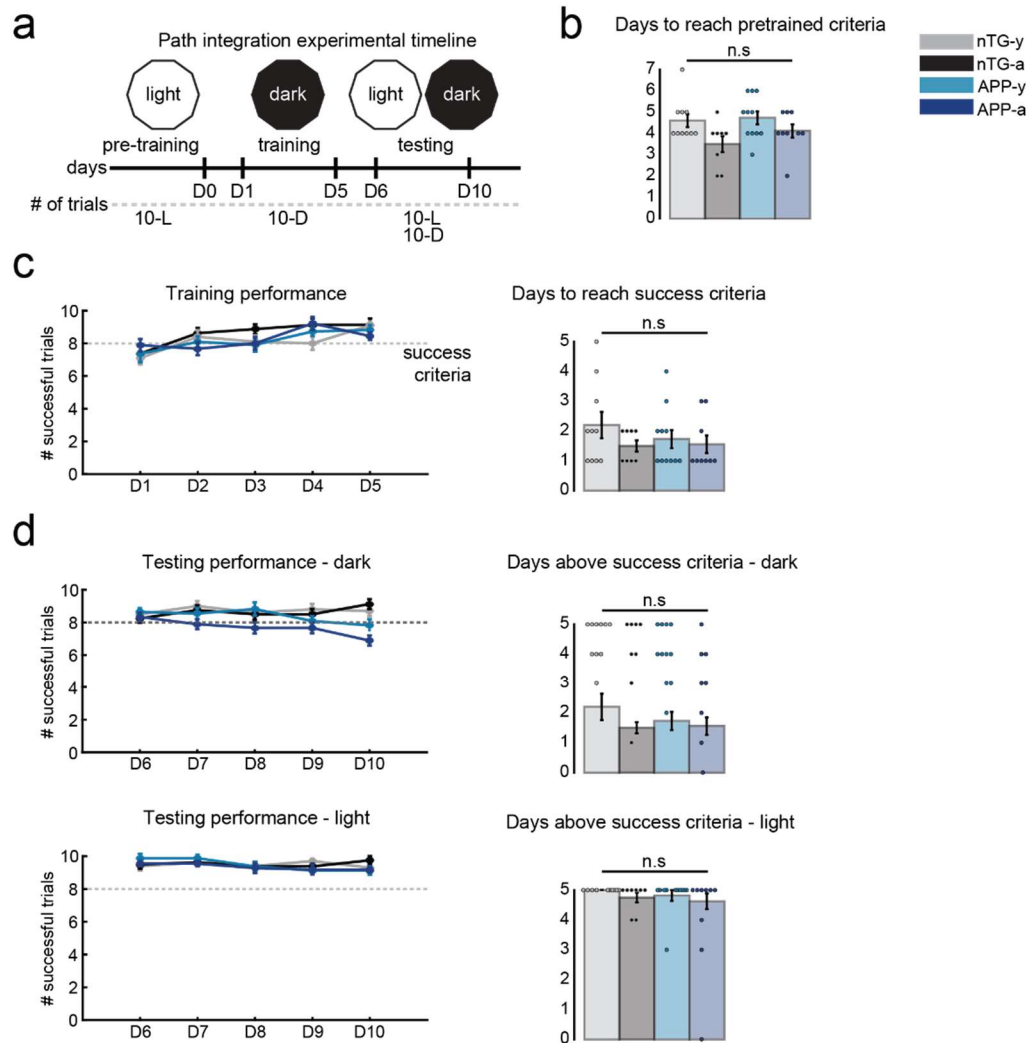
**Two-way ANOVA: Grid cell-head direction cell synchrony**

Source	Sum Square	df	MS	F	p
Age	37.53	1	37.53	7.07	= 0.0083
Genotype	34.11	1	34.11	6.43	= 0.0119
Interaction	16.08	1	16.08	3.03	= 0.08
Error	1289.16	243	5.31		
Total	1356.97	246			

**Supplementary Figure 17. Grid cell synchrony with interneurons and head-direction cells are both impaired in APP mice.** Two-way unbalanced ANOVAs compare the effects of age, genotype, and interaction on the mean co-activity within a 25 ms time window for grid cell-interneuron pairs, and grid cell-head direction cell pairs.

df = degrees of freedom, MS = mean square.

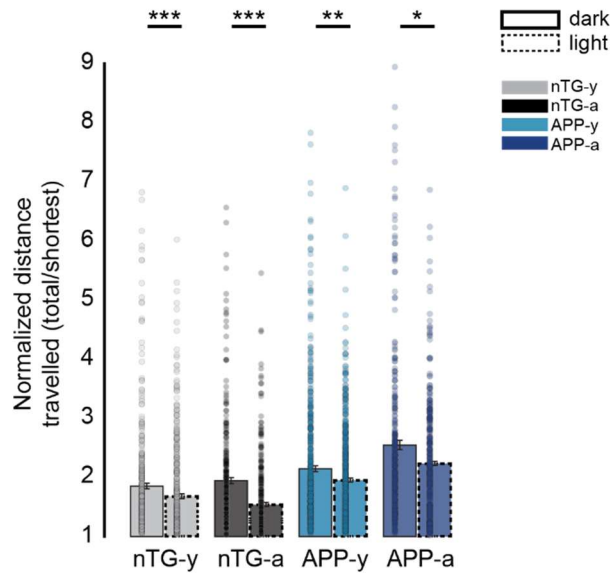
## Supplementary Figure 18



**Supplementary Figure 18. Experimental timeline for the path integration task and mouse performance across days.** **a** Experimental timeline for the food-foraging task. Days are indicated as D0, D1, etc. The number of trials that each mouse performed are indicated as 10-L (i.e., 10 light trials) and 10-D (i.e., 10 dark trials). **b** The number of days that it took mice in each group to achieve the success criteria in the pre-training phase (8/10 successful trials) (nTG-y-nTG-a:  $P = 0.079$ ; nTG-y-APP-y:  $P = 0.65$ ; APP-y-APP-a:  $P = 0.24$ ; nTG-a-APP-a:  $P = 0.28$ ) between groups (mice,  $n = 10$  for nTG-y;  $n = 8$  for nTG-a;  $n = 11$  for APP-y;  $n = 9$  for APP-a). **c** (Left) The number of successful trials achieved by mice across 5 days of training. (Right) The number of days within this training period that mice took to reach the success criteria (nTG-y-nTG-a:  $P = 0.42$ ; nTG-y-APP-y:  $P = 0.45$ ; APP-y-APP-a:  $P = 0.70$ ; nTG-a-APP-a:  $P = 0.84$ ) across groups (same sample

sizes as in **a**). **d** (Top-Left) Same as (**c**) but across 5 days of testing in dark conditions. (Top-Right) The number of days within this testing period that mice performed at or above the success criteria (nTG-y-nTG-a:  $P = 0.60$ ; nTG-y-APP-y:  $P = 0.24$ ; APP-y-APP-a:  $P = 0.11$ ; nTG-a-APP-a:  $P = 0.11$ ) across groups (same sample sizes as in **a**). (Bottom-Left) Same as (**c**) but across 5 days of testing in light conditions. (Bottom-Right) The number of days within this testing period that mice performed at or above the success criteria (nTG-y-nTG-a:  $P = 0.37$ ; nTG-y-APP-y:  $P = 0.39$ ; APP-y-APP-a:  $P = 0.21$ ; nTG-a-APP-a:  $P = 0.59$ ) between groups (same sample sizes as in **a**). nTG-y, non-transgenic young; nTG-a, non-transgenic adult; APP-y, APP young; APP-a, APP adult. Wilcoxon rank sum tests (two-sided) corrected for multiple comparisons using a Bonferroni-Holm correction were applied to analyze the data in Supplementary Fig. 18 **b-d**. Data in line graphs are presented as mean values  $\pm$  SEM. Data in bar graphs are presented as mean values  $\pm$  SEM; n.s, not significant. Source data are provided as a Source Data file.

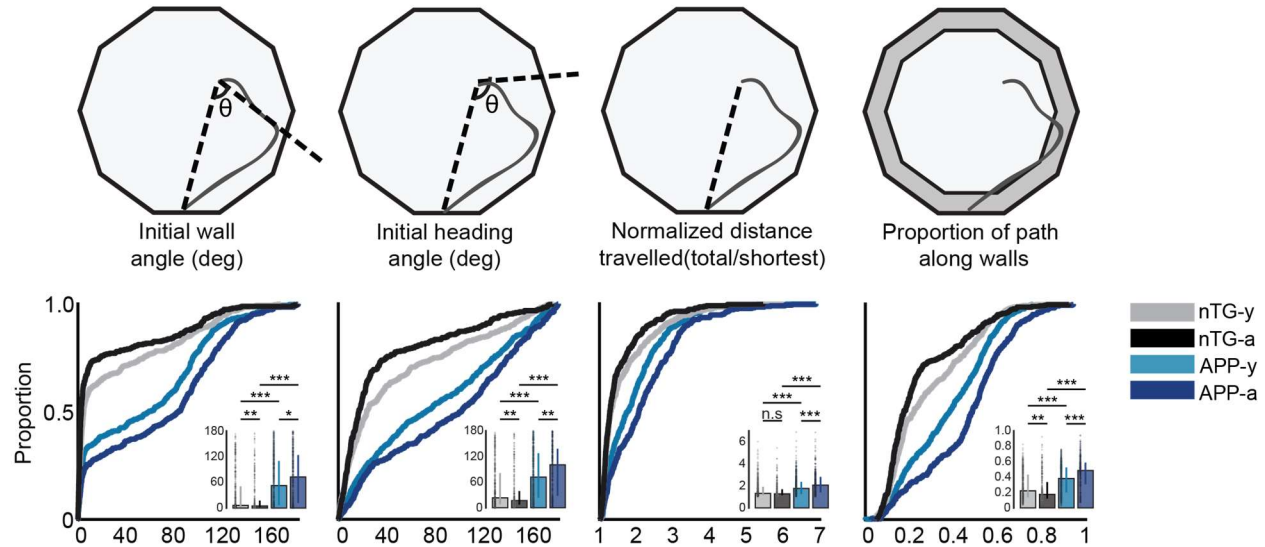
## Supplementary Figure 19



### Supplementary Figure 19. Overall navigation ability improves in light trials for all mice.

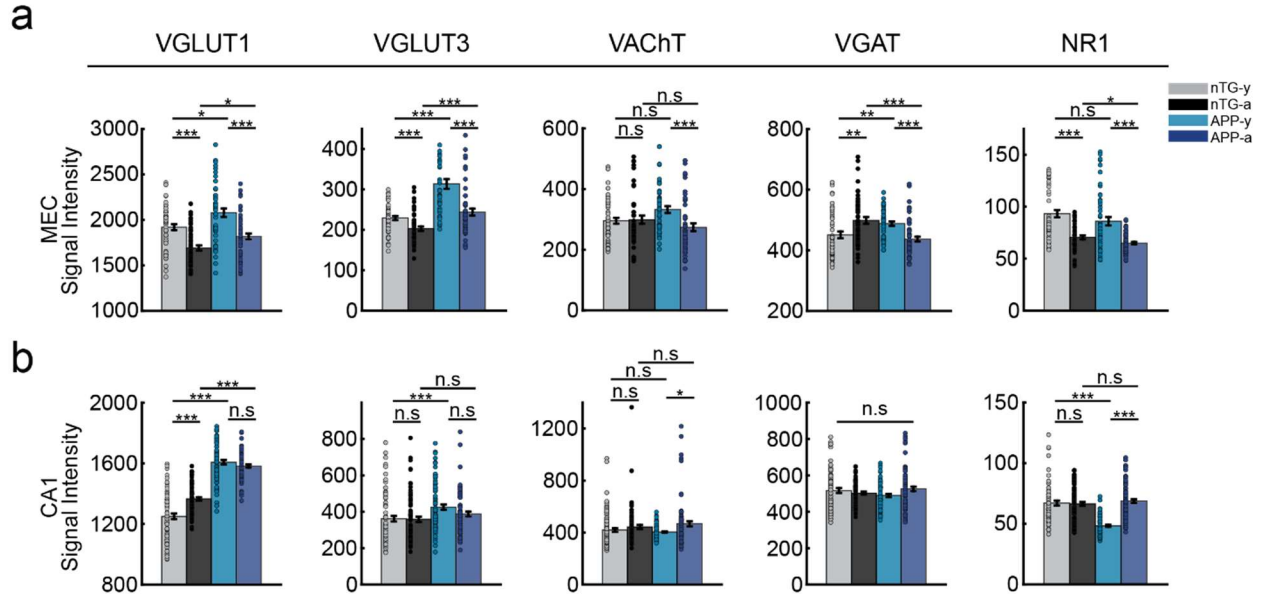
Normalized distance travelled in dark (solid lines) versus light (dashed lines) trials. (nTG-y:  $P = 6.9 \times 10^{-9}$ ; nTG-a:  $P = 1.4 \times 10^{-21}$ ; APP-y:  $P = 0.0084$ ; APP-a:  $P = 0.017$ ) (dark behavior trials,  $n = 377$  for nTG-y;  $n = 307$  for nTG-a;  $n = 500$  for APP-y;  $n = 311$  for APP-a; light behavior trials,  $n = 426$  for nTG-y;  $n = 344$  for nTG-a;  $n = 538$  for APP-y;  $n = 330$  for APP-a). nTG-y, non-transgenic young; nTG-a, non-transgenic adult; APP-y, APP young; APP-a, APP adult. Wilcoxon rank sum tests (two-sided) were applied to analyze the data in Supplementary Fig. 19. Data are presented as mean values  $\pm$  SEM; \* $P < 0.05$ , \*\* $P < 0.01$ , \*\*\* $P < 0.001$ ; Source data are provided as a Source Data file.

## Supplementary Figure 20



**Supplementary Figure 20. APP mice have impaired path integration ability in light conditions.** The initial wall angle (nTG-y vs. nTG-a:  $P = 0.0075$ ; nTG-y vs. APP-y:  $P = 1.1 \times 10^{-18}$ ; APP-y vs. APP-a:  $P = 0.013$ ; nTG-a vs. APP-a:  $P = 1.5 \times 10^{-32}$ ), the initial heading angle (nTG-y vs. nTG-a:  $P = 0.0029$ ; nTG-y vs. APP-y:  $P = 3.4 \times 10^{-17}$ ; APP-y vs. APP-a:  $P = 0.0044$ ; nTG-a vs. APP-a:  $P = 1.2 \times 10^{-33}$ ), the normalized distance travelled (nTG-y vs. nTG-a:  $P = 0.053$ ; nTG-y vs. APP-y:  $P = 7.7 \times 10^{-12}$ ; APP-y vs. APP-a:  $P = 6.3 \times 10^{-5}$ ; nTG-a vs. APP-a:  $P = 1.2 \times 10^{-26}$ ), and the proportion of the return path spent along the periphery (nTG-y vs. nTG-a:  $P = 0.0015$ ; nTG-y vs. APP-y:  $P = 8.2 \times 10^{-13}$ ; APP-y vs. APP-a:  $P = 9.5 \times 10^{-9}$ ; nTG-a vs. APP-a:  $P = 9.3 \times 10^{-35}$ ) between groups (behavior trials,  $n = 426$  for nTG-y;  $n = 344$  for nTG-a;  $n = 538$  for APP-y;  $n = 330$  for APP-a). nTG-y, non-transgenic young; nTG-a, non-transgenic adult; APP-y, APP young; APP-a, APP adult. Wilcoxon rank sum tests (two-sided) corrected for multiple comparisons using a Bonferroni-Holm correction were applied to analyze the data in Supplementary Fig. 20. Data in bar graphs are presented as median values  $\pm$  25<sup>th</sup> and 75<sup>th</sup> percentiles; \* $P < 0.05$ , \*\* $P < 0.01$ , \*\*\* $P < 0.001$ ; n.s., not significant. Source data are provided as a Source Data file.

## Supplementary Figure 21



**Supplementary Figure 21. Immunoautoradiographic labelling of synaptic markers in MEC and CA1. a** Signal intensity of VGLUT1 (nTG-y-nTG-a:  $P = 1.3 \times 10^{-5}$ ; nTG-y-APP-y:  $P = 0.014$ ; APP-y-APP-a:  $P = 1.1 \times 10^{-4}$ ; nTG-a-APP-a:  $P = 0.014$ ;  $n = 52$  nTG-y; 53 nTG-a; 48 APP-y; 55 APP-a), VGLUT3 (nTG-y-nTG-a:  $P = 1.9 \times 10^{-4}$ ; nTG-y-APP-y:  $P = 1.5 \times 10^{-8}$ ; APP-y-APP-a:  $P = 2.6 \times 10^{-6}$ ; nTG-a-APP-a:  $P = 2.3 \times 10^{-4}$ ;  $n = 52$  nTG-y; 50 nTG-a; 45 APP-y; 51 APP-a), VACHT (nTG-y-nTG-a:  $P = 0.87$ ; nTG-y-APP-y:  $P = 0.053$ ; APP-y-APP-a:  $P = 4.5 \times 10^{-4}$ ; nTG-a-APP-a:  $P = 0.051$ ;  $n = 47$  nTG-y; 45 nTG-a; 48 APP-y; 52 APP-a), VGAT (nTG-y-nTG-a:  $P = 0.0037$ ; nTG-y-APP-y:  $P = 0.0027$ ; APP-y-APP-a:  $P = 7.4 \times 10^{-6}$ ; nTG-a-APP-a:  $P = 2.1 \times 10^{-5}$ ;  $n = 49$  nTG-y; 50 nTG-a; 46 APP-y; 55 APP-a) and NR1 (nTG-y-nTG-a:  $P = 1.6 \times 10^{-5}$ ; nTG-y-APP-y:  $P = 0.063$ ; APP-y-APP-a:  $P = 2.7 \times 10^{-5}$ ; nTG-a-APP-a:  $P = 0.023$ ;  $n = 48$  nTG-y; 53 nTG-a; 51 APP-y; 58 APP-a) in the MEC. **b** Signal intensity of VGLUT1 (nTG-y-nTG-a:  $P = 4.6 \times 10^{-6}$ ; nTG-y-APP-y:  $P = 3.9 \times 10^{-21}$ ; APP-y-APP-a:  $P = 0.15$ ; nTG-a-APP-a:  $P = 4.5 \times 10^{-21}$ ;  $n = 79$  nTG-y; 80 nTG-a; 70 APP-y; 79 APP-a), VGLUT3 (nTG-y-nTG-a:  $P = 0.76$ ; nTG-y-APP-y:  $P = 5.7 \times 10^{-4}$ ; APP-y-APP-a:  $P = 0.066$ ; nTG-a-APP-a:  $P = 0.10$ ;  $n = 76$  nTG-y; 84 nTG-a; 81 APP-y; 77 APP-a), VACHT (nTG-y-nTG-a:  $P = 0.14$ ; nTG-y-APP-y:  $P = 0.30$ ; APP-y-APP-a:  $P = 0.039$ ; nTG-a-APP-a:  $P = 0.39$ ;  $n = 86$  nTG-y; 78 nTG-a; 82 APP-y; 87 APP-a) VGAT (nTG-y-nTG-a:  $P = 0.87$ ; nTG-y-APP-y:  $P = 0.33$ ; APP-y-APP-a:  $P = 0.074$ ; nTG-a-APP-a:  $P = 0.35$ ;  $n = 72$  nTG-

y; 69 nTG-a; 70 APP-y; 79 APP-a) and NR1 (NR1: nTG-y-nTG-a:  $P = 0.71$ ; nTG-y-APP-y:  $P = 2.1 \times 10^{-14}$ ; APP-y-APP-a:  $P = 9.4 \times 10^{-19}$ ; nTG-a-APP-a:  $P = 0.41$ ;  $n = 70$  nTG-y; 82 nTG-a; 72 APP-y; 85 APP-a) in CA1. Wilcoxon rank sum tests (two-sided) corrected for multiple comparisons using Bonferroni-Holm's correction were applied to Supplementary Fig. 21 **a-b**. Data are presented as mean values  $\pm$  SEM; \* $P < 0.05$ , \*\* $P < 0.01$ , \*\*\* $P < 0.001$ ; n.s, not significant. Source data are provided as a Source Data file.

# Supplementary Figure 22

a

## Linear mixed effects model predicting VGLUT3 expression in the MEC

### Model information

Number of observations : 198  
 Fixed effects coefficients : 3  
 Random effects coefficients : 48  
 Covariance parameters : 4

### Model fit statistics

AIC : 2071.4  
 BIC : 2094.4  
 Log Likelihood : -1028.7  
 Deviance : 2057.4

### Fixed effects coefficients (95% CIs):

Name	Estimate	Std. Error	tStat	DF	p	95% CI	
						LL	UL
Intercept	253.03	18.12	13.96	195	= 3.6e-31	217.29	288.77
Genotype	-60.5	21.78	-2.78	195	= 0.006	-103.45	-17.55
Age	48.23	21.96	2.2	195	= 0.0292	4.93	91.55

### Random effects covariance (95% CIs):

Subject(16 levels)	Estimate	95% CI	
		LL	UL
Intercept	39.48	25.95	60.05
* Genotype	< 0.001	NaN	NaN
* Age	22.15	19.98	24.56

Error	Estimate	95% CI	
		LL	UL
Residual	39.1	35.29	43.33

b

## Linear mixed effects model predicting VGLUT1 expression in CA1

### Model information

Number of observations : 308  
 Fixed effects coefficients : 3  
 Random effects coefficients : 48  
 Covariance parameters : 4

### Model fit statistics

AIC : 3687.8  
 BIC : 3713  
 Log Likelihood : -1836.9  
 Deviance : 3673.8

### Fixed effects coefficients (95% CIs):

Name	Estimate	Std. Error	tStat	DF	p	95% CI	
						LL	UL
Intercept	1590.7	21.47	74.09	305	= 4.8e-197	1548.5	1633
Genotype	-270.68	45.09	-6	305	= 5.5e-9	-359.41	-181.9
Age	-3.91	38.68	-0.1	305	= 0.92	-80.02	72.2

### Random effects covariance (95% CIs):

Subject(16 levels)	Estimate	95% CI	
		LL	UL
Intercept	39.6	17.22	91.03
* Genotype	96.99	30.2	311.5
* Age	61.3	9.05	415.14

Error	Estimate	95% CI	
		LL	UL
Residual	84.54	80.72	94.93

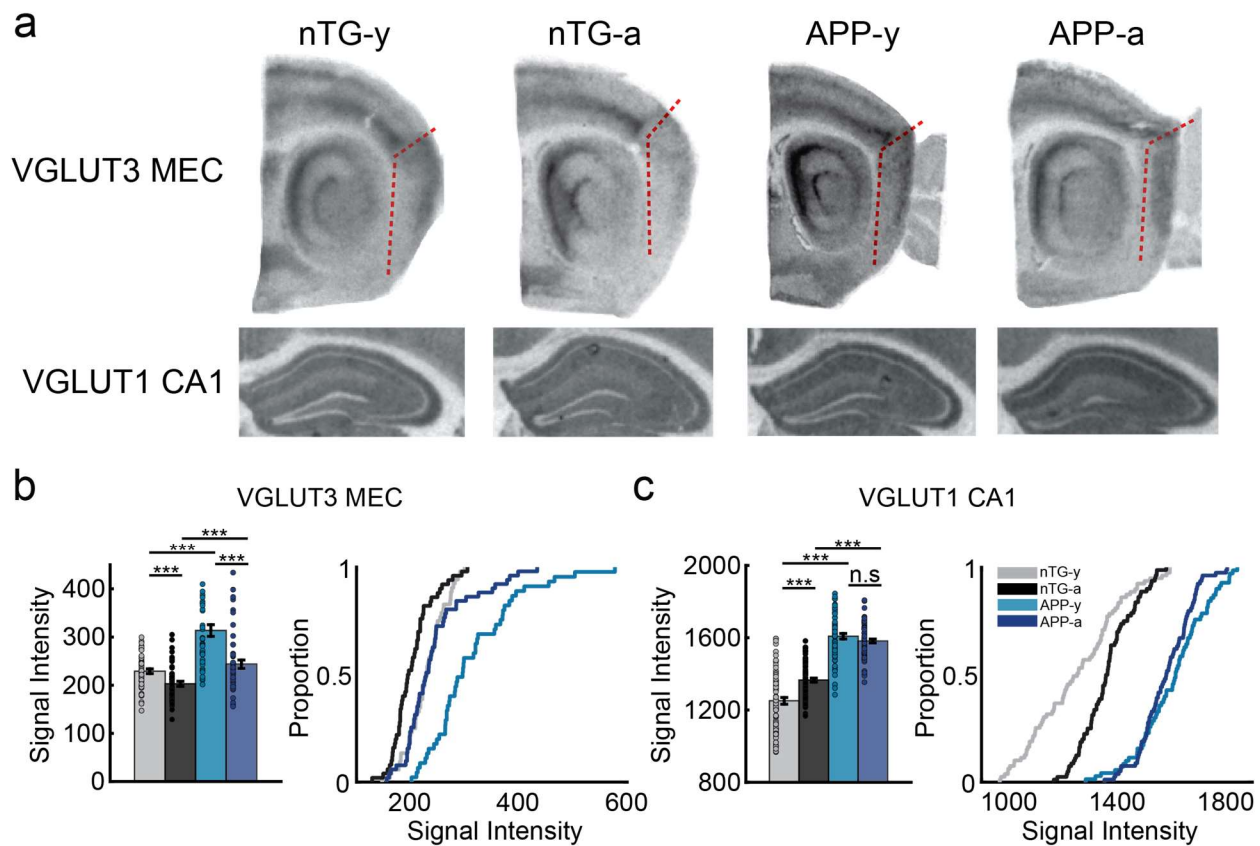
**Supplementary Figure 22. We used the fitlme function in MATLAB to perform linear mixed effects analyses on the relationship between the subjects' genotype (nTG and APP), age (young and adult) and expression of VGLUT3 and VGLUT1 levels in the MEC and CA1 respectively.** The fixed effects of the model comprised genotype and age (without interaction between the two). The random effects of the model comprised random intercepts by-subject, random slopes for the effects of genotype and age by-subject, and independence between the intercepts and slopes. P-values obtained in the model output were considered as the measurements for significance.

**a** Table shows the model information, statistics of fit, the fixed effects coefficients, and the random effects covariance parameters. In the fixed effects panel, the 'Intercept' refers to the aged APP experimental group; its estimate is the predicted mean VGLUT3 signal intensity. The estimates for genotype and age refer to the predicted slope change from the intercept. Std. Error refers to the standard error associated with the slope. T-values and P-values for the contribution of genotype and age are bolded. **b** Same as (**a**) but for levels of VGLUT1 in CA1.

tStat = T-value, CI = confidence interval, DF = degrees of freedom, LL = lower limit, UL = upper limit.

\* = independence between intercepts and slopes.

## Supplementary Figure 23



**Supplementary Figure 23. Pathological expression of MEC VGLUT3 levels and CA1 VGLUT1 levels in APP mice.** **a** Single slice examples of VGLUT3 and VGLUT1 expression in MEC and CA1 respectively. Darker signals indicate higher marker expression levels. **b** Signal intensity of VGLUT3 levels (nTG-y vs. nTG-a:  $P = 1.9 \times 10^{-4}$ ; nTG-y vs. APP-y:  $P = 1.5 \times 10^{-8}$ ; APP-y vs. APP-a:  $P = 2.6 \times 10^{-6}$ ; nTG-a vs. APP-a:  $P = 2.3 \times 10^{-4}$ ) in the MEC between groups (brain slice,  $n = 52$  for nTG-y;  $n = 50$  for nTG-a;  $n = 45$  for APP-y;  $n = 51$  for APP-a). **c** Signal intensity of VGLUT1 levels (nTG-y vs. nTG-a:  $P = 4.6 \times 10^{-6}$ ; nTG-y vs. APP-y:  $P = 3.9 \times 10^{-21}$ ; APP-y vs. APP-a:  $P = 0.15$ ; nTG-a vs. APP-a:  $P = 4.5 \times 10^{-21}$ ) in CA1 between groups (brain slice,  $n = 79$  for nTG-y;  $n = 80$  for nTG-a;  $n = 70$  for APP-y;  $n = 79$  for APP-a). nTG-y, non-transgenic young; nTG-a, non-transgenic adult; APP-y, APP young; APP-a, APP adult. Wilcoxon rank sum tests (two-sided) corrected for multiple comparisons using a Bonferroni-Holm correction were applied to analyze the data in Supplementary Fig. 23 **b-c**. Data in bar graphs are presented as mean

values  $\pm$  SEM; \* $P < 0.05$ , \*\* $P < 0.01$ , \*\*\* $P < 0.001$ ; n.s, not significant. Source data are provided as a Source Data file.

## Supplementary Figure 24

Two-way ANOVA: VGLUT3 signal in the MEC

Source	Sum Square (10 <sup>4</sup> )	df	MS(10 <sup>4</sup> )	F	p
Age	11.34	1	11.34	35.83	= 1e-8
Genotype	19.34	1	19.34	61.09	= 3.4e-13
Interaction	2.36	1	2.36	7.46	= 0.0069
Error	61.42	194	0.32		
Total	92.71	197			

Two-way ANOVA: VGLUT1 signal in CA1

Source	Sum Square (10 <sup>4</sup> )	df	MS(10 <sup>4</sup> )	F	p
Age	15.28	1	15.28	9.94	= 0.0018
Genotype	631.66	1	631.66	410.95	= 2.1e-58
Interaction	38.18	1	38.18	24.84	= 1e-6
Error	467.27	304	1.54		
Total	1150.26	307			

**Supplementary Figure 24. VGLUT3 levels in the MEC and VGLUT1 levels in the CA1 are both higher in APP mice.** Two-way unbalanced ANOVAs compare the effects of age, genotype, and interaction on VGLUT3 and VGLUT1 signal levels in the MEC and CA1 respectively.

df = degrees of freedom, MS = mean square.

## FORWARD TO CHAPTER 3

The data presented in Chapter 2 provide the first evidence that grid cells are disrupted during the early stages of pathology in a mouse model of early AD. Furthermore, these results support the viability of grid cell integrity and path integration deficits as early markers of AD. Given that grid cells are necessary for path integration in healthy animals, the logical interpretation is that a disrupted grid cell network causes early path integration impairments in J20 mice – and by extension, preclinical AD subjects or those at genetic risk of AD (*APOE-ε4* carriers). However, our data are correlational, and we did not directly show a causal link between grid cell coding and path integration performance. It could be that preclinical path integration deficits have nothing to do with grid cell disruption. Likewise, grid cell disruption might not result from impaired processing of self-motion.

In Chapter 3, to further substantiate a link between disrupted grid coding and path integration deficits in J20 mice, we investigated if disrupted early AD grid coding reflects increased noise across the network or a specific deficit in path integration, perhaps via an impairment in the integration of self-motion cues. We found that J20 grid cells were spatially unstable towards the center of the square arena but not near the borders, had qualitatively different spatial components that aligned parallel to the borders of the environment, and exhibited impaired integration of distance travelled via reduced theta phase precession. These results collectively suggest that early AD grid cell disruption reflects a preferential alignment to the external world and cause path integration impairments in preclinical individuals via reduced integration of self-motion cues.

## **Chapter 3: Grid cell disruption in a mouse model of early Alzheimer's disease reflects reduced integration of self-motion cues and increased influence of environmental geometry**

**Authors:** Johnson Ying<sup>1,2</sup>, Antonio Reboresda<sup>3,4</sup>, Motoharu Yoshida<sup>3,4,5</sup>, Mark P. Brandon<sup>1,2,\*</sup>

### **Affiliations:**

<sup>1</sup>Department of Psychiatry, Douglas Hospital Research Centre, McGill University, Montreal, QC, Canada.

<sup>2</sup>Integrated Program in Neuroscience, McGill University, Montreal, QC, Canada.

<sup>3</sup>German Center for Neurodegenerative Diseases (DZNE), Magdeburg 39120, Germany.

<sup>4</sup>Leibniz Institute for Neurobiology (LIN), Magdeburg 39120, Germany.

<sup>5</sup>Center for Behavioral Brain Sciences (CBBS), Magdeburg 39106, Germany.

\*Lead contact: [mark.brandon@mcgill.ca](mailto:mark.brandon@mcgill.ca)

## **Abstract**

Grid cell impairments and path integration deficits are sensitive markers of early Alzheimer's disease (AD). Converging evidence from human and rodent studies suggest that disrupted grid coding underlies path integration deficits in preclinical individuals. However, it still remains unclear if disrupted early AD grid coding reflects increased noise across the network or a specific deficit in path integration, perhaps via an impairment in the integration of self-motion cues. Here, we report in the J20 transgenic amyloid beta mouse model of early AD that grid cells were spatially unstable towards the center of the square arena but not near the borders, had qualitatively different spatial components that aligned parallel to the borders of the environment, and exhibited impaired integration of distance travelled via reduced theta phase precession. Our results suggest that disrupted early AD grid coding reflects reduced integration of self-motion cues but not environmental landmarks, providing further evidence that grid cell impairments underlie specific path integration deficits in preclinical individuals.

## Introduction

Grid cells in the medial entorhinal cortex (MEC) fire in multiple spatial locations to form a periodic hexagonal array that spans two-dimensional space (Fyhn et al., 2004; Hafting et al., 2005; Jacobs et al., 2013). This periodic code is implicated in path integration, a cognitive function involving the integration of self-motion cues to maintain one's sense of location relative to a starting point in space (Gil et al., 2018; McNaughton et al., 2006; Mittelstaedt & Mittelstaedt, 1980; Segen et al., 2022). Both grid cell and path integration impairments are sensitive markers of pathological decline during early AD in human subjects and mouse models of pathology (Bierbrauer et al., 2020; Coughlan et al., 2018; Kunz et al., 2015; Mucke et al., 2000; Segen et al., 2022; Ying et al., 2022).

These early grid impairments may result from disrupted processing of self-motion cues, which constitute necessary inputs that maintain grid representations in healthy animals (Buetfering et al., 2014; Campbell et al., 2018; Chen et al., 2019, 2016; Couey et al., 2013; Hafting et al., 2005; Kraus et al., 2015; Kropff et al., 2015; Miao et al., 2017; Pérez-Escobar et al., 2016; Sargolini et al., 2006; Winter, Clark, et al., 2015; Winter, Mehlman, et al., 2015). Yet, external landmarks also exert significant influences over grid coding, particularly in rectilinear environments where grid representations scale proportionally to manipulations along the borders (Barry et al., 2007). Furthermore, deformed grid hexagonal symmetry in asymmetrical enclosures such as trapezoids demonstrates the degree to which geometric landmarks compete with self-motion cues to generate grid firing (Krupic et al., 2015).

To distinguish if early AD grid cell impairments reflect increased noise across the network or a specific deficit in processing self-motion cues over external landmarks, we analyzed our *in vivo* electrophysiological dataset of MEC neurons recorded in the J20 transgenic amyloid beta

(A $\beta$ ) mouse model of early AD that expresses a mutant form of human amyloid precursor protein (APP) – referred to here as ‘APP mice’ (Mucke et al., 2000; Ying et al., 2022).

## Results

### Adult APP grid cells are spatially unstable in the center of the environment

We analyzed 4524 MEC neurons from 38 APP transgenic and 30 non-transgenic (nTG) littermates as they foraged for water droplets in a 75 cm square arena (*Summary of MEC recordings, Table S1; MEC Tetrode locations, Figure S1*) (Ying et al., 2022). Mice were recorded between the ages of 3-7 months, timepoints corresponding to the early stages of pathology prior to the expression of widespread A $\beta$  plaques (detailed pathology description in Materials and methods, *Experimental model and subject details*). Mice were categorized into two age groups: young mice between 3-4.5 months of age (APP-y and nTG-y) and aged mice between 4.5-7 months of age (APP-a and nTG-a). Cells with gridness scores (a measure of hexagonal spatial periodicity in the rate map) higher than the 99<sup>th</sup> percentile of a shuffled distribution (a gridness score above 0.54) were characterized as grid cells (Materials and methods, *Grid cell and head-direction cell selection*).

To quantify spatial stability of grid cells across the environment, we divided the spatial arena into “wall” or “center” regions. The wall length was selected to be 12 cm, corresponding to the body length of a mouse and approximately divides wall and center regions into equal surface areas (**Figure 1A**). Recordings were partitioned into two halves either by time (15 minutes each) or by the animal’s occupancy (Materials and methods, *Spatial stability analysis*). Both methods revealed greater center instability in APP-a grid cells, but wall stability was unchanged across groups (**Figures 1B-D**; n = 36, 64, 30 and 37 cells for nTG-y, nTG-a, APP-y, APP-a). We repeated our analysis in an unbiased manner by incrementally shifting the layer of spatial bins

corresponding to both wall and center regions (**Figure S2**). In both time-partitioned and occupancy-partitioned analyses, APP-a center stability was lower across multiple conditions. In contrast, wall stability generally remained unchanged across groups until more center spatial bins were included into the wall region (**Figures S2A and S2B**). Out of all groups, APP-a grid cells also had the most instances where stability was lower in the center versus the borders (**Figure S2C and S2D**). Greater instability towards the environmental center where the sparsity of external landmarks necessitates the use of path integration to maintain a stable grid code suggests that APP-a grid cells do not reliably process self-motion cues.

### **Adult APP grid cells exhibit fewer spatial Fourier spectral components**

Previously, we reported a disruption in APP-a grid cell hexagonal symmetry (Ying et al., 2022). However, it remains unclear if these disrupted patterns reflect increased random noise in the network or qualitatively different underlying spatial structures. To quantify structural differences of APP-a grid cells, we implemented a two-dimensional Fourier analysis to decompose a cell's spatial firing rate map into its basic spatial components (Krupic et al., 2012) (Materials and methods, *Generation of Fourier spectrums*). Grid cells typically had three components in the Fourier spectrum which could be visualized as images of spatial axes facing specific orientations offset by  $60^\circ$ , such that the sum of all component images produced the firing rate map (**Figure 2A**). Similar to prior findings, grid cell Fourier components had distinct wavelengths (spacing between axes) where modules scaled by multiples ranging from 1.34 to 1.59 in all groups (**Figure S3**) (Barry et al., 2007; Krupic et al., 2012; H. Stensola et al., 2012). To discount the inherent biases of grid cell selection criteria, we also applied the Fourier analysis to all recorded MEC cells. Most non-grid MEC cells typically had two Fourier components and adopted a quadrant-like arrangement of spatial axes with angular offsets being multiples of  $90^\circ$  (**Figure 2A**;  $n = 768, 997$ ,

720 and 1318 cells for nTG-y, nTG-a, APP-y, APP-a). We computed the polar autocorrelations of all recorded MEC cells by circularly shifting each cell's polar representation by  $360^\circ$  and found a noticeable decrease in  $60^\circ$  modulation but an increase in  $90^\circ$  modulation for APP-a mice (**Figure 2B**). These results suggest that APP-a spatial axes at the population level were less hexagonal and more quadrant-like.

Further quantification of Fourier component count revealed that APP-a mice had less 3-component grid cells. Grid cells in nTG-y, nTG-a and APP-y mice generally had three significant Fourier components, while grid cells in APP-a mice had a similar number of cells with two or three components (**Figure 2C**). Most non-grid MEC cells had two significant Fourier components (**Figure 2C**). There was a higher percentage of 3-component grid cells than 3-component MEC cells in all groups except for APP-a mice (**Figure 2D**; nTG-y:  $p < 0.001$ , nTG-a:  $p = 0.024$ , APP-y:  $p = 0.01$ , APP-a:  $p = 0.14$ ). On the other hand, there was a higher percentage of 2-component MEC cells than 2-component grid cells in nTG-y and APP-y mice, but not in nTG-a and APP-a mice (**Figure 2D**; nTG-y:  $p = 0.005$ , nTG-a:  $p = 0.20$ , APP-y:  $p = 0.03$ , APP-a:  $p = 0.93$ ). These results suggest that only APP-a mice had both a larger percentage of 2-component grid cells and a smaller percentage of 3-component grid cells.

To determine the type of spatial alignment adopted by these 2- and 3-component cells, we computed the angular difference of neighboring Fourier components. Angular offsets in grid cell neighboring components were mostly  $60^\circ$  (and occasionally  $90^\circ$ ) in nTG-y, nTG-a, and APP-y mice, but we observed similar percentages between  $60^\circ$  and  $90^\circ$  offsets in APP-a mice (**Figures 2E and 2F**;  $60^\circ \pm 10^\circ$ : nTG-y: 40%, nTG-a: 43%, APP-y: 40%, APP-a: 20%;  $90^\circ \pm 10^\circ$ : nTG-y: 11%, nTG-a: 12%, APP-y: 16%, APP-a: 22%). Furthermore, the ratio of  $60^\circ$  to  $90^\circ$  was substantially reduced in APP-a grid cells (**Figure 2E**;  $(60^\circ \pm 10^\circ)/(90^\circ \pm 10^\circ)$ : nTG-y: 3.62 nTG-a:

3.61 APP-y: 2.48 APP-a: 0.91). Compared to chance level (the average of observed percentages across all groups), only APP-a mice had significantly less instances of 60° but more of 90° (**Figures 2E and 2F**; APP-a vs. 60° chance:  $p = 1.13 \times 10^{-7}$ ; APP-a vs. 90° chance:  $p = 9.98 \times 10^{-4}$ ). These results suggest that APP-a grid cell axes deviate from a 3-component hexagonal alignment and more strongly adopt a 2-component quadrant-like alignment. Angular differences in the neighboring components of all MEC cells were predominantly multiples of 90° in all groups (**Figure 2E**). Relative to other groups, APP-a MEC cells had a ~60% decrease in 60° angular offsets and a ~15% increase in 90° angular offsets (**Figure 2F**; 60°±10°: nTG-y: 8.7%, nTG-a: 8.7%, APP-y: 8.7%, APP-a: 3.5%; 90°±10°: nTG-y: 25.5%, nTG-a: 24.9%, APP-y: 24.9%, APP-a: 28.6%).

#### **Adult APP grid cell spatial axes align parallel to environmental borders**

Reduced spatial stability towards the arena's center but not near the borders suggests that APP-a grid cells remained anchored to the environment despite a potential impairment of self-motion cue integration. To quantify this anchoring, we analyzed how hexagonal and quadrant-like spatial codes aligned to the environment's geometry. Most 2-component and 3-component cells adopted one of three alignment profiles (**Figure 3A**). Consistent with previous reports, many 3-component cells were either 30° or 60° hexagonally offset from the east wall (**Figure 3A**) (Krupic et al., 2012; H. Stensola et al., 2012; T. Stensola et al., 2015). On the other hand, most 2-component cells were aligned parallel to the borders at multiples of 90° (**Figure 3A**). APP-a mice had ~8% more MEC cells that adopted this quadrant-like alignment profile and 5-6% less cells that adopted hexagonal alignment profiles (**Figure 3A**; quadrant-like cells:  $p = 5.47 \times 10^{-10}$ , hexagonal cells:  $p = 4 \times 10^{-8}$ ).

Prior to visualizing the spatial alignment of grid cells, we considered the possibility that many 1- or 2-component grid cells may have been falsely classified 3-component grid cells as a result of Fourier components not being properly identified in the Fourier spectrum due to relaxed image detection parameters. To control for this possibility, we increased image detection thresholds to obtain an additional 29% (4/14 cells), 54% (14/26 cells), 46% (6/13 cells) and 33% (9/27 cells) 3-component grid cells from 1- and 2-component grid cells in nTG-y, nTG-a, APP-y, and APP-a mice, respectively (Materials and methods; **Figure S4**). From this corrected data set, we observed that all groups had 30° and 60° 3-component grid cells, or 90° 2-component grid cells (**Figure 3B**). Specifically, we found 28% (10/36 cells), 19% (12/64 cells), 23% (7/30 cells), and 46% (17/37 cells) 1- and 2-component grid cells aligned parallel to the borders in nTG-y, nTG-a, APP-y, and APP-a mice, respectively. APP-a mice had a greater percentage of 1- and 2-component grid cells by ~20-25% than other groups (**Figure 3B**; **Table S2**;  $p = 0.01$ ). Polar autocorrelations revealed that ~75% of grid cells were modulated at 60° intervals in nTG-y, nTG-a and APP-y mice, whereas ~25% of cells were modulated at 90° intervals (**Figures 3C and S5**). In contrast, APP-a grid cells were roughly equally split between 60° and 90° modulation (**Figure 3C**). Notably, 3-component grid cells had higher gridness scores than their 1- and 2-component counterparts in all groups (**Figure 3C**). These results demonstrate that our previously reported finding of disrupted grid cell hexagonal symmetry in APP-a mice is not due to increased random noise, but rather caused by a higher concentration of firing aligned parallel to the borders (Ying et al., 2022). We confirmed that our results are not artifacts caused by the parameters of our correction threshold to retrieve 3-component grid cells or the square dimensionality of rate map images (**Table S3 and Figure S6**).

## **Adult APP grid cells exhibit reduced theta modulation and positional coding via theta phase precession**

Given the importance of theta rhythmicity for grid cell spatial coding (Brandon et al., 2011; Koenig et al., 2011) and the proposed link between entorhinal or hippocampal theta rhythms and various forms of self-motion including running speed, positive acceleration and vestibular inputs (Hafting et al., 2008; Jacob et al., 2014; Jeewajee et al., 2008; Kropff et al., 2021; Maurer et al., 2005; O'Keefe & Recce, 1993; Ravassard et al., 2013; Skaggs et al., 1996; Terrazas et al., 2005; Winter, Clark, et al., 2015), we examined whether intrinsic theta rhythmicity of spiking was reduced in APP-a grid cells. Visualization of the spike-time autocorrelations of grid cells revealed weaker overall theta modulation than other groups (**Figure 4A**). Visualization of the power spectrums of the spike-time autocorrelations yielded a similar conclusion. APP-a grid cells showed weaker theta modulation around 8-10 Hz compared to other groups (**Figure 4B**). Next, we quantified the percentages of theta-modulated grid cells from the power spectrums of the spike-time autocorrelations (Materials and methods, *Theta modulation analyses*). There were 21-31% less theta-modulated APP-a grid cells than other groups ( $p = 0.009$ ) (**Figure 4C**; nTG-y: 69%, nTG-a: 77%, APP-y: 67%, APP-a: 46%). We repeated our quantifications in an unbiased manner for a wide range of temporal bin sizes between 1-10 ms and observed a consistent ~21-31% reduction in theta-modulated APP-a grid cells than other groups (**Figure 4D**).

A potential consequence of non-theta-modulated grid cells is their inability to encode distance travelled via a temporal code known as theta phase precession. As the animal travels across a firing field, a theta-modulated grid cell spikes at progressively earlier phases of theta oscillations in the local field potential (Hafting et al., 2008; O'Keefe & Recce, 1993). Oscillatory interference and continuous attractor network models suggest that theta phase precession

properties could allow grid cells to integrate spatial displacement on the basis of self-motion while planning future paths as part of a path integration system (Burgess, 2008; Burgess et al., 2007; Navratilova et al., 2012). To examine theta phase precession of grid cells across groups, we computed the strength of correlation between distance travelled across a field and spike theta phase, and observed an impairment in APP-a mice (**Figure 4E**). If theta modulation is a requirement for theta phase precession, then APP-a grid cells would logically exhibit less phase precession than other groups. Indeed, further quantification revealed that there were 28-35% less phase-precessing APP-a grid cells than other groups ( $p = 0.0022$ ) (**Figure 4F**; nTG-y: 50%, nTG-a: 50%, APP-y: 57%, APP-a: 22%). Together, these results suggest that APP-a grid cells may not reliably integrate self-motion via precisely-timed theta-related mechanisms.

## **Discussion**

Our results suggest that early grid cell disruption in the J20 mouse model of amyloidopathy reflects reduced integration of self-motion cues and increased influence of environmental geometry. Reduced spatial stability towards the center but not near the borders suggests that grid cell impairments predominantly arise from disrupted processing of self-motion. In parallel, reduced theta modulation and theta phase precession suggests that APP-a grid cells could not properly integrate self-motion cues or accurately encode positional information within theta cycles in the local field potential. In contrast, APP-a grid cells appeared to be more strongly influenced by environmental geometry. A Fourier spectral analysis revealed that disrupted grid spatial periodicity in APP-a mice was not as random as previously assumed (Ying et al., 2022), but directly explained by the degree of spiking aligned parallel to the borders. Grid cell patterns are hypothesized to arise from intrinsic network activity and then anchor to the outside world via external landmarks (Buetfering et al., 2014; Couey et al., 2013; Gardner et al., 2019; T. Stensola

& Moser, 2016; T. Stensola et al., 2015; Trettel et al., 2019). The strongest grid anchor appears to be the environmental geometry itself, as different enclosure shapes affect grid cell hexagonal symmetry (Krupic et al., 2015; T. Stensola & Moser, 2016; T. Stensola et al., 2015). Future experiments should investigate if hexagonal and quadrant-like spatial alignment profiles also persist in other types of environmental geometries that vary in polarisation and symmetry. Given that grid hexagonal symmetry is disrupted in trapezoidal geometries (Krupic et al., 2015), one might intuit that MEC spatial patterns will not be as definable as those observed in a square environment. Therefore, we emphasize that the quadrant-like grid firing reported here are limited to square recording environments until there is further evidence in non-square geometries.

What are the implications for reduced theta modulation and phase precession in adult APP mice? The oscillatory interference model posits that one mechanism by which grid cells integrate self-motion is interference of theta oscillations between upstream velocity-controlled oscillators (VCOs) (Burgess, 2008; Burgess et al., 2007; Hasselmo & Brandon, 2008). Different VCO firing frequencies vary according to the animal's movement speed along angular offsets of  $60^\circ$ . When multiple theta-modulated VCOs with preferred directions evenly spaced around  $360^\circ$  oscillate in phase, the thresholded sum of their directional interference patterns in a band-like manner produces grid hexagonal periodicity and theta phase precession. Alternatively, phase precession is proposed to be a 'look-ahead' mechanism to plan future routes and has been modeled in a continuous attractor network (Navratilova et al., 2012). Both oscillatory and continuous attractor models could form the foundations of a path integration system that allows for continuous tracking of position along directions offset by  $60^\circ$  and computation of translational vectors toward goal locations. For instance, neural network implementations of grid cells can be successfully trained to produce vector-based navigation by utilizing phase precession properties (Bush et al., 2015).

Specifically, the phase difference relationships of different grid cells encoding current and goal locations can accurately produce goal-directed translational vectors in large-scale two-dimensional spaces (Bush et al., 2015). The lack of phase precession in many APP-a grid cells could impair their ability to integrate self-motion and plan future paths in the environment's center, thus causing the grid cell network to adopt quadrant-like alignment that may integrate spatial displacement through other means such as visual cues and contact with environmental borders. The sequential organization of grid cell spikes within continuous theta cycles might also constitute a temporal readout of movement direction within short time windows (Zutshi et al., 2017). Theta phase precession suggests that past grid fields fire at earlier phases in a theta cycle while recent grid fields fire at later phases. Each theta cycle therefore describes past, current and future locations. This continuous phase code could underlie the animal's ability to infer position relative to a starting location when path integrating across long behavioral time scales. Phase precession has also been reported in other species including bats and humans, suggesting that phase coding serves a broad role in linking sequential locations and events (Eliav et al., 2018; Qasim et al., 2021).

Many real-world and virtual human path integration behavioral paradigms eliminate or control against the use of environmental borders (Allen et al., 2004; Bierbrauer et al., 2020; Howett et al., 2019; Mahmood et al., 2009; Mokrisova et al., 2016; Stangl et al., 2020). Partial or complete removal of external landmarks could force preclinical individuals to rely on self-motion information which they have difficulty integrating, thus leading to unstable and compromised fMRI grid-like signals (Bierbrauer et al., 2020; Kunz et al., 2015; Segen et al., 2022). Hexagonal and quadrant-like alignment may suggest general principles about how one encodes position via self-motion. Hexagonal structure is superior to quadrant-like structure in terms of angular resolution and sampling frequency between vertices (Mersereau, 1979). In the context of path

integration, 60° grid axes allow for more frequent updating of heading direction, as well as spatial displacement or movement speed between intersection points. These advantages may explain why grid cells in general adopt hexagonal symmetry, or why grid-like representations are modulated at 60° and not at 90° intervals (Doeller et al., 2010).

Tauopathy and amyloidopathy are pathological hallmarks of AD (Berron et al., 2021; Braak & Braak, 1991). While tauopathy is generally regarded as the main driver of entorhinal dysfunction in the general population, different tau and A $\beta$  mouse models independently show a shared disruption of grid cell hexagonal symmetry during early and late pathogenesis (Archetti et al., 2019; Braak & Braak, 1991; Fu et al., 2017; Johnson et al., 2016; Jun et al., 2020; Ossenkoppele et al., 2016; Ridler et al., 2020; Ying et al., 2022; Young et al., 2014). In a two-dimensional continuous attractor neural network model of grid cell activity, simulated AD synaptic damage resulting from the propagation of neurofibrillary tau tangles disrupted grid cell hexagonal symmetry (Zhi & Cox, 2021). Similar to APP-a mice, simulated healthy grid cells had three significant Fourier components offset by 60°. In contrast, simulated damaged grid cells had two, one, or no components depending on the magnitude of synaptic impairment. The similarities between these model simulations of tau propagation and our experimental results in an amyloid mouse model suggest that despite the different molecular pathways of tauopathy and amyloidopathy, the loss of grid hexagonal symmetry across multiple AD mouse models might initially occur through a similar process where the grid map detaches from the individual's self-motion while staying anchored to the external world. More broadly, our findings support existing theories which suggest that disrupted processing of self-motion by grid cells underlies path integration impairments reported during early AD (Bierbrauer et al., 2020; Howett et al., 2019; Kunz et al., 2015; Segen et al., 2022; Ying et al., 2022).

## **Acknowledgements**

We graciously thank S. Kim, Z. Ante, K. Harandian, Q. He, A. Ismailova, D. Patel, A. Zhen, and A. Milette-Gagnon for their assistance in experiments. We also thank A.T. Keinath, H.C. Yong, J.Q. Lee, J.C. Robinson and M. Oulé for providing helpful comments on prior versions of the manuscript, as well as all members of the Brandon laboratory for helpful discussions. This work was funded by CIHR Project Grants #367017 and #377074, an NSERC Discovery Grant #74105, a Scottish Rite Charitable Foundation Grant, a Canada Fund for Innovation Grant, and a Canada Research Chairs award to M.P.B. This work was also supported by the German Research Foundation (DFG) project YO177/7-1 and YO177/8-1 to M.Y. J.Y is supported by a Doctoral Training Grant from the Fonds de recherche du Québec, and previously by a Master's Training Grant from the Fonds de recherche du Québec and a CIHR Master's Training Fellowship.

## **Author contributions**

J.Y., A.R., M.Y., and M.P.B. conceived the project and wrote the manuscript. J.Y conducted all experiments. J.Y. and A.R. conducted analysis of data.

## **Declaration of interest**

Authors declare no competing interests.

## Figures and legends

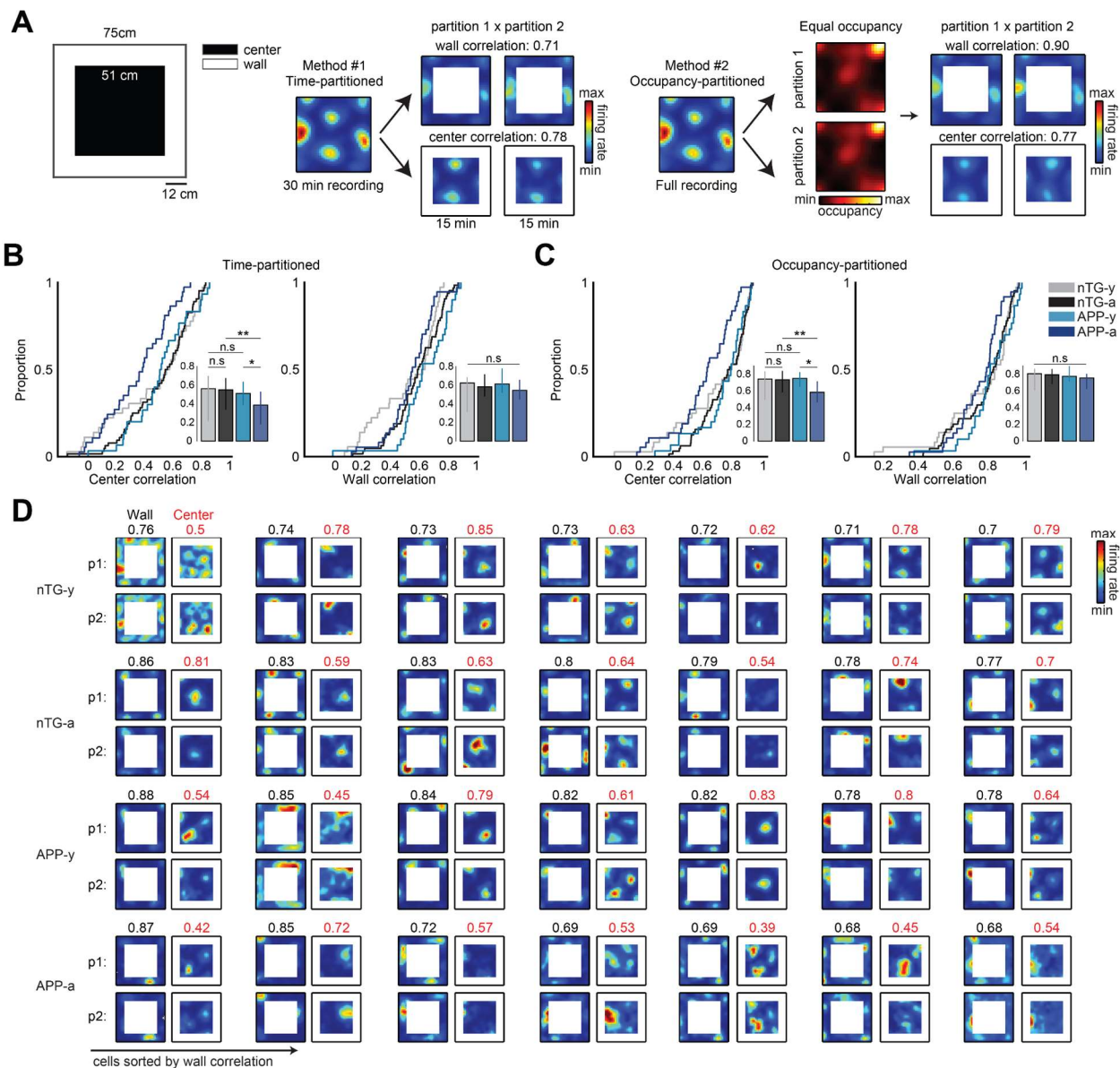


**Figure 1. Adult APP grid cells are spatially unstable in the center of the environment.**

(A) The spatial arena was divided into ‘wall’ and ‘center’ regions. The wall length was 12 cm. Spatial stability was calculated via two methods. A time-partitioned analysis split the first 30 minutes of each grid cell recording into two 15 minutes partitions. An occupancy-partitioned analysis split the entire recording into two maps where the occupancies in each spatial bin were the same. Higher correlation scores between wall or center partitions indicate higher spatial stability.

(B) Center stability is reduced in time-partitioned APP-a grid cell maps, but wall stability is preserved. Bars indicate medians, and error bars show the 25<sup>th</sup> and 75<sup>th</sup> percentile, two-way

ANOVA (center - age x genotype interaction:  $F(1, 163) = 7.2, p = 0.008$ ; wall - age x genotype interaction:  $F(1, 163) = 8.1, p = 0.005$ ), Wilcoxon rank sum post hoc tests with a Bonferroni-Holm correction.

(C) Center stability is reduced in occupancy-partitioned APP-a grid cell maps. Bars indicate medians, and error bars show the 25<sup>th</sup> and 75<sup>th</sup> percentile, two-way ANOVA (center - age x genotype interaction:  $F(1, 163) = 9.14, p = 0.0029$ ; wall - age x genotype interaction:  $F(1, 163) = 2.81, p = 0.10$ ), Wilcoxon rank sum post hoc tests with a Bonferroni-Holm correction.

(D) Time-partitioned rate map examples for seven grid cells with the highest wall stability in each group. Wall and center scores are indicated above each partition (p1 and p2) set in black and red, respectively. Wall correlation scores remained consistently high between groups, but center correlation scores were generally lower in APP-a grid cells.

For all panels, n.s = non-significant, \* $p < 0.05$ , \*\* $p < 0.01$ .

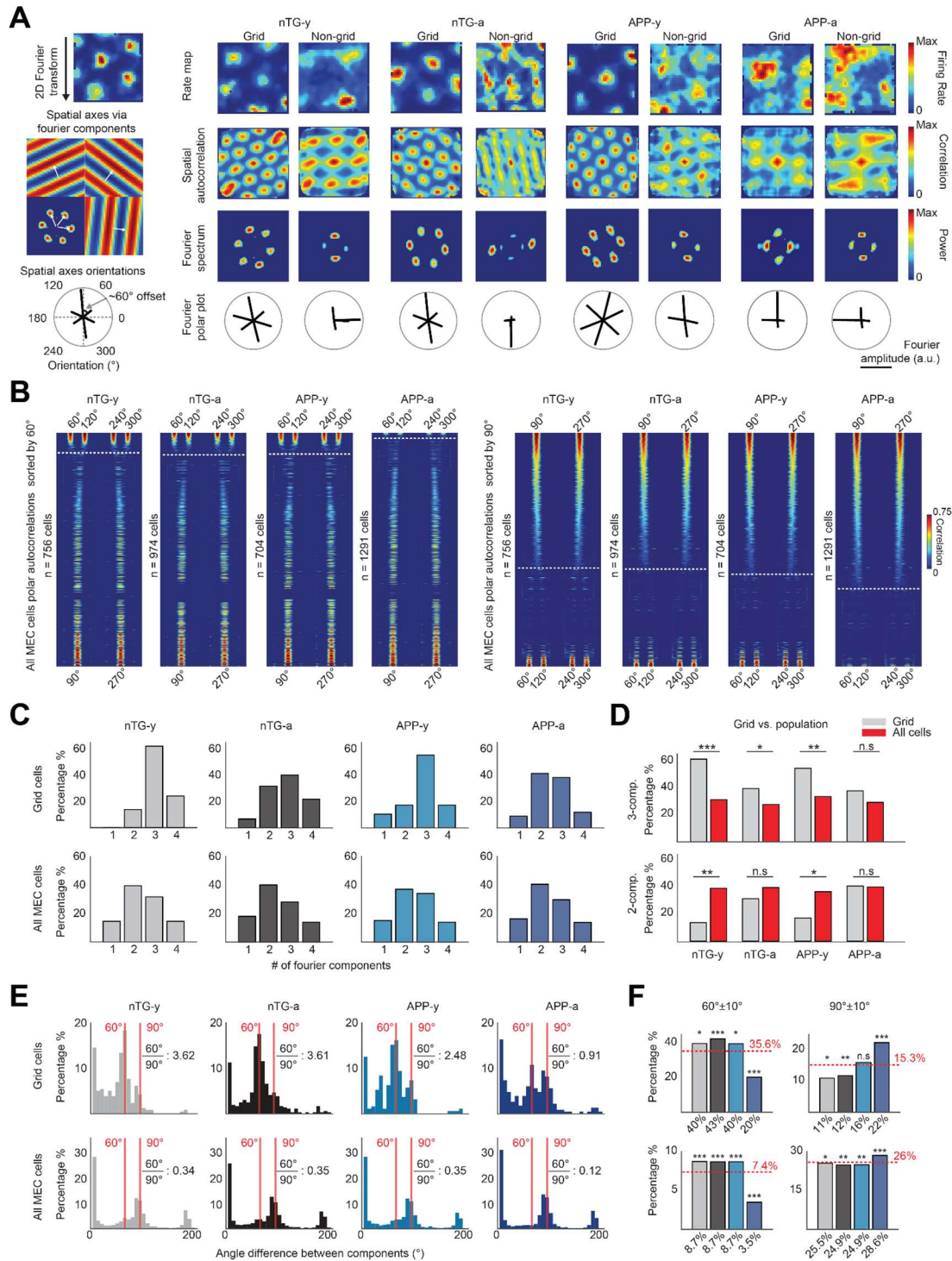


**Figure 2. Adult APP MEC neurons more frequently adopt quadrant-like spatial alignment.**

(A) A 2D Fourier transform decomposes the rate map into a small number of Fourier components. Each grid cell component can be visualized as an image of grid axes typically oriented at multiples

of  $60^\circ$ . The orientations of all Fourier components could be visualized as a polar plot. Single grid and non-grid spatially periodic cell examples are shown for all groups.

(B) Polar autocorrelations for all MEC cells sorted by the strength of hexagonal modulation at  $60^\circ$  multiples or by the strength of quadrant-like modulation at  $90^\circ$  multiples. Dashed white lines indicate where hexagonal modulation or quadrant-like modulation ends.

(C) Percentage distribution of cells that had one-to-four Fourier components for grid cells and all MEC cells.

(D) The percentages of grid cells that had either three (one-tailed t-test for proportions) or two components (two-tailed t-test for proportions) versus all MEC cells.

(E) Histograms show the distribution of angle difference between neighboring components of grid and all MEC cells. Solid red lines mark specific orientations.

(F) Bar graphs show the percentages of angular differences at  $60^\circ \pm 10^\circ$  and  $90^\circ \pm 10^\circ$  compared to an expected percentage calculated as the average of observed proportions across all groups (dotted red line). Binomial test.

For all panels, n.s = non-significant, \* $p < 0.05$ , \*\* $p < 0.01$ , \*\*\* $p < 0.001$ .

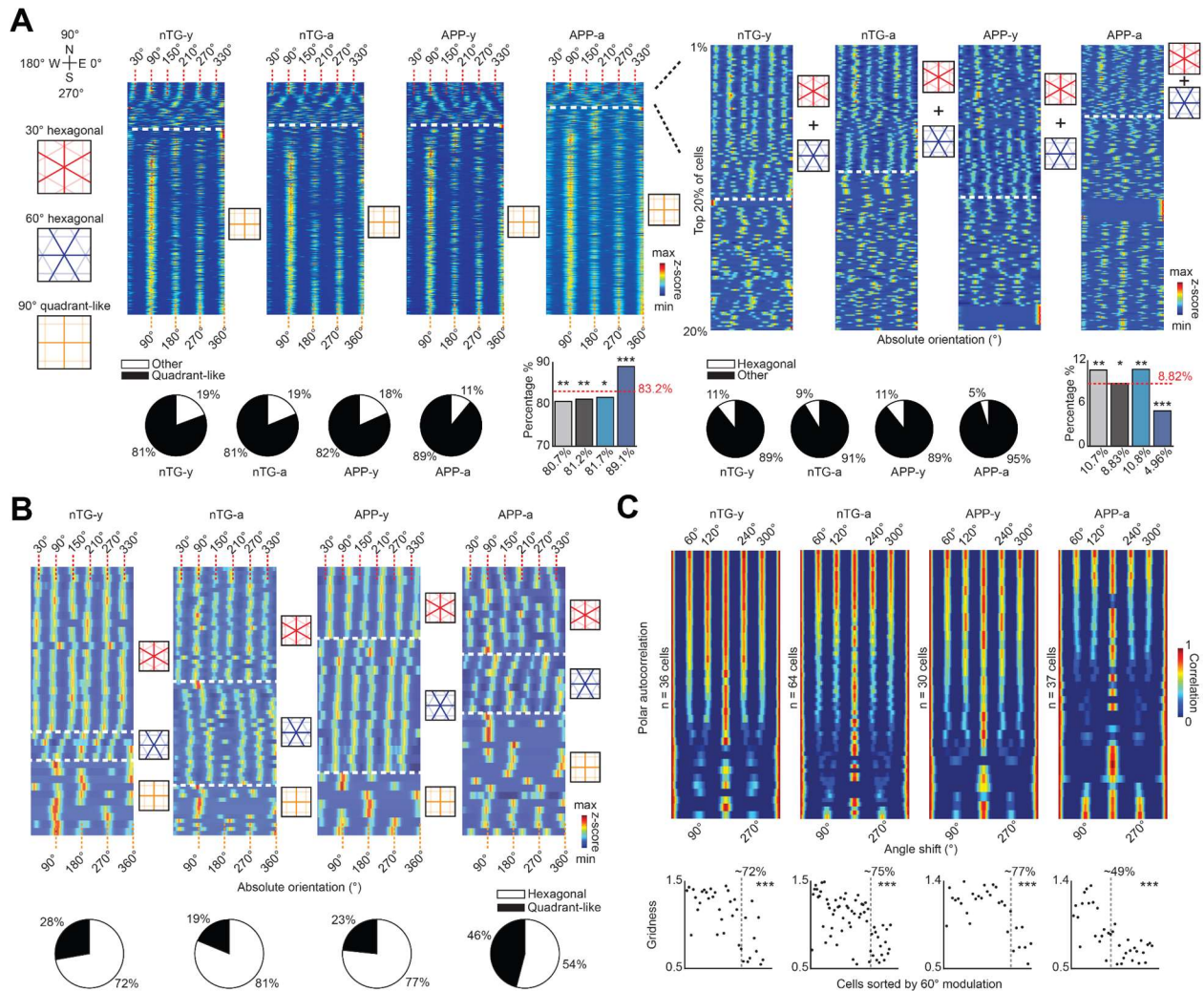


**Figure 3. Adult APP grid cells align parallel to the borders.**

(A) (Left-top) Absolute orientation of all cells relative to the recording environment. Dashed white lines indicate where quadrant-like alignment starts. (Left-bottom) Percentage distributions of quadrant-like cells between groups, and compared to the expected chance of recording them (dotted red line). Binomial test.

(Right-top) Zoomed-in view of the absolute orientations of the top 20% of cells in the left panel. Dashed white lines indicate where 30° or 60° hexagonal alignment ends. (Right-bottom) Percentage distributions of hexagonal cells between groups, and compared to the expected chance of recording them (dotted red line). Binomial test.

(B) Top: Absolute orientation of all grid cells relative to the recording environment. Grid cells could be grouped into 30° or 60° hexagonal alignment, as well as 90° quadrant-like alignment (boundaries separated by black dotted lines). To account for differences in Fourier power between

cells, colors indicate the z-score of each polar representation. Bottom: Percentage distributions of hexagonal or quadrant-like grid cells between groups.

(C) Polar autocorrelation for grid cells in all groups. Grid cells are sorted by the strength of hexagonal modulation at  $60^\circ$  multiples. Colors indicate correlation at each degree shift along the x-axis. Bottom: Gridness scores of grid cells sorted by their degree of hexagonal or quadrant-like modulation ( $90^\circ$  intervals) along the x-axis. The boundary between the two categories is indicated by the gray dotted lines, and the percentage of strongly hexagonally modulated grid cells are indicated for each group. Wilcoxon rank sum tests.

For all panels, n.s = non-significant, \* $p < 0.05$ , \*\* $p < 0.01$ , \*\*\* $p < 0.001$ .

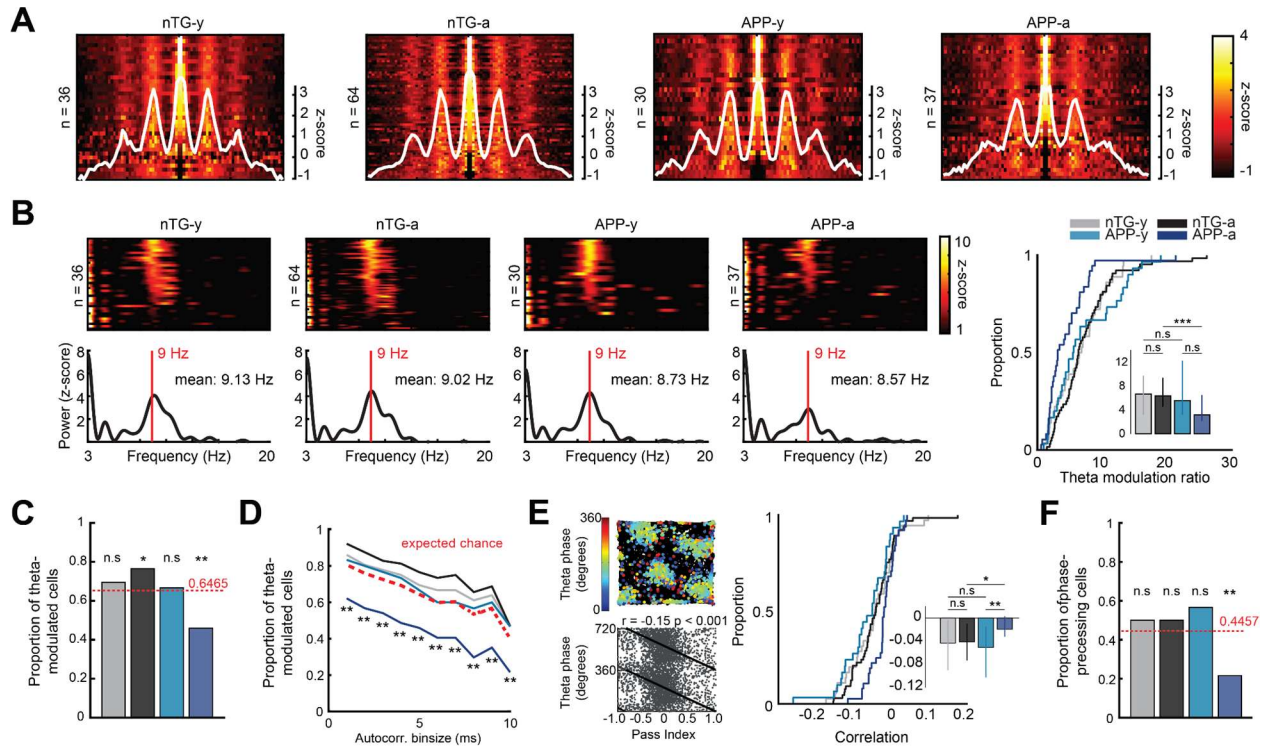


**Figure 4. Adult APP grid cells have reduced theta modulation and theta phase precession.**

(A) Color-coded raster plots of spike-time autocorrelations for grid cells across groups. White lines are the average autocorrelation curves.

(B) Left: Color-coded raster plots show the power spectrums of spike-time autocorrelations for grid cells across groups. Line graphs show the mean intrinsic frequency curve and red lines mark where a 9 Hz intrinsic frequency. Right: Theta modulation ratio is reduced in APP-a grid cells. Bars indicate medians, and error bars show the 25<sup>th</sup> and 75<sup>th</sup> percentile, two-way ANOVA (age x genotype interaction:  $F(1, 163) = 5.33, p = 0.022$ ), Wilcoxon rank sum post hoc tests with a Bonferroni-Holm correction.

(C) Proportions of significantly theta-modulated grid cells compared to the expected chance of recording them (dotted red line). Binomial test.

(D) Repetition of (C) when varying the bin size of the spike-time autocorrelation between 1 to 10 ms. In all conditions, there was a consistent decrease in significantly theta-modulated grid cells in APP-a mice.

(E) Left: Open field phase precession for an example grid cell. Trajectory of mouse in black with overlaid color-coded circles indicate the location and theta phase of spiking. Pass index values of -1 and +1 represent the entry and exit of a firing field, respectively. Right: The strength of correlation between the spiking phase and distance travelled across a firing field is reduced in APP-a mice. Data includes quadrant-like and hexagonal grid cells. Bars indicate medians, and

error bars show the 25<sup>th</sup> and 75<sup>th</sup> percentile, two-way ANOVA (age x genotype interaction:  $F(1, 163) = 5.34, p = 0.02$ ), Wilcoxon rank sum post hoc tests with a Bonferroni-Holm correction.

(F) Proportion of significantly phase-processing grid cells compared to the expected chance of recording them (dotted red line). Binomial test.

For all panels, n.s = non-significant, \* $p < 0.05$ , \*\* $p < 0.01$ .

## Supplementary Information

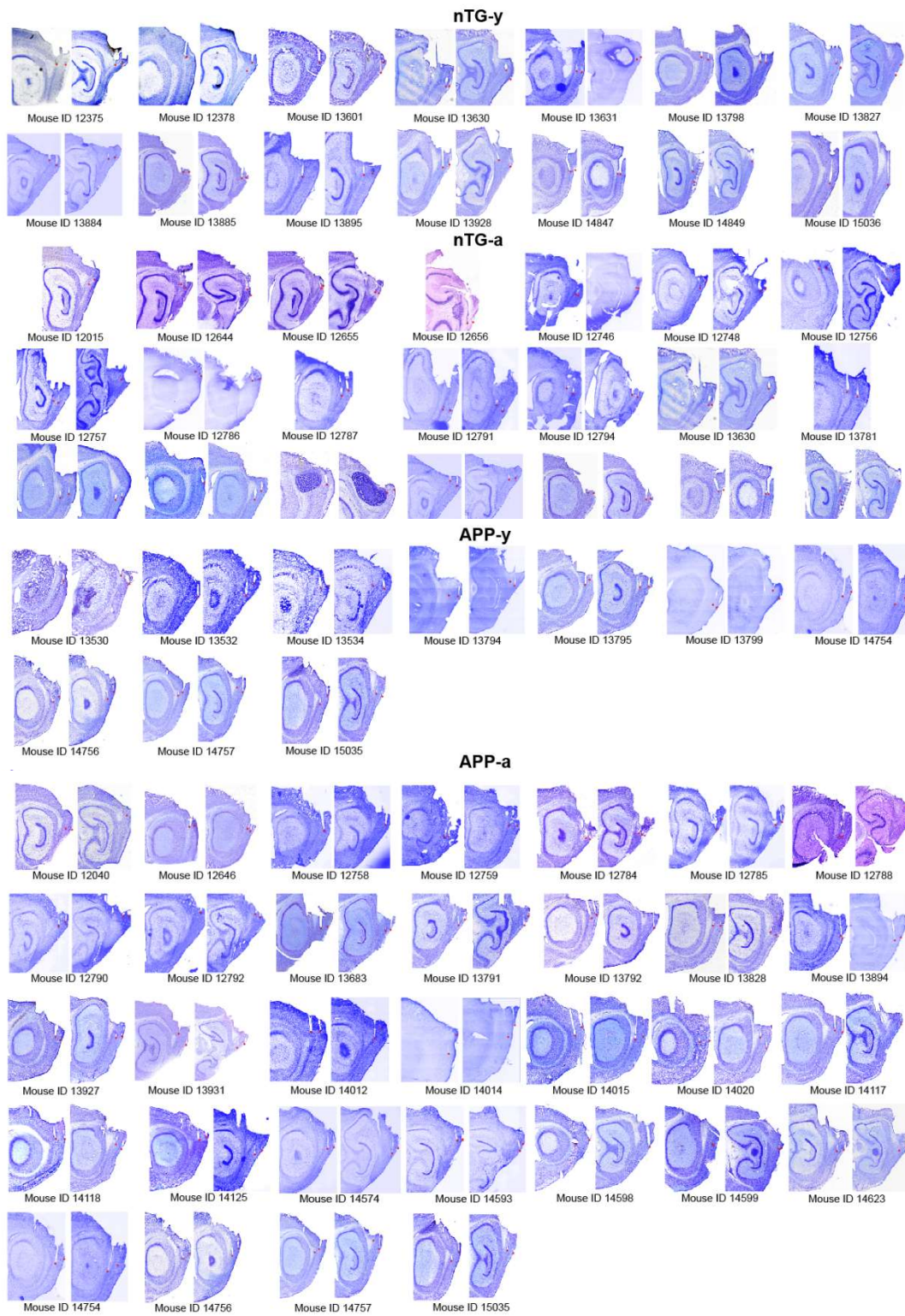


**Figure S1. Tetrode track locations.**



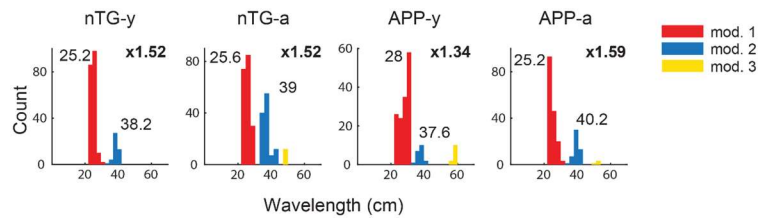


**Figure S3. Fourier component wavelengths.**

Distribution of Fourier component wavelengths for grid cells. Colors indicate different wavelength modules. The mean wavelength values for the red and blue modules are shown above, as well as the ratio between modules.

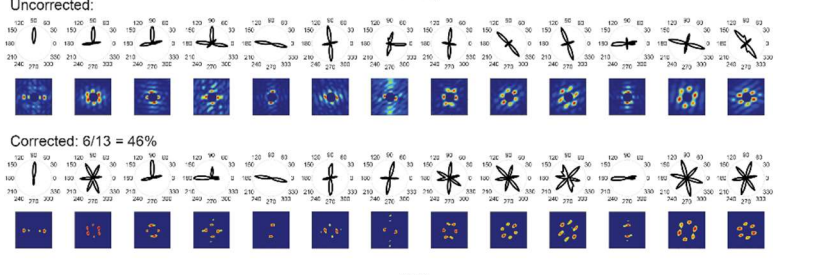
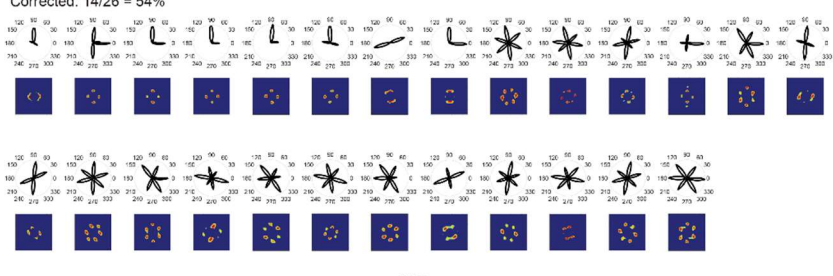
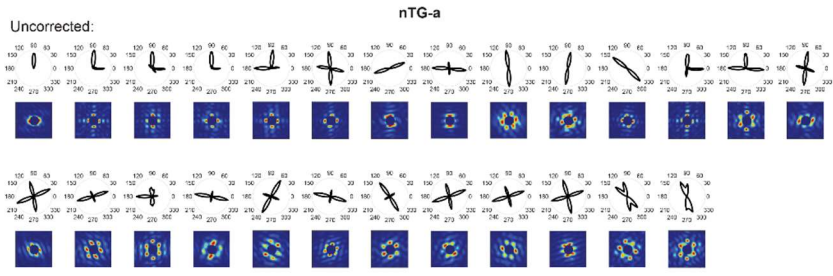
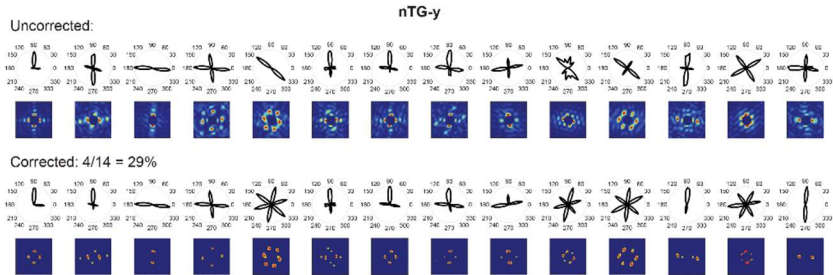


**Figure S4. Retrieval of 3-component hexagonal grid cells via correction.**

All 1-component or 2-component grid cells in the uncorrected group are shown by its polar representation and the raw Fourier spectrum. A mix of automatic and manually selected higher thresholds (see Table S3) were used to correct falsely classified cells. Each cell in the Corrected group is shown by the corrected polar representation and the more strongly filtered Fourier spectrum.

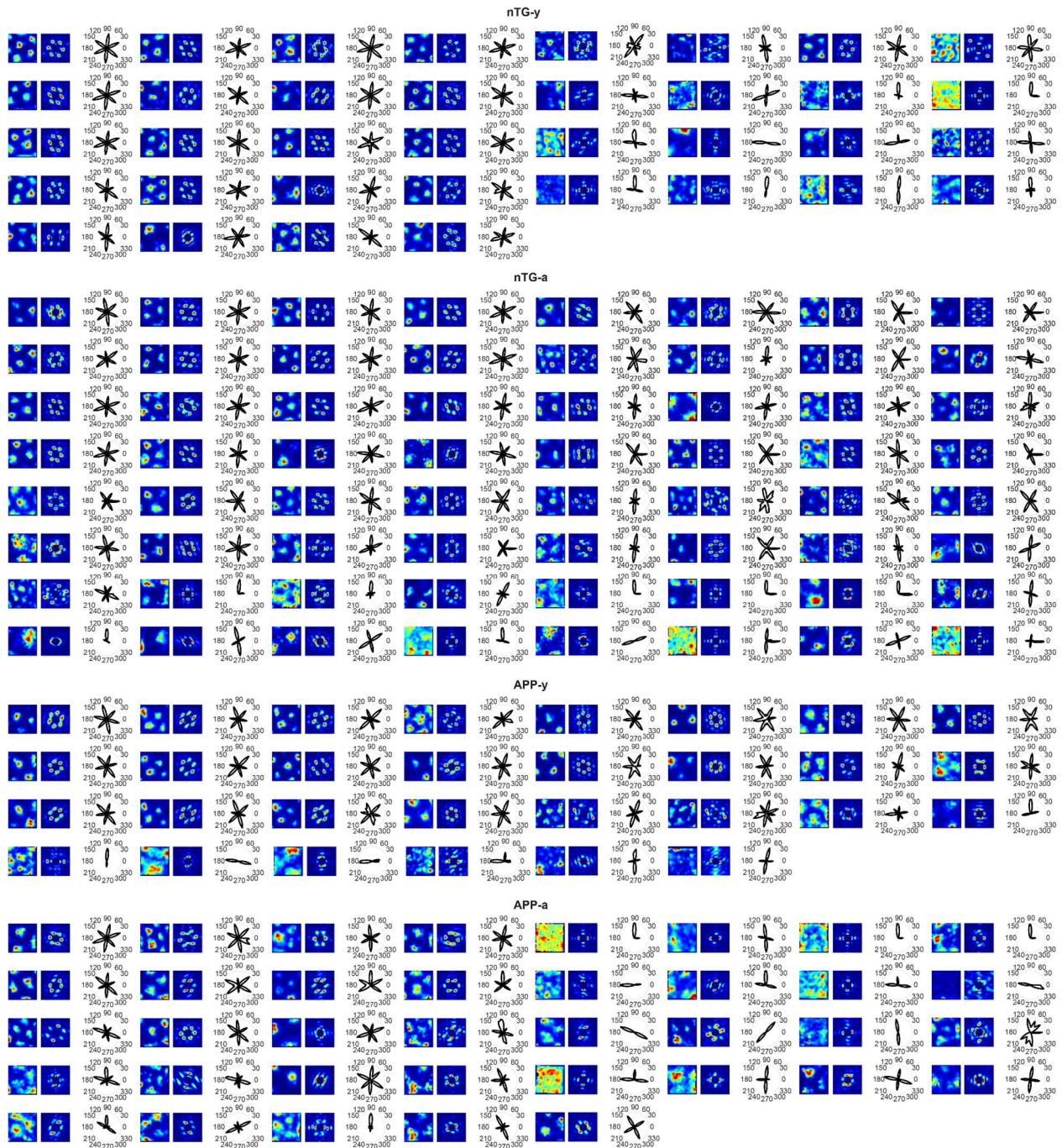


**Figure S5. Grid cells, their Fourier components, and polar representations.**

The spatial rate maps, Fourier components, and polar representations for all grid cells in Figure 3 are shown. The color scale of the rate maps indicates occupancy normalized firing rate. The color scale of the Fourier spectrums indicates Fourier power. The scale of the polar representations indicates Fourier power.

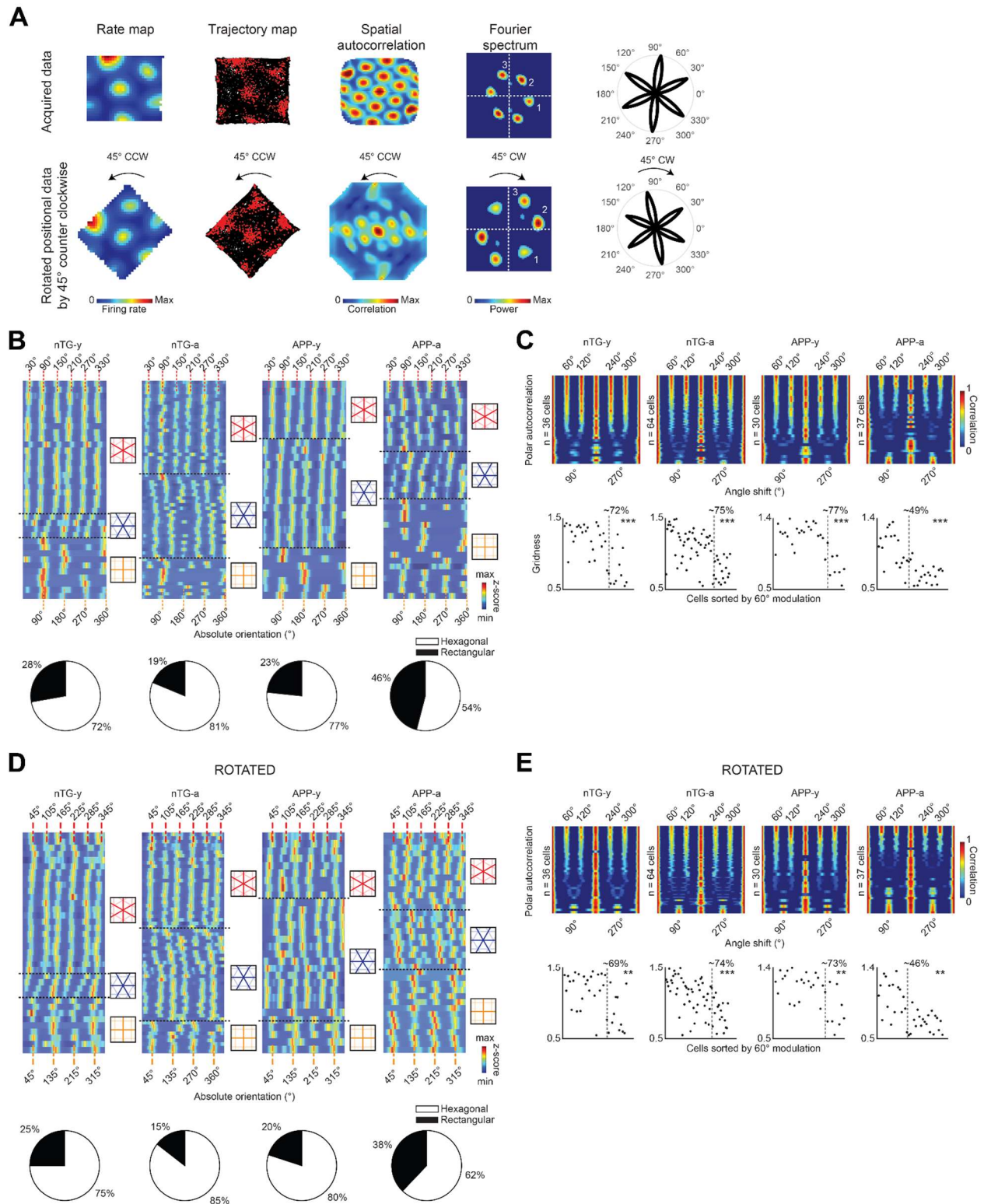


**Figure S6. Fourier components reflect rate map content, and not the square shape of images.** (A) Rotation of positional data by  $45^\circ$  clockwise causes an equal rotation in the Fourier spectrum.

(B) Top: Absolute orientation of all grid cells relative to the recording environment. Bottom: Percentage distributions of hexagonal or quadrant-like grid cells between groups.

(C) Polar autocorrelation for grid cells in all groups. Grid cells are sorted by the strength of hexagonal modulation at  $60^\circ$  multiples. Bottom: Gridness scores of grid cells sorted by their degree of hexagonal or quadrant-like modulation along the x-axis. The boundary between the two categories is indicated by the gray dotted lines, and the percentage of strongly hexagonally modulated grid cells are indicated for each group. Wilcoxon rank sum tests.

(D-E) Same as B-C, but for data when positional data was rotated by  $45^\circ$  clockwise.

For panels C and E, n.s = non-significant,  $**p < 0.01$ ,  $***p < 0.001$ .

## Methods

### Mice

J20 APP male mice (B6.Cg-Zbtb20 Tg(PDGFB-APPSwInd) 20Lms/2Mmjax) were obtained from The Jackson Laboratory (MMRRC stock #34836) and bred with female C57/BL6/j mice. Mice were individually housed on a 12-h light/dark cycle and underwent experiments during the light cycle. Housing room conditions of the mice were maintained at 20-22 degrees Celsius and 21-30% humidity. All experimental procedures were performed in accordance with McGill University and Douglas Hospital Research Centre Animal Use and Care Committee (protocol #2015-7725) and in accordance with Canadian Institutes of Health Research guidelines.

J20 mice undergo progressive neuronal loss in layers 2, 3 and 5 of the MEC. By 7.5 months of age, all layers exhibit a total loss of 16.3% of neurons compared to control mice, along with reduced density of presynaptic terminals by 7 months of age (Nagahara et al., 2013). By 6 months of age, region CA1 of the hippocampus also experiences 10%+ of neuronal loss compared to control mice. In parallel, marker-immunoreactivity and electron microscopy confirm the presence of synapse loss in the CA1 as early as 3 months. Besides neuronal and synaptic loss, the complement-dependent pathway and microglia are upregulated in a manner that is dependent on soluble A $\beta$  oligomeric levels in the hippocampus (Hong et al., 2016). On a related note, gliosis (activated astrocytes) and neuroinflammation (activated microglia) are elevated across age in the hippocampus by 6 months of age (Wright et al., 2013). Furthermore, *in vitro* slice electrophysiology experiments reveal that basal synaptic transmission recorded in CA1 and long-term potentiation in the Schaffer collateral–CA1 synapse are impaired by 3 months of age (Saganich et al., 2006). In terms of oscillatory activity, between 4-7 months of age, gamma oscillations are reduced in the parietal cortices which causes network hypersynchrony and are linked to a reduction in the voltage-gated sodium channel subunit Nav1.1 predominantly found in parvalbumin interneurons (Verret et al., 2012). Such hypersynchrony may be linked to spontaneous nonconvulsive seizure activity between 4-7 months, along with numerous inhibitory deficits in the dentate gyrus (Palop et al., 2007). At the behavioral level, J20 mice exhibit numerous spatial navigation impairments in the Morris water maze, the radial arm maze and a food-foraging path integration task in darkness (Cheng et al., 2007; Wright et al., 2013; Ying et al., 2022). To examine the impact of these A $\beta$ -mediated changes on neural coding during early pathology, we restricted our experiments between 3-7 months of age.

Single-unit recording data in the MEC were collected from 68 APP mice and non-transgenic littermates across four experimental groups: young APP mice (3-4.5 months of age), adult APP mice (4.5-7 months of age), young non-transgenic (nTG) mice (3-4.5 months of age), adult nTG mice (4.5-7 months of age). Thirty-one males and 37 females were used. Ten animals fell into multiple age groups. The male/female ratios were 6:5, 16:16, 9:5, and 11:10 for young APP, adult APP, young nTG, and adult nTG mice respectively.

### Surgery

On the day of surgery, mice were anesthetized using isoflurane (0.5% - 3% in O<sub>2</sub>) and administered carprofen (0.01 ml/g) subcutaneously. Three anchor screws were secured to the skull and a ground wire was positioned either above the cerebellum at midline position or the left visual cortex. A ‘versadrive’ containing four independently movable tetrodes (Axona, Inc) was implanted on top

of the right MEC at the following stereotaxic coordinates: 3.4 mm lateral to the midline, 0.25-0.40 mm anterior to the transverse sinus. Tetrodes were gold-plated to lower impedances to 150-250 k $\Omega$  at 1 kHz prior to surgery. The versadrive was angled at eight degrees in the posterior direction. Following placement, the versadrive was secured in place using Kwik-Sil and dental acrylic. The ground wire was soldered to the implant, and tetrodes were lowered 1.0 mm from the dorsal surface of the MEC. All surgical procedures were performed in accordance with McGill University and Douglas Hospital Research Centre Animal Use and Care Committee (protocol #2015-7725) and in accordance with Canadian Institutes of Health Research guidelines.

## **Neural Recordings**

Three days post-surgery, mice were placed on water restriction and maintained at 85% of their *ad libidum* weight throughout experiments. Mice were recorded in a 75 x 75 cm box. As mice explored their environments, water droplets were randomly scattered to motivate the subjects to sample the entire arena. Once mice provided good trajectory coverage, tetrodes were turned until theta rhythmic units were observed which indicated that the tetrodes had entered the MEC. Across days, tetrodes were advanced in increments of 25 microns to sample new putative MEC neurons.

To record spikes and local field potentials, versadrives were connected to a multichannel amplifier tethered to a digital Neuralynx (Bozeman, MT) recording system, and data were acquired using Cheetah 5.0 software (Neuralynx, Inc). Signals were amplified and band-pass filtered between 0.6 kHz and 6 kHz. Spike waveform thresholds were adjusted before each recording and ranged between 35-140  $\mu$ V depending on unit activity. Waveforms that crossed threshold were digitized at 32 kHz and recorded across all four channels of the given tetrode. Local field potentials were recorded across all tetrodes.

## **Histology**

Animals were anesthetized with Isoflurane and perfused intracardially using saline and 4% paraformaldehyde. Animal heads were left in 4% paraformaldehyde for 24-72 hours following perfusion, before brains were extracted. Brains sank in a 30% sucrose solution before being frozen and stored in a -80°C freezer. Sagittal brain sections (40 $\mu$ m) were obtained using a cryostat and Nissl-stained with a Cresyl violet solution. In cases where brain slices came off the glass slides during Nissl-staining, slices were instead mounted using a fluorescent DAPI labeling mounting medium.

Tetrode tracks were characterized to be in the superficial or deep layers based on the location of track tips. Only data collected from tetrodes within the MEC were included in analysis.

## **Spike sorting**

Single-units were isolated 'offline' manually using Offline Sorter 2.8.8 (Plexon, Inc). Neurons were separated based on peak amplitudes and principal component measures of spike waveforms. Evaluations of the presence of biologically realistic interspike intervals, temporal autocorrelations, and cross correlations confirmed single-unit isolation. The experimenter was blind to the age and genotype of the subjects and only well-separated clusters were included in analysis.

## **Position, direction, velocity estimation, and rate map construction**

Positional data was acquired at 30 frames per second at 720 x 480 pixel resolution (4.9 pixels per cm) using a camera purchased from Neuralynx (Bozeman, MT). The camera was elevated at a

height to fully capture the entire recording arena. The estimated position of the animal was the centroid of a group of red and green diodes positioned on the recording head stage. Head direction was calculated as the angle between the red and green diodes. Up to five lost samples due to occlusion of tracking LEDs, or reflections in the environment were replaced by a linear interpolation for both position and directional data. Running velocity was calculated using a Kalman filter. Rate maps were constructed by calculating the occupancy-normalized firing rate for 3cm x 3cm bins of positional data. Data were smoothed by a two-dimensional convolution with a pseudo-Gaussian kernel involving a three pixel (9 cm) standard deviation. In most analyses (when specified), rate maps were resized into squares of size 36 x 36 pixels or 26 x 26 pixels.

### **Gridness score**

We calculated the gridness score using the same procedure described in Brandon et al. 2011 (Brandon et al., 2011). This metric quantifies hexagonal periodicity in the firing rate map, while also accounting for elliptical eccentricity along one of two mirror lines that exist in a hexagonal lattice structure. Distortion along one of the mirror lines was corrected after determining the major and minor axes of the grid based on the six closest fields to the central peak of the rate map autocorrelogram. The entire autocorrelogram was compressed so that the major axis became equal to the minor axis. Large eccentricities where the minor axis was less than half of the major axis were not corrected. From the compressed autocorrelogram, we extracted a ring of the six closest peaks to the center peak. A rotational autocorrelation of this ring was calculated to observe the periodicity in paired pixel correlations across 180 degrees of rotation. The gridness score was computed as the difference between the highest correlation observed at 30, 90, or 150 degrees of rotation and the lowest correlation observed at 60 or 120 degrees of rotation.

### **Directionality**

The animal's head direction was collected in bins of 6 degrees and the number of spikes in each bin was divided by the time spent facing that direction. The mean resultant length (MRL) of the polar plot was taken as a metric of directional selectivity.

### **Grid cell and head-direction cell selection**

Grid cells and head direction cells were determined via a shuffling procedure. Spike trains from each neuron were randomly shifted in time by at least 30 seconds. We then calculated gridness and directionality measures. This process was repeated 50 times for each neuron, and the 99<sup>th</sup> percentile of the resulting distribution of scores was determined as the significance criteria for both measures. This resulted in a gridness threshold of 0.54 and directionality threshold of 0.21. Cells that passed these thresholds were characterized as grid cells and head direction cells, respectively.

### **Spatial stability analysis**

Time-partitioned analysis: Rate maps of size 26 x 26 pixels were created for each grid cell. The first 30 minutes of each recording was divided into two 15-minute partitions. Each rate map was divided into wall or center regions, depending on how many pixel layers each had. Next, the pixels corresponding to both regions were extracted for both partitions. A Pearson correlation was computed for wall or center time partitions.

Occupancy-partitioned analysis: A 26 x 26 pixel matrix (an 'occupancy map') tracked the number of time frames that the animal spent in each spatial bin throughout the full recording. All time

frames where the mouse was stationary (velocity < 5cm/s) were dropped. The values in each bin were then halved, and the resulting numbers represented the number of time frames per bin allocated to each partition. Time frames were then selected throughout the entire recording session in an ‘ascending’ or ‘monotonically increasing’ manner to build both partition maps. Rate maps of size 26 x 26 pixels were created for each partition. The rest of the analysis was the same as the time-partitioned analysis.

### Generation of Fourier spectrums

We followed the procedure used previously in Krupic et al. 2012 (Krupic et al., 2012). We used the `fft2` MATLAB function to compute the two-dimensional Fourier transform of the rate map of a given cell. Initial rate maps were unsmoothed at size 36 x 36 pixels and center zero-padded to have size 256 x 256 pixels in order to increase the spatial resolution of the Fourier spectrogram. After running `fft2` on the zero-padded rate map, the resulting amplitude spectrum was divided by the mean firing rate of the given cell to allow for comparison between cells that have different firing rates. The amplitude spectrum was element-wise squared to re-visualize the spectrum in the power domain.

We used the `fftshift` MATLAB function to shift low frequencies to the center and high frequencies to the periphery of the spectrum. Lastly, we created a two-dimensional gaussian loss function (where the bump values are 0) with a width of 1. This gaussian was centered at the strongest value pixel of the spectrum and element-wise multiplied. This procedure was done to erase the center block of energy that resulted from the `fft2` function.

### Identifying Fourier components

The Fourier power spectrum was first computed. To reduce effects of noise, the 75<sup>th</sup> percentile value of power in shuffled data (from the Voronoi procedure) was subtracted and negative values set to zero. To further control for noise, values lower than 25% of the resulting maximum power were also set to zero. These are higher thresholds than what was used by Krupic et al. 2012 (Krupic et al., 2012). However, to ensure that these thresholds do not bias our results, we varied this latter parameter in Table S3.

A zero matrix with the size of the Fourier spectrum was created. Any non-zero value in the corrected Fourier spectrum had its corresponding position in the zero matrix set to 1. Using the `regionprops` MATLAB function, Fourier components were individually identified as separate “regions”. To account for effects of noise, any regions with an area less than 10 pixels was discarded. Similar to Krupic et al. 2012, cells with more than 4 Fourier components were not included in analysis (Krupic et al., 2012).

To determine a component’s orientation, the distances (along the x- and y-axes) between the centroids of each region and the center of the Fourier spectrum were computed. The “wave vector” corresponding to the x- and y-displacements were calculated as:

$$k_x = \frac{2\pi * dx}{Nb}$$

$$k_y = \frac{2\pi * dy}{Mb}$$

Where dx and dy are the x- and y-displacements, respectively; N and M are the x- and y-axis lengths of the rate map (both 36 in our case); b is the bin size in meters (0.0208 in our data). The orientation of the wave vector was:

$$\varphi = \text{atan}\left(\frac{k_y}{k_x}\right)$$

And the orientation of the periodic band (or grid axes) is 90 degrees offset to the wave vector's orientation.

$$\theta = \varphi + 90^\circ$$

### **Fourier polar representations and autocorrelations**

To compute Fourier polar representations, we first plotted the orientations of individual Fourier components on a polar plot. The power corresponding to each orientation was that given component's Fourier power in the Fourier spectrum. The polar plot was then smoothed using a one-dimensional Gaussian kernel with a standard deviation of 13 degrees.

To compute Fourier polar autocorrelations, the smoothed polar plots were circularly shifted 360 degrees. At each degree shift, the Pearson correlation between the original and shifted polar profiles was computed.

### **Fourier wavelength identification**

To compute a Fourier component's wavelength, a line was drawn over the Fourier spectrum at the given component's orientation. This was achieved using the `improfile` MATLAB function, which draws a line between a specific start (the Fourier spectrum's center) and end point (a point exceeding the dimensions of the spectrum) on a given image (the spectrum). The distance away from the spectrum's center along this line which had the maximum Fourier power was taken as the wavelength.

### **Fourier orientation offset from reference axes**

A grid cell was first determined to be either a 30° or 60° hexagonal grid, or a 90° quadrant-like grid based on where the Fourier orientations faced. The reference axes for a 30° grid faced (30°, 90°, 150°, 210°, 270°, 330°). The reference axes for a 60° grid faced (0°, 60°, 120°, 180°, 240°, 300°). The reference axes for a 90° grid faced (0°, 90°, 180°, 270°). The angular difference between each Fourier component and its closest reference axis was calculated as the offset.

### **Theta modulation analyses**

To visualize theta modulation, spike-time autocorrelations were computed for each cell with 5ms temporal bins from a lag of -400 to 400ms. The resulting autocorrelations were convolved with a 25ms gaussian and z-score normalized. The average z-scored correlation curve for all cells was also plotted.

To compute intrinsic frequency, the spike-time autocorrelations were zero padded to 2<sup>13</sup> samples and the power spectrum was calculated using the Chronux toolbox function `MTSPECTRUMC` from Matlab. The intrinsic frequency of a given cell was taken as the frequency with the max power in the 6-12 Hz range. The theta modulation ratio was calculated as the mean power within 6-12 Hz, divided by the mean power between all other frequencies within 2-100 Hz. To be

considered a significantly theta-modulated cell, the mean power within 6-12 Hz needed to be four times greater than the mean power within 2-100 Hz (a theta modulation ratio greater than 4).

### **Phase precession**

The degree of grid cell phase precession was calculated via a ‘pass index’ analysis as described in Climer et al. 2013 (Climer et al., 2013). Briefly, this method quantifies precession by assessing the correlation of a cell’s firing in relation with theta phase as the mouse passes a spatial field. The spatial field locations were estimated using a ‘field index’ method that calculates the degree of occupancy-normalized firing within each bin of positional data. Field contours and centers were then generated by using various parameters involving the field index and firing rate. Lastly, based on the field index signal across a recording session, a mouse’s entry and exit of a spatial field could be estimated. The pass index was therefore determined by normalizing field index signal segments consisting of the passage across a spatial field between -1 and +1, where -1 represents the start of a pass, 0 represents the center, and +1 represents the end. Phase of spiking across field crossing was aligned to this normalized position and a linear-circular correlation was computed between field index and spiking phase (Kempster et al., 2012). A grid cell with a significant correlation at  $p < 0.05$  and a slope per pass between -1440 and -22 was classified as a phase-precessing cell.

### **Genotyping**

Tail samples were collected at weaning for genotyping, and also prior to brain perfusion. DNA samples were extracted and amplified using REDExtract-N-Amp™ Tissue PCR Kit (MilliporeSigma, XNAT-100RXN) and the primer sequence and PCR protocol from The Jackson Laboratory (MMRRC, 34836-JAX). Genotyping results were visualized with a QIAxcel instrument (Qiagen).

### **Quantification of neural data**

Single-unit data were obtained using Neuralynx (Bozeman, MT) software and isolated ‘offline’ manually using graphical cluster cutting software (Plexon, Inc) individually for each recording session. Custom MATLAB scripts were used to analyze neural data.

### **Statistical analysis**

Statistical analyses for neural and behavioral data were performed using MATLAB. Bars in bar graphs represent median values, and the error bars represent the 25<sup>th</sup> and 75<sup>th</sup> percentile.

Comparisons between two groups involving continuous data used unpaired, two-tailed Wilcoxon rank sum tests. Comparisons between more than two groups involving continuous data used a two-way ANOVA with age and genotype as the factors. A significant interaction effect was followed by post-hoc testing using unpaired, two-tailed Wilcoxon rank sum tests with a Bonferroni-Holm correction in the following four comparisons: nTG-y vs. nTG-a, nTG-y vs APP-y, APP-y vs. APP-a, nTG-a vs. APP-a.

In specific cases where proportions were compared between groups in Figure 2D, a one-tailed t-test for proportions was used to compare 3-component cells, and a two-tailed t-test for proportions was used to compare 2-component cells.

All remaining cases involving proportions in Figures 2F, 3A, 3B, 4C, 4D and 4F used binomial tests. A binomial test determines the probability of an outcome when there are only two possible

outcomes. In our case, the test determined if the obtained proportion by a group was equal or unequal (either lesser or larger) compared to expected chance. Expected chance was calculated as the average of the proportions obtained in all four groups. The rationale for calculating expected chance in this manner is assuming that all four animal groups were the same age and genotype, then the average of the four should provide a theoretical level of chance.

All statistical tests used an alpha value of 0.05. Significance was determined as follows: \*  $p < 0.05$ , \*\*  $p < 0.01$ , \*\*\*  $p < 0.001$ .

### Data and code availability

All data reported in this paper will be shared by the lead contact upon request. All original code has been deposited at GitHub [insert link] and is publicly available as of the date of publication. DOIs are listed in the key resources table. Any additional information required to reanalyze the data reported in this paper is available from the lead contact upon request.

### References

1. Allen, G. L., Kirasic, K. C., Rashotte, M. A., & Haun, D. B. M. (2004). Aging and path integration skill: kinesthetic and vestibular contributions to wayfinding. *Perception & Psychophysics*, *66*(1), 170–179.
2. Archetti, D., Ingala, S., Venkatraghavan, V., Wottschel, V., Young, A. L., Bellio, M., Bron, E. E., Klein, S., Barkhof, F., Alexander, D. C., Oxtoby, N. P., Frisoni, G. B., Redolfi, A., Alzheimer's Disease Neuroimaging Initiative, & for EuroPOND Consortium. (2019). Multi-study validation of data-driven disease progression models to characterize evolution of biomarkers in Alzheimer's disease. *NeuroImage. Clinical*, *24*(101954), 101954.
3. Barry, C., Hayman, R., Burgess, N., & Jeffery, K. J. (2007). Experience-dependent rescaling of entorhinal grids. *Nature Neuroscience*, *10*(6), 682–684.
4. Berron, D., Vogel, J. W., Insel, P. S., Pereira, J. B., Xie, L., Wisse, L. E. M., Yushkevich, P. A., Palmqvist, S., Mattsson-Carlgen, N., Stomrud, E., Smith, R., Strandberg, O., & Hansson, O. (2021). Early stages of tau pathology and its associations with functional connectivity, atrophy and memory. *Brain: A Journal of Neurology*, *144*(9), 2771–2783.
5. Bierbrauer, A., Kunz, L., Gomes, C. A., Luhmann, M., Deuker, L., Getzmann, S., Wascher, E., Gajewski, P. D., Hengstler, J. G., Fernandez-Alvarez, M., Atienza, M., Cammisuli, D. M., Bonatti, F., Pruneti, C., Percepe, A., Bellaali, Y., Hanseeuw, B., Strange, B. A., Cantero, J. L., & Axmacher, N. (2020). Unmasking selective path integration deficits in Alzheimer's disease risk carriers. *Science Advances*, *6*(35), eaba1394.
6. Braak, H., & Braak, E. (1991). Neuropathological staging of Alzheimer-related changes. *Acta Neuropathologica*, *82*(4), 239–259.
7. Brandon, M. P., Bogaard, A. R., Libby, C. P., Connerney, M. A., Gupta, K., & Hasselmo, M. E. (2011). Reduction of theta rhythm dissociates grid cell spatial periodicity from directional tuning. *Science (New York, N.Y.)*, *332*(6029), 595–599.
8. Buetfering, C., Allen, K., & Monyer, H. (2014). Parvalbumin interneurons provide grid cell-driven recurrent inhibition in the medial entorhinal cortex. *Nature Neuroscience*, *17*(5), 710–718.
9. Burgess, N. (2008). Grid cells and theta as oscillatory interference: theory and predictions. *Hippocampus*, *18*(12), 1157–1174.

10. Burgess, N., Barry, C., & O'Keefe, J. (2007). An oscillatory interference model of grid cell firing. *Hippocampus*, *17*(9), 801–812.
11. Bush, D., Barry, C., Manson, D., & Burgess, N. (2015). Using grid cells for navigation. *Neuron*, *87*(3), 507–520.
12. Campbell, M. G., Ocko, S. A., Mallory, C. S., Low, I. I. C., Ganguli, S., & Giocomo, L. M. (2018). Principles governing the integration of landmark and self-motion cues in entorhinal cortical codes for navigation. *Nature Neuroscience*, *21*(8), 1096–1106.
13. Chen, G., Lu, Y., King, J. A., Cacucci, F., & Burgess, N. (2019). Differential influences of environment and self-motion on place and grid cell firing. *Nature Communications*, *10*(1), 630.
14. Chen, G., Manson, D., Cacucci, F., & Wills, T. J. (2016). Absence of visual input results in the disruption of grid cell firing in the mouse. *Current Biology: CB*, *26*(17), 2335–2342.
15. Cheng, I. H., Scarce-Levie, K., Legleiter, J., Palop, J. J., Gerstein, H., Bien-Ly, N., Puoliväli, J., Lesné, S., Ashe, K. H., Muchowski, P. J., & Mucke, L. (2007). Accelerating amyloid-beta fibrillization reduces oligomer levels and functional deficits in Alzheimer disease mouse models. *The Journal of Biological Chemistry*, *282*(33), 23818–23828.
16. Climer, J. R., Newman, E. L., & Hasselmo, M. E. (2013). Phase coding by grid cells in unconstrained environments: two-dimensional phase precession. *The European Journal of Neuroscience*, *38*(4), 2526–2541.
17. Couey, J. J., Witoelar, A., Zhang, S.-J., Zheng, K., Ye, J., Dunn, B., Czajkowski, R., Moser, M.-B., Moser, E. I., Roudi, Y., & Witter, M. P. (2013). Recurrent inhibitory circuitry as a mechanism for grid formation. *Nature Neuroscience*, *16*(3), 318–324.
18. Coughlan, G., Laczó, J., Hort, J., Minihane, A.-M., & Hornberger, M. (2018). Spatial navigation deficits - overlooked cognitive marker for preclinical Alzheimer disease? *Nature Reviews. Neurology*, *14*(8), 496–506.
19. Doeller, C. F., Barry, C., & Burgess, N. (2010). Evidence for grid cells in a human memory network. *Nature*, *463*(7281), 657–661.
20. Eliav, T., Geva-Sagiv, M., Yartsev, M. M., Finkelstein, A., Rubin, A., Las, L., & Ulanovsky, N. (2018). Nonoscillatory phase coding and synchronization in the bat hippocampal formation. *Cell*, *175*(4), 1119-1130.e15.
21. Fu, H., Rodriguez, G. A., Herman, M., Emrani, S., Nahmani, E., Barrett, G., Figueroa, H. Y., Goldberg, E., Hussaini, S. A., & Duff, K. E. (2017). Tau pathology induces excitatory neuron loss, grid cell dysfunction, and spatial memory deficits reminiscent of early Alzheimer's disease. *Neuron*, *93*(3), 533-541.e5.
22. Fyhn, M., Molden, S., Witter, M. P., Moser, E. I., & Moser, M.-B. (2004). Spatial representation in the entorhinal cortex. *Science (New York, N.Y.)*, *305*(5688), 1258–1264.
23. Gardner, R. J., Lu, L., Wernle, T., Moser, M.-B., & Moser, E. I. (2019). Correlation structure of grid cells is preserved during sleep. *Nature Neuroscience*, *22*(4), 598–608.
24. Gil, M., Ancau, M., Schlesiger, M. I., Neitz, A., Allen, K., De Marco, R. J., & Monyer, H. (2018). Impaired path integration in mice with disrupted grid cell firing. *Nature Neuroscience*, *21*(1), 81–91.
25. Hafting, T., Fyhn, M., Bonnevie, T., Moser, M.-B., & Moser, E. I. (2008). Hippocampus-independent phase precession in entorhinal grid cells. *Nature*, *453*(7199), 1248–1252.
26. Hafting, T., Fyhn, M., Molden, S., Moser, M.-B., & Moser, E. I. (2005). Microstructure of a spatial map in the entorhinal cortex. *Nature*, *436*(7052), 801–806.

27. Hasselmo, M. E., & Brandon, M. P. (2008). Linking cellular mechanisms to behavior: entorhinal persistent spiking and membrane potential oscillations may underlie path integration, grid cell firing, and episodic memory. *Neural Plasticity*, 2008, 658323.
28. Hong, S., Beja-Glasser, V. F., Nfonoyim, B. M., Frouin, A., Li, S., Ramakrishnan, S., Merry, K. M., Shi, Q., Rosenthal, A., Barres, B. A., Lemere, C. A., Selkoe, D. J., & Stevens, B. (2016). Complement and microglia mediate early synapse loss in Alzheimer mouse models. *Science (New York, N.Y.)*, 352(6286), 712–716.
29. Howett, D., Castegnaro, A., Krzywicka, K., Hagman, J., Marchment, D., Henson, R., Rio, M., King, J. A., Burgess, N., & Chan, D. (2019). Differentiation of mild cognitive impairment using an entorhinal cortex-based test of virtual reality navigation. *Brain: A Journal of Neurology*, 142(6), 1751–1766.
30. Jacob, P.-Y., Poucet, B., Liberge, M., Save, E., & Sargolini, F. (2014). Vestibular control of entorhinal cortex activity in spatial navigation. *Frontiers in Integrative Neuroscience*, 8, 38.
31. Jacobs, J., Weidemann, C. T., Miller, J. F., Solway, A., Burke, J. F., Wei, X.-X., Suthana, N., Sperling, M. R., Sharan, A. D., Fried, I., & Kahana, M. J. (2013). Direct recordings of grid-like neuronal activity in human spatial navigation. *Nature Neuroscience*, 16(9), 1188–1190.
32. Jeewajee, A., Barry, C., O’Keefe, J., & Burgess, N. (2008). Grid cells and theta as oscillatory interference: electrophysiological data from freely moving rats. *Hippocampus*, 18(12), 1175–1185.
33. Johnson, K. A., Schultz, A., Betensky, R. A., Becker, J. A., Sepulcre, J., Rentz, D., Mormino, E., Chhatwal, J., Amariglio, R., Papp, K., Marshall, G., Albers, M., Mauro, S., Pepin, L., Alverio, J., Judge, K., Philiossaint, M., Shoup, T., Yokell, D., ... Sperling, R. (2016). Tau positron emission tomographic imaging in aging and early Alzheimer disease. *Annals of Neurology*, 79(1), 110–119.
34. Jun, H., Bramian, A., Soma, S., Saito, T., Saido, T. C., & Igarashi, K. M. (2020). Disrupted place cell remapping and impaired grid cells in a knockin model of Alzheimer’s disease. *Neuron*, 107(6), 1095-1112.e6.
35. Kempter, R., Leibold, C., Buzsáki, G., Diba, K., & Schmidt, R. (2012). Quantifying circular-linear associations: hippocampal phase precession. *Journal of Neuroscience Methods*, 207(1), 113–124.
36. Koenig, J., Linder, A. N., Leutgeb, J. K., & Leutgeb, S. (2011). The spatial periodicity of grid cells is not sustained during reduced theta oscillations. *Science (New York, N.Y.)*, 332(6029), 592–595.
37. Kraus, B. J., Brandon, M. P., Robinson, R. J., 2nd, Connerney, M. A., Hasselmo, M. E., & Eichenbaum, H. (2015). During running in place, grid cells integrate elapsed time and distance run. *Neuron*, 88(3), 578–589.
38. Kropff, E., Carmichael, J. E., Moser, E. I., & Moser, M.-B. (2021). Frequency of theta rhythm is controlled by acceleration, but not speed, in running rats. *Neuron*, 109(6), 1029-1039.e8.
39. Kropff, E., Carmichael, J. E., Moser, M.-B., & Moser, E. I. (2015). Speed cells in the medial entorhinal cortex. *Nature*, 523(7561), 419–424.
40. Krupic, J., Bauza, M., Burton, S., Barry, C., & O’Keefe, J. (2015). Grid cell symmetry is shaped by environmental geometry. *Nature*, 518(7538), 232–235.

41. Krupic, J., Burgess, N., & O'Keefe, J. (2012). Neural representations of location composed of spatially periodic bands. *Science (New York, N.Y.)*, 337(6096), 853–857.
42. Kunz, L., Schröder, T. N., Lee, H., Montag, C., Lachmann, B., Sariyska, R., Reuter, M., Stirnberg, R., Stöcker, T., Messing-Floeter, P. C., Fell, J., Doeller, C. F., & Axmacher, N. (2015). Reduced grid-cell-like representations in adults at genetic risk for Alzheimer's disease. *Science (New York, N.Y.)*, 350(6259), 430–433.
43. Mahmood, O., Adamo, D., Briceno, E., & Moffat, S. D. (2009). Age differences in visual path integration. *Behavioural Brain Research*, 205(1), 88–95.
44. Maurer, A. P., Vanrhoads, S. R., Sutherland, G. R., Lipa, P., & McNaughton, B. L. (2005). Self-motion and the origin of differential spatial scaling along the septo-temporal axis of the hippocampus. *Hippocampus*, 15(7), 841–852.
45. McNaughton, B. L., Battaglia, F. P., Jensen, O., Moser, E. I., & Moser, M.-B. (2006). Path integration and the neural basis of the “cognitive map.” *Nature Reviews. Neuroscience*, 7(8), 663–678.
46. Mersereau, R. M. (1979). The processing of hexagonally sampled two-dimensional signals. *Proceedings of the IEEE. Institute of Electrical and Electronics Engineers*, 67(6), 930–949.
47. Miao, C., Cao, Q., Moser, M.-B., & Moser, E. I. (2017). Parvalbumin and somatostatin interneurons control different space-coding networks in the medial entorhinal cortex. *Cell*, 171(3), 507–521.e17.
48. Mittelstaedt, M.-L., & Mittelstaedt, H. (1980). Homing by path integration in a mammal. *The Science of Nature*, 67(11), 566–567.
49. Mokrisova, I., Laczó, J., Andel, R., Gazova, I., Vyhnalek, M., Nedelska, Z., Levcik, D., Cerman, J., Vlcek, K., & Hort, J. (2016). Real-space path integration is impaired in Alzheimer's disease and mild cognitive impairment. *Behavioural Brain Research*, 307, 150–158.
50. Mucke, L., Masliah, E., Yu, G. Q., Mallory, M., Rockenstein, E. M., Tatsuno, G., Hu, K., Kholodenko, D., Johnson-Wood, K., & McConlogue, L. (2000). High-level neuronal expression of abeta 1-42 in wild-type human amyloid protein precursor transgenic mice: synaptotoxicity without plaque formation. *The Journal of Neuroscience: The Official Journal of the Society for Neuroscience*, 20(11), 4050–4058.
51. Nagahara, A. H., Mateling, M., Kovacs, I., Wang, L., Eggert, S., Rockenstein, E., Koo, E. H., Masliah, E., & Tuszynski, M. H. (2013). Early BDNF treatment ameliorates cell loss in the entorhinal cortex of APP transgenic mice. *The Journal of Neuroscience: The Official Journal of the Society for Neuroscience*, 33(39), 15596–15602.
52. Navratilova, Z., Giocomo, L. M., Fellous, J.-M., Hasselmo, M. E., & McNaughton, B. L. (2012). Phase precession and variable spatial scaling in a periodic attractor map model of medial entorhinal grid cells with realistic after-spike dynamics. *Hippocampus*, 22(4), 772–789.
53. O'Keefe, J., & Recce, M. L. (1993). Phase relationship between hippocampal place units and the EEG theta rhythm. *Hippocampus*, 3(3), 317–330.
54. Ossenkoppele, R., Schonhaut, D. R., Schöll, M., Lockhart, S. N., Ayakta, N., Baker, S. L., O'Neil, J. P., Janabi, M., Lazaris, A., Cantwell, A., Vogel, J., Santos, M., Miller, Z. A., Bettcher, B. M., Vessel, K. A., Kramer, J. H., Gorno-Tempini, M. L., Miller, B. L., Jagust, W. J., & Rabinovici, G. D. (2016). Tau PET patterns mirror clinical and neuroanatomical variability in Alzheimer's disease. *Brain: A Journal of Neurology*, 139(5), 1551–1567.

55. Palop, J. J., Chin, J., Roberson, E. D., Wang, J., Thwin, M. T., Bien-Ly, N., Yoo, J., Ho, K. O., Yu, G.-Q., Kreitzer, A., Finkbeiner, S., Noebels, J. L., & Mucke, L. (2007). Aberrant excitatory neuronal activity and compensatory remodeling of inhibitory hippocampal circuits in mouse models of Alzheimer's disease. *Neuron*, *55*(5), 697–711.
56. Pérez-Escobar, J. A., Kornienko, O., Latuske, P., Kohler, L., & Allen, K. (2016). Visual landmarks sharpen grid cell metric and confer context specificity to neurons of the medial entorhinal cortex. *ELife*, *5*. <https://doi.org/10.7554/eLife.16937>
57. Qasim, S. E., Fried, I., & Jacobs, J. (2021). Phase precession in the human hippocampus and entorhinal cortex. *Cell*, *184*(12), 3242–3255.e10.
58. Ravassard, P., Kees, A., Willers, B., Ho, D., Aharoni, D. A., Cushman, J., Aghajan, Z. M., & Mehta, M. R. (2013). Multisensory control of hippocampal spatiotemporal selectivity. *Science (New York, N.Y.)*, *340*(6138), 1342–1346.
59. Ridler, T., Witton, J., Phillips, K. G., Randall, A. D., & Brown, J. T. (2020). Impaired speed encoding and grid cell periodicity in a mouse model of tauopathy. *ELife*, *9*. <https://doi.org/10.7554/eLife.59045>
60. Saganich, M. J., Schroeder, B. E., Galvan, V., Bredesen, D. E., Koo, E. H., & Heinemann, S. F. (2006). Deficits in synaptic transmission and learning in amyloid precursor protein (APP) transgenic mice require C-terminal cleavage of APP. *The Journal of Neuroscience: The Official Journal of the Society for Neuroscience*, *26*(52), 13428–13436.
61. Sargolini, F., Fyhn, M., Hafting, T., McNaughton, B. L., Witter, M. P., Moser, M.-B., & Moser, E. I. (2006). Conjunctive representation of position, direction, and velocity in entorhinal cortex. *Science (New York, N.Y.)*, *312*(5774), 758–762.
62. Segen, V., Ying, J., Morgan, E., Brandon, M., & Wolbers, T. (2022). Path integration in normal aging and Alzheimer's disease. *Trends in Cognitive Sciences*, *26*(2), 142–158.
63. Skaggs, W. E., McNaughton, B. L., Wilson, M. A., & Barnes, C. A. (1996). Theta phase precession in hippocampal neuronal populations and the compression of temporal sequences. *Hippocampus*, *6*(2), 149–172.
64. Stangl, M., Kanitscheider, I., Riemer, M., Fiete, I., & Wolbers, T. (2020). Sources of path integration error in young and aging humans. *Nature Communications*, *11*(1), 2626.
65. Stensola, H., Stensola, T., Solstad, T., Frøland, K., Moser, M.-B., & Moser, E. I. (2012). The entorhinal grid map is discretized. *Nature*, *492*(7427), 72–78.
66. Stensola, T., & Moser, E. I. (2016). Grid cells and spatial maps in entorhinal cortex and hippocampus. In *Research and Perspectives in Neurosciences* (pp. 59–80). Springer International Publishing.
67. Stensola, T., Stensola, H., Moser, M.-B., & Moser, E. I. (2015). Shearing-induced asymmetry in entorhinal grid cells. *Nature*, *518*(7538), 207–212.
68. Terrazas, A., Krause, M., Lipa, P., Gothard, K. M., Barnes, C. A., & McNaughton, B. L. (2005). Self-motion and the hippocampal spatial metric. *The Journal of Neuroscience: The Official Journal of the Society for Neuroscience*, *25*(35), 8085–8096.
69. Trettel, S. G., Trimper, J. B., Hwaun, E., Fiete, I. R., & Colgin, L. L. (2019). Grid cell co-activity patterns during sleep reflect spatial overlap of grid fields during active behaviors. *Nature Neuroscience*, *22*(4), 609–617.
70. Verret, L., Mann, E. O., Hang, G. B., Barth, A. M. I., Cobos, I., Ho, K., Devidze, N., Masliah, E., Kreitzer, A. C., Mody, I., Mucke, L., & Palop, J. J. (2012). Inhibitory interneuron deficit links altered network activity and cognitive dysfunction in Alzheimer model. *Cell*, *149*(3), 708–721.

71. Winter, S. S., Clark, B. J., & Taube, J. S. (2015). Spatial navigation. Disruption of the head direction cell network impairs the parahippocampal grid cell signal. *Science (New York, N.Y.)*, 347(6224), 870–874.
72. Winter, S. S., Mehlman, M. L., Clark, B. J., & Taube, J. S. (2015). Passive transport disrupts grid signals in the parahippocampal cortex. *Current Biology: CB*, 25(19), 2493–2502.
73. Wright, A. L., Zinn, R., Hohensinn, B., Konen, L. M., Beynon, S. B., Tan, R. P., Clark, I. A., Abdipranoto, A., & Vissel, B. (2013). Neuroinflammation and neuronal loss precede A $\beta$  plaque deposition in the hAPP-J20 mouse model of Alzheimer’s disease. *PloS One*, 8(4), e59586.
74. Ying, J., Keinath, A. T., Lavoie, R., Vigneault, E., El Mestikawy, S., & Brandon, M. P. (2022). Disruption of the grid cell network in a mouse model of early Alzheimer’s disease. *Nature Communications*, 13(1), 886.
75. Young, A. L., Oxtoby, N. P., Daga, P., Cash, D. M., Fox, N. C., Ourselin, S., Schott, J. M., Alexander, D. C., & Alzheimer’s Disease Neuroimaging Initiative. (2014). A data-driven model of biomarker changes in sporadic Alzheimer’s disease. *Brain: A Journal of Neurology*, 137(Pt 9), 2564–2577.
76. Zhi, Y., & Cox, D. (2021). Neurodegenerative damage reduces firing coherence in a continuous attractor model of grid cells. *Physical Review. E*, 104(4–1), 044414.
77. Zutshi, I., Leutgeb, J. K., & Leutgeb, S. (2017). Theta sequences of grid cell populations can provide a movement-direction signal. *Current Opinion in Behavioral Sciences*, 17, 147–154.

## **Chapter 4: General Discussion**

In this thesis, we investigated how the medial entorhinal grid cell network is disrupted during the early stages of pathology in the J20 (APP) mouse model of AD. We conducted single-unit recordings in the MEC and CA1 in APP mice between the ages of 3-7 months, an age range that precedes the widespread expression of amyloid plaques in this transgenic model [27]. APP-y grid cells had reduced temporal synchrony with local HD cells and interneurons. APP-a grid cells had reduced spatial periodicity and spatial stability, along with reduced temporal synchrony. These results highlight a progressive impairment of grid cell coding throughout early pathology. Further analysis revealed that disrupted grid cell coding in APP-a mice reflected an increased influence of environmental geometry instead of self-motion cues. APP-a grid cells were spatially unstable towards the center but not near the borders, exhibited reduced theta modulation and theta phase precession, and had increased spiking aligned parallel to the borders. This progressive grid cell coding impairment also correlated to reduced path integration performance in a food-foraging task during complete darkness. In parallel, we found that spatial coding of entorhinal non-grid cells and CA1 place cells remained intact. Together, these results 1) support the viability of grid cell integrity and spatial navigation deficits as early markers of AD; 2) suggest that early AD grid cell impairments reflect a preferential spatial alignment to the external world and likely cause path integration deficits in preclinical individuals via reduced integration of self-motion cues.

### **4.1. How can grid cell impairments explain path integration deficits**

Grid cells require excitatory, inhibitory and head direction inputs [115,122,130,133]. A portion of MEC interneurons are also speed cells [131]. Our temporal synchrony analysis suggests that grid cells could not effectively integrate speed and heading information on short time scales. Proprioceptive and vestibular inputs are the dominant sources of self-motion information in the

food-foraging task during complete darkness. An inability to effectively integrate these cues by grid cells on the outbound paths may account for homing errors despite grid hexagonal symmetry remaining intact. Of course, there may be other explanations (not mutually exclusive) for the early path integration impairments in APP-y mice. For instance, APP-y mice may have deficient higher level cognitive processing involving working memory, attention and postural control [5]. A previous study showed that APP mice had impaired working memory performance on the radial arm maze by 3-4 months of age [222]. Reduced working memory might affect one's ability to remember longer outbound paths, which in turn would affect homing behavior [223]. These higher cognitive processes may also account for the path integration deficits in healthy adults or AD patients, but data in support of these theories remain sparse [5]. An alternative explanation is that these early path integration impairments are caused by deficits in other neural systems involved in path integration, such as the postsubiculum, as well as various thalamic and brainstem nuclei [224]. Other undetermined factors caused by transgene expression may have also caused path integration deficits in APP-y mice.

Numerous grid cell impairments could explain the more pronounced path integration deficits in APP-a mice. Reduced grid cell spatial periodicity is the obvious culprit given that a previous study showed a causal link between grid cell coding and path integration performance in healthy mice [113]. Greater grid spatial instability towards the environmental center but not near the borders further suggests that the underlying explanation for the behavioral impairment is the grid cell network's inability to process self-motion cues. Reduced theta modulation and distance coding via theta phase precession support this interpretation. There was a significant reduction in theta rhythmic grid cells compared to other groups, suggesting that they could not effectively integrate self-motion cues via precisely-timed theta-related mechanisms [52,110,122,127,225–

230]. As consequence, there was also a reduction in theta phase-processing grid cells. Computational models convey the significance of reduced theta modulation and phase precession. The oscillatory interference model posits that grid cells integrate heading and speed information via the interference of theta oscillations between upstream VCOs [231,232]. When multiple theta-modulated VCOs with angular offsets of  $60^\circ$  evenly spaced around  $360^\circ$  oscillate in phase, the thresholded sum of their directional interference patterns in a band-like manner produces grid hexagonal periodicity and theta phase precession. Alternatively, phase precession has also been successfully modeled in continuous attractor networks and is proposed to be a ‘look-ahead’ mechanism to plan future routes [233]. Continuous attractor models generate grid cell activity via intrinsic network connectivity that integrates heading and speed information [26]. Both oscillatory and continuous attractor models could form the foundations of a path integration system that allows for continuous tracking of position along directions offset by  $60^\circ$  and computation of translational vectors toward goal locations. The lack of phase precession in many APP-a grid cells could impair their ability to integrate self-motion and plan future paths in the environment’s center. Indeed, when path integrating in the food-foraging task, in addition to increased travel distance and angular errors on the homing path, APP-a mice spent more time along the environment periphery. This suggests that APP-a mice could not plan effective routes back to the refuge and instead relied on a simpler but inefficient thigmotaxic strategy.

This thigmotaxic strategy is particularly noteworthy given that APP-a grid cells had increased firing aligned parallel to the borders. Our Fourier analysis revealed that disrupted grid cell spatial periodicity did not merely reflect random spatial noise, but rather an increase in spatial alignment to the enclosure’s geometry. This result persisted at the population level and was therefore not biased by our grid cell selection criteria. Environmental geometry appears to be the

strongest grid anchor and is likely the only source of allocentric influence in the food-foraging task [84,90,234]. Increased spiking aligned parallel to the borders suggests that grid cells cannot integrate self-motion cues and may rely more on the spatial layout of the external world to compensate. This interpretation might explain why APP-a mice were more thigmotaxic on the homing path than other groups. On a related note, APP-a mice were also more thigmotaxic on outbound paths, whereas APP-y mice were not (data not shown).

## **4.2. Parallels to human AD literature**

In general, path integration impairments in AD patients are thought to arise from a combination of degraded sensory processing along with tauopathy and amyloidopathy directly affecting the neural substrates that govern path integration that include, but are not limited to, the grid cell network [5]. Path integration deficits correlate with greater levels of CSF amyloid and tau [11], as well as *APOE-ε4* status [12,13]. Multiple mouse models of tauopathy and amyloidopathy exhibit grid and place cell coding deficits that correlate with impaired spatial behavior towards the later stages of pathology [214–221]. In the rTg4510 tau model, impaired grid cell firing was accompanied by reduced firing rate-by-speed modulation in MEC cells [221]. Tauopathy might therefore reduce integration of movement speed which is necessary for grid cell firing and path integration [94,112]. Place cells in rTg4510 mice were also spatially unstable and not anchored to any particular location [219]. Similar findings were observed in pure amyloid and triple transgenic mouse models [215,217]. The consistency of reported impairments despite the inherent differences of mouse models provides compelling evidence that tauopathy and amyloidopathy target the neural substrates of path integration.

The key novelty of our findings versus other AD mouse model studies is that we restricted our experimental timeline to an age range which just preceded the widespread expression of

amyloid plaques. Our results therefore provide the first evidence at the single cell level in an AD mouse model that there is a progressive impairment in the grid cell network across early pathology. In human subjects, *APOE*- $\epsilon$ 4 effects on path integration performance appear to worsen across age, suggesting that grid-like representations may undergo a similar progressive impairment [12]. In general, AD-related pathological effects on PI are likely to take place early on in life given that grid-like representations are impaired in *APOE*- $\epsilon$ 4 carriers as young as 18 years of age [9]. For instance, there is a profound loss of layer 2 EC neurons in individuals with mild forms of AD [235,236]. Progressive EC neuronal loss is also observed in AD mouse models [237,238], and the majority of grid cells are in layer 2. AD pathology also alters inhibitory circuits [239], while grid cells require inhibitory inputs [130,132,133]. A proportion of PV interneurons that innervate grid cells are also speed-modulated [93,130,131], suggesting impaired integration of movement speed by grid cells [221]. Lastly, certain types of neurons characterized by their protein composition may be particularly vulnerable to AD pathology. Aside from PV interneurons, reelin-positive neurons in EC layer 2 expressed intracellular A $\beta$  in a rat model of amyloidosis before the expression of A $\beta$  plaques [240]. Given that the layer 2 stellate cell population involves various spatially-tuned cell types including grid cells [241], the grid cell network could be particularly vulnerable to early AD pathogenesis.

### **4.3. Parallels to other APP mouse models**

Place cells have also been recorded in other APP mouse models. The spatial tuning of place cells in Tg2576 mice remained intact at the earliest incidence of A $\beta$  plaques [214], similar to our results. In the 3xTg triple transgenic mouse model of both APP and tau pathology, place cells exhibited spatial instability on a linear track preceding the expression of amyloid plaques [217]. One explanation for this result is the additional presence of tau

pathology in 3xTg mice. In a different study involving a chimeric APP mouse model where the onset of APP expression could be controlled, place cell stability was also impaired on a linear track [215]. However, this disruption took place 9.5 months following APP expression, a pathogenic timepoint that is much later than ours. Lastly, a study reported that grid cells and place cells were disrupted in an APP knock-in mouse model [218]. Despite already have moderate levels of plaque formation throughout the brain, these young APP knock-in mice still did not show any impaired place cell coding, which is consistent with our findings. However, Jun et al. suffers from extremely low sample sizes of recorded cells and inappropriate statistical designs. For these reasons, the conclusions of their study are difficult to interpret. Our place cell results are best comparable to those in Tg2576 mice [214] because recordings were done in an open field during the earliest detection of amyloid plaques. From this perspective, our results are consistent with what is currently known about A $\beta$  pathology and place cell coding. To this growing body of knowledge, we show that impairments in grid cell firing emerge prior to place cell disruption.

Grid cell spatial periodicity is also disrupted during late pathology in both tau and amyloid mouse models - EC-Tau, rTg4510 and APP-KI [218,220,221]. All studies, including ours, assessed spatial periodicity using the gridness score (a measurement of hexagonal symmetry in the spatial firing pattern). Our Fourier analysis suggests that the loss of grid spatial periodicity does not reflect increased random noise, but rather stronger spatial alignment parallel to the borders. In a two-dimensional continuous attractor neural network model of grid cell activity, simulated AD synaptic damage resulting from the propagation of neurofibrillary tau tangles disrupted grid cell hexagonal symmetry [242]. Similar to our APP-a mice, simulated healthy grid cells had three significant Fourier components offset by 60°. In

contrast, simulated damaged grid cells had two, one, or no components depending on the magnitude of synaptic impairment. The similarities between these model simulations of tau propagation and our experimental results in an amyloid mouse model suggest that despite the different molecular pathways of tauopathy and amyloidopathy, the loss of grid hexagonal symmetry across multiple AD mouse models might initially occur through a similar process where the grid map detaches from the individual's self-motion while staying anchored to the external world.

#### **4.4. Potential circuit-level mechanisms for grid cell impairments**

Our results address several possible circuit-level explanations that could underlie reduced grid cell coding in APP mice. Prior studies have shown that inputs from the anterior thalamic nuclei, the dorsal hippocampus, and the medial septum are each independently necessary for normal grid cell activity [115,122,128,129]. MEC HD cells did not show any impairments in directional tuning, suggesting that projections from the anterior thalamic nuclei remained intact. CA1 place cells remained spatially selective, stable, and had high firing rates, indicating that reduced feedback from the hippocampus cannot explain grid cell deficits in APP-a mice.

The medial septum might be an area of interest of further investigation because local field potential theta frequencies in APP-y and APP-a mice were slower by  $\sim 0.2$  Hz than nTG mice. It has been shown that reduction of local field potential theta oscillations via medial septal inactivation disrupted both grid cell spatial periodicity and theta rhythmicity in healthy animals [128]. Considering that APP-a grid cells had reduced spatial periodicity and theta rhythmicity, pacing local field potential theta at faster frequencies by optogenetically manipulating PV interneurons (the main GABAergic cell type in the medial septum) [243–

245] might constitute a rescue approach that would lock the spike-phase relationship of grid cells to the stimulated frequency. Pure oscillatory interference models or hybrid models containing elements of both oscillatory interference and continuous attractors posit that the baseline grid cell frequency is driven by theta oscillations from the medial septum. Recalibrating the baseline grid cell frequency to a normal endogenous range might rescue spatial periodicity, intrinsic theta rhythmicity and theta phase precession. A recent study adopted this optogenetic strategy in healthy rats by pacing theta beyond the normal endogenous range of 6-10 Hz [245]. Interestingly, grid cells kept their spatial patterns but there was a complete abolishment of theta phase precession. These results suggest that septal theta inputs may not be necessary for grid cell spatial patterns but do affect grid cell temporal properties such as theta phase precession.

However, APP-y grid cells do not have reduced spatial periodicity, intrinsic theta rhythmicity or theta phase precession. Yet, APP-y mice local field potential theta was still 0.2 Hz slower. This optogenetic rescue might therefore not rescue spatial periodicity, intrinsic theta rhythmicity and theta phase precession. Instead, restoring local field potential theta (and subsequently increasing grid cell intrinsic frequency) might rescue the reduced grid cell temporal synchrony with local HD cells and interneurons that both APP-y and APP-a mice exhibit. In either case, rescuing any of these grid cell impairments could potentially improve path integration performance. Ultimately, optogenetic pacing of medial septal theta inputs is perhaps the most promising circuit-level manipulation to consider for future experiments. A rescue of grid cell properties and a simultaneous improvement in path integration would establish causal evidence that grid cells cause path integration impairments in preclinical individuals.

Alternatively, perhaps this 0.2 Hz reduction in local field potential theta is minor and insignificant. Considering that theta power and speed modulation of theta were preserved in APP mice, medial septal theta-generating inputs to the MEC may be unaffected. Nevertheless, our findings could still indicate a subtle impairment of basal forebrain inputs that innervate the grid cell network; one candidate could be decreased septal cholinergic inputs [246], as a selective loss of basal forebrain cholinergic neurons in the nucleus basalis of Meynert is observed in familial AD patients [247,248].

#### **4.5. Grid cells and path integration tasks have clinical value**

To date, numerous AD clinical trials have failed due to the difficulty in identifying the initial stages of pathology such that interventions are applied too late [5]. For instance, current cognitive assessments – the dominant method for AD diagnosis – rely heavily on episodic memory tests. Yet, episodic memory loss is also common in other pathologies such as frontotemporal dementia or general aging [211], and appears to be more sensitive to later stages of AD – thereby offering limited clinical utility [6,212]. Therefore, the true value of grid cell integrity (or grid-like fMRI representations in human subjects) and path integration performance lies in their predictive power (along with other biomarkers such as amyloid and tau) to accurately identify individuals most suitable for early intervention. Grid-like fMRI and path integration performance may also serve as assessment tools to determine the efficacy of treatments. Beyond clinical diagnosis, pinpointing individuals most at risk of AD could be particularly useful when identifying novel therapeutic targets. It is impractical to run large-scale molecular or genome-wide studies in the entire population in hopes of determining what other molecular or genetic markers could be causing AD. However, narrowing the subject pool of interest renders these questions more feasible to ask.

Our results also show for the first time that path integration behavioral deficits are present in an AD mouse model during early pathology. These findings further justify the implementation of path integration tasks as a clinical diagnostic tool. AD clinical diagnosis predominantly relies on the appearance of cognitive impairments in subjects, yet there is a great discrepancy in sensitivity between modern biomarkers and available cognitive markers. *In-vivo* A $\beta$  and tau biomarkers including PET, CSF and blood biomarkers show changes decades before clinical symptoms, yet their presence does not guarantee the appearance of cognitive impairments which may be influenced by risk factors and individual variability [186,206].

Likewise, our behavioral findings further support cross-species translation between animal models and human subjects. Path integration tasks are relatively similar in rodents and humans. Our food-foraging task involves the same elements of homing behavior observed in the triangle completion task commonly used in human subjects. The efficacy of cross-species translation relies on standardization. Many intervention studies in rodents rely on the Morris water maze, a task that is infrequently used in AD cognitive assessments [6,210,212]. Given their simplicity, path integrations tasks allow for similar experimental setups between rodents and humans which is ideal for bridging the research gap across species. With that said, there are still minor differences between path integration tasks in rodents and humans, and a truly standardized task between species would be ideal.

Lastly, path integration tasks are practical because they are economically viable. For instance, they can be adapted into computerized tasks that can be performed using smartphones, desktop computers or tablets [5]. Importantly, computerized tasks are inexpensive and yield comparable results to real-life navigation [249]. On a related note, our results suggest that behavioral readouts of path integration performance offer a window into grid cell or grid fMRI

integrity without the need for time-consuming and expensive single-cell recordings. Large-scale path integration behavioral studies in the general population without the costs incurred by brain imaging is economical and could accelerate clinical intervention.

## **Conclusion and summary**

To investigate the neural circuit operations that may cause path integration behavioral deficits in preclinical AD patients, we conducted *in-vivo* electrophysiological recordings of spatially-tuned neurons in the MEC and region CA1 of the hippocampus in the J20 transgenic A $\beta$  mouse model of early AD. Entorhinal grid cells showed reduced spatial periodicity, spatial stability, and synchrony with interneurons and head-direction cells. In contrast, the spatial coding of non-grid cells within the MEC, and place cells within CA1, remained intact. Grid cell deficits emerged at the earliest incidence of A $\beta$  fibril deposition and correlated with impaired spatial memory performance in a path integration task. Further analysis revealed that environmental geometry exerted greater influence on J20 grid cell coding than self-motion. J20 grid cells were spatially unstable towards the center of the square arena but not near the borders, exhibited impaired integration of distance travelled via theta phase precession, and had increased spiking aligned parallel to the borders. Our results suggest that early AD grid cell impairments reflect a preferential alignment to the external world and likely cause path integration deficits in preclinical individuals via reduced integration of self-motion cues. More broadly, our results suggest that grid cell integrity (or grid-like fMRI representations in human subjects) and path integration performance are sensitive clinical early AD diagnostic tools and valuable assessment metrics of therapeutic efficacy.

## References

1. (2022) 2022 Alzheimer's disease facts and figures. *Alzheimers. Dement.* 18, 700–789
2. Alzheimer's Disease International (2021) World Alzheimer Report 2021. Journey through the diagnosis of dementia
3. Velandia, P.P. *et al.* (2022) Global and regional spending on dementia care from 2000-2019 and expected future health spending scenarios from 2020-2050: An economic modelling exercise. *EClinicalMedicine* 45, 101337
4. Panza, F. *et al.* (2019) A critical appraisal of amyloid- $\beta$ -targeting therapies for Alzheimer disease. *Nat. Rev. Neurol.* 15, 73–88
5. Segen, V. *et al.* (2022) Path integration in normal aging and Alzheimer's disease. *Trends Cogn. Sci.* 26, 142–158
6. Coughlan, G. *et al.* (2018) Spatial navigation deficits - overlooked cognitive marker for preclinical Alzheimer disease? *Nat. Rev. Neurol.* 14, 496–506
7. Mittelstaedt, M.-L. and Mittelstaedt, H. (1980) Homing by path integration in a mammal. *Sci. Nat.* 67, 566–567
8. Etienne, A.S. and Jeffery, K.J. (2004) Path integration in mammals. *Hippocampus* 14, 180–192
9. Kunz, L. *et al.* (2015) Reduced grid-cell-like representations in adults at genetic risk for Alzheimer's disease. *Science* 350, 430–433
10. Mokrisova, I. *et al.* (2016) Real-space path integration is impaired in Alzheimer's disease and mild cognitive impairment. *Behav. Brain Res.* 307, 150–158
11. Howett, D. *et al.* (2019) Differentiation of mild cognitive impairment using an entorhinal cortex-based test of virtual reality navigation. *Brain* 142, 1751–1766
12. Bierbrauer, A. *et al.* (2020) Unmasking selective path integration deficits in Alzheimer's disease risk carriers. *Sci. Adv.* 6, eaba1394
13. Coughlan, G. *et al.* (2020) Functional connectivity between the entorhinal and posterior cingulate cortices underpins navigation discrepancies in at-risk Alzheimer's disease. *Neurobiol. Aging* 90, 110–118
14. Morris, R.G. *et al.* (1982) Place navigation impaired in rats with hippocampal lesions. *Nature* 297, 681–683
15. Smith, M.L. and Milner, B. (1981) The role of the right hippocampus in the recall of spatial location. *Neuropsychologia* 19, 781–793
16. Steffenach, H.-A. *et al.* (2005) Spatial memory in the rat requires the dorsolateral band of the entorhinal cortex. *Neuron* 45, 301–313
17. Hafting, T. *et al.* (2005) Microstructure of a spatial map in the entorhinal cortex. *Nature* 436, 801–806
18. Sargolini, F. *et al.* (2006) Conjunctive representation of position, direction, and velocity in entorhinal cortex. *Science* 312, 758–762
19. O'Keefe, J. and Dostrovsky, J. (1971) The hippocampus as a spatial map. Preliminary evidence from unit activity in the freely-moving rat. *Brain Res.* 34, 171–175
20. Ekstrom, A.D. *et al.* (2003) Cellular networks underlying human spatial navigation. *Nature* 425, 184–188
21. Jacobs, J. *et al.* (2013) Direct recordings of grid-like neuronal activity in human spatial navigation. *Nat. Neurosci.* 16, 1188–1190

22. Hasselmo, M.E. *et al.* (2017) Models of spatial and temporal dimensions of memory. *Curr. Opin. Behav. Sci.* 17, 27–33
23. O’Keefe, J. and Nadel, L. (1978) *The Hippocampus as a Cognitive Map*, Oxford University Press
24. Samsonovich, A. and McNaughton, B.L. (1997) Path integration and cognitive mapping in a continuous attractor neural network model. *J. Neurosci.* 17, 5900–5920
25. Burgess, N. and O’Keefe, J. (1996) Neuronal computations underlying the firing of place cells and their role in navigation. *Hippocampus* 6, 749–762
26. McNaughton, B.L. *et al.* (2006) Path integration and the neural basis of the “cognitive map.” *Nat. Rev. Neurosci.* 7, 663–678
27. Mucke, L. *et al.* (2000) High-level neuronal expression of abeta 1-42 in wild-type human amyloid protein precursor transgenic mice: synaptotoxicity without plaque formation. *J. Neurosci.* 20, 4050–4058
28. Gallistel, C.R. (1990) *The organization of learning*, MIT Press
29. Mursell, J.L. (1922) The stimulus-response relation. *Psychol. Rev.* 29, 146–162
30. Packard, M.G. and McGaugh, J.L. (1992) Double dissociation of fornix and caudate nucleus lesions on acquisition of two water maze tasks: further evidence for multiple memory systems. *Behav. Neurosci.* 106, 439–446
31. Tolman, E.C. (1948) Cognitive maps in rats and men. *Psychol. Rev.* 55, 189–208
32. Fyhn, M. *et al.* (2004) Spatial representation in the entorhinal cortex. *Science* 305, 1258–1264
33. Burwell, R.D. and Amaral, D.G. (1998) Perirhinal and postrhinal cortices of the rat: interconnectivity and connections with the entorhinal cortex. *J. Comp. Neurol.* 391, 293–321
34. Burwell, R.D. and Amaral, D.G. (1998) Cortical afferents of the perirhinal, postrhinal, and entorhinal cortices of the rat. *J. Comp. Neurol.* 398, 179–205
35. Furtak, S.C. *et al.* (2007) Functional neuroanatomy of the parahippocampal region in the rat: the perirhinal and postrhinal cortices. *Hippocampus* 17, 709–722
36. Caballero-Bleda, M. and Witter, M.P. (1993) Regional and laminar organization of projections from the presubiculum and parasubiculum to the entorhinal cortex: an anterograde tracing study in the rat. *J. Comp. Neurol.* 328, 115–129
37. Vogt, B.A. and Miller, M.W. (1983) Cortical connections between rat cingulate cortex and visual, motor, and postsubicular cortices. *J. Comp. Neurol.* 216, 192–210
38. van Groen, T. and Wyss, J.M. (1990) The connections of presubiculum and parasubiculum in the rat. *Brain Res.* 518, 227–243
39. Shibata, H. (1993) Direct projections from the anterior thalamic nuclei to the retrohippocampal region in the rat. *J. Comp. Neurol.* 337, 431–445
40. Canto, C.B. *et al.* (2008) What does the anatomical organization of the entorhinal cortex tell us? *Neural Plast.* 2008, 381243
41. van Strien, N.M. *et al.* (2009) The anatomy of memory: an interactive overview of the parahippocampal-hippocampal network. *Nat. Rev. Neurosci.* 10, 272–282
42. Sekino, Y. *et al.* (1997) Delayed signal propagation via CA2 in rat hippocampal slices revealed by optical recording. *J. Neurophysiol.* 78, 1662–1668
43. Kohara, K. *et al.* (2014) Cell type-specific genetic and optogenetic tools reveal hippocampal CA2 circuits. *Nat. Neurosci.* 17, 269–279
44. Chevaleyre, V. and Siegelbaum, S.A. (2010) Strong CA2 pyramidal neuron synapses define a powerful disinaptic cortico-hippocampal loop. *Neuron* 66, 560–572

45. Hjorth-Simonsen, A. and Jeune, B. (1972) Origin and termination of the hippocampal perforant path in the rat studied by silver impregnation. *J. Comp. Neurol.* 144, 215–232
46. Hjorth-Simonsen, A. (1972) Projection of the lateral part of the entorhinal area to the hippocampus and fascia dentata. *J. Comp. Neurol.* 146, 219–232
47. Witter, M.P. (2007) Intrinsic and extrinsic wiring of CA3: indications for connectional heterogeneity. *Learn. Mem.* 14, 705–713
48. Kitamura, T. *et al.* (2014) Island cells control temporal association memory. *Science* 343, 896–901
49. O’Keefe, J. (1976) Place units in the hippocampus of the freely moving rat. *Exp. Neurol.* 51, 78–109
50. Wilson, M.A. and McNaughton, B.L. (1993) Dynamics of the hippocampal ensemble code for space. *Science* 261, 1055–1058
51. Jung, M.W. *et al.* (1994) Comparison of spatial firing characteristics of units in dorsal and ventral hippocampus of the rat. *J. Neurosci.* 14, 7347–7356
52. Maurer, A.P. *et al.* (2005) Self-motion and the origin of differential spatial scaling along the septo-temporal axis of the hippocampus. *Hippocampus* 15, 841–852
53. Kjelstrup, K.B. *et al.* (2008) Finite scale of spatial representation in the hippocampus. *Science* 321, 140–143
54. Rich, P.D. *et al.* (2014) Place cells. Large environments reveal the statistical structure governing hippocampal representations. *Science* 345, 814–817
55. O’Keefe, J. and Conway, D.H. (1978) Hippocampal place units in the freely moving rat: why they fire where they fire. *Exp. Brain Res.* 31, 573–590
56. Muller, R.U. and Kubie, J.L. (1987) The effects of changes in the environment on the spatial firing of hippocampal complex-spike cells. *J. Neurosci.* 7, 1951–1968
57. Thompson, L.T. and Best, P.J. (1989) Place cells and silent cells in the hippocampus of freely-behaving rats. *J. Neurosci.* 9, 2382–2390
58. Hayman, R.M.A. *et al.* (2003) Context-specific acquisition of location discrimination by hippocampal place cells. *Eur. J. Neurosci.* 18, 2825–2834
59. Leutgeb, S. *et al.* (2004) Distinct ensemble codes in hippocampal areas CA3 and CA1. *Science* 305, 1295–1298
60. Leutgeb, J.K. *et al.* (2005) Progressive transformation of hippocampal neuronal representations in “morphed” environments. *Neuron* 48, 345–358
61. Wills, T.J. (2005) Attractor dynamics in the hippocampal representation of the local environment. *Science* 308, 873–876
62. Alme, C.B. *et al.* (2014) Place cells in the hippocampus: eleven maps for eleven rooms. *Proc. Natl. Acad. Sci. U. S. A.* 111, 18428–18435
63. Ziv, Y. *et al.* (2013) Long-term dynamics of CA1 hippocampal place codes. *Nat. Neurosci.* 16, 264–266
64. Ferbinteanu, J. and Shapiro, M.L. (2003) Prospective and retrospective memory coding in the hippocampus. *Neuron* 40, 1227–1239
65. Zhang, S. and Manahan-Vaughan, D. (2015) Spatial olfactory learning contributes to place field formation in the hippocampus. *Cereb. Cortex* 25, 423–432
66. Aronov, D. *et al.* (2017) Mapping of a non-spatial dimension by the hippocampal–entorhinal circuit. *Nature* 543, 719–722
67. Pastalkova, E. *et al.* (2008) Internally generated cell assembly sequences in the rat hippocampus. *Science* 321, 1322–1327

68. Buzsáki, G. and Moser, E.I. (2013) Memory, navigation and theta rhythm in the hippocampal-entorhinal system. *Nat. Neurosci.* 16, 130–138
69. Muller, R.U. *et al.* (1987) Spatial firing patterns of hippocampal complex-spike cells in a fixed environment. *J. Neurosci.* 7, 1935–1950
70. Thompson, L.T. and Best, P.J. (1990) Long-term stability of the place-field activity of single units recorded from the dorsal hippocampus of freely behaving rats. *Brain Res.* 509, 299–308
71. Lever, C. *et al.* (2002) Long-term plasticity in hippocampal place-cell representation of environmental geometry. *Nature* 416, 90–94
72. Dong, C. *et al.* (2021) Distinct place cell dynamics in CA1 and CA3 encode experience in new environments. *Nat. Commun.* 12, 2977
73. Taube, J.S. *et al.* (1990) Head-direction cells recorded from the postsubiculum in freely moving rats. I. Description and quantitative analysis. *J. Neurosci.* 10, 420–435
74. Taube, J.S. *et al.* (1990) Head-direction cells recorded from the postsubiculum in freely moving rats. II. Effects of environmental manipulations. *J. Neurosci.* 10, 436–447
75. Stackman, R.W. and Taube, J.S. (1997) Firing properties of head direction cells in the rat anterior thalamic nucleus: dependence on vestibular input. *J. Neurosci.* 17, 4349–4358
76. Taube, J.S. (2007) The head direction signal: origins and sensory-motor integration. *Annu. Rev. Neurosci.* 30, 181–207
77. Langston, R.F. *et al.* (2010) Development of the spatial representation system in the rat. *Science* 328, 1576–1580
78. Wills, T.J. *et al.* (2010) Development of the hippocampal cognitive map in preweanling rats. *Science* 328, 1573–1576
79. Goodridge, J.P. *et al.* (1998) Cue control and head direction cells. *Behav. Neurosci.* 112, 749–761
80. Boccara, C.N. *et al.* (2010) Grid cells in pre- and parasubiculum. *Nat. Neurosci.* 13, 987–994
81. Brun, V.H. *et al.* (2002) Place cells and place recognition maintained by direct entorhinal-hippocampal circuitry. *Science* 296, 2243–2246
82. Stensola, H. *et al.* (2012) The entorhinal grid map is discretized. *Nature* 492, 72–78
83. Krupic, J. *et al.* (2012) Neural representations of location composed of spatially periodic bands. *Science* 337, 853–857
84. Stensola, T. *et al.* (2015) Shearing-induced asymmetry in entorhinal grid cells. *Nature* 518, 207–212
85. Fyhn, M. *et al.* (2007) Hippocampal remapping and grid realignment in entorhinal cortex. *Nature* 446, 190–194
86. Chen, G. *et al.* (2016) Absence of visual input results in the disruption of grid cell firing in the mouse. *Curr. Biol.* 26, 2335–2342
87. Pérez-Escobar, J.A. *et al.* (2016) Visual landmarks sharpen grid cell metric and confer context specificity to neurons of the medial entorhinal cortex. *Elife* 5
88. Diehl, G.W. *et al.* (2017) Grid and nongrid cells in medial entorhinal cortex represent spatial location and environmental features with complementary coding schemes. *Neuron* 94, 83–92.e6
89. Stensola, T. and Moser, E.I. (2016) Grid cells and spatial maps in entorhinal cortex and hippocampus. In *Research and Perspectives in Neurosciences*, pp. 59–80, Springer International Publishing
90. Krupic, J. *et al.* (2015) Grid cell symmetry is shaped by environmental geometry. *Nature* 518, 232–235

91. Solstad, T. *et al.* (2008) Representation of geometric borders in the entorhinal cortex. *Science* 322, 1865–1868
92. Lever, C. *et al.* (2009) Boundary vector cells in the subiculum of the hippocampal formation. *J. Neurosci.* 29, 9771–9777
93. Kropff, E. *et al.* (2015) Speed cells in the medial entorhinal cortex. *Nature* 523, 419–424
94. Hinman, J.R. *et al.* (2016) Multiple running speed signals in medial entorhinal cortex. *Neuron* 91, 666–679
95. Høydal, Ø.A. *et al.* (2019) Object-vector coding in the medial entorhinal cortex. *Nature* 568, 400–404
96. McNaughton, B.L. *et al.* (1996) Deciphering the hippocampal polyglot: the hippocampus as a path integration system. *J. Exp. Biol.* 199, 173–185
97. Etienne, A.S. *et al.* (1996) Path integration in mammals and its interaction with visual landmarks. *J. Exp. Biol.* 199, 201–209
98. Müller, M. and Wehner, R. (1988) Path integration in desert ants, *Cataglyphis fortis*. *Proc. Natl. Acad. Sci. U. S. A.* 85, 5287–5290
99. Merkle, T. *et al.* (2006) Uncertainty about nest position influences systematic search strategies in desert ants. *J. Exp. Biol.* 209, 3545–3549
100. Wittlinger, M. *et al.* (2006) The ant odometer: stepping on stilts and stumps. *Science* 312, 1965–1967
101. Maaswinkel, H. *et al.* (1999) Hippocampectomized rats are impaired in homing by path integration. *Hippocampus* 9, 553–561
102. Whishaw, I.Q. *et al.* (2001) Dead reckoning (path integration) requires the hippocampal formation: evidence from spontaneous exploration and spatial learning tasks in light (allothetic) and dark (idiothetic) tests. *Behav. Brain Res.* 127, 49–69
103. Campbell, M.G. *et al.* (2021) Distance-tuned neurons drive specialized path integration calculations in medial entorhinal cortex. *Cell Rep.* 36, 109669
104. Jacob, P.-Y. *et al.* (2017) Medial entorhinal cortex and medial septum contribute to self-motion-based linear distance estimation. *Brain Struct. Funct.* 222, 2727–2742
105. Van Cauter, T. *et al.* (2013) Distinct roles of medial and lateral entorhinal cortex in spatial cognition. *Cereb. Cortex* 23, 451–459
106. Knierim, J.J. *et al.* (1995) Place cells, head direction cells, and the learning of landmark stability. *J. Neurosci.* 15, 1648–1659
107. Quirk, G.J. *et al.* (1990) The firing of hippocampal place cells in the dark depends on the rat's recent experience. *J. Neurosci.* 10, 2008–2017
108. Gothard, K.M. *et al.* (1996) Dynamics of mismatch correction in the hippocampal ensemble code for space: interaction between path integration and environmental cues. *J. Neurosci.* 16, 8027–8040
109. Jeffery, K.J. *et al.* (1997) Directional control of hippocampal place fields. *Exp. Brain Res.* 117, 131–142
110. Terrazas, A. *et al.* (2005) Self-motion and the hippocampal spatial metric. *J. Neurosci.* 25, 8085–8096
111. Bjerknes, T.L. *et al.* (2018) Path integration in place cells of developing rats. *Proc. Natl. Acad. Sci. U. S. A.* 115, E1637–E1646
112. Winter, S.S. *et al.* (2015) Passive transport disrupts grid signals in the parahippocampal cortex. *Curr. Biol.* 25, 2493–2502

113. Gil, M. *et al.* (2018) Impaired path integration in mice with disrupted grid cell firing. *Nat. Neurosci.* 21, 81–91
114. Allen, K. *et al.* (2014) Impaired path integration and grid cell spatial periodicity in mice lacking GluA1-containing AMPA receptors. *J. Neurosci.* 34, 6245–6259
115. Bonnevie, T. *et al.* (2013) Grid cells require excitatory drive from the hippocampus. *Nat. Neurosci.* 16, 309–317
116. Muessig, L. *et al.* (2016) Place cell networks in pre-weanling rats show associative memory properties from the onset of exploratory behavior. *Cereb. Cortex* 26, 3627–3636
117. Muessig, L. *et al.* (2015) A developmental switch in place cell accuracy coincides with grid cell maturation. *Neuron* 86, 1167–1173
118. Bush, D. *et al.* (2014) What do grid cells contribute to place cell firing? *Trends Neurosci.* 37, 136–145
119. Chen, G. *et al.* (2019) Differential influences of environment and self-motion on place and grid cell firing. *Nat. Commun.* 10, 630
120. Valerio, S. and Taube, J.S. (2012) Path integration: how the head direction signal maintains and corrects spatial orientation. *Nat. Neurosci.* 15, 1445–1453
121. Butler, W.N. *et al.* (2017) The head-direction signal plays a functional role as a neural compass during navigation. *Curr. Biol.* 27, 1259–1267
122. Winter, S.S. *et al.* (2015) Spatial navigation. Disruption of the head direction cell network impairs the parahippocampal grid cell signal. *Science* 347, 870–874
123. Vanderwolf, C.H. (1969) Hippocampal electrical activity and voluntary movement in the rat. *Electroencephalogr. Clin. Neurophysiol.* 26, 407–418
124. McFarland, W.L. *et al.* (1975) Relationship between hippocampal theta activity and running speed in the rat. *J. Comp. Physiol. Psychol.* 88, 324–328
125. Sławińska, U. and Kasicki, S. (1998) The frequency of rat's hippocampal theta rhythm is related to the speed of locomotion. *Brain Res.* 796, 327–331
126. Hinman, J.R. *et al.* (2011) Septotemporal variation in dynamics of theta: speed and habituation. *J. Neurophysiol.* 105, 2675–2686
127. Jeewajee, A. *et al.* (2008) Grid cells and theta as oscillatory interference: electrophysiological data from freely moving rats. *Hippocampus* 18, 1175–1185
128. Brandon, M.P. *et al.* (2011) Reduction of theta rhythm dissociates grid cell spatial periodicity from directional tuning. *Science* 332, 595–599
129. Koenig, J. *et al.* (2011) The spatial periodicity of grid cells is not sustained during reduced theta oscillations. *Science* 332, 592–595
130. Buetfering, C. *et al.* (2014) Parvalbumin interneurons provide grid cell-driven recurrent inhibition in the medial entorhinal cortex. *Nat. Neurosci.* 17, 710–718
131. Ye, J. *et al.* (2018) Entorhinal fast-spiking speed cells project to the hippocampus. *Proc. Natl. Acad. Sci. U. S. A.* 115, E1627–E1636
132. Couey, J.J. *et al.* (2013) Recurrent inhibitory circuitry as a mechanism for grid formation. *Nat. Neurosci.* 16, 318–324
133. Miao, C. *et al.* (2017) Parvalbumin and somatostatin interneurons control different space-coding networks in the medial entorhinal cortex. *Cell* 171, 507–521.e17
134. Martin, M.M. *et al.* (2007) Medial septum lesions disrupt exploratory trip organization: evidence for septohippocampal involvement in dead reckoning. *Physiol. Behav.* 90, 412–424
135. Martin, M.M. and Wallace, D.G. (2007) Selective hippocampal cholinergic deafferentation impairs self-movement cue use during a food hoarding task. *Behav. Brain Res.* 183, 78–86

136. Doeller, C.F. *et al.* (2010) Evidence for grid cells in a human memory network. *Nature* 463, 657–661
137. Shine, J.P. *et al.* (2016) The human retrosplenial cortex and thalamus code head direction in a global reference frame. *J. Neurosci.* 36, 6371–6381
138. Eichenbaum, H. *et al.* (1987) Cue-sampling and goal-approach correlates of hippocampal unit activity in rats performing an odor-discrimination task. *J. Neurosci.* 7, 716–732
139. Dahm, R. (2006) Alzheimer’s discovery. *Curr. Biol.* 16, R906-10
140. Selkoe, D.J. (1991) The molecular pathology of Alzheimer’s disease. *Neuron* 6, 487–498
141. de la Torre, J.C. (2002) Alzheimer disease as a vascular disorder: nosological evidence. *Stroke* 33, 1152–1162
142. Kowalski, K. and Mulak, A. (2019) Brain-gut-Microbiota axis in Alzheimer’s disease. *J. Neurogastroenterol. Motil.* 25, 48–60
143. McBrayer, M. and Nixon, R.A. (2013) Lysosome and calcium dysregulation in Alzheimer’s disease: partners in crime. *Biochem. Soc. Trans.* 41, 1495–1502
144. Mohandas, E. *et al.* (2009) Neurobiology of Alzheimer’s disease. *Indian J. Psychiatry* 51, 55–61
145. Glenner, G.G. and Wong, C.W. (1984) Alzheimer’s disease: initial report of the purification and characterization of a novel cerebrovascular amyloid protein. *Biochem. Biophys. Res. Commun.* 120, 885–890
146. Masters, C.L. *et al.* (1985) Amyloid plaque core protein in Alzheimer disease and Down syndrome. *Proc. Natl. Acad. Sci. U. S. A.* 82, 4245–4249
147. Kang, J. *et al.* (1987) The precursor of Alzheimer’s disease amyloid A4 protein resembles a cell-surface receptor. *Nature* 325, 733–736
148. Goldgaber, D. *et al.* (1987) Characterization and chromosomal localization of a cDNA encoding brain amyloid of Alzheimer’s disease. *Science* 235, 877–880
149. Tanzi, R.E. *et al.* (1987) Amyloid beta protein gene: cDNA, mRNA distribution, and genetic linkage near the Alzheimer locus. *Science* 235, 880–884
150. Robakis, N.K. *et al.* (1987) Molecular cloning and characterization of a cDNA encoding the cerebrovascular and the neuritic plaque amyloid peptides. *Proc. Natl. Acad. Sci. U. S. A.* 84, 4190–4194
151. Bachurin, S.O. *et al.* (2017) Drugs in clinical trials for Alzheimer’s disease: The major trends. *Med. Res. Rev.* 37, 1186–1225
152. Hardy, J. and Allsop, D. (1991) Amyloid deposition as the central event in the aetiology of Alzheimer’s disease. *Trends Pharmacol. Sci.* 12, 383–388
153. Hardy, J.A. and Higgins, G.A. (1992) Alzheimer’s disease: the amyloid cascade hypothesis. *Science* 256, 184–185
154. Levy, E. *et al.* (1990) Mutation of the Alzheimer’s disease amyloid gene in hereditary cerebral hemorrhage, Dutch type. *Science* 248, 1124–1126
155. Goate, A. *et al.* (1991) Segregation of a missense mutation in the amyloid precursor protein gene with familial Alzheimer’s disease. *Nature* 349, 704–706
156. Eckman, C.B. *et al.* (1997) A new pathogenic mutation in the APP gene (I716V) increases the relative proportion of A beta 42(43). *Hum. Mol. Genet.* 6, 2087–2089
157. De Jonghe, C. *et al.* (2001) Pathogenic APP mutations near the gamma-secretase cleavage site differentially affect A beta secretion and APP C-terminal fragment stability. *Hum. Mol. Genet.* 10, 1665–1671

158. Tcw, J. and Goate, A.M. (2017) Genetics of  $\beta$ -amyloid precursor protein in Alzheimer's disease. *Cold Spring Harb. Perspect. Med.* 7, a024539
159. Sherrington, R. *et al.* (1995) Cloning of a gene bearing missense mutations in early-onset familial Alzheimer's disease. *Nature* 375, 754–760
160. Levy-Lahad, E. *et al.* (1995) Candidate gene for the chromosome 1 familial Alzheimer's disease locus. *Science* 269, 973–977
161. Rogaev, E.I. *et al.* (1995) Familial Alzheimer's disease in kindreds with missense mutations in a gene on chromosome 1 related to the Alzheimer's disease type 3 gene. *Nature* 376, 775–778
162. Games, D. *et al.* (1995) Alzheimer-type neuropathology in transgenic mice overexpressing V717F beta-amyloid precursor protein. *Nature* 373, 523–527
163. Sasaguri, H. *et al.* (2017) APP mouse models for Alzheimer's disease preclinical studies. *EMBO J.* 36, 2473–2487
164. Lanoiselée, H.-M. *et al.* (2017) APP, PSEN1, and PSEN2 mutations in early-onset Alzheimer disease: A genetic screening study of familial and sporadic cases. *PLoS Med.* 14, e1002270
165. Corder, E.H. *et al.* (1993) Gene dose of apolipoprotein E type 4 allele and the risk of Alzheimer's disease in late onset families. *Science* 261, 921–923
166. Schmechel, D.E. *et al.* (1993) Increased amyloid beta-peptide deposition in cerebral cortex as a consequence of apolipoprotein E genotype in late-onset Alzheimer disease. *Proc. Natl. Acad. Sci. U. S. A.* 90, 9649–9653
167. Mattsson, N. *et al.* (2018) Prevalence of the apolipoprotein E  $\epsilon$ 4 allele in amyloid  $\beta$  positive subjects across the spectrum of Alzheimer's disease. *Alzheimers. Dement.* 14, 913–924
168. Bagaria, J. *et al.* (2021) Importance of GWAS in finding un-targeted genetic association of sporadic Alzheimer's disease. *Mol. Cell. Toxicol.* DOI: 10.1007/s13273-021-00130-z
169. Lippa, C.F. *et al.* (1996) Familial and sporadic Alzheimer's disease: neuropathology cannot exclude a final common pathway. *Neurology* 46, 406–412
170. Yankner, B.A. *et al.* (1989) Neurotoxicity of a fragment of the amyloid precursor associated with Alzheimer's disease. *Science* 245, 417–420
171. Morris, G.P. *et al.* (2014) Inconsistencies and controversies surrounding the amyloid hypothesis of Alzheimer's disease. *Acta Neuropathol. Commun.* 2, 135
172. Wisniewski, T. *et al.* (1993) Apolipoprotein E: binding to soluble Alzheimer's beta-amyloid. *Biochem. Biophys. Res. Commun.* 192, 359–365
173. Castellano, J.M. *et al.* (2011) Human apoE isoforms differentially regulate brain amyloid- $\beta$  peptide clearance. *Sci. Transl. Med.* 3, 89ra57
174. Mawuenyega, K.G. *et al.* (2010) Decreased clearance of CNS beta-amyloid in Alzheimer's disease. *Science* 330, 1774
175. Terry, R.D. *et al.* (1991) Physical basis of cognitive alterations in Alzheimer's disease: synapse loss is the major correlate of cognitive impairment. *Ann. Neurol.* 30, 572–580
176. Lue, L.F. *et al.* (1999) Soluble amyloid beta peptide concentration as a predictor of synaptic change in Alzheimer's disease. *Am. J. Pathol.* 155, 853–862
177. Jansen, W.J. *et al.* (2015) Prevalence of cerebral amyloid pathology in persons without dementia. *JAMA* 313, 1924
178. Shankar, G.M. *et al.* (2008) Amyloid-beta protein dimers isolated directly from Alzheimer's brains impair synaptic plasticity and memory. *Nat. Med.* 14, 837–842
179. Walsh, D.M. and Selkoe, D.J. (2007) A beta oligomers - a decade of discovery. *J. Neurochem.* 101, 1172–1184

180. Yang, T. *et al.* (2017) Large soluble oligomers of amyloid  $\beta$ -protein from Alzheimer brain are far less neuroactive than the smaller oligomers to which they dissociate. *J. Neurosci.* 37, 152–163
181. Kosik, K.S. *et al.* (1986) Microtubule-associated protein tau (tau) is a major antigenic component of paired helical filaments in Alzheimer disease. *Proc. Natl. Acad. Sci. U. S. A.* 83, 4044–4048
182. Di, J. *et al.* (2016) Abnormal tau induces cognitive impairment through two different mechanisms: synaptic dysfunction and neuronal loss. *Sci. Rep.* 6, 20833
183. Braak, H. and Braak, E. (1991) Neuropathological staging of Alzheimer-related changes. *Acta Neuropathol.* 82, 239–259
184. Shi, Y. *et al.* (2017) ApoE4 markedly exacerbates tau-mediated neurodegeneration in a mouse model of tauopathy. *Nature* 549, 523–527
185. van der Kant, R. *et al.* (2020) Amyloid- $\beta$ -independent regulators of tau pathology in Alzheimer disease. *Nat. Rev. Neurosci.* 21, 21–35
186. Jack, C.R., Jr *et al.* (2013) Tracking pathophysiological processes in Alzheimer’s disease: an updated hypothetical model of dynamic biomarkers. *Lancet Neurol.* 12, 207–216
187. Crary, J.F. *et al.* (2014) Primary age-related tauopathy (PART): a common pathology associated with human aging. *Acta Neuropathol.* 128, 755–766
188. Braak, H. and Braak, E. (1997) Frequency of stages of Alzheimer-related lesions in different age categories. *Neurobiol. Aging* 18, 351–357
189. Price, J.L. and Morris, J.C. (1999) Tangles and plaques in nondemented aging and “preclinical” Alzheimer’s disease. *Ann. Neurol.* 45, 358–368
190. Lewis, J. *et al.* (2001) Enhanced neurofibrillary degeneration in transgenic mice expressing mutant tau and APP. *Science* 293, 1487–1491
191. Oddo, S. *et al.* (2003) Triple-transgenic model of Alzheimer’s disease with plaques and tangles: intracellular A $\beta$  and synaptic dysfunction. *Neuron* 39, 409–421
192. Klunk, W.E. *et al.* (2004) Imaging brain amyloid in Alzheimer’s disease with Pittsburgh Compound-B. *Ann. Neurol.* 55, 306–319
193. Chien, D.T. *et al.* (2013) Early clinical PET imaging results with the novel PHF-tau radioligand [F-18]-T807. *J. Alzheimers. Dis.* 34, 457–468
194. Lee, J.C. *et al.* (2019) Diagnosis of Alzheimer’s disease utilizing amyloid and tau as fluid biomarkers. *Exp. Mol. Med.* 51, 1–10
195. Johnson, K.A. *et al.* (2016) Tau positron emission tomographic imaging in aging and early Alzheimer disease. *Ann. Neurol.* 79, 110–119
196. Ossenkoppele, R. *et al.* (2019) Associations between tau, A $\beta$ , and cortical thickness with cognition in Alzheimer disease. *Neurology* 92, e601–e612
197. Bejanin, A. *et al.* (2017) Tau pathology and neurodegeneration contribute to cognitive impairment in Alzheimer’s disease. *Brain* 140, 3286–3300
198. Aschenbrenner, A.J. *et al.* (2018) Influence of tau PET, amyloid PET, and hippocampal volume on cognition in Alzheimer disease. *Neurology* 91, e859–e866
199. Schwarz, A.J. *et al.* (2016) Regional profiles of the candidate tau PET ligand 18F-AV-1451 recapitulate key features of Braak histopathological stages. *Brain* 139, 1539–1550
200. Schöll, M. *et al.* (2016) PET imaging of tau deposition in the aging human brain. *Neuron* 89, 971–982
201. Therriault, J. *et al.* (2022) Biomarker modeling of Alzheimer’s disease using PET-based Braak staging. *Nat Aging* 2, 526–535

202. McKhann, G. *et al.* (1984) Clinical diagnosis of Alzheimer's disease: report of the NINCDS-ADRDA Work Group under the auspices of Department of Health and Human Services Task Force on Alzheimer's Disease. *Neurology* 34, 939–944
203. Jack, C.R., Jr *et al.* (2011) Introduction to the recommendations from the National Institute on Aging-Alzheimer's Association workgroups on diagnostic guidelines for Alzheimer's disease. *Alzheimers. Dement.* 7, 257–262
204. Jack, C.R., Jr *et al.* (2018) NIA-AA Research Framework: Toward a biological definition of Alzheimer's disease. *Alzheimers. Dement.* 14, 535–562
205. Braak, H. and Del Tredici, K. (2011) The pathological process underlying Alzheimer's disease in individuals under thirty. *Acta Neuropathol.* 121, 171–181
206. Vemuri, P. *et al.* (2011) Cognitive reserve and Alzheimer's disease biomarkers are independent determinants of cognition. *Brain* 134, 1479–1492
207. Sperling, R.A. *et al.* (2011) Testing the right target and right drug at the right stage. *Sci. Transl. Med.* 3, 111cm33
208. Yiannopoulou, K.G. *et al.* (2019) Reasons for failed trials of disease-modifying treatments for Alzheimer disease and their contribution in recent research. *Biomedicines* 7, 97
209. Jack, C.R., Jr *et al.* (2019) Prevalence of biologically vs clinically defined Alzheimer spectrum entities using the National Institute on aging-Alzheimer's Association research framework. *JAMA Neurol.* 76, 1174
210. Dubois, B. *et al.* (2014) Advancing research diagnostic criteria for Alzheimer's disease: the IWG-2 criteria. *Lancet Neurol.* 13, 614–629
211. Tromp, D. *et al.* (2015) Episodic memory in normal aging and Alzheimer disease: Insights from imaging and behavioral studies. *Ageing Res. Rev.* 24, 232–262
212. Hornberger, M. and Piguet, O. (2012) Episodic memory in frontotemporal dementia: a critical review. *Brain* 135, 678–692
213. Berron, D. *et al.* (2021) Early stages of tau pathology and its associations with functional connectivity, atrophy and memory. *Brain* 144, 2771–2783
214. Cacucci, F. *et al.* (2008) Place cell firing correlates with memory deficits and amyloid plaque burden in Tg2576 Alzheimer mouse model. *Proc. Natl. Acad. Sci. U. S. A.* 105, 7863–7868
215. Zhao, R. *et al.* (2014) Impairments in experience-dependent scaling and stability of hippocampal place fields limit spatial learning in a mouse model of Alzheimer's disease. *Hippocampus* 24, 963–978
216. Cayzac, S. *et al.* (2015) Altered hippocampal information coding and network synchrony in APP-PS1 mice. *Neurobiol. Aging* 36, 3200–3213
217. Mably, A.J. *et al.* (2017) Impairments in spatial representations and rhythmic coordination of place cells in the 3xTg mouse model of Alzheimer's disease. *Hippocampus* 27, 378–392
218. Jun, H. *et al.* (2020) Disrupted place cell remapping and impaired grid cells in a knockin model of Alzheimer's disease. *Neuron* 107, 1095-1112.e6
219. Cheng, J. and Ji, D. (2013) Rigid firing sequences undermine spatial memory codes in a neurodegenerative mouse model. *Elife* 2, e00647
220. Fu, H. *et al.* (2017) Tau pathology induces excitatory neuron loss, grid cell dysfunction, and spatial memory deficits reminiscent of early Alzheimer's disease. *Neuron* 93, 533-541.e5
221. Ridler, T. *et al.* (2020) Impaired speed encoding and grid cell periodicity in a mouse model of tauopathy. *Elife* 9
222. Wright, A.L. *et al.* (2013) Neuroinflammation and neuronal loss precede A $\beta$  plaque deposition in the hAPP-J20 mouse model of Alzheimer's disease. *PLoS One* 8, e59586

223. Kim, S. *et al.* (2013) Contrasting effects on path integration after hippocampal damage in humans and rats. *Proc. Natl. Acad. Sci. U. S. A.* 110, 4732–4737
224. Clark, B.J. and Taube, J.S. (2012) Vestibular and attractor network basis of the head direction cell signal in subcortical circuits. *Front. Neural Circuits* 6, 7
225. Hafting, T. *et al.* (2008) Hippocampus-independent phase precession in entorhinal grid cells. *Nature* 453, 1248–1252
226. O’Keefe, J. and Recce, M.L. (1993) Phase relationship between hippocampal place units and the EEG theta rhythm. *Hippocampus* 3, 317–330
227. Skaggs, W.E. *et al.* (1996) Theta phase precession in hippocampal neuronal populations and the compression of temporal sequences. *Hippocampus* 6, 149–172
228. Kropff, E. *et al.* (2021) Frequency of theta rhythm is controlled by acceleration, but not speed, in running rats. *Neuron* 109, 1029-1039.e8
229. Jacob, P.-Y. *et al.* (2014) Vestibular control of entorhinal cortex activity in spatial navigation. *Front. Integr. Neurosci.* 8, 38
230. Ravassard, P. *et al.* (2013) Multisensory control of hippocampal spatiotemporal selectivity. *Science* 340, 1342–1346
231. Burgess, N. (2008) Grid cells and theta as oscillatory interference: theory and predictions. *Hippocampus* 18, 1157–1174
232. Burgess, N. *et al.* (2007) An oscillatory interference model of grid cell firing. *Hippocampus* 17, 801–812
233. Navratilova, Z. *et al.* (2012) Phase precession and variable spatial scaling in a periodic attractor map model of medial entorhinal grid cells with realistic after-spike dynamics. *Hippocampus* 22, 772–789
234. Barry, C. *et al.* (2007) Experience-dependent rescaling of entorhinal grids. *Nat. Neurosci.* 10, 682–684
235. Gómez-Isla, T. *et al.* (1996) Profound loss of layer II entorhinal cortex neurons occurs in very mild Alzheimer’s disease. *J. Neurosci.* 16, 4491–4500
236. Kordower, J.H. *et al.* (2001) Loss and atrophy of layer II entorhinal cortex neurons in elderly people with mild cognitive impairment. *Ann. Neurol.* 49, 202–213
237. Nagahara, A.H. *et al.* (2013) Early BDNF treatment ameliorates cell loss in the entorhinal cortex of APP transgenic mice. *J. Neurosci.* 33, 15596–15602
238. de Calignon, A. *et al.* (2012) Propagation of tau pathology in a model of early Alzheimer’s disease. *Neuron* 73, 685–697
239. Palop, J.J. *et al.* (2007) Aberrant excitatory neuronal activity and compensatory remodeling of inhibitory hippocampal circuits in mouse models of Alzheimer’s disease. *Neuron* 55, 697–711
240. Kobre-Flatmoen, A. *et al.* (2016) Reelin-immunoreactive neurons in entorhinal cortex layer II selectively express intracellular amyloid in early Alzheimer’s disease. *Neurobiol. Dis.* 93, 172–183
241. Rowland, D.C. *et al.* (2018) Functional properties of stellate cells in medial entorhinal cortex layer II. *Elife* 7
242. Zhi, Y. and Cox, D. (2021) Neurodegenerative damage reduces firing coherence in a continuous attractor model of grid cells. *Phys. Rev. E.* 104, 044414
243. Zutshi, I. *et al.* (2018) Hippocampal neural circuits respond to optogenetic pacing of theta frequencies by generating accelerated oscillation frequencies. *Curr. Biol.* 28, 1179-1188.e3

244. Quirk, C.R. *et al.* (2021) Precisely timed theta oscillations are selectively required during the encoding phase of memory. *Nat. Neurosci.* 24, 1614–1627
245. Lepperød, M.E. *et al.* (2021) Optogenetic pacing of medial septum parvalbumin-positive cells disrupts temporal but not spatial firing in grid cells. *Sci. Adv.* 7, eabd5684
246. Coyle, J.T. *et al.* (1983) Alzheimer's disease: a disorder of cortical cholinergic innervation. *Science* 219, 1184–1190
247. Whitehouse, P.J. *et al.* (1981) Alzheimer disease: evidence for selective loss of cholinergic neurons in the nucleus basalis. *Ann. Neurol.* 10, 122–126
248. Liu, A.K.L. *et al.* (2015) Nucleus basalis of Meynert revisited: anatomy, history and differential involvement in Alzheimer's and Parkinson's disease. *Acta Neuropathol.* 129, 527–540
249. Coutrot, A. *et al.* (2019) Virtual navigation tested on a mobile app is predictive of real-world wayfinding navigation performance. *PLoS One* 14, e0213272